STRUCTURAL AND CHOLESTEROL BINDING PROPERTIES OF THE AMYLOID

PRECURSOR PROTEIN C-TERMINAL FRAGMENT C99 AND THE ETIOLOGY OF

ALZHEIMER'S DISEASE

By

Paul John Barrett

Dissertation

Submitted to the Faculty of the

Graduate School of Vanderbilt University

in partial fulfillment of the requirements

for the degree of

DOCTOR OF PHILOSOPHY

in

Biochemistry

December, 2013

Nashville, Tennessee

Approved by:

Professor Charles Sanders, Ph.D.

Professor Anne Kenworthy, Ph.D.

Professor Bruce Carter, Ph.D.

Professor Walter J. Chazin, Ph.D.

Professor Richard Armstrong, Ph.D.

To my loving wife,

Caitlyn Barrett

And my loving parents,

William and Linda Barrett

ACKNOWLEDGMENTS

discussions on how we should start a "Nature Non-Methods" journal. A thanks goes to my loving parents, William and Linda Barrett and Catherine and Edward Whitten, all of whom have never stopped supporting me. The same thanks goes to my sisters Caitlin and Megan Barrett and Carlyn Whitten, as well as to my brother Charles Whitten. The relationships I have developed with all of you over these past 5 years could not be stronger, and I look forward to many fun family adventures in the future. Last, but certainly not least, I need to give my never-ending gratitude to my loving wife Dr. Caitlyn Barrett. Without her love, kindness, and constant support the completion of graduate school would have been an insurmountable task. I cannot express how truly grateful I am for her and how much she did to help me accomplish this.

My love and thanks goes to all mentioned and many more not. You will always be in my thoughts and heart, and know that I could not accomplish this without you.

TABLE OF CONTENTS

Page

LIST OF TABLES

LIST OF FIGURES

LIST OF ABBREVIATIONS

Aβ	Amyloid-β
AD	Alzheimer's Disease
AICD	APP Intracellular Domain
AMPS	2-Acrylamido-2-methylpropane sulfonic acid
ApoE	Apolipoprotein E
APP	Amyloid Precursor Protein
CAC	Critical Aggregation Concentration
CHAPSO	3-[(3-Cholamidopropyl)dimethylammonio]-2-hydroxy-1-propanesulfonate
CMC	Critical Micelle Concentration
CRAC	Cholesterol Recognition Amino Acid Consensus
CSA	Chemical Shift Anisotropy
CSI	Chemical Shift Indexing
CW	Continuous Wave
CYP46	24S-cholesterol hydroxylase
DD	Dipole-Dipole
DEER	Double Electron Electron Resonance
DHPC	Dihexanoylphosphatidylcholine
DioC18	3,3'-Dioctadecyloxacarbocyanine Percholorate
DLS	Dynamic Light Scattering
DMPC	Dimyristoylphosphatidylcholine
DMSO	Dimethyl Sulfoxide
DR6	Death Receptor 6
DTT	Dithiothreitol
EGFR	Epithelial Growth Factor Receptor

EPR	Electron Paramagnetic Resonance
ER	Endoplasmic Reticulum
FAD	Familial Alzheimer's Disease
FID	Free Induction Decay
FRET	Fluorescence Resonance Energy Transfer
GPMV	Giant Plasma Membrane Derived Vesicles
GSM	γ-Secretase Modulator
GUV	Giant Unilamellar Vesicle
HDX	Hydrogen Deuterium Exchange
HMGCoA	3-Hydroxy-3-Methylglutaryl-Coenzyme-A Reductase
HSQC	Heteronuclear Single Quantum Coherence
IMAC	Immobilized Metal Affinity Chromatography
INEPT	Insensitive Nuclei Enhanced by Polarization Transfer
IPTG	Isopropyl β-D-1-Thiogalactopyranoside
ITO	Indium Tin Oxide
L_d	Liquid Disordered
LMPG	Lyso-Myristoylphosphatidylglycerol
L_o	Liquid Ordered
mGluR	Metabotropic Glutamate Receptor
MTSL	*S*-(2,2,5,5-tetramethyl-2,5-dihydro-1H-pyrrol-3-yl)methyl methanethiosulfonate
MWCO	Molecular Weight Cut Off
NMDAR	N-Methyl-D-Aspartate Receptor
NMR	Nuclear Magnetic Resonance
NOE	Nuclear Overhauser Enhancement
NSAID	Non-Steroidal Anti Inflammatory Drug

PDB	Protein Data Bank
PELDOR	Pulsed Electron-Electron Double Resonance
POPC	Phosphatidlycholine
POPE	Phosphatidylethanolamine
POPI	Phosphatidylinostitol
POPS	Phosphatidylserine
PRE	Paramagnetic Relaxation Ehancement
PS	Power Saturation
RDC	Residual Dipolar Coupling
RF	Radio Frequency
Rho-PE	1,2-dioleoyl-*sn*-glycero-3-phosphoethanolamine-N-(lissamine rhodamine B sulfonyl) (ammonium salt)
RMSD	Residual Mean Squared Deviation
sAPPα	Soluble Cleavage Product of APP by α-Secretase
sAPPβ	Soluble Cleavage Product of APP by β-Secretase
SDS	Sodium dodecyl sulfate
Seladin-1	Selective Alzheimer's Disease Indicator
SM	Sphingomyelin
SPR	Surface Plasmon Resonance
TEM	Transmission Electron Microscopy
TGN	Trans-Golgi Network
TMD	Transmembrane Domain
TROSY	Transverse Relaxation Optimized Spectroscopy

CHAPTER I

INTRODUCTION

Alzheimer's disease (AD) is the most prevalent form of dementia worldwide. Currently, it is estimated that nearly 40 million people suffer from this devastating form of dementia, and it is estimated that, if the current forms of treatment and diagnosis persist, this number will jump to 120 million as soon as 2050 (*1*). New treatment and diagnostic methods are still being developed, as we are only beginning to understand the mechanisms that drive this disease. The following work will attempt to put forth novel information showing both how structural biological information and cholesterol/protein interactions may play key roles in the etiology and pathology of AD.

Historical Perspective

It was in 1907 when Dr. Alois Alzheimer published the results of his findings following the autopsy of his patient, Auguste Deter. Prior to his publication, Dr. Alzheimer spent 4 years with Ms. Deter, during which her case appeared so unusual that it could not be classified as any recognizable illness. Alzheimer reported Ms. Deter as "unable to understand any situation" and "her memory is seriously impaired, if objects are shown to her, she names them correctly, but almost immediately afterwards she has forgotten everything" (*2*). As Ms. Deter's illness progressed, it was noted that her complex symptoms sometimes appeared stronger, and on other days weaker, but they never reached a critical level. Before performing the autopsy, Alzheimer could only find a slight hardening of the radial arteries as a means for diagnosis.

Post-mortem analysis of brain tissue showed an evenly atrophic brain, with the larger vascular tissues showing increased arteriosclerosis. Alzheimer also noticed two

key phenotypical changes present in Ms. Deter's brain tissue. The first was described as "Inside of a cell which appears to be quite normal, one or several fibrils can be distinguished by their unique thickness and capacity for impregnation." Alzheimer noticed that these "fibrils" were found next to apoptotic neurons. The second component noticed was described as "minute miliary foci which as caused by the deposition of a special substance in the cortex." In addition to these clear changes in the brain tissue, Alzheimer further commented that "Approximately ¼ to $^1/_3$ of all neurons in the cortex show these changes. Many neurons, especially those in the upper layer, have completely disappeared" (*2*).

While he did not know it, Alzheimer had described the key defining pathological features of AD. The "fibrils" he discovered were aggregations of the hyperphosphorylated microtubule stabilizing protein tau; which are now commonly referred to as neurofibrillary tangles. The "miliary foci" were aggregations of the Aβ peptide; commonly referred to as Aβ or amyloid plaques. As of the present date, the clinical definition of AD is a form of dementia characterized by the presence of proteinaceous deposits in the cerebral vessels and in the parenchyma of the affected brain region. Regions implicated in AD include the prefrontal and entorhinal cortex and the hippocampus, regions of the brain associated with memory formation, cognitive function, expression of emotions, and other higher level brain functions (*1*). One anecdote of particular interest to Dr. Alzheimer's findings was not only did he describe the initial pathology of AD, but his patient also developed the disease at the early age of 51, making this also the first documented case of early onset AD; also known as familial Alzheimer's disease (FAD) (*3*), since it is caused by specific, inherited mutations.

The "deposition of a special substance" described by Alzheimer was eventually isolated 77 years later by Dr. George Glenner and Caine Wong at UCSD in 1984. While it was known these depositions were amyloid like in nature (aggregates of a β-sheet

stacked protein), the identity of the initiating protein was unknown. By using polarization microscopy, Glenner and Wong were able to isolate these amyloid aggregates from the meningeal vessels of post-mortem AD patient brains. Following the isolation and subsequent purification by HPLC, Glenner and Wong identified a peptide of 4,200 daltons (4.2 kDa) and termed it the Aβ, or amyloid β polypeptide. Interestingly, Glenner and Wong also identified an additional peak at lower abundance during the HPLC study of 4 kDa. This was the first evidence that the Aβ polypeptide is not only the cleavage product of a larger protein, but that different Aβ lengths could have different aggregation properties (*4*). Three years later, the lab of Benno Müller-Hill determined that the Aβ peptide was in fact a cleavage product of a larger protein, by showing that the Aβ peptide came from the Amyloid Precursor Protein (APP), a transmembrane protein of neuronal origin approximately 695 amino acids in length (*5*).

The Amyloid Hypothesis

The evidence provided by Alios Alzheimer and others indicated that the Aβ peptide, and more specifically the ability of this protein to oligomerize and aggregate, was important to the progression of AD. It was apparent that dysregulation in the function of Aβ, and most likely APP, could strongly promote a cascade of cellular changes that drove the development of AD. This became known as the "amyloid hypothesis" (*6*). The amyloid hypothesis was initially put forth in 1991 by John Hardy and David Allsop, when they discovered that the gene encoding APP was found on chromosome 21; the same chromosome that causes Down syndrome (*7*). It was later found by Nistor and colleagues that patients with Down syndrome exhibit AD like symptoms by age 40, implicating APP as a potential link between the two diseases (*8*). Hardy and Allsop hypothesized that altered regulation in the metabolism of APP led to the overproduction of Aβ during AD. The amyloid hypothesis has since evolved from the

initial findings of Hardy and Allsop, and now it includes many different risk factors, such as genetic and environmental influences, that can cause the dysregulation of APP metabolism and not only promote Aβ generation, but also enhance the deleterious effects of its oligomerization and aggregation. Figure 1.1 highlights the cascade of events involved in the amyloid hypothesis.

The Amyloid Hypothesis
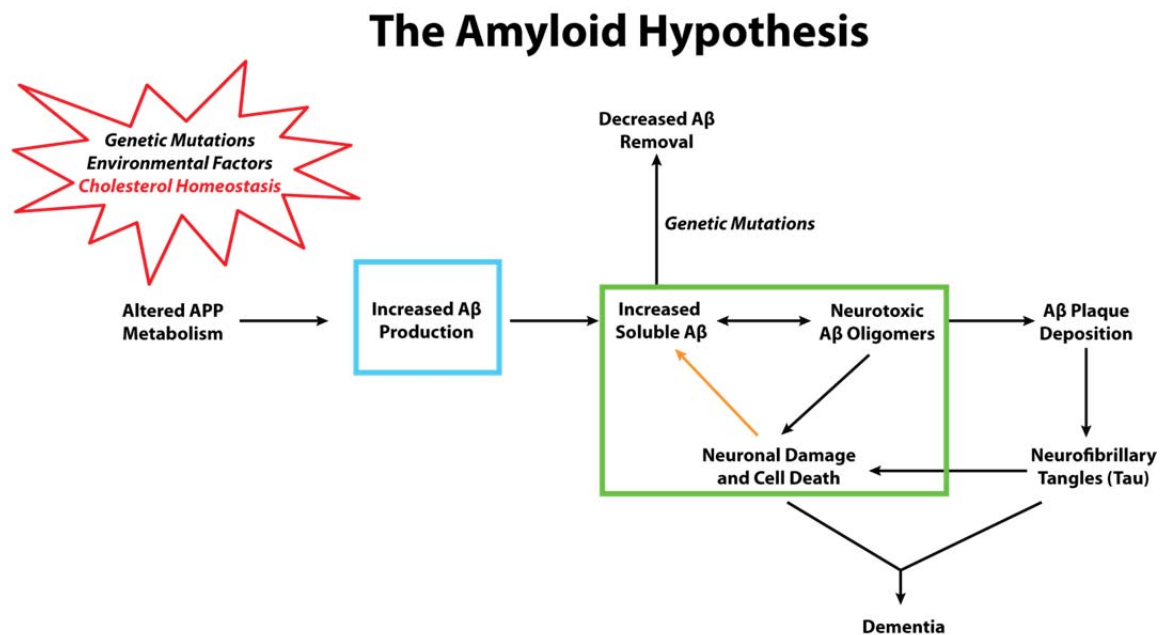
Figure 1.1. The amyloid hypothesis is a series of events that leads to the overproduction of the Aβ peptide, which causes neuronal cell death, and ultimately leads to dementia. APP metabolism in the cell can be altered by a number of factors (highlighted red). This work will focus on cholesterol homeostasis. This altered metabolism leads to an increase in Aβ production (highlighted in cyan). Studies below will show mechanisms that potentially lead to this increase in Aβ levels. Overproduction of the Aβ peptide is followed by Aβ oligomerization and neuronal cell death (highlighted in green). Neuronal cell death is a potential mechanism that feeds back into this loop by releasing additional Aβ back into the brain (highlighted with the orange arrow). All these factors lead to the phenotype of dementia seen in patients with AD.

The goal of this thesis is to gain a better understanding of how structural and functional features of proteins within the amyloid hypothesis, specifically APP and its proteolytic components, may contribute to increased Aβ production, and ultimately, AD.

The Biological Role of APP

In order to gain a better understanding of how APP can contribute to the overproduction of Aβ during AD, it is essential to know the biological role APP plays in maintaining cell viability, especially in neuronal cells, as any alteration in this function may contribute to AD pathogenesis. Efforts to define the ultimate function of APP in neurons have proven difficult, however, as the sequence, knockout trials, and other experiments have suggested multiple roles the protein may fill.

The amyloid precursor protein (APP) is a single-pass transmembrane protein that is expressed throughout the body (*9*). There are various isoforms found, with the major form in the brain being 695 amino acids in length (*5*). Of these amino acids, only approximately 70 residues make up the transmembrane helix and C-terminal intracellular domain, leaving an extremely large, multi-domain extracellular N-terminus that includes heparin, F-Spondin, and collagen binding regions (*10*). These characteristics led initial studies to speculate that APP may function as a putative receptor or adhesion molecule at the membrane surface. The large, multi-domain extracellular region had many structural similarities to known receptors, such as Notch and EGFR (*11, 12*), as well as select Integrin dimers (*13*).

Congruent with functioning either as a receptor or as an adhesion protein are the multiple GxxxG motifs within the transmembrane helix of APP (*14-16*). These are known motifs within helical transmembrane proteins that allow for avid homo- and heterodimerization, based on the high level of close packing and van der Waals interactions provided by the small glycine residues (*17-19*). It is through this mechanism which EGFR functions, where upon binding an extracellular ligand, EGFR transmembrane dimerization occurs, initiating a signaling cascade within the cell (*20-22*). Additionally, it is known that these GxxxG interactions occur in different Integrin systems,

allowing for activation/deactivation of the Integrin complex (*23-25*). Though empirical evidence suggests APP may function as a membrane receptor or adhesion protein, researchers have been hard pressed to identify the absolute biological function of full length APP. In addition to this fact, recent evidence has suggested that the GxxxG motifs of APP may not only function as a dimerization domain, but also as a cholesterol binding region, suggesting alternate biological functions modulated by the same transmembrane region (*26-28*). Recent work from Pierrot *et al* collaborates the importance of the cholesterol interaction, as they showed that increases in cholesterol content increase APP expression(*29*). Taken in conjunction with the finding that the transmembrane region of APP can bind cholesterol, it highlights the hypothesis that APP may function as a cholesterol sensor within the cell membrane (*30*).

Competing Cleavage Pathways of APP

While the exact function of APP is still being explored, it is widely accepted that APP is able to be cleaved by multiple enzymes in two distinct mechanisms, known as the Non-Amyloidogenic and Amyloidogenic pathways, as certain cleavage products of the amyloidogenic pathway lead to AD onset (*10, 15, 31-34*). The non-amyloidogenic pathway, which is the more common of the two cleavage cascades, is initiated by cleavage, or "shedding" by the transmembrane enzyme α-secretase, a member of the metalloprotease family (*35, 36*). Cleavage by α-secretase occurs at residue L688 (using the APP770 numbering nomenclature), releasing a large, soluble ectodomain (sAPPα) and forming the transmembrane fragment C83 (83 amino acids in length). Cleavage of APP by α-Secretase occurs at the plasma membrane surface (*1*). Following cleavage by α-Secretase, C83 is subject to subsequent cleavage within the membrane by an enzyme complex called γ-Secretase (*31*). γ-Secretase consists of four transmembrane proteins; presenilin-1 or -2 (PS-1/PS-2), anterior pharynx defective (APH-1), presenilin

enhancer-2 (PSEN-2), and nicastrin (*37-39*), with the active site occurring between two aspartyl residues within presenilin. Cleavage of C83 occurs within the cell membrane, splitting the transmembrane helix into two components, a signaling peptide called P3 and the APP intracellular domain (AICD) (*31*). The details of γ-Secretase cleavage will be discussed in further detail later on.

The residues cleaved by α-secretase cleavage are proximal to the cell membrane surface (*28*), and it has been shown that when moved to a rigid membrane environment (Liquid ordered domains), α-secretase cleavage can be inhibited (*40*). This is of particular importance as it is postulated that endogenous α-secretase cleavage occurs in fluid membrane domains on the cell membrane surface that are devoid of cholesterol and sphingomyelin and it has been shown that elevated levels of cholesterol may actively inhibit α-secretase cleavage of APP (*41-43*). When overexpressed in cells, mice, or injected into adult animals, sAPPα has been shown to enhance cognitive ability by promoting neuron growth, neuron survival, and neuron motility and improving synaptic density (*44, 45*). Interestingly, these were the same results reported during full length APP overexpression studies (*46*), and when the subsequent RNAi studies were performed, these results were ameliorated (*47*), suggesting that α-Secretase cleavage of APP plays a role in neuron outgrowth and possibly in neuron protection.

The amyloidogenic pathway is initiated by the enzyme β-Secretase (BACE1), a transmembrane protein that is part of the aspartyl protease family (*48*). β-Secretase cleavage occurs only sixteen residues N-terminal to the α-Secretase cleavage location at residue D672. β-Secretase cleavage sheds a large, soluble ectodomain (sAPPβ) and generates a transmembrane peptide called C99 (99 amino acids in length). Cleavage by β-Secretase occurs in early and late endosomes, which have a lower pH to facilitate the aspartyl cleavage mechanism. In order for β-Secretase cleavage to occur, APP and β-Secretase must be transported into endocytic vesicles, either by endocytosis from the

plasma membrane or by movement from the trans golgi network into endosomal compartments (*49*). Similar to C83, C99 is subject to cleavage by the enzyme complex γ-secretase. The AICD polypeptide is again generated, but instead of the signaling P3 peptide, cleavage of C99 by γ-secretase generates the Aβ peptide (*31, 35, 50*), which can accumulate overtime and lead to the onset of AD. While ultimately the over generation, oligomerization, and aggregation of the Aβ peptide is what leads to AD, by gaining a deeper understanding of the amyloidogenic pathway we will ultimately discover what drives the overproduction of the Aβ peptide in AD.

At first glance it may seem that the amyloidogenic pathway serves no purpose other than to promote AD progression, as this cleavage pathway endogenously occurs at a much lower frequency than the non-amyloidogenic pathway, but the cleavage products of the amyloidogenic pathway serve a unique biological function as well. Nikolaev et al showed that sAPPβ serves as a ligand for Death Receptor 6 (DR6). Upon binding DR6, sAPPβ activates caspase 6 and caspase 3, causing axonal and neuronal cell body apoptotic degradation (*51*). sAPPβ production was stimulated by growth factor deprivation, suggesting that β-Secretase cleavage could be a natural response to changes in growth factor levels within the brain. It is also interesting to note that β-Secretase cleavage may not promote AD by only producing the Aβ peptide, but by also promoting neuron death by the overproduction of sAPPβ.

In order to gain a better understanding of the driving force behind overstimulation of the amyloidogenic pathway in AD, we must first understand what factors promote one pathway over the other. Figure 1.2 summarizes the steps in the non-amyloidogenic and amyloidogenic cleavage pathways.
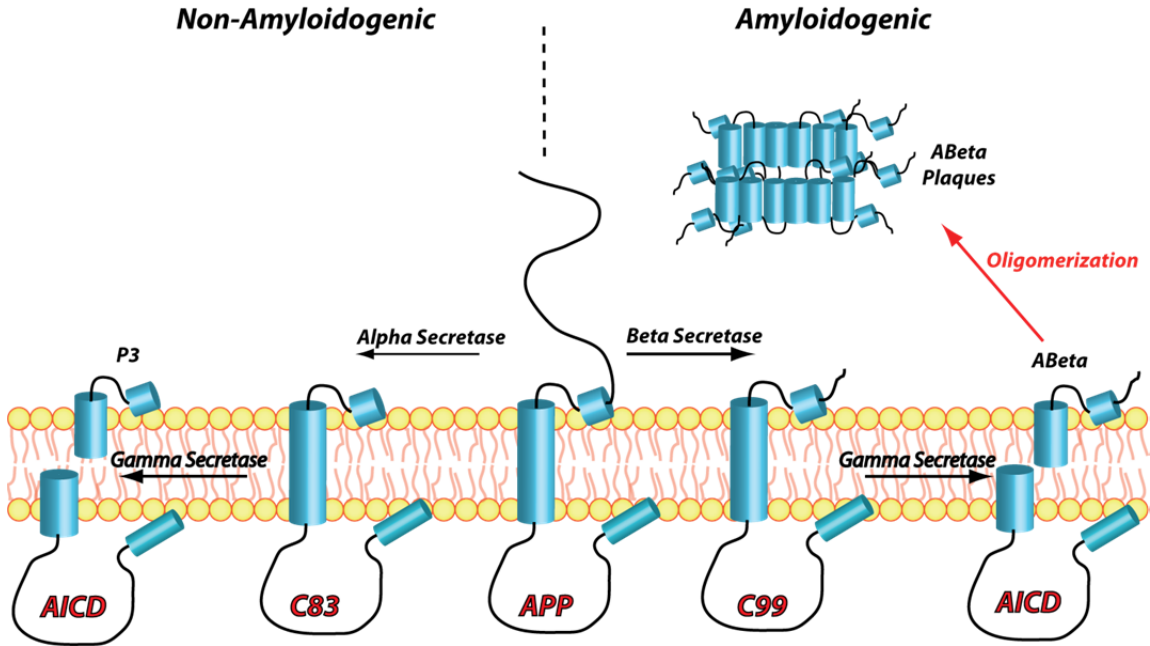
Figure 1.2. The cascade of cleavage events involved in the non-amyloidogenic and amyloidogenic processing of APP. The non-amyloidogenic cleavage pathway is initiated by cleavage of APP by the enzyme α-Secretase. This cleavage sheds a large, soluble domain and generates the transmembrane fragment C83 (83 amino acids in length). C83 is then cleaved within the membrane by the enzyme complex γ-Secretase, releasing the p3 peptide and the APP intracellular domain (AICD). Amyloidogenic processing of APP is initiated by the enzyme β-Secretase. This generates the membrane protein C99 (99 amino acids in length). C99 is subject to cleavage by γ-Secretase, generating the same AICD, but instead of the benign p3 peptide, the neurotoxic Aβ peptide is generated. It is this peptide that can go on to oligomerize and lead to cell death as well as aggregate and form the hallmark Aβ plaques found in AD.

As stated above, changes in growth factor levels may be one factor. In addition, it has been shown that oxidative damage can play a role in stimulating the amyloidogenic pathway (*52-55*). While there are numerous genetic and environmental factors that have been shown to enhance the amyloidogenic cleavage of APP, the overarching goal of this work will be to focus on two key components that could promote amyloidogenesis; the structure of C99 (the amyloidogenic product of APP cleavage by β-Secretase and the direct precursor to the Aβ peptide) and the ability of C99 to specifically bind cholesterol.

By investigating the structure of C99, we will gain an understanding of how Aβ is generated by γ-Secretase cleavage. By investigating the ability of C99 to bind cholesterol, information will be gained as to how cholesterol levels in the cell membrane, and more specifically, how microenvironments enriched in cholesterol known as "lipid rafts" (Liquid ordered [L_o] domains), may impact the balance between the non-amyloidogenic and amyloidogenic cleavage pathways.

Modulation of γ-Secretase Cleavage by Pharmaceutical Compounds[1]

Among the therapeutic targets for AD, the amyloidogenic pathway has long been a principle focus (*6*). Familial early onset AD (FAD) is associated with autosomal dominant mutations in APP and in the catalytic subunits (PS-1/PS-2) of the intramembrane protease that processes it, γ-Secretase (*3*). According to the amyloid hypothesis, oligomeric forms of Aβ are the principle agents underlying disease pathogenesis. The Aβ polypeptide is generated by proteolysis of APP. Cleavage of APP by β-Secretase yields C99, which is then heterogeneously processed by γ-Secretase to generate Aβ species with a variety of lengths, the principle species being Aβ40, as it is 40 residues in length (*57*). While Aβ40 is the predominant length of the peptide formed, pro-AD risk factors are those that stimulate the production of a more toxic Aβ species, known as Aβ42. Genetic mutations (to APP or PS), alterations in cholesterol metabolism, and oxidative damage are some of the key players known to increase the Aβ42/Aβ40 ratio, and are thus termed pro-AD risk factors (*41, 58-62*). Because Aβ is thought to be central in the pathogenesis of AD, inhibiting its production is

---

[1] (Portions of this section were adapted from the published work Nonspecificity of binding of γ-Secretase Modulators to the Amyloid Precursor Protein by Beel et al in *Biochemistry56.*   *Beel, A. J., Barrett, P., Schnier, P. D., Hitchcock, S. A., Bagal, D., Sanders, C. R., and Jordan, J. B. (2009) Nonspecificity of Binding of γ-Secretase Modulators to the Amyloid Precursor Protein, Biochemistry 48, 11837-11839.*)

a potential therapeutic strategy. Although significant progress has been made in the identification and development of potent γ-Secretase inhibitors, their clinical application has been limited by significant toxicities resulting from the interference with processing of other γ-Secretase substrates, particularly Notch (*63*). Indeed, γ-Secretase is a highly promiscuous protease with more than 60 identified substrates (*31*).

The discovery that a subset of nonsteroidal anti-inflammatory drugs (NSAIDs) could selectively reduce Aβ42 production without abrogating Notch cleavage suggested an alternative therapeutic approach for AD (*64*). The Aβ42 lowering activity of these γ-Secretase modulators (GSMs) was recapitulated in cell-free assays of γ-Secretase activity. Several groups have produced data suggesting that GSMs interact allosterically with presenilin, thereby modifying the enzyme's conformation (*65-67*). Additionally, recent work shows that GSMs directly interact with presenilin, giving even more evidence for the mechanism of GSM action (*68, 69*). Moreover, GSMs were observed to influence the cleavage of an unrelated substrate by signal peptide peptidase, an enzyme homologous to the presenilin subunit of γ-Secretase, suggesting that the modulators interact with the enzyme rather than the substrate (*70*). Corroborating the premise that GSMs are enzyme-targeting was the finding that certain NSAID GSMs can also influence the precise γ-Secretase cleavage of Notch (*71*). Okochi *et al* have shown that Notch cleavage is modulated, but not inhibited, by NSAID GSMs, providing a plausible explanation for the lack of adverse Notch-related toxicities of such compounds (*71*).

Nonspecificity of Binding of γ-Secretase Modulators to the Amyloid Precursor Protein

Previous work from the Golde and Multhaup laboratories postulate that GSMs specifically target APP, its C-terminal derivatives, and the Aβ peptide, providing an alternative explanation for the apparent specificity that GSMs exert on cleavage of C99 (*72-74*). Work from the Golde lab demonstrated that application of biotinylated

photoactivatable affinity probe derivaties of certain GSMs, namely, fenofibrate (an Aβ42 increasing GSM) and tarenflurbil (an Aβ42 lowering agent), to CHAPSO detergent extracts from human neuroglioma H4 cells failed to label any core γ-Secretase subunits but instead produced covalent conjugates with C83, the product of α-Secretase cleavage of APP. While labeling of C99 did not appear to take place in those same extracts, purified recombinant C99 in CHAPSO containing solutions could be modified by derivatized fenofibrate and tarenflurbil, an interaction subject to complete abrogation by a number of other GSMs. Photoaffinity labeling of purified C99 was localized to residues G700-L705, the first GxxxG motif found within the transmembrane helix (*72*).

Additional studies from the Multhaup lab suggested that GSMs not only bind with high affinity to C99, but also bind the Aβ polypeptide (*73, 74*). Using surface plasma resonance (SPR) studies, molecular dynamics, and TOXCAT analyses, these studies suggested that GSMs once again interacted with the GxxxG motifs found within the transmembrane helix of C99, and that the addition of GSMs could actively break C99 dimers in a concentration dependent manner, leading to the hypothesis that the mechanism of GSM ability to lower Aβ production was to modulate APP dimerization. Taken together these studies suggest a novel mechanism for how the interaction between APP and various GSMs may modulate Aβ levels, both in cellular and purified systems.

Based on the data presented in these papers, we thought to further the understanding of how the GSM molecules were interacting with C99 in a more specific manner. To investigate the putative binding of GSMs to APP and its derivatives, we monitored the spectroscopic response of purified and monodisperse uniformly ^{15}N (U-^{15}N) C99 to addition of GSMs in a membrane-like environment. Human C99 was expressed, labeled, and purified into LMPG micelles. Titrations of U-^{15}N C99 in LMPG micelles with the GSMs tarenflurbil, indomethacin, fenofibrate, and sulindac sulfide

revealed no evidence of specific binding, even at compound concentrations in the millimolar range. Figure 1.3 shows a representative titration experiment with the GSM tarenflurbil.
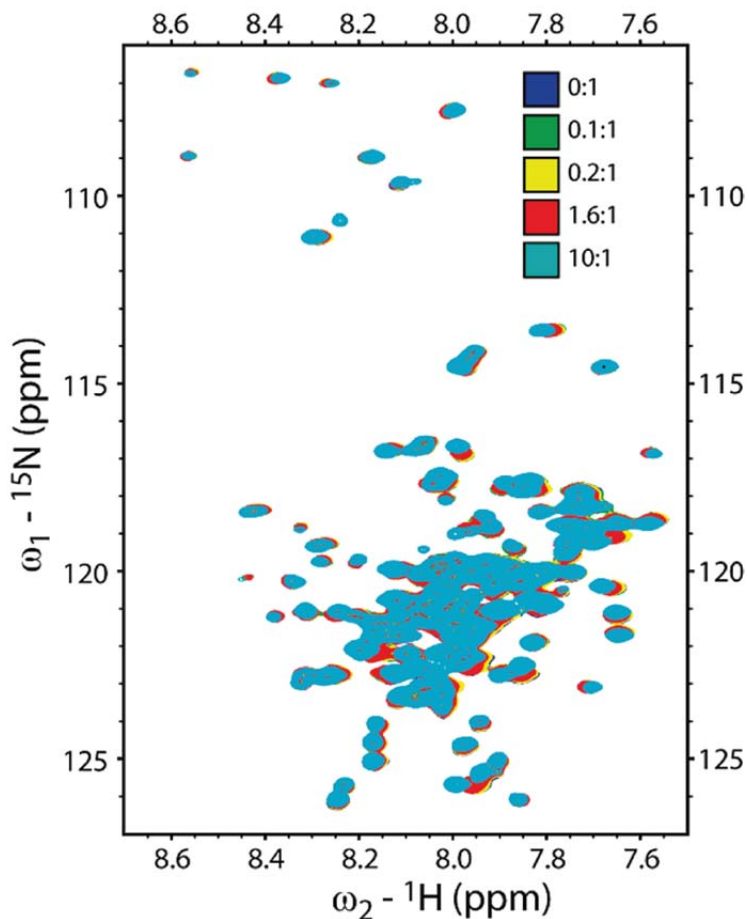
Figure 1.3. Titration of [U-15N]C99 with tarenflurbil as monitored using 600 MHz 1H-15N TROSY NMR. Samples contained 1 mM [U-15N]C99 in 200 mM LMPG micelles at pH 6.5 and 45°C and the indicated molar ratios of tarenflurbil to C99. The modest changes observed indicate only nonspecific interactions.

While the titration of tarenflurbil induces modest chemical shift perturbations in the ^{1}H-^{15}N TROSY-HSQC spectra of C99, the concentration dependence of the changes observed is not consistent with avid and specific binding of the protein by the GSMs. Moreover, the C99 NMR resonances that undergo GSM-induced shifts tend to differ from GSM to GSM, as might be expected for nonspecific interactions. In no case were

the peaks from residues in the putative GSM binding site (G700-L705) seen to be among those that shifted the most in response to addition of GSMs. In addition, experiments of a reciprocal nature were performed in which titrations of U-[15]N C99 in LMPG micelles with tarenflurbil were monitored using the ^{19}F NMR signal from this GSM. Figure 1.4 reveals that the ^{19}F signal from tarenflurbil neither shifts nor is significantly broadened relative to free ligand over a range of GSM/C99 molar ratios from 0.1 to 1 (at ca. 250μM C99), indicating a lack of significant binding.

A. Titration of C99

B. Negative Control Titration of KCNE1
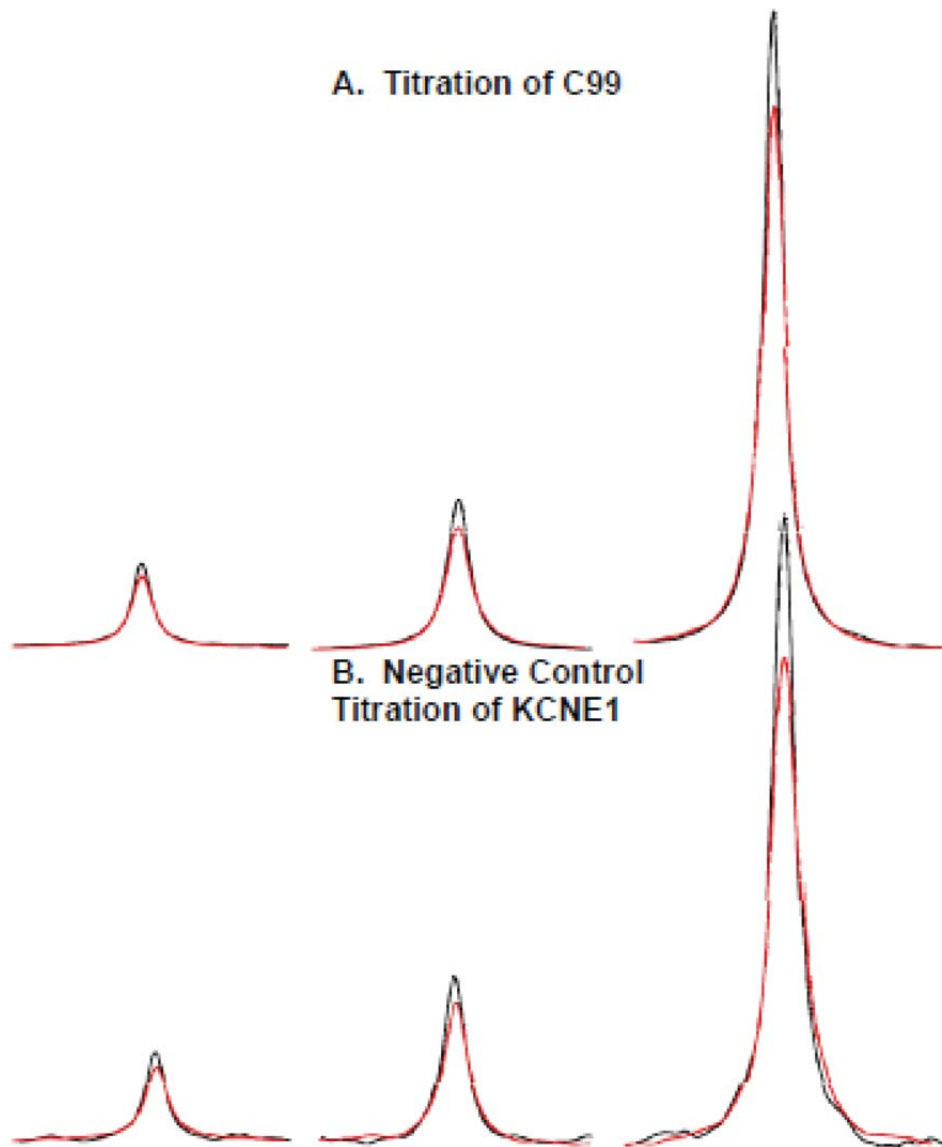
Figure 1.4. 19F NMR-monitored titration of (A) 250uM U-15N-C99 and (B) 200uM U-15N-KCNE1 (negative control) in 10% LMPG with tarenflurbil at pH 6.5 and 45 degrees C. Red curves represent the addition of 25uM, 50uM, and 250uM tarenflurbil to protein-containing solutions. Black – control series with no protein. Notice that the modest linebroadening in samples with protein present are similar for both C99 and KCNE1 samples. KCNE1 is a 129 residue single span membrane protein that modulates certain voltage-gated potassium channels. It is here used as negative control protein to which GSMs are not expected to bind.

These results indicate that nonaggregated C99 in LMPG micelles exhibits no specific

avidity for GSMs and related compounds. These results were recapitulated for C99 in

CHAPSO micelles, indicating that the detergent used was not causing the disparities between our work and the Golde and Multhaup studies.

While these results were encouraging for understanding the mechanism of GSM action, we were determined to find the reason for which others found that GSMs interacted with the APP protein and its derivatives. Chapter III will discuss recent work in greater depth to highlight the mechanism driving the nonspecific interaction between APP and the GSM molecules.

The Role of Cholesterol in Amyloidogenesis

For over 20 years there has been increasing evidence that suggests the lipid molecule cholesterol is intimately related to the etiology of AD (*41, 42, 75-80*). While the direct mechanism behind cholesterols impact on the development of AD is unclear, research groups have found that both increased and decreased levels of cholesterol may promote AD progression; it is clear that the molecule, and its homeostasis within the brain, play an important role in disease pathogenesis. Numerous studies suggest that increased levels of cholesterol can simultaneously promote β-Secretase cleavage of APP while actively inhibiting α-Secretase cleavage (*40, 42, 78, 81, 82*). Concurrent with these findings, the enzyme β-Secretase is often associated with regions of the plasma membrane enriched in cholesterol, often referred to as "lipid rafts" (*33*), demonstrating a direct link of between cholesterol and promotion of the amyloidogenic pathway. Lastly, early AD studies showed that when mice or rabbits were fed high cholesterol diets, they exhibited an increase in Aβ production (*83-85*). This is in accord with the finding that patients with hypercholesterolemia have an increased prevalence of AD (*86*). While we now predict that plasma cholesterol levels do not impact brain cholesterol levels, the link is still intriguing. In contrast to these findings it has been shown that decreased levels of cholesterol may promote the amyloidogenic pathway, by forcing APP and β-Secretase to

interact under cellular conditions where they normally would not (*87*). This and later

sections will serve to show how the cholesterol molecule may be implicated in promoting

Aβ production as and present a concept of how both increased and decreased

cholesterol levels may both promote AD.

Cholesterol Metabolism in the Brain

In order to gain a better understanding of how cholesterol plays a key role in the

etiology of AD, one must first understand how cholesterol homeostasis is regulated in

the brain and how alterations in this homeostasis could lead to the development of AD.

The regulation of cholesterol levels within the brain are highly complex, as the blood

brain barrier prevents cholesterol within the circulation from entering the brain, leading to

the brain having to generate all of its cholesterol *de novo (88)*. This was proved by two

separate studies by Bloch *et al* and Waelsch *et al* where cholesterol doped with D_2O was

fed to adult rats and both groups saw that the brain and spinal cord were completely

devoid of deuterated cholesterol, leading to the conclusion that there was little, if any,

exchange of plasma and brain cholesterol (*89, 90*). As a consequence, it was found that

cholesterol in the brain has an extremely long half-life, with the bulk of cholesterol

remaining for approximately 5 years (*91*).

Cholesterol synthesis is a complicated, multi-step process, with the limiting

reaction being catalyzed by the enzyme 3-hydroxy-3-methylglutaryl-coenzyme-A

reductase (HMGCoA reductase) in the endoplasmic reticulum (ER) (*92*). This enzyme is

regulated by a potent negative feedback loop that affects activity, stability, and gene

regulation (*93*). Many potential anti-AD therapeutics are inhibitors of HMGCoA

reductase, and epidemiological studies have demonstrated that select inhibitors known

as statins have the ability to decrease AD risk (*94*). However, the exact mechanism of

the effect of statins on AD is still unclear, as these compounds cannot cross the blood

17

brain barrier, and thus cannot directly lower brain cholesterol levels, and due to the fact that the brain regulates its own cholesterol synthesis, decreased plasma cholesterol is also an unlikely mechanism for the success of statins (*60*). The current thinking is that statins, while not directly lowering cholesterol levels within the brain, are able to promote enhanced brain oxygenation and clearance of the accumulating Aβ peptide, but this hypothesis is still being tested (*94*).

While cholesterol production in the brain on the whole is thought to be fairly consistent over time, the production of cholesterol by different neural cell types varies greatly with time. During early development, all cells within the brain generate cholesterol at a high rate, to stimulate neuron development and plasma membrane production. However, with time, mature neurons lose the capability to produce cholesterol (*95*). It is thought this occurs because neurons need to focus cellular energy on transmitting signals within the brain, and the metabolic cost of producing cholesterol is too great. While neurons may not generate cholesterol, the demand for cholesterol in these cells is extremely high, as there is constant turnover of the plasma membrane during neurotransmitter release and uptake. To circumvent this problem, cells within the brain known as astrocytes produce 2-3 times the normal level of cholesterol of other brain cells (*88*). Cholesterol generated in these cells is then transported to neurons by the ApoE family of proteins. There are four isoforms of ApoE found within the brain, and all function by forming lipoprotein complexes to shuttle cholesterol from astrocytes to neurons. One particular ApoE form, ApoE4, is a pro-AD risk factor. The exact mechanism of how this protein increases Aβ levels is still not well understood, but it is known that ApoE4 can not only modify cholesterol homeostasis, but also may play a role in facilitating clearance of Aβ, thus dysregulation of either or both of these functions may contribute to AD (*96, 97*). Interestingly, ApoE2 is thought to be a therapeutic agent

against AD, making regulation of the production of these two proteins of high importance (*98*).

ApoE family members are not the only proteins that have been implicated as Pro-AD risk factors involved in cholesterol regulation. In fact, APP has been shown to play an important role in cholesterol homeostasis within the brain. Recent work from Pierrot *et al* has shown that APP expression is upregulated in response to increased levels of cholesterol in neurons (*29*). The study ultimately demonstrated that the function of increased APP levels was to decrease the overall levels of cholesterol within the cells. It has also been shown that the Aβ peptide has the ability to inhibit HMGCoA reductase, thus abrogating the synthesis of cholesterol (*87*). In addition, Aβ has been shown to impair SREBP2 processing, a key step in a cells ability to monitor membrane cholesterol levels (*29*). This has led to the hypothesis that APP may serve as a putative cholesterol sensor within the membrane, and that the amyloidogenic pathway, under normal circumstances, facilitates this process. Overall, it has been shown that APP plays a central role in the monitoring of cholesterol turnover, and that this function is essential for proper neuronal function in the brain.

Two other proteins demonstrating altered expression levels and possible genetic contributions to AD pathogenesis are cholesterol 24-hydroxylase (CYP46) (*99*) and selective AD indicator-1 (Seladin-1) (*100*), as they have been implicated in both cholesterol turnover and synthesis in the brain. CYP46 is the enzyme that converts cholesterol to 24-hydroxycholesterol. This is of particular importance as this is the only cholesterol analogue that is able to cross the blood brain barrier and leave the brain, thus stimulating cholesterol synthesis and turnover. A study by Lund *et al* showed an increased amount of CYP46 in the brains of aged humans and mice compared to youths (*99*). Work from the Ledesma lab has implicated the age dependent increase of CYP46 with a decrease of membrane cholesterol levels in hippocampal neurons, both *in vitro*

and *in vivo (95)*. While the initial results from this study suggested that the loss of cholesterol was neuroprotective, this work will argue that over time this decrease in cholesterol may serve to initiate the amyloidogenic pathway. In addition to potentially playing an important role for modulating Aβ levels, this increase in 24-hydroxycholesterol in aged patients may serve as a potential biomarker for assessing risk of developing AD.

Another potential protein that plays a key role in cholesterol homeostasis in the brain is Seladin-1. Seladin-1 is the last protein in the cascade of events that generate cholesterol, and functions to convert the cholesterol analogue desmosterol to native cholesterol (*101*). Seladin-1 has been shown to be down regulated in the brains of AD patients (*102*), with the resulting phenotype being an overproduction of desmosterol and a decrease in cholesterol levels. These results are replicated in Seladin-1 deficient mice (*103*). As with the overexpression of CYP46, the down regulation of Seladin-1 is consistent with decreased levels of cholesterol within the brain of AD patients. As aging proceeds in non-AD individuals, there is a moderate loss of cholesterol within the brain of approximately 20%. While this decrease is termed normal, and in fact, a slight decrease in cholesterol has been shown to be neuroprotective, a 30% loss of cholesterol in the brain has been shown to be a pro-AD risk factor (*95*). This work will go on to argue that the alterations found within the CYP46 and Seladin-1 expression levels will contribute to a model of AD progression, which will ultimately combine both the loss and gain of cholesterol levels seen in different AD studies.

Cholesterol Rich Membrane Domains and Their Role in AD

The plasma membrane of cells is a complex and crowded environment, consisting of an intricate, but precise, mixture of lipids and proteins. While at first glance this environment may seem quite chaotic and random, cells have developed mechanisms of sorting and organizing this mosaic environment. One such method is

the formation of regions of the membrane known as cholesterol rich domains, regions often referred to as lipid rafts or liquid ordered (L_o) domains, that have distinct biophysical and biochemical properties that separate them from the bulk, or liquid disordered (L_d), membrane environment (104, 105). These cholesterol rich membrane domains form when cholesterol molecules in the membrane congregate with specific lipids, namely a lipid known as sphingomyelin (106). Sphingomyelin (SM) has a unique acyl chain structure when compared with other phospholipids of the plasma membrane, allowing it to pack much tighter together when stabilized by cholesterol. This packing is enabled by the structure of the (SM) acyl chain, which contains a single unsaturated carbon double bond at the 2-3 position, as compared to most phospholipids, which contain an unsaturated carbon double bond (and sometimes more) at the 9-10 position. The double bond position in SM permits an acyl chain structure that is almost linear, allowing close packing of lipids in the presence of cholesterol and creating an ordered lipid environment. The double bond found in phospholipids at the 9-10 position creates a kink in the acyl chain, inhibiting close packing and creating a more fluid membrane environment.

Formation of cholesterol rich domains is highly sensitive to the concentration of the lipids present, and domain formation will not occur in model membranes unless the cholesterol concentration is approximately 15 mol% with a SM concentration of about 25 mol% (107). These values are for model membranes in isolation, and the conditions for which cholesterol rich domain formation occur in cellular membranes is still highly debated, with the current estimate that cellular membranes are comprised of 30% lipids and 70% proteins, by dry weight (88). However, it is known that in the plasma membrane of neurons, the cholesterol concentration is approximately 10-20%, with myelinated regions containing up to 25-30% (88, 108). These levels are well within the range needed to generate cholesterol rich domain formation, and it is even hypothesized

21

that these domains can form as early as the trans-golgi network (TGN) (*109*). As cholesterol levels steadily increase from the ER through the TGN to the plasma membrane (*75*), even slight alterations in cholesterol levels in these different organelles may impact Aβ production. The idea that different organelles may impact the cleavage of APP was first introduced in the study by Hartmann *et al*, where it was shown that Aβ40 is preferentially generated in the TGN, while Aβ42 mainly originates from the ER (*110*). While these findings are potentially important for understanding the regulation of Aβ production, the mechanism of action is still not understood. Recent findings from our lab will show how the interaction between APP and cholesterol and the properties of cholesterol rich domains may stimulate Aβ40 or Aβ42 production.

While the overall concentration of cholesterol within the plasma membrane has an estimated range, the concentration between the inner (cytofacial) and outer (exofacial) layers (leaflets) of the cell membrane are quite different and are highly dependent on the age of the neuron (*111*). This concept was first put forth by Friedhelm Schroeder, who argued that as one ages, the localization of cholesterol moves from the cytofacial to the exofacial leaftlet (*112*). Using the synaptic plasma membrane of young (3-4 months) c57bl/6j mice, it was shown that the exofacial leafleat was comprised mostly of phosphatidlycholine (POPC) and SM, while the cytofacial leaflet consisted mainly of phosphatidylethanolamine (POPE), phosphatidylserine (POPS), and posphatidylinositol (POPI). 85% of the total membrane cholesterol was found in the cytofacial leaflet (*113*). This asymmetrical distribution of lipids and cholesterol led to the exofacial leaflet being much more fluid in nature compared to the cytofacial leaflet; with an effect equivalent to approximately a 6° change in temperature on bulk membrane fluidity (*111*). If extrapolated to humans, this would leave only 15% of the total membrane cholesterol in the exofacial leaflet in young adults, the same leaflet where APP would potentially bind cholesterol.

When the same mice were studied at 14 months of age, it was noted that the exofacial leaflet contained 24% of the total membrane cholesterol. When the presynaptic membranes were examined after 25 months, 32% of the total cholesterol resided in the exofacial leaflet, suggesting that as neurons age, there is a shift of cholesterol from the cytofacial to the exofacial membrane leaflet (*114*). This increase in cholesterol in the exofacial leaflet may serve to increase the total number of cholesterol rich domains in the exofacial leaflet, since this is the only leaflet in which SM residues. This is consistent with the findings that cholesterol rich domains preferentially form only in the exofacial membrane leaflet (*115*). An increase in cholesterol rich domains, as well as total cholesterol, could potentially increase the amyloidogenic processing of APP and lead to an increase in Aβ production. One finding of particular interest is that mice deficient in ApoE proteins showed an even greater increase in exofacial cholesterol (2 fold) with age, suggesting that changes in ApoE function may exacerbate cholesterol rich domain formation in the exofacial leaflet (*111*).

As mentioned above, the formation of cholesterol rich domains (lipid rafts) is thought to be intimately connected with amyloidogenic processing of APP by β-Secretase (*33, 34, 60, 81, 111, 116-118*). In addition to the evidence that increased cholesterol increases Aβ production (*85, 119*), there is considerable evidence showing that Aβ production is dependent on cholesterol rich domain formation. Targeting of APP to cholesterol rich domains was noticed when studying Niemann Pick type C disease, which causes the accumulation of free cholesterol in late endosomal compartments with increased Aβ production (*120*). Work from the Herman group showed that increases in membrane cholesterol stimulate β-Secretase cleavage of APP and that β-Secretase co-localizes with cholesterol in detergent resistant membranes (which correlate to cholesterol rich domains) (*85*). Work from Kai Simons lab has shown APP and β-Secretase co-localization in detergent resistant membranes from purified neurons (*33*),

23

indicating both components can reside in the same membrane domains. Studies from intact cells validated this study by using fluorescence resonance energy transfer (FRET) studies to show close proximity of APP and β-Secretase both at the cell surface and in early endosomes (*121*).

Interestingly, when a cholesterol rich domain targeting sequence is added to β-Secretase (*34*) or when APP and β-Secretase are cross-linked by antibodies in cholesterol rich domains (*122*), the rate of Aβ production is greatly enhanced. Further work from the Simons lab showed that Aβ generation is dependent upon cholesterol rich domain formation, and that when these domains are prevented from forming by decreasing cholesterol levels or by the chemical methyl β-cyclodextrin, the subsequent Aβ levels are decreased. When β-Secretase is prevented from entering cholesterol rich domains, Aβ production is completely inhibited. A key component to this process noted by the Simons group was that in order for β-Secretase cleavage to occur, not only did both APP and β-Secretase need to co-localize in cholesterol rich domains, but endocytosis was needed (*33*). Blocking clathrin-mediated endocytosis greatly decreased the amount of Aβ produced, indicating the bulk of β-Secretase cleavage occurs after both APP and β-Secretase are engulfed into the cell in the same endocytic vesicle. It is thought that during this process, APP and β-Secretase do not need to be localized to the same cholesterol rich domain, but that the act of endocytosis, which is cholesterol rich domain mediated, brings enzyme and substrate into closer proximity for cleavage to occur (*123*). This is due to the fact that there are approximately only 30 or so protein molecules per cholesterol rich domain, so a mechanism would be needed to increase the local protein concentration for efficient amyloidogenic cleavage (*124*). Blocking endocytosis had no impact on α-Secretase cleavage, further implicating cholesterol rich domains in promoting the amyloidogenic pathway (*116*). All of these findings are consistent with the literature that states α-Secretase cleavage occurs in the

ER and at the plasma membrane and β-Secretase cleavage occurs in endocytic vesicles, indicating that incorporation into cholesterol rich domains may promote Aβ production by segregation into different cell organelles (*75*).

In addition to regulating endocytosis and subcellular localization, the biophysical properties of cholesterol rich domains may also play an important role in promoting non-amyloidogenic or amyloidogenic processing of APP. Work from Kojro *et al* has shown that increased membrane fluidity (low cholesterol levels) in neuron membranes stimulated the non-amyloidogenic pathway by increasing α-Secretase cleavage activity and APP content in the cell membrane, where it will preferentially undergo α-Secretase cleavage (*42*). The converse effect of decreasing α-Secretase cleavage of APP when localized in cholesterol rich domains has also been seen. A study by Marenchino *et al* showed that when placed in model membranes that have the same biophysical properties of cholesterol rich domains (based on the order of the lipids used), the α-Secretase cleavage site of APP was embedded into the membrane, and became less accessible to the enzyme (*40*). When combined with the ability of C99 to bind cholesterol (*26*), and the evidence that APP resides in cholesterol rich domains when cleaved in the amyloidogenic pathway(*33, 43*), the hypothesis was generated that cholesterol binding by APP may actively inhibit α-Secretase cleavage by occluding the α-Secretase cleavage site.

While important for production of Aβ peptides, cholesterol rich domains are also thought to play an important role in promoting cell death during AD (*117*). Seminal work from Dennis Selkoe showed that oligomeric forms of Aβ, specifically spherical trimer-hexamers to 24mer aggregates, and not monomers or higher order fibrils, were the neurotoxic species in AD (*125*). This does not exclude large order aggregates and fibrils of the Aβ from being neurotoxic, as these forms can be cytotoxic indirectly by activating an inflammatory response with activation of glial cells, resulting in the production of cell

damaging cytokines (*87*), however this is not initiated until cell death from Aβ oligomers has occurred. It is now thought that the oligomerization of Aβ is initiated by Aβ binding to the cell membrane (*126*), specifically in cholesterol rich domains (*127*). Work from the Youkin lab showed that Aβ co-purified in detergent resistant membrane fractions from cultured neurons, rodent brains, and the brains of human patients with AD, linking cholesterol rich domains with Aβ oligomerization (*127*). Importantly, Aβ has been shown to accumulate in presynaptic terminals in AD cortex where it co-localizes with the cholesterol rich domain markers, such as cholesterol and the lipid ganglioside GM1 (*128*). Like sphingomyelin, gangliosides are a family of lipids that are often associated with cholesterol rich domains (*129*). Mounting evidence suggests that gangliosides within cholesterol rich domains appear to be the main driving force behind the oligomerization of Aβ on neuronal membranes. The development of AD within certain brain regions has been found to correlate with increased ganglioside levels (*130*). In addition, exogenously applied Aβ was shown to bind to neuronal membranes and to redistribute into cholesterol rich domains where it co-localized with ganglioside GM1 in a time-dependent manner (*131, 132*). These results suggest that not only cholesterol rich domains as a whole, but also specific lipid components, may be responsible for initiating the cascade of events that promotes Aβ oligomerization, opening potential new avenues for therapeutic intervention in AD.

Furthermore, recent evidence suggests that the interplay between Aβ and cholesterol rich domains may not be limited to promoting Aβ oligomerization. Multiple studies have shown that the Aβ oligomers that form in cholesterol rich domains can go on to bind a variety of membrane proteins, alter their membrane localization, and ultimately promote neuronal cell death. One such membrane protein is the N-methyl-D-aspartate receptor (NMDARs), a major class of glutamate receptors in the brain found at the postsynaptic membrane of excitatory synapses (*133*).   NMDARs function by

permitting the rapid influx of Ca^{2+}, which triggers long-term potentiation (LTP) in the brain, which is important for maintaining synapses ([134]). NMDARs function by localizing to cholesterol rich domains, a lateral membrane translocation mediated both by phosphorylation of NMDARs and the interaction with the cholesterol rich associated proteins flotillin-1 and -2 ([135-137]). Interestingly, APP has been shown to also associate with flotillin-2, adding another piece of evidence linking APP processing and Aβ generation to cholesterol rich domains ([49]). By examining hippocampal slices, it was found that NMDARs and Aβ co-localize ([138]). Further evidence showed that Aβ oligomers were able to co-immunoprecipitate with NMDAR subunits ([139]). Aβ oligomers were found to decrease NMDAR-dependent influx of Ca^{2+} into dendritic spines by preventing NMDARs from localizing to cholesterol rich membrane domains, ([140]) using a mechanism that also involved the phosphorylation of tau, another dysregulated protein important in the pathogenesis of AD ([141]). This decrease in Ca^{2+} resulted in the loss of LTP, leading to the loss of synapses between neurons and neuronal impairment ([142]).

Another membrane protein that exhibits altered function in the presence of Aβ oligomers is the metabotropic glutamate receptor 5 (mGluR5), a protein that plays an important role in Ca^{2+} mobilization and the modulation of LTP in hippocampal neurons ([143, 144]). Unlike the NMDARs, which function as ion channels, mGluRs are G-protein coupled receptors ([145]). Work from the lab of Antoine Triller showed that mGluR5 was a putative Aβ oligomer receptor by showing co-localization of fluorescently labeled Aβ with the receptor in hippocampal neurons ([139]). The work went on to show that the Aβ oligomers formed complexes with mGluR5 receptor, which altered the lateral distribution of the receptor into dendritic spines followed by Ca^{2+} dysregulation. It was also noted that Aβ oligomers induced a time-dependent increase in cholesterol rich domain associated mGluR5 as noticed as a decrease in receptor mobility and aggregation. This

aggregation led to a constitutively active receptor as the protein was permanently residing within a pathological signaling platform (*139*).

The interaction between Aβ, membrane receptors, and cholesterol rich domains is not limited to only NMDARs and mGluRs; these are the most studied receptors to date. Increasing evidence suggests that cholesterol rich domains serve as signaling platforms for proper neuronal function (*117*), and the sequestration or occlusion of receptors from these domains by Aβ oligomers leads to aberrant cellular signaling, and ultimately neuronal death. While more research is needed to substantiate these ideas, this is promising research identifying how the Aβ peptide actually initiates cell death during AD.

Experimental Overview[2]

Protein structure determination is a vital component for understanding of how proteins function, and an invaluable technique for developing the production of effective therapeutics (*147*). While there are multiple methods of protein structure determination, including X-ray crystallography and cryo-electron microscopy; nuclear magnetic resonance (NMR) spectroscopy has seen numerous recent advancements that enhance its ability to determine high resolution protein structures, specifically of membrane proteins like C99 (*146, 148*). As NMR-based structure determination is becoming more routine and compatible with larger protein systems, because in addition to to static protein structures it can also provide dynamic information about a proteins motion, something many other structure determination methods cannot do. This section of the

---

[2] (Portions of this section were adapted from the published work "The Quiet Renaissance of Protein NMR by Barrett et al, published in *Biochemistry146.* *Barrett, P. J., Chen, J., Cho, M.-K., Kim, J.-H., Lu, Z., Mathew, S., Peng, D., Song, Y., Van Horn, W. D., and Zhuang, T. (2013) The quiet renaissance of protein nuclear magnetic resonance, ibid. 52, 1303-1320.*)

introduction will deal with the practical considerations and experiments used for determining the three dimensional structure of C99 (*26*).

Nuclear Magnetic Resonance Spectroscopy

NMR spectroscopy is a strikingly diverse technique, enabling researchers to obtain detailed information regarding protein structure, dynamics, and the surrounding chemical environment. There are two main types of NMR spectroscopy used for investigating the properties of biological compounds, solution state and solid state NMR. As the names suggest, solution state NMR studies proteins suspended in aqueous solutions while solid state NMR utilizes molecules in a crystalline (solid) state. For purposes of clarity, the NMR methods discussed in this section will relate exclusively to solution state NMR, as that was the method used to study C99. Scientists Isidor Rabi, Felix Bloch, and Mills Purcell noticed that certain atomic nuclei, such as hydrogen (^{1}H) and phosphorous (^{31}P) had the ability to absorb radio frequency (RF) energy when placed in an aligned magnetic field (*149, 150*). When this absorption occurred, it was termed that the nucleus was *in resonance*. Subsequent work showed that different atomic nuclei resonate at different rates when placed in different magnetic fields, leading to unique chemical signals, known as chemical shifts (*151*). While it is true that NMR spectroscopy can be utilized for studying a wide array of biological molecules such as proteins, nucleic acids, sugars, and more, the focus of this work is on the use of NMR spectroscopy to study the structure and function of proteins, so for simplicity the following paragraphs will highlight applications for proteins only. Figure 1.5 shows a flow chart for how a basic NMR experiment works.
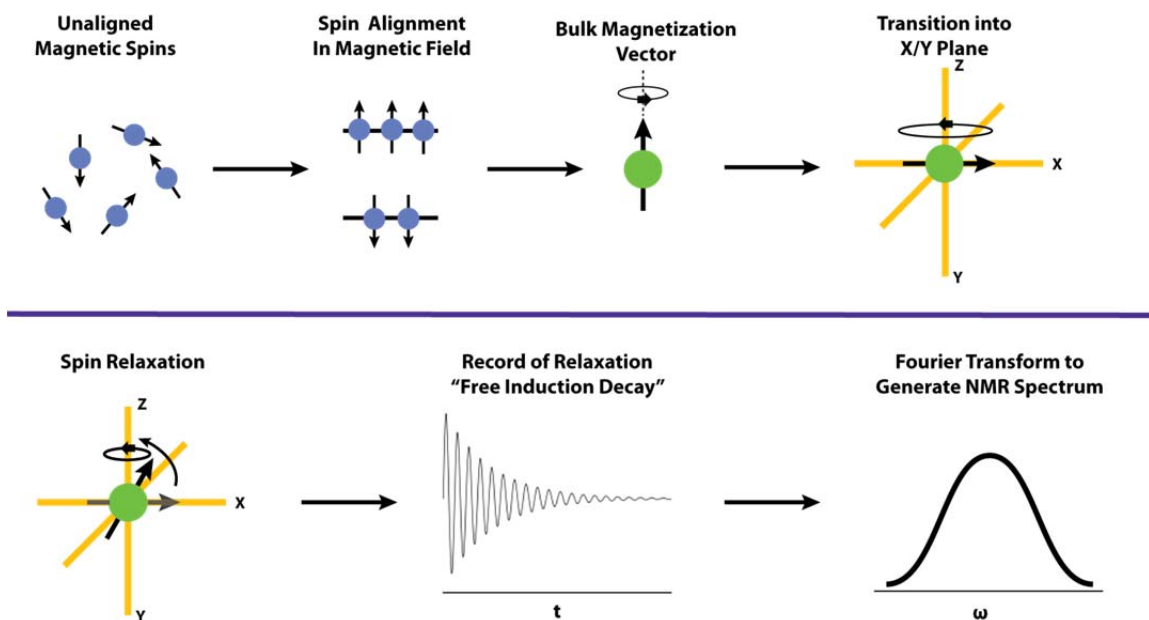
Figure 1.5. A schematic flow chart of the process for how an NMR experiment works. Prior to being placed in the NMR spectrometer (magnet), the magnetic spins of the system are randomly oriented. Following placement in the spectrometer, the spins align parallel or anti-parallel to the direction of the static magnetic field. The orientation of these spins can be summed and due to the ½ spin number of the NMR active nuclei, the overall spin orientation can be represented as a single vector (bulk magnetization). RF energy can be absorbed by the spins, which can change the orientation of the bulk magnetization from the Z plane into the X/Y plane. Due to angular momentum, this vector will precess within the X/Y plane. As the absorbed energy is released to the system, the bulk magnetization will relax back to the Z plane. This energy is recorded as a free induction decay, which can undergo a Fourier transformation to generate the NMR spectrum.

While a number of recent advances are based on using NMR methods of formidable complexity, simple 1-D solution NMR methods can be used to address highly significant biological questions. A variation of this approach involves fluorine NMR. ^{19}F is a spin-½ nucleus with an NMR sensitivity that approaches that of protons, making it easy to obtain satisfactory signal-to-noise at short acquisition times even for dilute samples of large proteins and complexes. Moreover, ^{19}F NMR chemical shifts are highly sensitive to local environment, such that ^{19}F NMR generally yields well-resolved 1-D NMR spectra, (*152, 153*) making ^{19}F is an excellent reporter probe in binding studies or

in studies of protein folding or conformational changes. ^{19}F probes can be attached to proteins by chemical modification of cysteine thiol sites (*154*) or via incorporation of labeled amino acids. (*153, 155, 156*)

1D NMR is an extremely powerful technique, as a single experiment can give massive amounts of information regarding the properties of a protein, but NMR spectroscopy has the ability to link multiple NMR active nuclei, such as coupling all ^{15}N and ^{1}H spins together, by manipulating the pulses used during the experiment. This is known as a 2D experiment, since instead of analyzing only one dimension (one nuclei), we are now looking at two. 2D NMR spectroscopy was developed to enhance spectral resolution, thereby reducing the level of NMR peak overlap seen in 1D experiments. It should be noted that 2D NMR is not the limit, and the use of higher ordered multidimensional NMR is common practice when investigating the structure and function of proteins. While there are many different types of 2D NMR experiments, this work will focus exclusively on the <u>h</u>eteronuclear <u>s</u>ingle <u>q</u>uantum <u>c</u>oherence (HSQC) experiment (*157*) as it is the main experiment used in the various NMR studies described herein.

The HSQC experiment is a common 2D NMR experiment used to investigate structural changes and binding events in proteins. In this spectrum, the horizontal axis represents the proton (^{1}H) chemical shift and the vertical axis represents the chemical shift of a hetero nucleus, such as ^{15}N or ^{13}C. The NMR spectrum for an HSQC experiment shows the chemical shift for each correlated proton-heteroatom bond as a single peak in the 2D plane, similar in style to a contour map. When performing an ^{15}N HSQC for a protein, each peak represents one amino acid, based on the N-H bond found within the protein backbone. The chemical shift (location) of each peak is dependent on the chemical environment of each nuclear spin. Even without knowing which peak corresponds to which amino acid, one can determine if a protein is folded as well as get a prediction of the secondary and tertiary structure of the protein based on

the dispersion of the chemical shifts. Using higher dimensional NMR techniques (such as 3D NMR which correlate ^{1}H, ^{15}N, and ^{13}C nuclear spins), it is possible to assign which amino acid in the protein corresponds to which peak in the NMR spectrum. Using this information, it is possible to determine which residues interact with ligands or other proteins as they are added to the chemical environment, as only peaks that experience a change in their chemical environment (involved in the binding event or undergo some structural change) will show a perturbation in the chemical shift.

While the ^{15}N HSQC is a useful experiment, it is limited by the size of the protein it can study. Relaxation properties of proteins give rise to the NMR signal, and when proteins become large the nuclear spins relax at a faster rate, due to the fact that the elevated mass causes the protein system to tumble in solution at a much slower rate. This increased relaxation rate leads to broadening of the NMR signal, such to a point that no signal can be detected. The size limit for standard HSQC experiments is ~ 35kDa. Advancements in experimental design led to the development of transverse optimized spectroscopy (TROSY) (*158*), which allows for the basic heteronuclear correlation technique to be extended to larger proteins up to ~100 kDa in size. In an HSQC spectrum in which decoupling has not been applied, peaks appear as multiplets due to J-coupling. Crucially the different multiplet components have different widths. This is due to constructive or destructive interaction between different relaxation mechanisms. Typically relaxation for large proteins at high magnetic field strengths the transverse (T_2) is dominated by the dipole-dipole (DD) mechanism and the chemical shift anisotropy (CSA) mechanism. As the relaxation mechanisms are generally correlated but contribute to the overall relaxation rate of a given component with different signs, the multiplet components relax with very different overall rates. The TROSY experiment is designed to select the one component for which the relaxation is slowest, leading to a single, sharp peak in the spectrum. This significantly increases both spectral resolution

and sensitivity, both of which are at a premium when studying large and complex biomolecules, relative to a corresponding HSQC spectrum(*158*).

This approach significantly extends the molecular mass range of molecules that can be studied by NMR, but it generally requires high magnetic fields to achieve the necessary balance between the CSA and DD relaxation mechanisms; CSAs scale with field strength, while dipole-dipole couplings are field-independent. Since this technique only serves to select a component of the HSQC experiment, the resulting NMR spectrum still shows a series of peaks, each representing one amino acid within the protein (for the ^{1}H, ^{15}N TROSY-HSQC experiment). Figure 1.6 shows a representative TROSY-HSQC for C99.
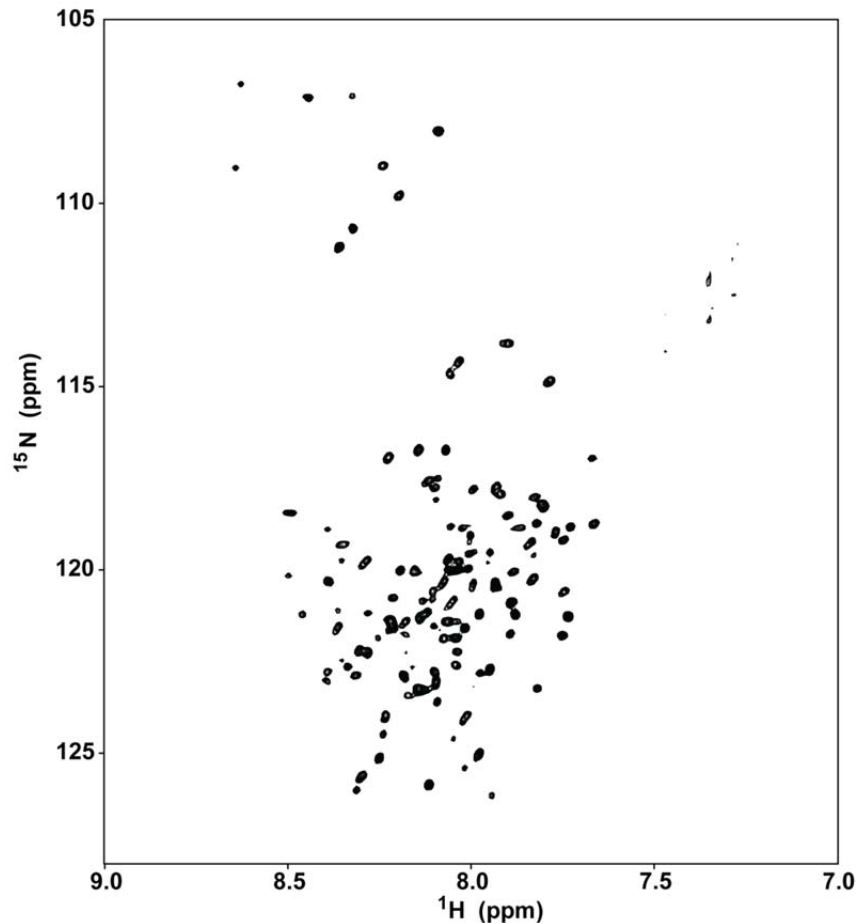
Figure 1.6. A representative 2D ^{1}H,^{15}N HSQC-TROSY NMR spectrum of C99 in LMPG detergent micelles. The horizontal dimension represents the proton dimension and the vertical dimension represents the nitrogen dimension. Each peak represents a single amino acid from the protein, with the location (chemical shift) of the peak being dependent upon the chemical environment surrounding the amino acid.

C99 Preparation and Experimental Considerations

As stated above, in order to perform these higher dimensional NMR experiments, the protein being studied must have NMR active nuclei, such as ^{13}C or ^{15}N, incorporated into the amino acids. While there are a variety of methods for incorporating ^{15}N into proteins, such as cell free expression (*159*) and injecting living cells with ^{15}N labeled compounds (*160, 161*), the method utilized for the studies of C99 was to overexpress the protein in *E. Coli* while supplementing the bacterial medium with ^{15}N labeled

ammonium chloride (*162-164*) in a growth medium devoid of all other nitrogen sources. The human C99 gene was cloned into a pET-21a vector, with an added methionine encoded at the N-terminus and an added spacer/His-purification tag (QGRILQISITLAAALEHHHHHH) at the C-terminus. This vector was then used to transform the BL21(DE3) strain of *Escherichia coli (28)*. C99 overexpression was driven by inducing the cells with isopropyl thiogalactoside (IPTG). Following overexpression of C99, the *E. Coli* cells were lysed and the protein was purified via immobilized metal affinity chromatography with nickel resin. The resulting purified protein was enriched with ^{15}N for NMR studies. Further details on C99 preparation and purification are found in the methods section of Chapter II.

In addition to incorporating NMR active nuclei into the protein for NMR studies, another consideration for preparing C99 was the ability to effectively mimic the hydrophobic environment of the cell membrane. Since C99 is a transmembrane protein, in order for the protein to be properly folded and functional, the hydrophobic environment of the lipid bilayer must be replicated. Due to the size limitations of NMR, it is impractical to study membrane proteins using native lipids, as the system is too large to study. Multiple membrane mimetics have been utilized, but for the studies on C99 two distinct mimetics were used, detergent micelles (*165-167*) and lipid bicelles (*167-169*).

Detergent micelles form when surfactants (detergents) are placed in an aqueous solution above a critical concentration (critical micelle concentration, CMC) when detergent aggregation can occur. Micelles form due to the chemical structure of the detergent molecules used to form them. Detergents are similar in structure to lipids, as each contains a polar head group and a hydrophobic tail, but opposed to lipids, detergent molecules normally have an acyl chain forming the hydrophobic tail, not two. When a concentration above the CMC is reached, it is energetically favorable for the hydrophobic tails of the detergent molecules to cluster together and exclude any

35

surrounding water, driving the formation of a spheroid shape. It is in this hydrophobic environment that the transmembrane region of C99 is inserted. For the studies of C99 in detergent micelles, the detergent lyso-myristoylphosphatidylglycerol (LMPG) was used. LMPG contains a single, saturated acyl chain of 14 carbons linked to a glycerol head group, resulting in a net negative charge.

Lipid bicelles are the practical middle ground for solution NMR between detergent micelles and native lipid bilayers, in the fact that they contain lipid molecules with two acyl chains, but are small enough in size to be studied by solution NMR. Bicelles are formed by mixing two amphipathic compounds, one a lipid with two acyl chains in the hydrophobic tail and the other an amphipathic molecule, such as a detergent. During mixing, the lipid components come together to form a lipid bilayer, which is then capped on either end by the amphipathic molecules to prevent any hydration of the hydrophobic environment. As with detergent micelles, the transmembrane protein being studied inserts into the hydrophobic environment of the bicelle, only in this mimetic the hydrophobic region more closely replicates the lipid bilayer found within the cell membrane. In addition to being a better membrane mimetic, bicelles allow the incorporation of other hydrophobic molecules, such as cholesterol, so binding studies with these compounds can be performed and monitored by NMR studies. Figure 1.7 shows a cartoon representation comparing detergent micelle and lipid bicelle structures.
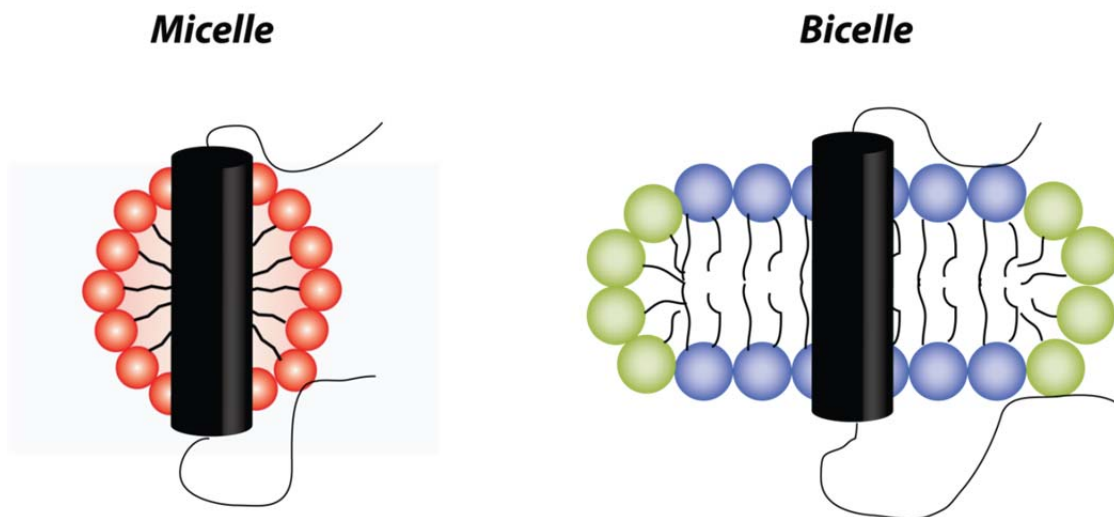
Figure 1.7. A comparison between micellar and bicellar structures. A representative membrane protein is shown by the black cylinder. Detergent micelles are represented on the left by the red molecules. A detergent micelle can be thought of as a hydrophobic inner tube around the membrane spanning region of a protein. A bicelle is shown on the right by the blue and green molecules. The blue molecules represent lipids with two acyl chains. The green molecules represent detergent molecules that cap the ends of the bicelle. A bicelle can be thought of as having the shape of a hockey puck, with the lipid bilayer forming the middle of the puck.

NMR Experiments for 3D Structure Determination

The process for structure determination by NMR requires two key components; the first being known as obtaining "assignments", where each NMR resonance is assigned to a specific amino acid. The second component is obtaining an abundance of NMR structural restraints, such as long and short range distances between atoms and the orientation of specific atomic bonds within the protein (*170, 171*). While there are a variety of methods used to facilitate the acquisition of structural restraints, this section will focus solely on the experiments used for determination of the 3D backbone structure of C99 at a modest resolution. When working with membrane proteins it is often difficult to obtain high resolution structures, as the larger size of the protein/membrane complex limits the NMR signal. Following the procurement of numerous experimentally obtained

structural restraints, these parameters are converted using computational methods (*172*).

Prior to obtaining structural restraints for 3D structure determination, the NMR assignment process must be completed. This preliminary work was performed and published from the Sanders lab prior to the 3D structure determination (*28*). The assignment process utilizes a variety of triple resonance (3D) NMR experiments, which connect the atoms of the protein amino acid chain by using the NMR active nuclei ^{15}N, ^{13}C, and ^{1}H (*162, 173-175*). By manipulating the nuclear spins, specific atoms within the amino acid chain can be correlated to each other through bonds. For example, there are two key 3D NMR experiments that allow one to "walk" along the protein backbone, connecting consecutive amino acids by transferring the magnetization between them through bonds, essentially tracing the linkage between the amino acids. These two experiments are called HNCA and HN(CO)CA (Figure 1.8).
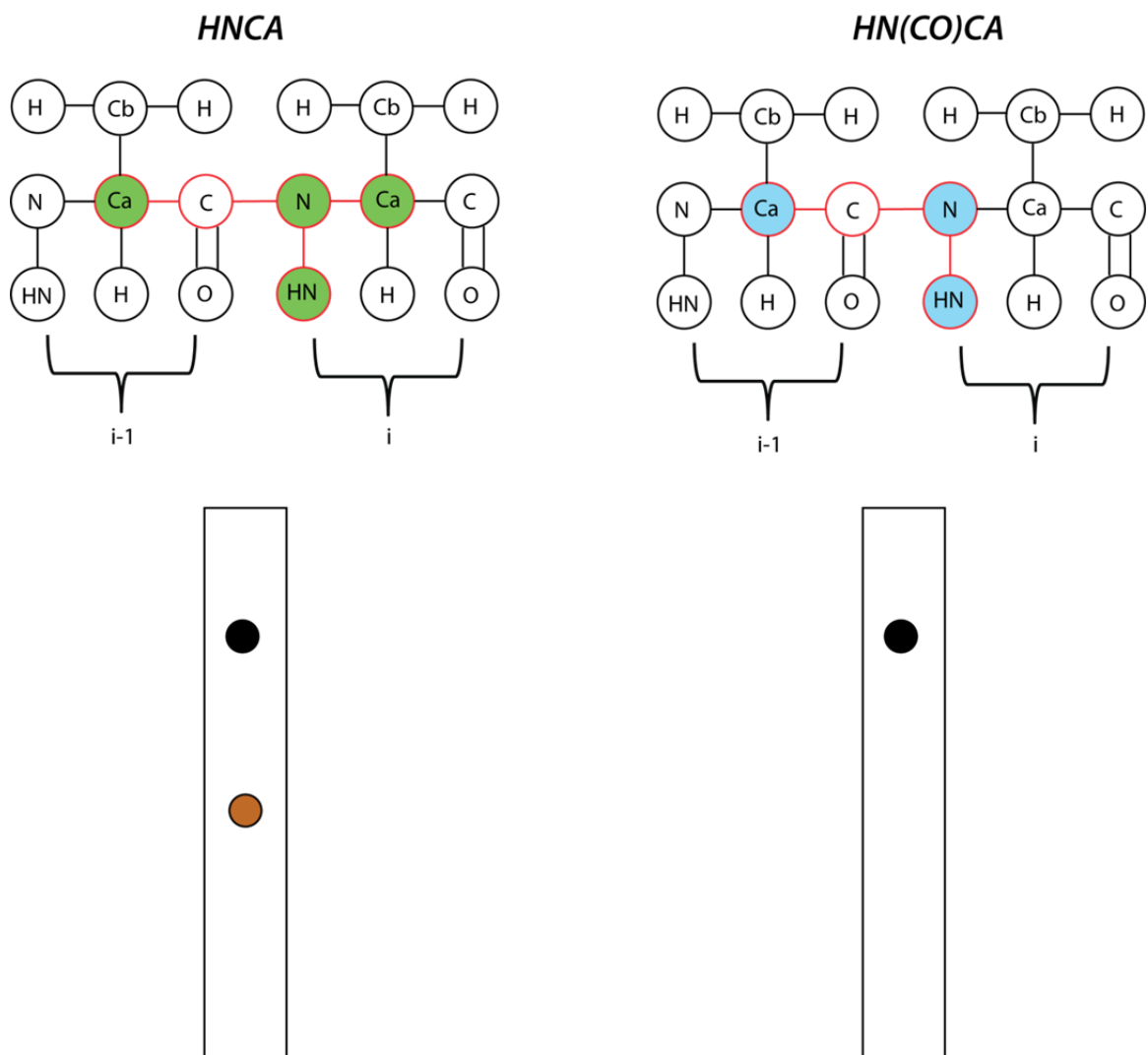
Figure 1.8. Cartoon representation of backbone assignment experiments HNCA and HN(CO)CA. In these two NMR experiments, magnetization is transferred between ^{1}H, ^{15}N, and ^{13}C atoms within the protein backbone. When performing an HNCA (left) experiment, magnetization is transferred to the ^{13}Ca atom in both the initiating (i) residues as well as the previous residue (i-1). The bottom panel represents an NMR spectrum, showing the two different resonances for residues i and i-1. When performing an HN(CO)CA (right), magnetization is transferred *only* through the carbonyl carbon (CO) to residues i-1. This is shown in the bottom panel as only 1 NMR resonance. By combining the data obtained in both experiments, it is possible to "link" all the residues together through the backbone atoms.

In the HNCA experiment, the resulting NMR spectrum shows two peaks, one from the alpha carbon from residue *i* and the other from the alpha carbon in residue *i-1*. These

two carbon atoms are linked through bonds two the same amide proton via the identical nitrogen atom. The resulting NMR spectrum from the HN(CO)CA experiment shows *only* the NMR resonance from the *i-1* alpha carbon, as the magnetization from this experiment must be transferred through the carbonyl bond (CO) to the previous amino acid (*176*). By connecting a string of amino acids via this method, it is possible to assign which residue belongs to which resonance, by comparing the sequence of the string to the amino acid sequence of the protein. While these two experiments are an effective way of determining the assignments of NMR resonances, a variety of different NMR pulse programs have been developed to enhance the process and ensure a complete assignment process.

Due to the challenges presented by membrane proteins, structural analysis is based only on backbone resonances. Following completion of the backbone resonance assignment, the first set of structural restraints is also collected. By examining the chemical shift of the ^{13}C resonances, restraints on the secondary structure and torsion angles of the protein backbone can be estimated. Secondary structures are analyzed by performing chemical shift indexing (CSI) analysis (*177, 178*). During CSI analysis, the chemical shift values of all carbon resonances are compared to known values for structures with random coils. Based on the resulting patterns, it can be determined if the protein has any alpha helical or beta sheet secondary structural elements. In addition to information about secondary structure, the carbon chemical shift values can also be calculated to torsion angles, in this case using the computer software TALOS+ (*179*).

In addition to the structural information from chemical shifts, additional structural restraints are acquired in the form of long and short range internuclear distances between atoms and the orientation of bond vectors. Traditionally speaking, structure determination of soluble proteins is done almost exclusively using an NMR phenomenon called nuclear Overhauser enhancement (NOE) (*180-183*). When studying membrane

proteins such as C99, it is difficult to assign all of the proton resonances due to the high level of spectral overlap, but more importantly due to the fact that the large protein/micelle complex tumbles too slowly, leading to rapid relaxation and broadening of NMR signals. Due to these complications, it is not uncommon that when working with membrane proteins the NOE experiment is used to not collect the bulk of the distance restraints between atoms, but instead to collect distances between the amide protons within the protein backbone, facilitating the process of secondary structure determination as well hydrogen bonding networks. It is not impossible to collect distance restraints using the NOE experiment for membrane proteins, and with recent advancements in labeling techniques and NMR pulse programs (*184-187*) this is becoming more frequent, but for the studies done on C99, only amide proton-proton distances were obtained.

To circumvent the problem of a lack of distance restraints from limited NOE data, long range distance restraints between atoms were obtained using a phenomenon known as paramagnetic relaxation enhancement (PRE) (*188*). Early in the development of NMR, the physics of nuclear relaxation enhancement arising from the presence of proximal paramagnetic species was explored (*189*). NMR signals are broadened to a degree that is proportional to $1/r^6$, where r is the distance between the paramagnet and the NMR nucleus. This broadening stems from the PRE phenomenon. In biological NMR, paramagnets can be added to samples as free probes (such as Mn(II) and Gd(III) and their chelates) or can be attached to proteins either through metal ion coordination or by modifying free cysteines with thiol-reactive nitroxide spin labeled compounds such as MTSL ((*S*-(2,2,5,5-tetramethyl-2,5-dihydro-1H-pyrrol-3-yl)methyl methanethiosulfonate) (*188, 190-195*). PRE of NMR sites can be quantified using methods as simple as recording 1- or 2-D NMR spectra of matched samples, one containing a paramagnet and the other in which the paramagnet is absent or quenched to a diamagnetic form. The PRE effect can be detected over a broad range from

approximately 0 to 25 Å for a proton experiencing relaxation enhancement from a nitroxide spin label. The distance can be extended to approximately 35 Å if a more dominant paramagnetic species is used (e.g. Mn^{2+}) (196).

The most common PRE measurements today involve use of 2-D $^{1}H,^{15}N$-HSQC or TROSY to measure the distances between a nitroxide spin label fixed at a specific protein site and the backbone amide protons of the same protein, an experiment that can generate dozens of distances from a single pair of NMR spectra. The derived distances can be used as a source of restraints for structure determination (188, 197). Such measurements have proven especially important for structural studies of challenging molecules where only the backbone chemical shift assignments are available, as is commonly the case for integral membrane proteins (26, 171, 192, 197-199). Most recently, the use of the PRE effect has been extended to aid in the NMR assignment process (200, 201), increase the sensitivity of NMR experiments (202), serve as a route to map intermolecular binding surfaces of macromolecular complexes (203, 204), elucidate the active/binding sites of proteins (192), map the topology of membrane proteins (28), and probe dynamic and sparsely populated states of macromolecules (193, 205, 206).

While the advent of PRE experiments for determining long range distance restraints during structure determination has greatly advanced our abilities to determine structures of membrane proteins, the lack of close range (2-5Å) distances can lead to the loss of finer details during structure calculations, such as bent or kinked helical segments. To complement the distances obtained from PRE and NOE experiments in order to determine a more accurate structure, residual dipolar couplings (RDCs) can be collected (207-209). RDCs are the measurement of magnetic interactions between two spins that are coupled (bonded) together when the molecule being studied is placed in a partially aligned media. RDCs are a vector quantity and have an angular dependence to

42

the external magnetic field. Under standard solution NMR conditions, proteins tumble isotropically, thus averaging out any RDC vector quantities between atoms. However, when placed in a partially aligned media, these vector quantities are no longer averaged out, and can thus be calculated by comparing the NMR spectrum of the isotropic sample to the anisotropic sample. The magnitude of the RDC is proportional to the angle between the coupled spins and the external magnetic field. By determining the RDC between two atoms, it is possible to back calculate the angle of that vector relative to the molecular frame.

The standard way of implementing RDC experiments by NMR is to use a 2D ^{15}N-^{1}H HSQC experiment and collect two NMR spectra, one of an isotropic sample and one of a matched anisotropic sample. Anisotropy can be introduced into the media by a variety of methods; the most common of which are using large magnetically susceptible bicelles that align in the external magnetic field, bacterial phage molecules, or by soaking a low percentage polyacrylamide gel with the protein solution and then stretching the gel, causing the polyacrylamide matrix to collapse and limit the protein motion (*208*). RDC experiments for C99 were performed using the stretched polyacyrmalide gel method. After the magnitude of the couplings are determined by measuring the separation in frequency between peaks from both NMR spectra, the values can be incorporated into structure calculations to provide orientation information regarding the two spins coupled together. In addition to ^{15}N-^{1}H backbone RDC experiments, it is possible to measure RDCs between other atoms, such as ^{13}C and ^{1}H. Additional levels of RDC experiments continue to increase the precision and accuracy of structures determined by NMR spectroscopy (*210*).

Validation of NMR Structures Using Electron Paramagnetic Resonance Spectroscopy

Structure determination by NMR spectroscopy gives researchers invaluable information regarding not only the overall architecture of a protein, but also how dynamics may influence protein function. However, when studying membrane proteins, it is difficult to ascertain whether certain properties of the protein are native to the structure, or are an artifact of the model membrane used. To solve this issue, many NMR studies supplement the information gained with electron paramagnetic resonance (EPR) spectroscopy experiments. EPR spectroscopy is a method similar to NMR spectroscopy, but allows proteins to be studied in lipid vesicles, which are a much closer membrane mimetic to the plasma membrane of cells. Like NMR, EPR monitors the transition of magnetic spins, but instead of monitoring nuclear spins, EPR monitors the transitions of unpaired electrons. Additionally, instead of being placed in a static magnetic field and having RF energy pulsed into the system, as with NMR, EPR utilizes an older magnetic resonance approach in which the input of energy is scanned across a range of frequencies with the implantation of an oscillating magnetic field (*211*). As with the use of PRE measurements in NMR, the unpaired electron for EPR experiments is incorporated into the protein using the molecule MTSL. When the frequency reaches a resonance value, energy is absorbed by the unpaired electron, resulting in an energy state transition. This transition is recorded, is Fourier Transformed, and the derivative of this signal is taken giving rise to the traditional EPR spectrum seen. CW EPR can be used to monitor the local dynamics and motion of the incorporated MTSL spin label. If incorporated into a region with dampened dynamics and motion, such as a region of the protein that is well structured or located within the plasma membrane, the resulting EPR spectrum will be broad. When incorporated into a region that is dynamic in nature, such as an unstructured loop that is solvent exposed, the EPR spectrum will appear sharp (Figure 1.9) (*212*).

Line Width and Mobility

τ_c = 0.1 ns
Fast motion limit

τ_c = 1 ns
Fast motion

τ_c = 10 ns
Slow motion

τ_c = 100 ns
Rigid limit

CW-EPR X-band
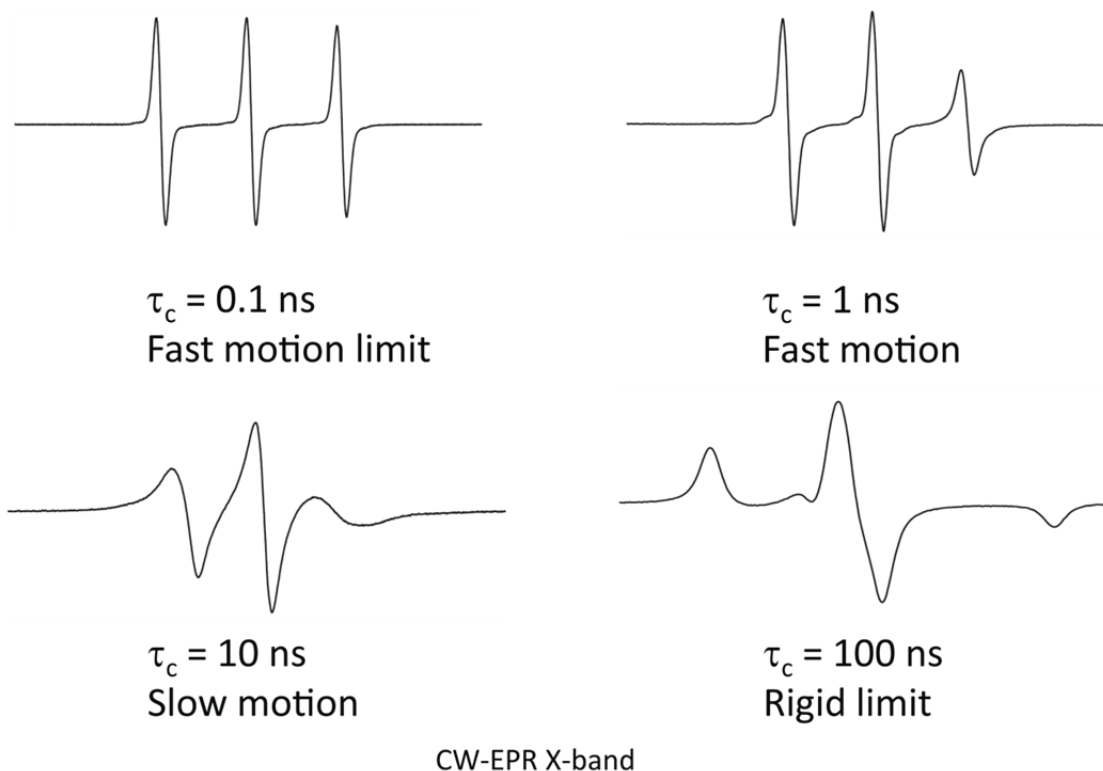
Figure 1.9. Representative EPR spectra indicating how EPR lineshape changes between fast and slow motion. As motioned is dampened, the EPR trace becomes broader (as shown in the bottom right panel).

In addition to monitoring protein movement and dynamics, single MTSL labeled proteins can undergo an EPR experiment known as power saturation (*213-215*). Power saturation studies utilize the phenomenon that paramagnetic molecules, such as oxygen and nickel, can influence the relaxation rate of the unpaired electron center, thus changing the EPR signal recorded. When studying membrane proteins, power saturation studies are important for determining the membrane penetration of individual residues, once modified with MTSL. This is due to the fact that nickel EDDA (NiEDDA)

is hydrophilic and will not penetrate the membrane and oxygen (O_2) is hydrophobic and will preferentially partition into the lipid bilayer (*213*). Close proximity to either compound will result in a drastic change in the EPR signal based on the enhanced rate of spin relaxation. This change is then monitored over a range of microwave frequencies. By taking the ratio of accessibility between NiEDDA and O_2 when compared to a non-paramagnetic standard (nitrogen), the penetration into the membrane of each residue can be obtained.

In addition to gaining information of protein mobility and membrane topology, when two MTSL spin label sites are incorporated into a protein, the double electron electron resonance (DEER) EPR method can determine discrete distances between the two spin label sites (*216-218*). DEER, also known as PELDOR or Pulsed ELDOR, uses two separate microwave frequencies to examine the coupling between two electron spins in order to make a distance measurement, typically between two nitroxide spin labels. In the experiment, a Hahn Echo sequence is used to produce an echo for the spins in resonance with the probe microwave frequency. At a time τ_2 after the first echo, a second π pulse is applied to form a refocused echo. At a separate microwave frequency, the pump frequency, a π pulse is applied to invert the population of a separate set of spins. This π pulse is then incremented in time and the intensity of the refocused echo is monitored. The set of spins affected by the probe frequency experiences a different magnetic environment before and after the pump π pulse. The change in the magnetic environment affects the ability of the magnetization to be called back with the second probe π pulse. The net effect is a modulation in the intensity of the refocused echo with a periodicity that is a function of the strength of the coupling and therefore, the distance, between the two electron spins (*219*).

Initial Structural Studies of C99

As stated above, the backbone resonance assignment for C99 was previously accomplished and published by the Sanders lab (*28*). In addition to assigning each residue to an NMR resonance, the completion of the backbone assignment also allows for initial secondary structure analysis of the protein using chemical shift indexing (CSI) analysis (*177, 178, 220*). CSI analysis of C99 indicated that in addition to a helical transmembrane helix, the protein contained two other regions that had helical secondary structure; a 6 residue helical turn from residues V688-V694 (termed the N-helix due to its location N-terminal to the transmembrane helix) and the extreme C-terminus of the protein (C-helix) (*26, 28*). In addition to the backbone resonance assignment and secondary structure analysis, this previous work also established the membrane topology of C99 in lyso-myristoylphosphatidylglycerol (LMPG) detergent micelles. The membrane topology studies determined which regions of C99 were embedded in the hydrophobic environment of the detergent micelle and which regions were exposed to the solvent. These studies were performed by adding paramagnetic probes to the protein NMR sample and monitoring changes within the NMR TROSY-HSQC spectrum. Paramagnetic probes function by enhancing the relaxation rate of proximal NMR nuclei (*188*). This enhancement in relaxation is manifested as broadening of the NMR signal for those nuclei, and in extreme cases, the complete disappearance of the resonance from the NMR spectrum. By using the paramagnetic probes 16-doxylstearic acid (16-DSA) (inside the micelle) and Gd(III)-diethylenetriaminepentaacetic acid (Gd-DTPA) (outside the micelle), Beel *et al* were able to determine which regions of C99 were within the detergent micelle and uncover the first experimantlly determined glimpses into the protein topology. They discovered that in addition to the transmembrane helix, the two

other helical regions of the protein (N-helix and C-helix), were also both embedded in the membrane (Figure 1.10) (*28*).
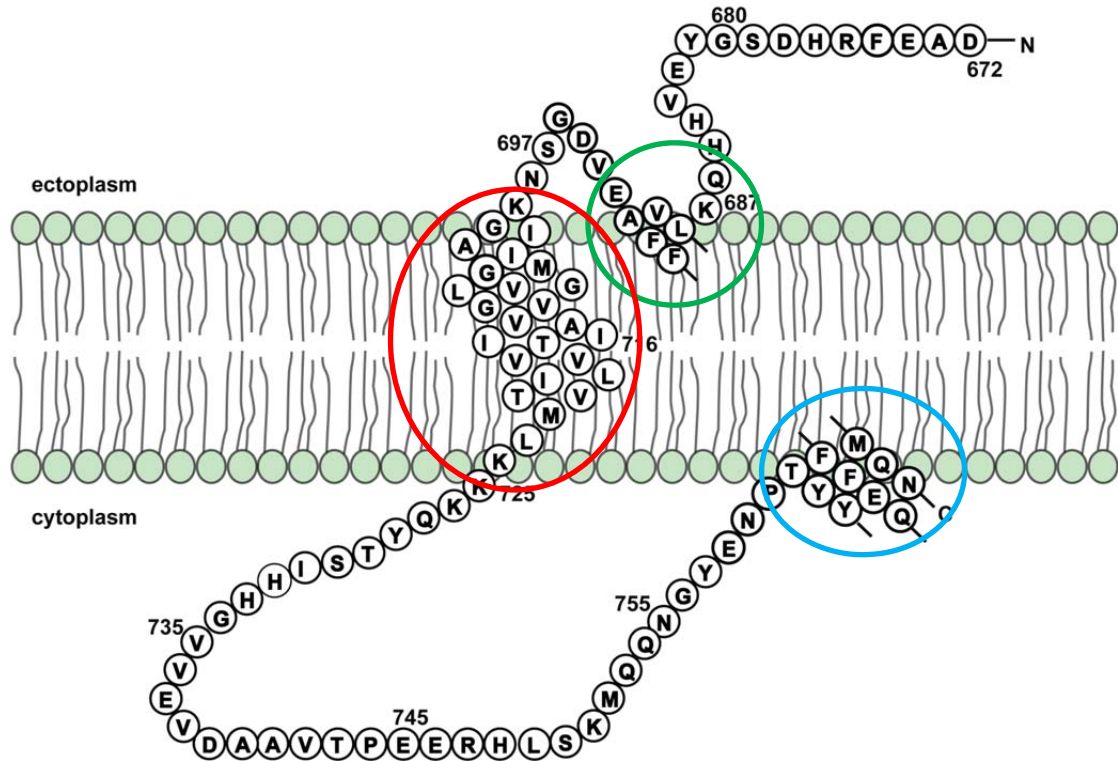
Figure 1.10. A 2D topology plot of C99 in a cartoon lipid bilayer. C99 possesses three regions that are α-helical. Residues 688-694 (circled in green), residues 700-723 (circled in red), and residues 762-770 (circled in cyan).

The discovery of these additional membrane bound regions of C99 shed some initial light on how the structure of the protein may play a role in regulating its function. It was noted that both membrane embedded helices contained two consecutive phenylalanine residues, leading to the speculation that these residues may help to anchor the helical structure into the membrane. This hypothesis was corroborated by work from the lab of Tobias Ulmer when his lab determined the 3D structure of the αIIbβ3 integrin and showed a similar phenomenon (*221*). Linking the N-helix to the

transmembrane helix is a short, five residue loop (N-loop), and when examined in the 2D topology plot, the overall structure from the N-helix through the transmembrane domain provides what appears to be a ligand binding pocket for a lipid or other hydrophobic molecule. In fact, initial work from Beel *et al* showed that this region of C99 was able to specifically bind the soluble cholesterol analogue β-Cholbimalt, suggesting the first biochemical evidence that C99 could potentially bind native cholesterol (*28, 30*).

While the exact function of APP is still being elucidated, it is known that APP is able to undergo rapid turnover from the plasma membrane to endocytic vesicles through clathrin mediated endocytosis (*1, 9, 33, 49, 77*). Contained within the C-helix of APP is a known trafficking amino acid sequence, NPxY, which allows for the binding of a variety of adaptor proteins to promote APP internalization (*222, 223*). A potential new hypothesis to study would be that the membrane proximity of the C-helix allows for preferential interactions with different adaptor proteins under different cellular conditions, either promoting or inhibiting APP internalization. If found to be true, this may be a way of preventing the overproduction of Aβ peptides, as their generation occurs only after endocytosis of APP and β-Secretase (*81, 224*). While the initial work performed by Beel *et al* set a great foundation for how the structure of C99 regulates AD, determination of a 3D structure of the protein was the next step into gaining a better understanding of how the structure of this protein regulated its function.

Giant Unilamellar Vesicles to Study Cholesterol Rich Domains

As previously noted, there is an ever present link between APP, cholesterol rich domains, and AD. However, the exact understanding of how all these components lead to increased Aβ production and neuronal death is still unclear. Recent evidence from our lab indicates that the β-Secretase cleavage product of APP, C99, can specifically bind cholesterol in the bicelle model membrane system (*26*). This result gives strong

biochemical evidence that C99, and potentially APP, can bind cholesterol under conditions found within the plasma membrane of cells. Our findings led to the hypothesis that cholesterol binding by APP promotes the amyloidogenic cleavage pathway in AD by increasing the partitioning of APP to cholesterol rich domains.

To study the impact cholesterol binding has on C99 membrane partitioning, we developed a method to monitor this membrane partitioning by confocal fluorescence microscopy using the model membrane system known as giant unilamellar vesicles (GUVs) (*225-227*). GUVs are a powerful technique for investigating cholesterol rich domain formation and membrane protein partitioning, as the exact lipid content can be manipulated very easily, but more importantly, the formation process creates GUVs that can be imaged by microscopy, as they range from 10-100µM in diameter. This allows for the incorporation of fluorescent lipid probes or fluorescently labeled protein molecules to actively image cholesterol rich domains and changes in protein membrane localization. The process of cholesterol rich domain formation in GUVs has been rigorously studied for a variety of lipid mixtures (*228-233*). These experiments have determined phase diagrams of ternary mixtures of lipids, all of which include an unsaturated lipid (i.e. POPC), a saturated lipid (i.e. SM), and cholesterol. Within this phase diagram are regions where co-existing liquid disordered (L_d) and liquid ordered (L_o) cholesterol rich domain formation occurs. It is within these regions that our studies were performed to monitor C99 membrane partitioning (Figure 1.11).
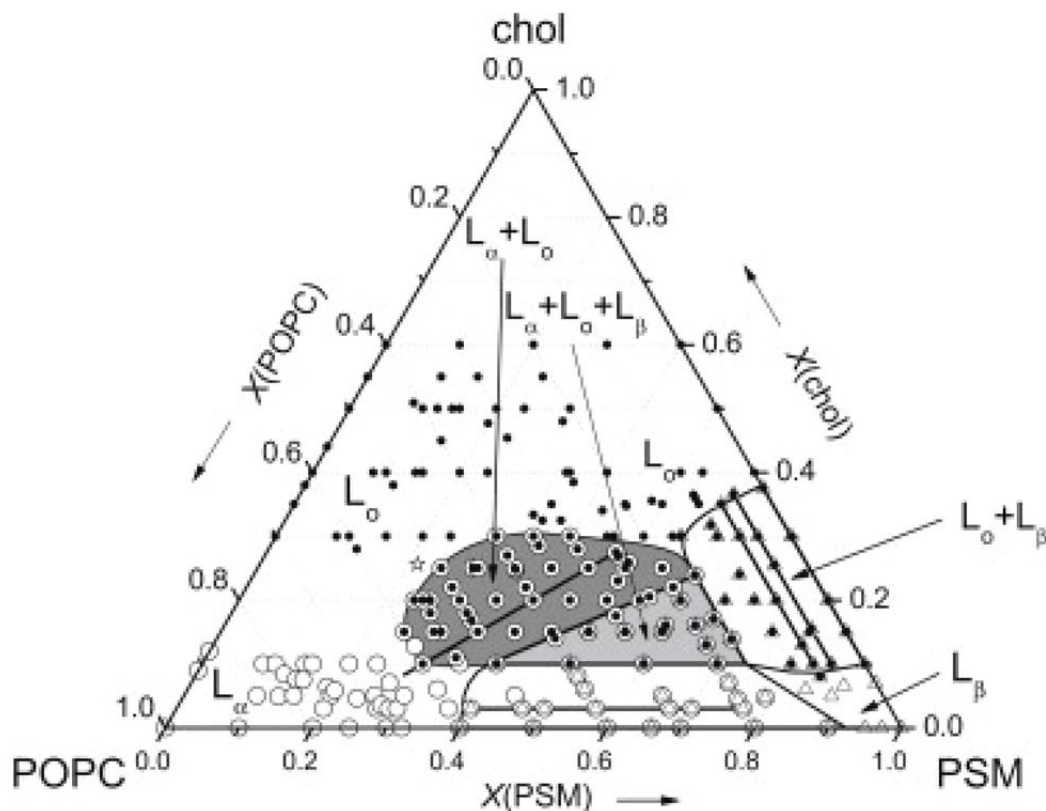
Figure 1.11. The phase diagram for the ternary lipid mixture of POPC/SM/Cholesterol. The region highlighted in dark grey represents the regime used for future experimental studies, that contains both liquid disordered (L_d) and cholesterol rich (L_o) domains. *X* represents the mol fraction of each lipid. This figure was modified with permission from (*233*).

The details of GUV experiments will be covered in more depth in later chapters, but as an introduction GUVs are formed by exposing a multi-layer lipid film to a process known as electroformation (*234*). The lipid film is created by taking a mixture of lipids in chloroform and dehydrating them on an indium tin oxide (ITO) glass microscope slide. By mixing lipids in chloroform, one can manipulate the percentage of lipids to generate cholesterol rich domains with different properties, such as size and dynamics. Electroformation is a process that involves connecting the ITO slides to a wave generator, which outputs an applied voltage of 1-2 volts using a sinusoidal wave with a frequency of approximately 10 Hz. A combination of electrostatic, mechanical,

hydrophobic, and van der Waals interactions force the multi-layered lipid film to separate into the surrounding aqueous buffer where GUVs spontaneously form (*234-236*).

Summary

The purpose of the following chapters is to help elucidate how the structure and function of C99 contribute to increased Aβ production during AD. Three stories will be told in all. The first will highlight how 3D structure determination of membrane proteins can show how protein structure and dynamics impact protein function. It will be shown that C99 possess a flexible transmembrane helix, and that this flexibility may serve to regulate γ-Secretase cleavage. The second component will highlight how GSM compounds modulate γ-Secretase activity through a mechanism independent of interactions with APP. In addition, this section will also show results of how previous studies interpreted that GSMs specifically interact with APP and the Aβ peptide. The last story will highlight how cholesterol binding influences C99 membrane partitioning in GUVs, and how this partitioning can be controlled by the presence of different sterols. These findings will further support that cholesterol rich domains play an important role in Aβ production, and that manipulating APP's preference for these domains may be a potential therapeutic not yet studied to ameliorate the effects of AD.

CHAPTER II

THREE-DIMENSIONAL STRUCTURE OF C99[3,4]

Introduction

Alzheimer's disease (AD) is a severe form of dementia that current affects nearly 40 million people worldwide, a number that is estimated to increase by the year 2050 to roughly 120 million (*1*). The production and subsequent aggregation of amyloid-β (Aβ) peptides are widely thought to play a central role in most forms of AD (*1, 238*); accordingly, factors that increase Aβ production and oligomerization or that reduce its elimination increase the risk of AD.

Amyloidogenic cleavage of full-length amyloid precursor protein (APP) by β-Secretase generates the transmembrane protein C99 (APP$_{672-770}$, also known as β-CTF, figure 2.1).

Figure 2.1. Primary sequence and domain organization for C99 as determined in this work, with transmembrane glycines highlighted (red). The uppermost numbering scheme, based on full length APP, is used in this work. The middle numbering system is based on the numbering of the most common splice variant of APP found in neurons. The bottom numbering system is based on that of the amyloid-β peptide. Most structural studies in this work included an added purification tag at the C-terminus with the sequence – QGRILQISITLAAALEHHHHHH. It is well known that tags at the C-terminus of C99 do not interfere with its processing by γ-Secretase.

The transmembrane domain (TMD) of C99 is then processively but imprecisely cleaved by γ-Secretase to release the Aβ polypeptides (*239, 240*). Cleavage by γ-Secretase is believed to be initiated at either the ε48 (linking T719 and L720) or ε49 (L720/V721) sites and continues by release of tri- and tetrapeptides after proteolysis at alternate ζ- (ζ45 = I716/V717; ζ45 = V717/I718), and γ-sites (γ37 = G708/G709; γ38 = G709/V710, γ40 = V711/I712, γ42 = A713/T714), resulting in two distinct product lines. Successive cleavage leads to release of the most abundant Aβ40 and the minor Aβ42 and Aβ38 peptides. Structural information on C99 may provide insight into amyloidogenesis; however, previous structural studies have employed only low resolution methods or have focused on TMD-only containing fragments (*16, 28, 241-243*). It is imperative that a structure be determined for the intact full length C99 protein in order to elucidate the diverse biological roles of APP. In addition, information gained from the 3D structure of C99 will permit for a better understanding of how cleavage by γ-Secretase occurs within

the membrane, and show possible mechanisms for regulating the Aβ42-Aβ40 ratio. Lastly, there are inherited mutations in APP that can results in AD onset early in life, called Familial Alzheimer's disease (FAD). The structure and stability of wild-type C99 can then be compared to known FAD mutants, which may illuminate possible mechanisms for FAD pathogenesis.

Extensive work by Beel *et al* in 2008 determined the secondary structure of C99 utilizing chemical shift indexing (CSI) analysis from backbone ^{13}C NMR resonances. In addition, this study also revealed a novel membrane topology of C99 utilizing paramagnetic probes during NMR experiments (*28*). These studies determined that in addition to a helical TMD, C99 possesses two additional segments that have α-helical secondary structure; a region spanning residues 689-694, called the N-helix, and the extreme C-terminus of the protein (residues 762-770), named the C-helix. Using the paramagnetic probe studies it was found that both of these regions are embedded in the micelle. By determining the 3D structure of C99, we will not only validate the findings of Beel *et al* in a 3D model, but also lay the groundwork for future studies that will impact how AD is understood and treated.

Materials and Methods

NMR Sample Preparation and Resonance Assignments for C99 in LMPG Micelles

As described previously (*28*), the cDNA for full length human C99 was cloned into a modified pET21a plasmid. To facilitate spin labeling or alanine scanning of C99, a series of single-cysteine and site-directed alanine mutant forms of C99 were generated using QuickChange site-directed mutagenesis (Stratagene). The protein was then expressed in *E. coli* with either an added N-terminal His6-Gly- tag or a C-terminal tag that includes a His6 sequence (*28*). The protein was then purified in into lyso-

myristoylphosphatidylglycerol (LMPG) micelles (*28*). LMPG is a phospholipid-like detergent. Relative to other micelles and also to isotropic bicelles, LMPG micelles were found to yield NMR spectra of superior quality for this protein (*28*). NMR samples of C99 contained 0.25 mM protein and 10% LMPG in 100 mM imidazole, 2 mM EDTA, and 10% D2O, pH 6.5. NMR data was collected at 45°C on either a Varian Inova 900 MHz spectrometer with a cryoprobe, a Bruker Avance 800 MHz spectrometer with a cryoprobe, or a Bruker Avance 600 MHz spectrometer with a conventional probe. Backbone resonance assignments were previously reported (*28*) and were deposited in the BioMagResBank (www.bmrb.wisc.edu) with accession number 15775.

Use of NMR Chemical Shifts as Restraints and Measurement of NOE Restraints for C99 in LMPG Micelles

Backbone $^{13}C\alpha$, $^{13}C\beta$, ^{13}CO, ^{15}N chemical shifts were used to estimate backbone dihedral angles using the program TALOS+ (*179*). Only restraints that were classified by this program as being in the highest confidence category were used in structural calculations. Chemical shift index (CSI) analysis (*220*) was also implemented to assess secondary structure for hydrogen bond restraints. ^{1}H-^{1}H NOEs were obtained using the 3D (^{1}H, ^{1}H, ^{15}N)-TROSY-NOESY experiment (120 ms NOE mixing time) on uniformly-^{13}C/^{15}N double-labeled C99 in LMPG micelles at 900 MHz(*28*). 65 amide-amide NOEs were used in structural calculations. Measurements of *side chain-side chain* NOEs were not feasible because of the difficulty of assigning side chain resonances in a large protein-detergent complex that has been shown to exhibit generally unfavorable transverse relaxation rates(*28*). NH-NH NOEs were assigned by correlating diagonal amide parent resonances with coupled amide resonances via the TROSY spectrum. Spectra were analyzed using NMRView (*244*) and assigned using Sparky (*245*).

Measurement of Residual Dipolar Couplings for C99 in LMPG Micelles

Stretched neutral polyacrylamide gels (7.0% acrylamide concentration, 0.5% AMPS, and acrylamide/bisacrylamide molar ratio of 50:1) were prepared according to Chen *et al* (*210*). Cylindrical polyacrylamide gels were cast with a 7.0 mm diameter in 100 mM imidazole, pH 6.5 buffer in the absence of detergent and then cut to 1.5 cm in length. This was followed by soaking gels in three successive changes of 100 mM imidazole buffer (pH 6.5). 1 mL of a U-^{2}H/^{15}N-C99 in an LMPG micelle solution (see above NMR sample conditions) was then soaked into the wet gel for at least 48 hours. The gel was subsequently stretched (using a device from New Era Enterprises, Vineland, NJ) into an open-ended NMR tube with a 4.2 mm inner diameter. The stretched gel was 2.2 cm in length. The concentration of C99 in the 500 μl gel was determined to be 0.45 mM by measuring the C99 concentration in the solution remaining outside of the gel after soaking. ^{1}H-^{15}N residual dipolar couplings (RDCs) were measured using a uniformly ^{2}H, ^{15}N-labeled sample at 800 MHz by acquiring a pair of 2D ^{1}H-^{15}N TROSY spectra in an interleaved manner, one in which the ideal TROSY components were selected and one in which the semi-TROSY (TROSY in the ^{15}N dimension, anti-TROSY in the ^{1}H dimension) peaks were selected. The J+D couplings were then measured in the ^{1}H dimension. The difference in the observed couplings between aligned and isotropic samples correspond to the ^{1}H-^{15}N dipolar couplings(*7, 8*). An example of the RDC data is shown in figure 2.2.
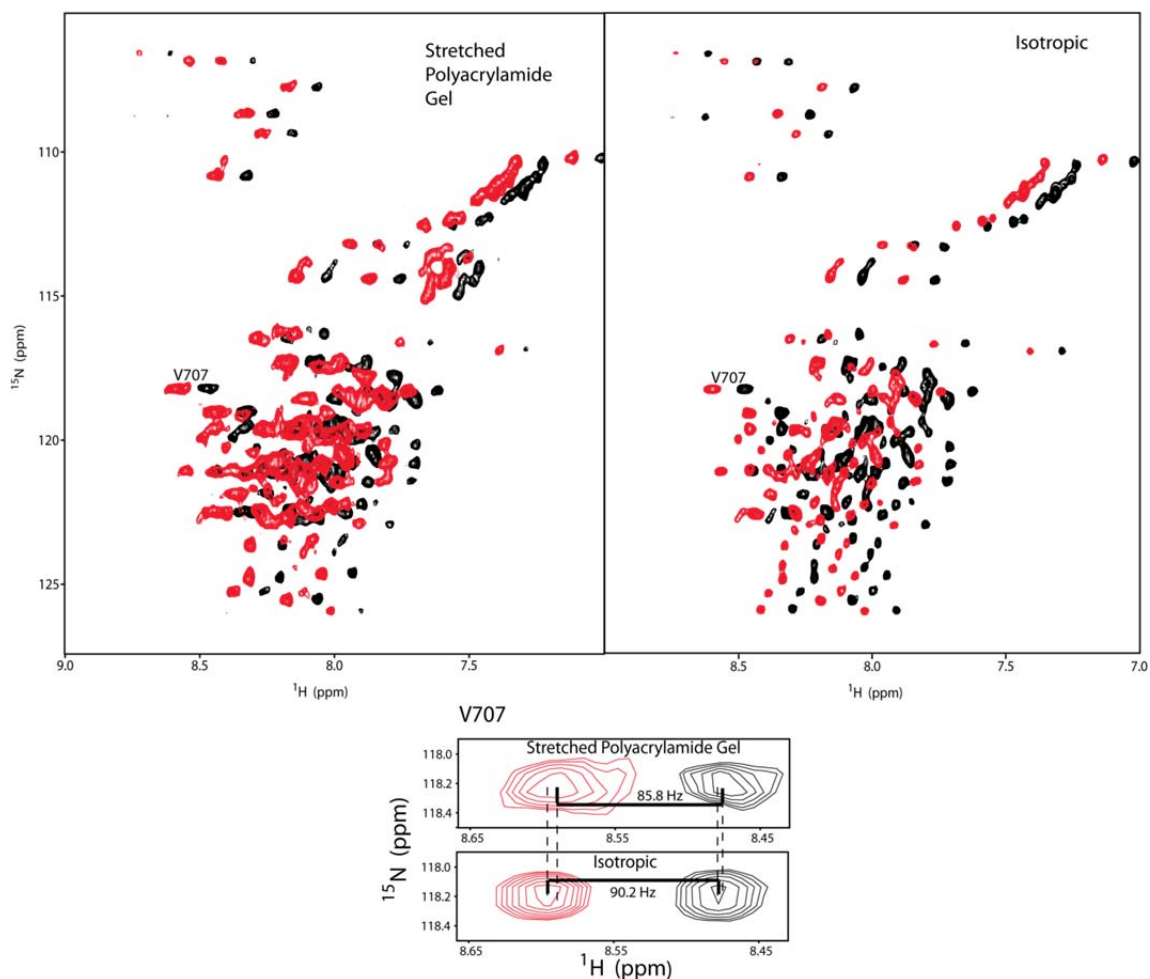
Figure 2.2. Measurement of HN RDCs for C99. The top panel shows the ^{1}H, ^{15}N-TROSY NMR spectra of C99 in LMPG micelles in a stretched polyacrylamide gel and in a free (isotropic) solution. The spectrum for the aligned sample (polyacrylamide) was collected at 800 MHz using U-^{2}H, ^{15}N C99 in a stretched 7% acrylamide, 0.5% AMPS gel, under otherwise standard sample conditions (10% LMPG micelles, pH 6.4, 318K). The red and black spectra denote semi-TROSY and TROSY resonances respectively. The bottom panel shows superimposed TROSY (black) and semi-TROSY (red) peaks for residue V707, found in the TMD.

Preparation of Spin-Labeled C99 for NMR Paramagnetic Relaxation Enhancement

(PRE) Measurements

Wild type C99 has no Cys residues. Select residues were mutated to cysteine using the Quik-Change protocol (Stratagene Company, La Jolla, CA, USA) utilizing wholeplasmid PCR. From the C99 plasmid, a total of four single-Cys mutants were

prepared: Val695Cys, Gly700Cys, Leu705Cys, and Leu723Cys. These mutations were selected to be located on relatively immobile sites: V695C is located in the N-terminal helix, G700C and L723C mark the termini of the transmembrane helix, and L705C is located towards the middle of the transmembrane helix. Prior to PRE measurements, [1]H-^{15}N TROSY experiments were performed to validate that these mutations did not perturb the native structure of C99. Single-Cys mutant forms of C99 were overexpressed and purified as described for wild type(*28*). After purification, each cysteine mutant was concentrated to 0.5mM and the pH was lowered to 6.5. Samples were then reduced with 2.5mM DTT, with gentle agitation at room temperature for 24 hours to ensure complete conversion to Cys-SH. To verify this, samples were analyzed by SDS-PAGE. Mutants were then Cys-modified by the thiol-reactive nitroxide free radical probe, 1-oxyl-2,2,5,5-tetramethylpyrroline-3-methyl-methanethiosulfonate (MTSL, Toronto Research Chemicals, Toronto, Canada). MTSL was added to 10 mM from a 250 mM solution in dimethylsulfoxide into a 0.5 mM C99 solution (buffer: 100 mM imidazole, 2 mM EDTA, 2.5 mM DTT, 0.05% LMPG, pH 6.5), which was then gently agitated at room temperature for 30 minutes, followed by incubation at 37ºC for 3 hours. Samples were then buffer-exchanged into a 50mM phosphate, 0.05% LMPG, pH 7.8. Following buffer exchange, samples were bound to Ni(II)-chelate chromatography resin in a column, which was then washed with 100 mL of 50mM phosphate, 0.05% LMPG, pH 7.8 to remove excess MTSL. The spin-labeled C99 was eluted using elution buffer (250mM imidazole, 0.05% LMPG, pH 7.8). Samples were then processed (as above) to achieve standard NMR conditions (100mM imidazole, 10% LMPG, 10% D2O, 2mM EDTA, pH 6.5). Prior to NMR PRE experiments, the % of nitroxide spin-labeling for each C99 sample was quantitated by double-integrating EPR resonances from each labeled sample relative to the signal from a 100 µM TEMPOL standard. In all cases, the

efficiency of spin-labeling was >90%.

NMR Paramagnetic Relaxation Enhancement-Based Distance Measurements for C99

Paramagnetic relaxation enhancement (PRE) experiments were used to measure long range distance restraints. For each spin-labeled single-cysteine mutant, a pair of 2D ^{1}H-^{15}N TROSY spectra were acquired for spin-labeled C99: one for the spin-labeled protein in the paramagnetic form, and one after adding ascorbic acid (to 7.5 mM) to the sample in order to reduce the nitroxide, yielding the diamagnetic species. The spectra for each pair of paramagnetic and diamagnetic samples were processed and then zero-filled in both t_1 and t_2 dimensions. The spectra were then analyzed to measure PRE-based differences in peak intensities using the programs nmrPipe (*246*), nmrView (*244*), and Sparky (*245*). Intensity ratios of peaks from the oxidized and reduced spectra were converted into paramagnetic relaxation rate enhancements (PREs, R2sp) by estimating the additional transverse relaxation needed to reduce peak intensity relative to diamagnetic conditions by the observed intensity ratio using the following equation (*188*):

(1) $I_{ox} / I_{red} = R2 \exp(-R2_{sp} \tau) / (R2 + R2_{sp})$

The intrinsic R2 were estimated from the ^{1}H line widths from diamagnetic samples. Tau (τ) was the duration of the INEPT delay in the TROSY pulse sequence (13.3 msec). The $R2_{sp}$ values were then calculated from the above equation using Microsoft Excel and converted into distances using the following equation:

(2) $r = [K/R2_{sp} (4\tau_c + 3\tau_c / (1 + \omega h^2 \tau_c^2))]^{1/6}$

where r is the distance between the electron and nuclear spins (in angstroms), τ_c is the correlation time for the electron-nuclear interaction, ωh is the Larmor frequency of the nuclear spin ($600.13 \times 10^6 \sec^{-1} \times 2\pi$) and K is 1.23×10^{-32} cm^6/s^2 (*188*). The rotational

correlation times (τ_c) were calculated based on previously reported backbone amide ^{15}N T$_1$ and T$_2$ relaxation values for C99(*28*). An example of the PRE data collected is shown in figure 2.3.
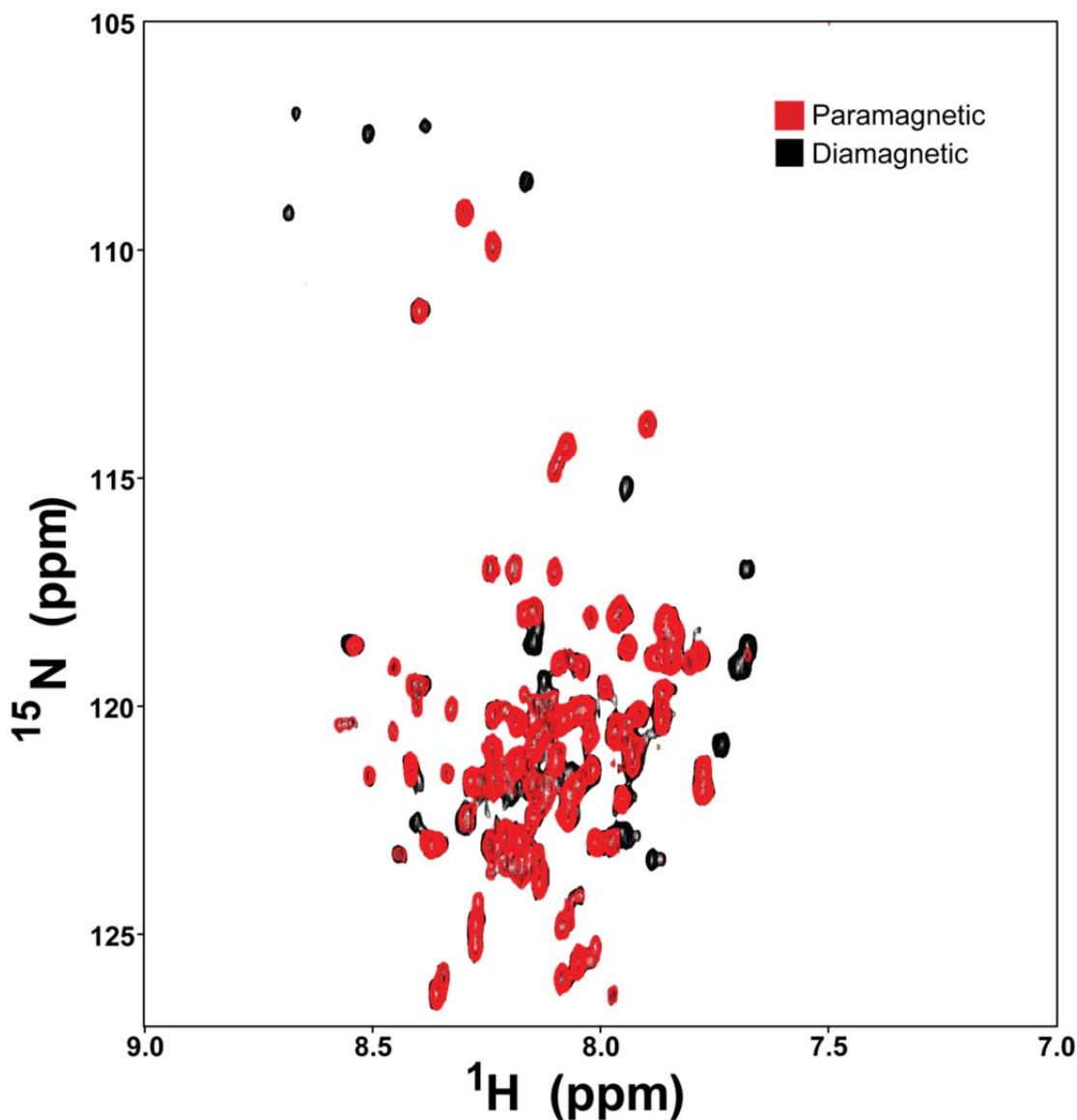
Figure 2.3. Representative ^{15}N TROSY PRE data used to derive long range distance restraints used in structure determination of C99. PRE data from spin-labeled V695C C99 are shown as the overlay of two NMR spectra. The red spectrum represents the paramagnetic state of the MTSL probe (active) and the black spectrum represents the diamagnetic state after the MTSL probe has been reduced. These data were recorded for a 250µM U-[15]N C99 sample at 800 MHz, 318K, pH 6.5 in the presence of 1mM EDTA, 100mM imidazole, 10% LMPG micelles, and 10% D_2O.

Structural Calculations for C99 in LMPG Micelles

Initially, structural calculations were carried out for full length C99 (all 99

residues). However, it became apparent from these calculations that the N-terminus prior to residue 687 is disordered, as is the C-loop extending from residues 724 to 759. While the C-helix (residues 760 to 770) is a well-ordered α-helix and is located at the membrane (i.e. micelle) interface, it is not restrained in terms of placement with respect to the TMD. Given the above considerations, we completed the final structural calculations using only the relatively ordered N-helix, N-loop, and transmembrane domains plus a few residues on either side (683 to 728). It is the outcome of these final calculations that are represented by PDB deposition 2LP1. Unambiguously assigned ^{1}H(N)-^{1}H(N) NOEs were employed as structural restraints, as were backbone dihedral angles (φ, ϕ) generated using TALOS+. Hydrogen bond restraints for the N-terminal helix and transmembrane helix were applied based on the results of CSI analysis and H/D exchange rates ([237]). PRE distance restraints were classified in different categories as described ([188]). Resonances with paramagnetic/diamagnetic intensity ratios less than 0.15 were classified as "close" and therefore restrained to being between 2 and 19Å from a given MTSL modified cysteine residue. Resonances with intensity ratios between 0.15 and 0.85 were converted to distances as described above (and ([188])), with uncertainties of ±4Å. Peaks unaffected by the paramagnetic probe (intensity ratio >0.85) were restrained to being between 21 and 74Å. These distance restraints were implemented as pseudo-NOEs from the nitroxidecontaining pyrroline ring to the backbone amide hydrogen utilizing MTSL-labeled pseudo-atoms, known as CYSP residues ([172]). RDC data was only incorporated for the N-terminal helix and transmembrane helix. Data-restrained structural calculations were carried out using a slightly modified version of the XPLOR-NIH v2.24 'anneal.py' structure calculation script ([172]). Calculations started with an extended C99 template with randomized backbone torsion angles followed by 1000 cycles of Powell energy minimization. Simulated

annealing was performed using 15,000 steps at 3500 K with gradual cooling to 100K. During the cooling stage the van der Waals interactions were increased by varying the force constant of the atom-atom repulsive term from 0.5 to 4 kcal·mol^{-1}·Å^{-4} with an initial effective atom radius of 0.5Å. Hydrogen bond restraints were enforced with flat-well harmonic potentials, with the force constant being fixed at 25 kcal·mol^{-1}·Å^{-4}. Force constants for NOE, PRE, and RDC restraints were ramped from 1, 1, and 0.01 to 30, 30, and 1 kcal·mol^{-1}·Å^{-4}, respectively. Dihedral terms were ramped from 5 to 500 kcal·mol^{-1}·Å^{-4}. Default anneal.py values and parameters were used for all other restraints and steps. During the structure calculations, the van der Waals interaction involving CYSP residues were turned to zero to avoid steric clashes between the side chains of these residues that were not present under experimental conditions (where, at most, only a single CYSP site would be present. After the high temperature simulated annealing was complete, a round of torsion angle minimization and full atom minimization was carried out using 500 steps of Powell energy minimization. CYSP residues were mutated back to wild type residues using a Pymol based script and subjected to three rounds of Powell energy minimization, consisting of 100, 60, and 200 steps to optimize side chain packing. Of the 100 output structures, the 30 lowest energy structures were used to generate an ensemble. When aligned to the average structure, the N-terminal helix (residues 688-695) displayed an RMSD of 0.731Å. The transmembrane domain (residues 699-723) exhibited an RMSD of 0.508Å when compared to the average TMD structure. The RMSD for both domains (residues 688-723) when compared to the average structure was 1.023Å. A summary of the structure calculations and the related statistics for the results are presented in Table 1. The protein databank code is 2LP1.

Table 1

NMR distance, dihedral, and RDC restraints

Total Restraints	232
Distance Restraints	141
Total NOE	65
Inter-residue	65
Sequential ($|i-j|=1$)	43
Medium Range ($|i-j|<4$)	22
Long Range ($|i-j|>5$)	0
PRE restraints	63
Hydrogen Bonds	13
Total dihedral angle restraints	65
phi	33
psi	32
RDC restraints	26

Structure Statistics

Violations (mean and s.d.)	
Distance restraints (Å)	0.000 ± 0.000
Dihedral angle restraints (°)	0.004 ± 0.001
RDC (Hz)	0.515 ± 0.213
Deviations from idealized geometry	
Bond lengths (Å)	0.001 ± 0.000
Bond angles (°)	0.351 ± 0.052
Impropers (°)	0.288 ± 0.005
Main chain atom r.m.s.d. to the mean structure (Å)	
N-terminal Helix (688-694)	0.731
Transmembrane Helix (699-723)	0.508
Residues 689-723	1.023
Ramachandran plot* (%)	
Most favored regions	96.3
Additionally allowed regions	3.7
Generously allowed regions	0.0
Disallowed regions	0.0

There are no distance, dihedral angle restraint, and RDC violations greater that 0.5Å, 5°, and 1.5 Hz respectively

*Statistics applied to N-terminal Helix (aa 688-694) and transmemrane helix (aa 699-723) for the top 30 lowest energy structures

Table 1. Structural statistics for the ensemble of the 30 lowest energy structures for C99.

Amide H/D Exchange Rate Measurements

C99 with a C-terminal tag containing His_6 was recombinantly expressed in uniformly ^{15}N-labeled form and purified in to lyso-myristoylphosphatidylglycerol micelles as described previously (*247*), followed by adjustment of the pH to 6.5. $^{15}N^1H$-^{15}N

TROSY-HSQC experiments were serially recorded using a 900MHz Bruker spectrometer on a C99 sample after mixing with a 10X volume excess of 100% D_2O. A 500µL U-^{15}N-C99 NMR sample was mixed with 5 mL of 100% D_2O in 100 mM Imidazole, pH 6.5. The sample was then concentrated back to 500 µL using a 30 kDa cutoff filter. Final C99 samples contained 0.2 mM U-^{15}N-C99 in 10% LMPG (w/v), 100mM Imidazole, pH 6.5 in ca. 100% D2O. TROSY experiments were performed at times points starting at 0 h, 2 h, 8 h, 16 h, and 24 h after mixing with the D_2O. The 0 hour time point was recorded on the C99 NMR sample prior to the 10x excess of D2O. Identical NMR experiments were performed at each time point, with 128 scans and 256 incremented being performed. To quantify the exchange data, peak intensity was monitored at each time point and compared to the reference sample prior to D_2O addition (time = 0). Amide protons of residues exposed to the solvent or not in a H-bonding network will disappear from the TROSY spectrum once the proton is exchanged for a deuteron. For each experiment, the total acquisition time was approximately 6 h, such that the temporal resolution of observed H/D exchange process is low. For this reason, we limited our analysis to comparison of the exchange states represented by the TROSY spectra collected over the 2-8 h and 16-22 h time ranges (figure 2.4). By 2-8 h in 100% D_2O all observable peaks in dynamic loop regions had effectively disappeared from the TROSY-HSQC spectrum. All regions of predicted helical secondary structure (residues 688-694, and 699-723) did not exchange with the D_2O until at least 16 h, many showing little exchange at all. The only segments for which H/D exchange rates were consistent with stable secondary structure are those previously determined to be helical (*247*).
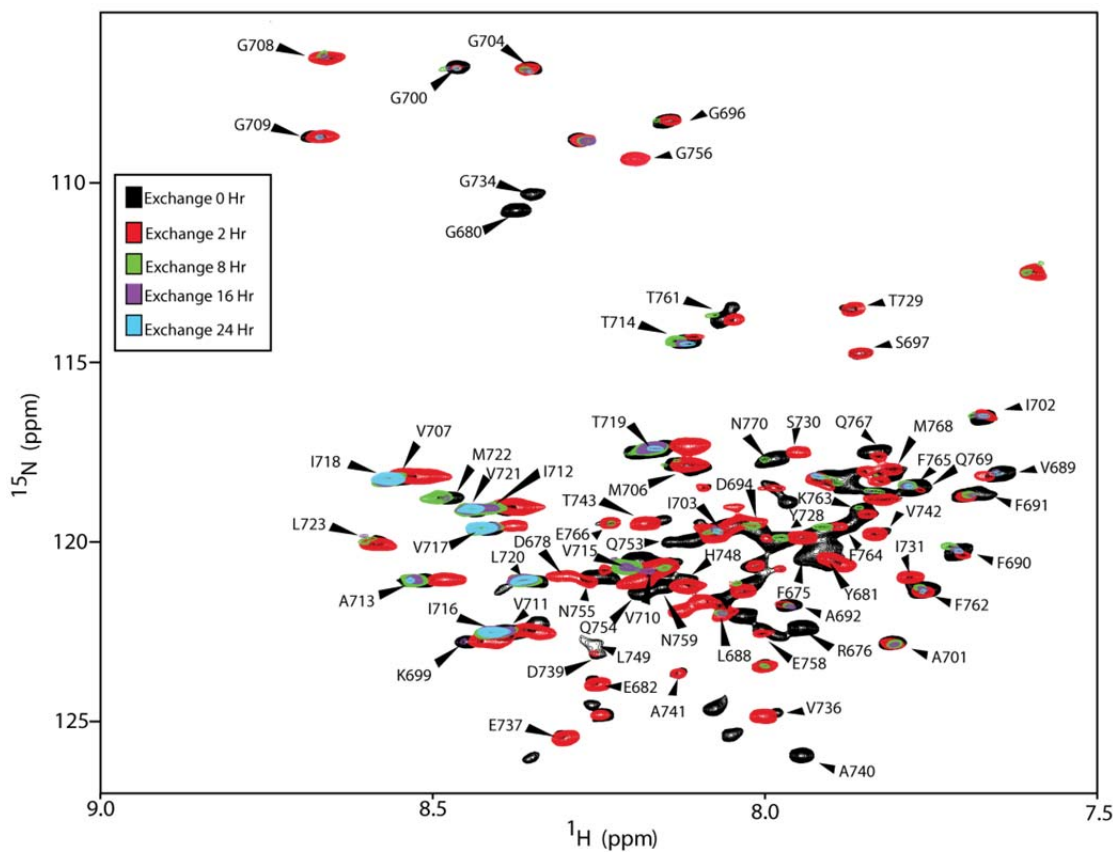
Figure 2.4. Use of NMR to monitor exchange of C99 backbone amide protons for deuterons as a function of time. This figure depicts the overlay of five 900 MHz ^{1}H, ^{15}N-TROSY NMR spectra of C99, collected at different points of time following dilution of C99 into D_2O. The black spectrum shows the reference spectrum collected in an H_2O solution. Red, green, purple, and cyan spectra reveal the state of changes after 2, 8, 16, and 24 hr, respectively. All NMR resonances that could be accurately assigned are labeled. It should be noted that because each spectrum required 6 hr of acquisition time, the actual time reflected by the data is a window spanning the designated time plus 6 hr, with the observed spectra being weighted toward the early part of the 6 hr window because of the way the 2-D NMR data are collected (most of the signal is detected in the early increments of the 2D experiment).

Reconstitution of Spin-Labeled C99 into POPC/POPG Vesicles for EPR Studies

Reconstitution of C99 into lipid vesicles was initiated by purifying the protein as described above, with the only difference being that the final elution buffer consisted of 0.2% SDS in lieu of 0.05% LMPG. Purified single-cysteine mutants forms of C99 were then conjugated to MTSL using the same spin-labeling protocol as described above for

67

PRE measurements. Spin-labeled C99 in SDS was concentrated using centrifugal ultrafiltration to a final concentration of 1mM. The concentrated C99 solution was then mixed with a stock SDS/lipid mixture of 400mM SDS/75mM POPC/25mM POPG (400mM SDS:100mM lipid), resulting in a clear solution. The final C99:lipid molar ratio was set to 1:400. The SDS/lipid solution was prepared by multiple cycles of freeze/thawing to ensure complete conversion to mixed micelles. The C99/SDS/lipid mixture was then subjected to extensive dialysis to remove all SDS present, during which process C99/POPC/POPG vesicles spontaneously formed. The 4L dialysis buffer (50mM imidazole and 2.25mM EDTA at pH 6.5) was changed three times daily. The completion of SDS removal was determined when the C99/lipid solution became cloudy and the surface tension of the dialysate indicated complete removal of detergent. The C99/lipid vesicles solution was then extruded using a 50 nm filter to generate unilamellar vesicles.

Continuous Wave (CW) EPR Measurements

X-band CW-EPR spectra were collected at 9.8 GHz on a Bruker EMX spectrometer with a TM110 cavity (Bruker Biospin, Billerica, MA) using 5 mW microwave power and 1 G field modulation at 100 kHz. Samples were prepared were prepared as described in the above sections. For each, 20 microliters were transferred to a 50 microliter glass capillary (Kimble Glass, Inc., Vineland, NJ). EPR data was collected at 298K.

Power Saturation EPR Measurement of Membrane Depth for Spin-Labeled Sites of C99

Spin labeled C99 was reconstituted into POPC/POPG liposomes as described above with a protein/lipid molar ratio of 1:400. The accessibilities of the spin label to

oxygen (lipophilic) and NiEDDA (hydrophilic) were determined using power saturation methodology. 5 microliters of each sample were taken up into a gas-permeable plastic capillary (TPX) and mounted into an ER4123D resonator (BrukerBiospin, Billerica, MA). To establish oxygen-free conditions (for both the control and for the samples containing 5 mM NiEDDA), samples were equilibrated with flow of nitrogen gas for 15 min prior to and during the measurement. For samples in which oxygen was allowed to be present to serve as a lipophilic probe the use of nitrogen gas was replaced by atmospheric air (20% oxygen). A 25 G scan of the central resonance line for each mutant was carried out using a 1 G modulation amplitude of 100 kHz frequency. A total of 24 scans were separately recorded at microwave powers ranging from 1 mW to 200 mW with increments of 1 dB attenuation. The central line height (A) was then plotted against the square root of the incident microwave power (P) and fitted into the following equation with I, $P_{1/2}$, and ε as adjustable parameters (214).

$$(3) \qquad A = I\left(P^{\frac{1}{2}}\right)\left[\frac{\left(1+(2^{\frac{1}{\varepsilon}}-1)*P\right)}{P_{1/2}}\right]^{-\varepsilon}$$

Membrane depth (Φ) was expressed numerically as a dimensionless value according to the following equation (214).

$$(4) \qquad \Phi = \ln\left[\frac{P_{\frac{1}{2}}(O_2)-P_{\frac{1}{2}}(N_2)}{P_{\frac{1}{2}}(NiEDDA)-P_{\frac{1}{2}}(N_2)}\right]$$

An example of the data from these power saturation EPR experiments is shown in figure 2.5.
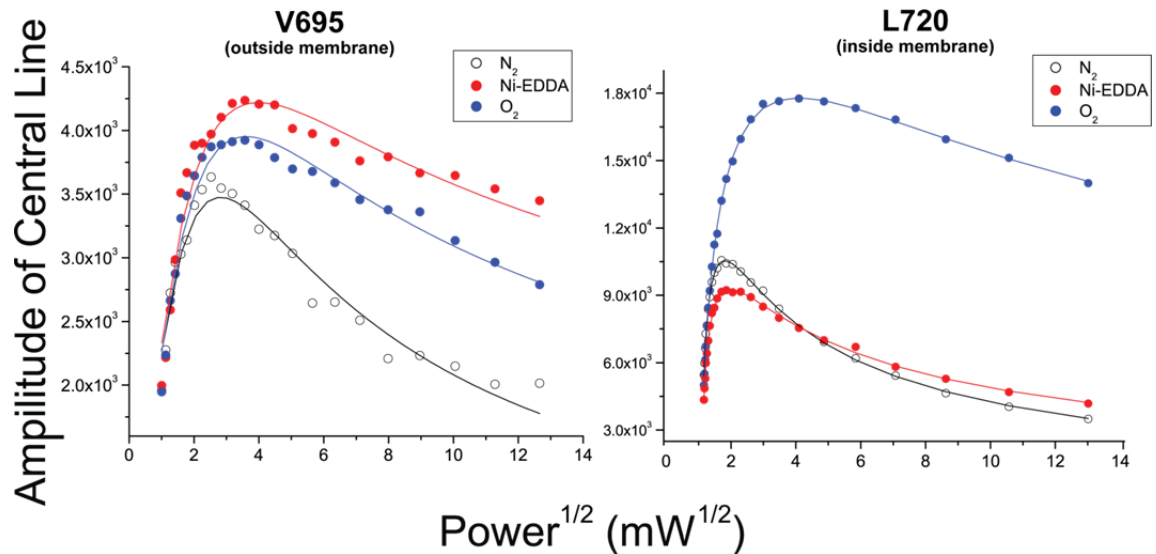
Figure 2.5. **Representative power saturation accessibility data for C99 in bilayered POPC/POPG vesicles. The panel on the left shows power saturation accessibility measurements for spin-labeled V695C C99 in POPC/POPG proteoliposomes, representing a spin labeled site (695) that is located in the N-Helix. The panel on the right shows power saturation accessibility measurements for spin-labeled L720 C99 in POPC/POPG vesicles, representing a site that is located inside the bilayer. Samples consisted of approximately 100µM C99, and were ~90% MTSL-labeled. C99 was reconstituted into POPC/POPG vesicles with a protein/lipid molar ratio of 1:400. The accessibilities of the spin label to oxygen and NiEDDA were determined using a power saturation methodology (see methods). Membrane accessibilities determined from this data for the many other sites probed are presented in figure 2.10A.**

Four-Pulse DEER Measurements and Data Analysis to Determine Distances Between Spin-Labels in C99

Double spin-labeled C99 was either reconstituted into LMPG micelles or into bilayered POPC/POPG vesicles as described above with a spin label concentration range of 200 to 300 µM (2X the C99 concentration). 30% (w/w) glycerol was added to the sample to serve as a cryoprotective agent. The sample was loaded into 2.4 mm inner diameter quartz capillaries (Wilmad LabGlass, Buena, NJ). After the resonator was cooled to 80K, the capillary was mounted into a plastic rod. The rod was then inserted into the resonator quickly to avoid a temperature increase.

Experiments were continued after waiting for the temperature to stabilize at 80K. Four-pulse DEER experiments were performed at X-band (9.5 GHz) on a Bruker EleXsys E580 spectrometer equipped with a Bruker split ring resonator (ER 4118X-MD5). A standard four-pulse sequence (*219*) was employed with a 32 ns π pulse and a 16 ns π/2 pulse. All measurements were performed at 80 K using an Oxford CF935 cryostat with an Oxford ITC4 temperature controller.

All DEER data were analyzed using in-house software that simultaneously fits the background signal as a function of both the effective spin concentration and the radius of the molecule while determining the specific interactions of interest using distance distribution defined as a sum of Gaussians. The advantage of this approach is that it takes into account the excluded volume of the molecule, typically giving a better fit to the data than those obtained using *a priori* background correction. DEER data and results are illustrated for the case of doubly (sites 700 and 723) spin-labeled C99 in LMPG micelles in figure 2.6.
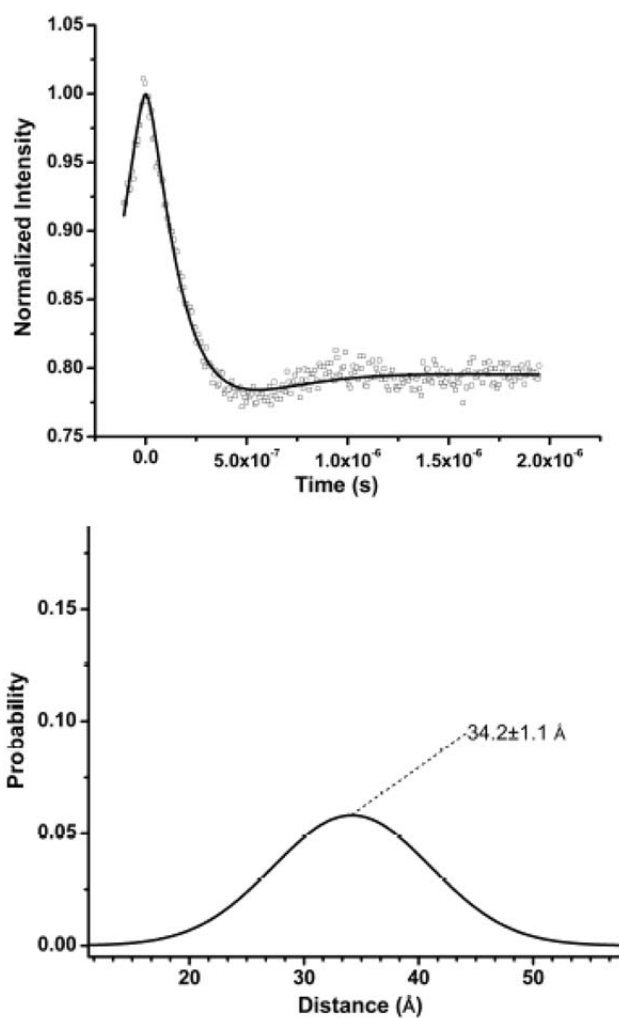
Figure 2.6. DEER data for C99 in LMPG micelles. C99 was MTSL spin-labeled at both residues G700C and L723C, the two ends of the transmembrane domain. The sample contained 200μM C99, 250μM imidazole, 10% (w/w) LMPG, 30% (w/w) glycerol at a pH of 6.5. The DEER experiment was conducted on a Bruker E-580 spectrometer equipped with an X-band MD5 resonator at 80K. The dipolar evaluation of the DEER signal after the baseline correction is presented in the top panel. The average distance and distribution are presented in the bottom panel.

Results

3D Structure Determination of C99

The backbone structure of C99 in lyso-myristoylphosphatidylglycerol (LMGP) detergent micelles was determined by nuclear magnetic resonance (NMR) restraints that included residual dipolar couplings (RDCs) and distances derived from paramagnetic

relaxation enhancement (PRE) experiments (Figure 2.7). To prevent dimerization (*14-16, 28*), we used an 800:1 LMPG:C99 ratio. C99 is composed of three helical domains. A short extracellular "N-helix" (residues 689-694) is connected by an interfacial "N-loop" (695-699) to the helical TMD (700-723). The N-helix is embedded in the membrane surface and dynamically samples a range of orientations around the TMD helix axis (Fig 2.7b). A third helix at the C-terminus (residues 762-770) is surface-associated but structurally uncoupled from the TMD by the intervening 38-residues "C-loop" (734-761).

The NMR structure reveals that the TM helix of C99 is highly curved, with the apex of curvature being located near glycine residues 708 and 709, close to the center of the micelle (Fig 2.7).
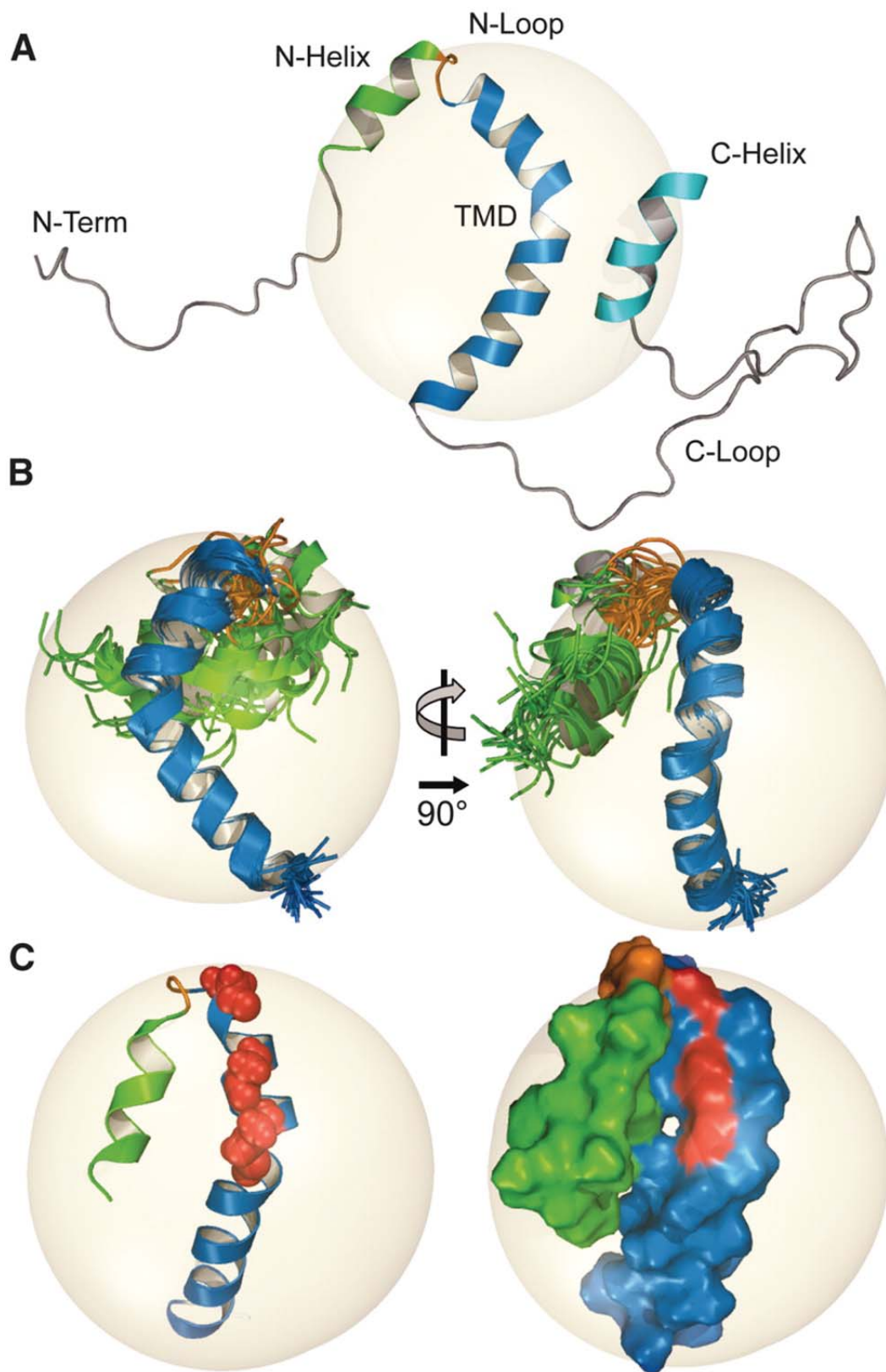
Figure 2.7. Structure of C99 in LMPG micelles. (A) Representative structure from a preliminary structural ensemble that illustrates the disorder of the N-terminus and C-loop and the interfacial location of the C-helix. The 35Å sphere inscribed on the structures of these figures represents an LMPG detergent micelle. (B) The 30 lowest energy structures in which the disordered N-terminus (residues 672-685) and cytosolic domain (726-770) are omitted. (C) Representative structure from (B) with atoms for glycine residues 700, 704, 708, and 709 highlighted (red) in van der Waals mode (left panel) and as a surface representation (right).

Pulsed EPR double electron-electron resonance (DEER) experiments confirmed that the TMD curvature in LMPG micelles had an average end to end distance of 34.2 ± 0.5Å. With the use of EPR, we found that mutations of G708/G709 to L708/L709 only modestly straightens the helix (average distance now 35.3 ± 0.5Å), suggesting that the curvature of the TMD derives only partially from the glycine pair (figure 2.10C). In addition to containing two glycine residues at the apex of curvature, the TMD also contains 14 β-branched amino acids (leucine, isoleucine, valine), over 50% of the total TMD amino acid composition (figure 2.8).
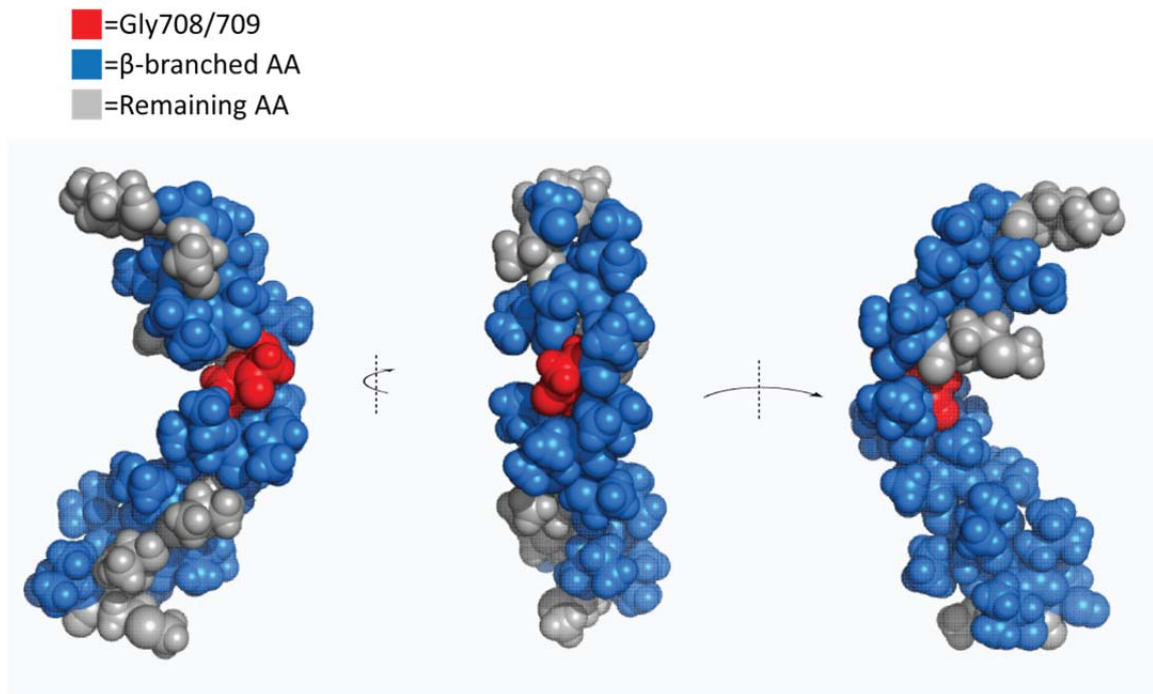
Figure 2.8. **Structure of C99 TMD highlighting β-branched amino acids. Three views of the TMD of C99 are shown with all amino acids represented as spheres. All β-branched amino acids are highlighted in blue, and glycines 708 and 709, which are responsible for the flexibility of the TMD are shown in red. All other amino acids are shown in grey.**

It is know that a high abundance of β-branched amino acids can distort the ideal packing of methyl groups, limiting the conformational space residues can adopt and resulting in distorted helical structures (*248*). We speculate that is the combination of two, dynamic glycine residues at the middle of the TMD and the abundance of β-branched amino acids that generate the curved TMD structure of C99. The ranges of distances sampled around the mean by the G708L and G708L/G709L mutations are dramatically reduced compared to those of the wild type (figure 2.10C). This suggests that G708 confers flexibility to the TMD.

Amide H/D Exchange Supports a Flexible TMD

Confirming the flexible nature of the TMD was a collaborative effort with the lab of Dieter Langosch, which utilized both NMR spectroscopy and molecular dynamics to monitor and model the dynamic nature of the TMD of C99/APP. The rationale of the study was to determine the backbone dynamics of the APP TMD helix by recording amide exchange kinetics, which is a powerful way to analyze the conformational equilibria along a protein sequence. The exchange kinetics of amides that are potentially involved in intramolecular H-bonding reports local and transient unfolding of secondary structure (*249-252*).

C99 was recombinantly expressed in uniformly ^{15}N-labeled form and purified into LMPG micelles. LMPG is a close analogue of natural phospholipids and is generally regarded as a mild detergent. C99 dimerizes with only very modest affinity in LMPG micelles(*28, 253*) and H-/D-exchange (HDX) studies were carried out using a high (1000:1) LMPG:C99 mol ratio which only the monomeric form of the protein was present (*26*). An aliquot of concentrated U-^{15}N-C99 stock solution was diluted into D_2O and ^{1}H,^{15}N-TROSY spectra were recorded at time intervals, allowing monitoring of the disappearance of the backbone amide ^{1}H,^{15}N cross peaks due to replacement of the amide protons with deuterons (figure 2.4). Because each TROSY spectrum required 6 hours of acquisition time, exact quantification of amide exchange rates from these data is not possible. However, comparison from the 2 hr and 16 hr time points provides a very clear assessment of the relative rates of amide exchange in C99 in LMPG micelles (figure 2.9).
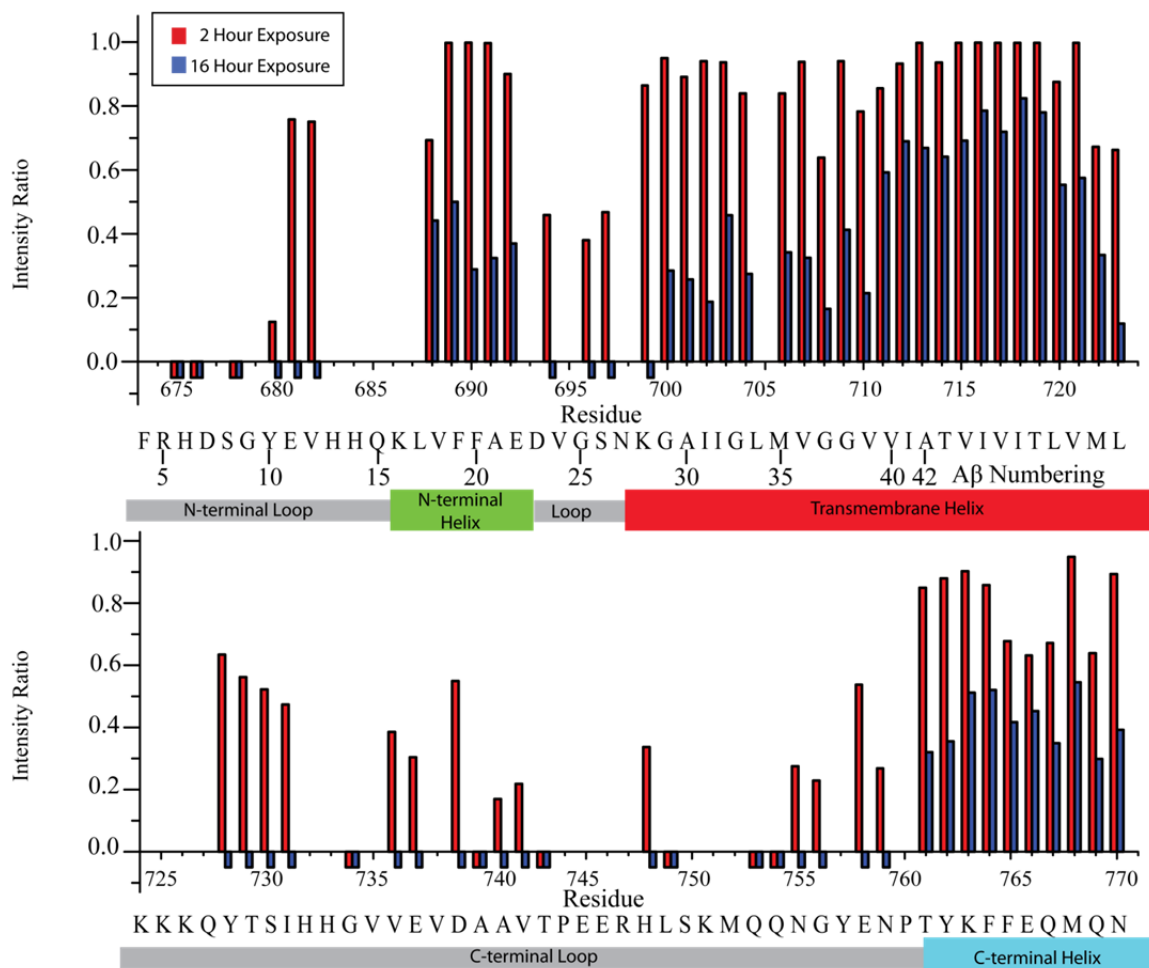
Figure 2.9. Time-dependent replacement of amide protons with deuterons upon dilution of C99 into D₂O solution. The intensity ratio is for the peak intensity observed after exchange with D$_2$O for 2 (red bars) or 16 (blue bars) hr relative to a nonexchanged "time=0" reference sample. Negative bars indicate that the peaks had disappeared completely, while the absence of either a positive or negative bar indicates that data was not measure for that site because of difficulties due to peak overlap or assignment. The known topology of C99 is shown below each graph, with helical regions indicated by large, colored rectangles and dynamic loops by gray, small rectangles. The numbering given in the upper line refers to full-length APP numbering while the lower line gives Aβ numbering. Data was collected for 0.2mM U-^{15}N C99 in 10% LMPG micelles at pH 6.5 and 45°C.

C99 contains three domains in which DHX rates are relatively rapid, reaching completion at 16 hr. These are (i) the N-terminus, (ii) the N-loop, and (iii) the C-loop. Within these segments are sites that are completely exchanged even at 2 hr, and other sites with significant retention of protons are seen at 2 hr. These results are consistent

with the previous NMR studies of micellar C99 and of the isolated intracellular domain in solution have suggested that these segments do not adopt stable secondary or tertiary structure, although some local transient structure is evident (*28, 254, 255*). Further, based on significant protection from exchange even after 16 hr at 318K, the exchange data are consistent with the presence of both a surface-associated α-helix just prior to the TMD (N-helix) and one formed by the residues of the C-terminus (C-helix) (*26*).

The exchange data for the TMD is complex. While exchange is at no position complete at 16 hr, the N-terminal portion of the TMD (G700-V711, N-TM) shows much lower protection (most evident for the 16 hr data of figure 2.9) than the I712 to I718 segment of the C-terminal portion of the TMD (C-TM) that includes the γ- and ζ-cleavage sites. Some evidence for "fraying" of the C-TM is evident in the transition from I718 (at which protection is high even after 16 hr) to the end of this domain at L723. These results indicate significantly greater helix backbone dynamics at, and/or greater access of water to, sites located in N-TM as compared to C-TM, except near the frayed C-terminus of the TMD.

Validation of C99 Structure in Lipid Vesicles

To validate the membrane topology and TMD curvature determined in the C99 structural studies, various EPR methods were utilized to examine these structural features in a lipid bilayer. Power saturation EPR measurements for spin labeled C99 (figure 2.10A and figure 2.5) confirmed that the span of the TMD is the same in both micelles and lipid vesicles and that the N- and C-helices are surface associated, indicating the membrane topology of C99 previously determined (*28*) and calculated during the structural studies were not artifacts of the micellar environment. Pulsed EPR DEER experiments confirmed that the TMD curvature also occurs in lipid bilayers (Figure 2.10C and figure 2.6). The measured end-to-end average distance in micelles

(34.2 ± 0.5Å) is consistent with the NMR structure and nearly identical to the distance

measured in lipid vesicles (33.5 ± 1.0Å)
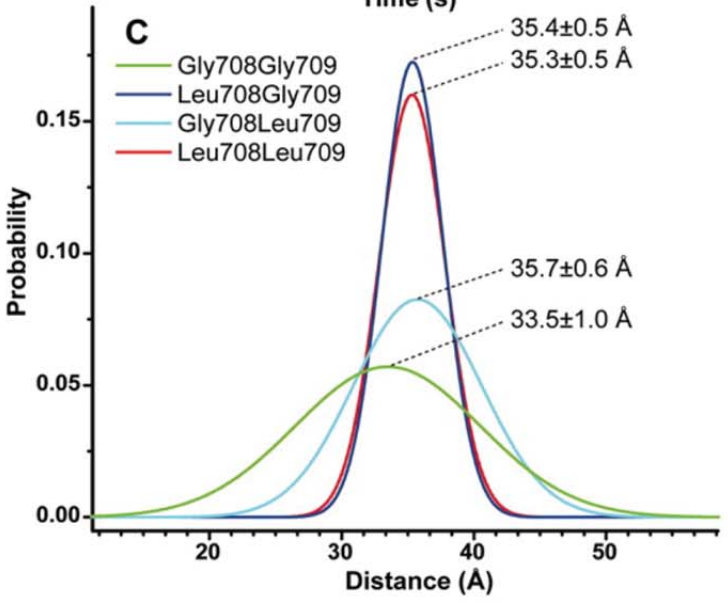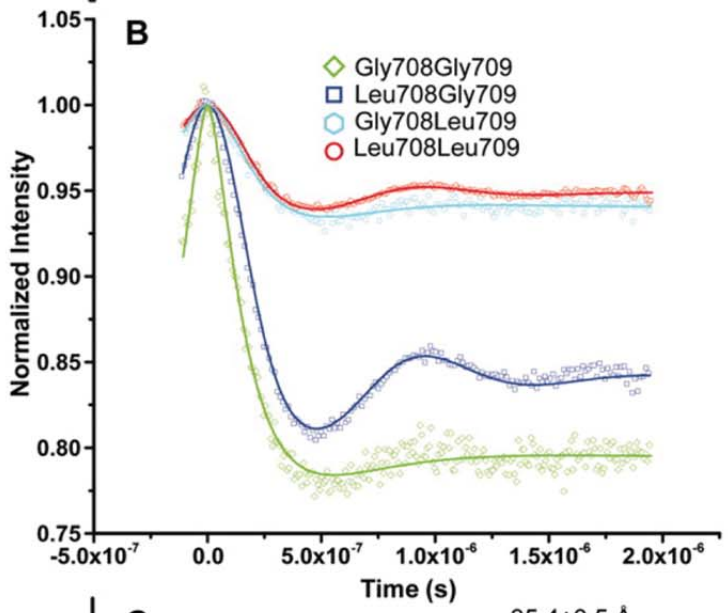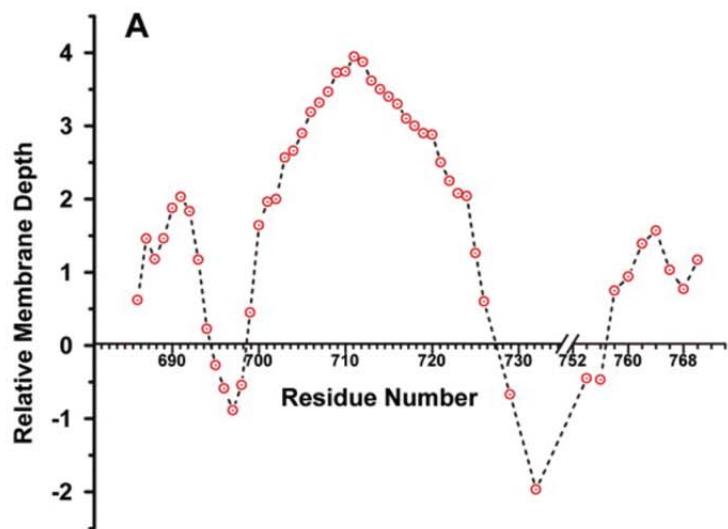
Figure 2.10. EPR studies of C99 in 1:4 1-palmitoyl-2-oleoly-phosphatidylglcerol:1-palmitoyl-2-oleoyl-phosphatidylcholine (POPG/POPC) lipid vesicles. (A) Bilayer depth parameters measured for spin-labeled sites on C99 as determined form power saturation EPR measurements. Positive values indicate burial in the membrane, whereas negative values indicate exposure to water. Through the samples used for NMR structure determination contained a C-terminal purification tag (see caption to figure 2.1), the samples used for measurements involving the C-terminal site (752-770) did not contain this tag, such that these measurements verify that the membrane association of the C-terminus is not the result of the presence of a non-native tag sequence. (B) X-band DEER time evolutions measured at 80K for C99 that was spin-labeled at the ends of its TMD (sites 700 and 723). Results are shown for C99 with its wild-type sequence, except for the two spin-labeled sites, and for C99 that was additionally subjected to Gly-to-Leu mutations at G708 and G709. (C) Distance distributions between the spin labels measured from the DEER data from (B). The SD associated with each average distance relates to the uncertainty of the average, not the population distribution around the average.

Discussion

The flexibly curved nature of the TMD may be well suited for its interactions with γ-Secretase. Medium-resolution electron microscopy structures of the full assembled and activated γ-Secretase (*256, 257*) suggest a sluice-like active site that might best accommodate a substrate with a curved TMD (figure 2.11).
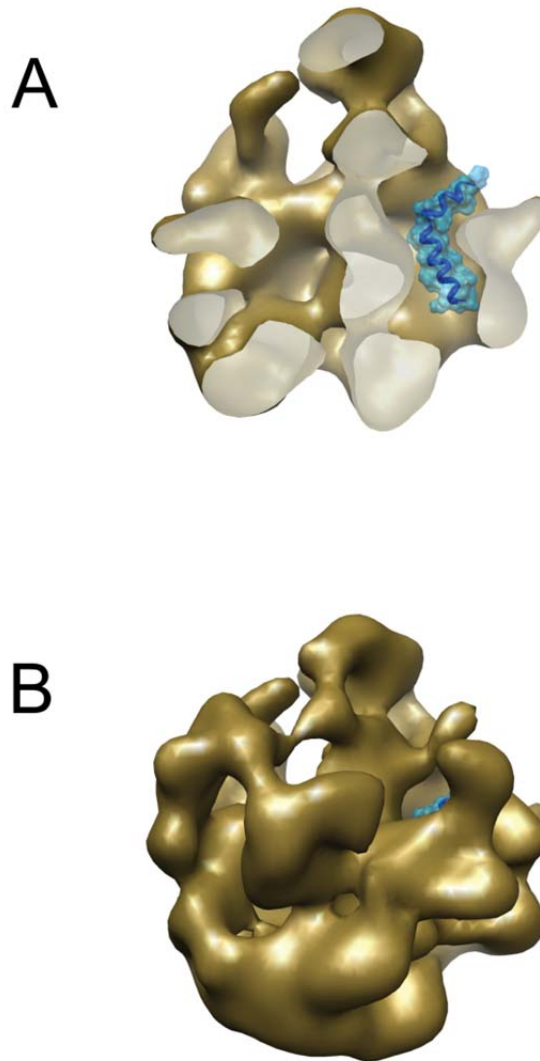
Figure 2.11. Transmembrane domain of C99 (blue) docked into the active site of γ-Secretase (from the 12Å cryo-EM structure of Osenkowski *et al* (*256*)). (A) Cutaway view showing C99 at the putative active site. (B) Same view as in (A) but γ-Secretase is shown in full surface mode.

Analogous active sites have been observed for other intramembrane proteases (*258, 259*). TMD flexibility may also promote the processive cleavage of C99 by γ-Secretase, with flexibility colluding with random thermal motion to allow the TMD to slide through the active-site channel. Curvature may also play a role in exposing scissile bonds for proteolytic access.

The surface associated N-helix and N-loop immediately following the cleavage site (K687) for non-amyloidogenic α-Secretase processing contain a number of familial AD mutation sites (*260*) and, in conjunction with the extracellular end of the TMD, appear to play crucial roles in determining the ratio of short versus the more toxic long forms of the Aβ peptides released by γ-Secretase (*14, 15*). A space-filling surface representation (figure 2.7C) suggests that these segments may also partially occlude approach by another TMD to the glycine zipper GxxxGxxxG (X, any amino acid) sequence located on the extracellular end of the TMD, which helps to explain the weakness of C99 self-association.

The organization of the N-loop and N-helix with respect to the membrane surface and the TMD is consistent with the possibility of a lipid binding site centered around the N-helix/N-loop/TMD structural element, as suggested by previous studies (*28, 243*). Titrations of C99 with cholesterol were carried out using bicelles as the model membranes and will be discussed in further detail in chapter IV.

In conclusion, determination of the structure of C99 provides insight into amyloidogenesis. The flexibly curved TMD of C99 offers insight into how it is recognized and proteolyzed by γ-Secretase. The structure of C99 can potentially assist in the design and optimization of C99-selective AD therapeutics that act by altering its interactions with γ-Secretase.

Deatherage for comments on this manuscript. Coordinates for the structure of C99 have

been deposited in the Protein Data Bank (accession code 2LP1).

CHAPTER III

NSAID-BASED γ –SECRETASE MODULATORS DO NOT BIND TO THE AMYLOID- β

POLYPEPTIDE[5]

Introduction

Alzheimer's disease (AD) is one of the most common neurodegenerative disorders, affecting more than 26 million people worldwide - a number that is expected to more than quadruple by the year 2050 (*262*). AD is characterized by cognitive decline induced by a loss of neurons and synapses in the cerebral cortex (*263*). This degeneration of neural activity is associated with the existence of extracellular amyloid plaques and intracellular neurofibrillary tangles, both of which characterize the pathology of the disease (*264*).   The neural plaques are comprised of insoluble deposits of amyloid-β (Aβ) peptides, which result from sequential proteolytic cleavage reactions of the amyloid precursor protein (APP) involving β- and γ-secretase. The APP substrate is first cleaved by β-secretase (BACE-1) to release its large ectodomain from a 99 residue transmembrane bound C-terminal fragment (C99, also referred to as APP-β-CTF). C99 then serves as a substrate for γ-secretase, cleavage by which results in release of the APP intracellular domain (AICD) and the amyloid-β polypeptide. The Aβ produced is not completely homogeneous, but varies in length from 37 to 49 amino acids, with Aβ42 and Aβ40 being the most prominent products. Aβ42 is believed to be the most neurotoxic of the amyloid-β polypeptides due to its particularly high propensity to form toxic

aggregates that go on to form the amyloid plaques that are the hallmark of AD pathology.

The well-defined pathology of AD, first described in the mid-1980s (*265-268*), set the stage for the proposal of the "amyloid hypothesis" by John Hardy (*269*), which postulates that accumulation of Aβ in the brain is the primary cause of AD pathology. The amyloid hypothesis is strongly supported by the observation that all mutations of APP or the Presenilin component of γ-secretase observed in early onset Alzheimer's disease (EOAD) or familial Alzheimer's disease (FAD) either result in an increase in total Aβ levels or in the production of Aβ42 relative to Aβ40 – thus supporting the relationship between the production of Aβ42 and the clinical symptoms of AD (*263, 269, 270*).

To date, there are only five FDA approved treatments for AD in the United States, all of which treat cognitive decline and symptoms of the disease (*263*). Therefore, the development of a disease-modifying agent—one that prevents or reverses the pathology of the disease—represents a significant unmet medical need. Two promising targets from a drug discovery perspective are β- and γ-secretase. The development of potential therapeutics targeting these two proteins has been extensively reviewed (*271-273*). Among the proposed strategies, development of agents that *modulate* γ-secretase has recently received much attention. A γ-secretase modulator (GSM) is defined as a molecule that changes the relative proportions of the Aβ isoforms produced by γ-secretase (particularly Aβ42 vs. the less toxic Aβ40), without altering the overall rate of APP processing (*263*). The first GSMs originated from non-steroidal anti-inflammatory drugs (NSAIDs), which were reported to reduce the occurrence of AD in patients using these drugs (*274-276*). The early NSAIDs, including sulindac sulfide, flurbiprofen, and ibuprofen, were shown to reduce the levels of the highly amyloidogenic Aβ42 (*274, 277, 278*). Recent photoaffinity-cross-linking experiments led to the proposal that GSMs bind directly to the transmembrane APP/C99 substrate (*279*) to form a

complex that somehow then modulates γ-secretase cleavage. The site of GSM binding within C99 was proposed to be located in its N-terminal Aβ42 domain. However, recent NMR studies from our labs failed to reveal any binding of the GSMs flurbiprofen and fenofibrate to monomeric or dimeric C99 in micellar model membranes, with the only detectable binding being to C99 aggregates, which was found to be of a non-specific and non-stoichiometric nature (*280*). More recently, Multhaup *et al*. have countered our findings based on SPR, NMR, and bacterial reporter assay results which they interpret as providing proof that the NSAID-based GSM sulindac sulfide binds avidly and specifically to both Aβ42 and C99 (*281, 282*).

We hypothesize that alternative interpretations are merited for some of the key results from Multhaup *et al* and also that some of their experiments may have had unrecognized artifacts. Concerns are as follows: The SPR dose/response curves for binding of sulindac sulfide to immobilized Aβ42 was seen in that work to be linear over the full range tested (5-100 micromolar, figures 2A and S2D in (*281*)), which is inconsistent with the interpretation of binding/dissociation kinetics data derived from the same set of experiments leading to determination of an apparent dissociation constant (K_d) of 30 μM. In addition, the authors note in the supplementary information that the apparent K_d varied with concentration and that the stoichiometry of the purported Aβ42:Sulindac Sulfide complex varied from 0.2:1 to 2:1. Rather than attributing this to self-association of the compound itself, the authors concluded that the compound bound to multiple binding sites on the Aβ42 peptide. It was also unclear whether the immobilized Aβ42 on their SPR sensor chips represented monomeric peptide or whether the process of coating the surface with Aβ42 might have locally over-concentrated this peptide, such that its sensor-associated structural state reflects an oligomeric or aggregated form. NMR spectra of 100 μM Aβ42 before and after addition of 300 μM sulindac sulfide were also presented and showed a profound drug-induced change in the

spectrum of the peptide (Figure 3 in (*281*)). However, a complete titration series was not carried out, which precludes the possible use of this data to support specific and stoichiometric complex formation between the GSM and Aβ42. Moreover, the NMR spectrum of Aβ42 in the presence of the drug could be interpreted as reflecting the formation of high molecular weight oligomers or aggregates since many peaks were seen to disappear. The possibility that the GSM might itself be aggregated at 300 μM was not considered, despite the facts that sulindac sulfide is a very hydrophobic compound and that the amyloid-β polypeptides are known to associate non-specifically with small molecule aggregates (*283, 284*).

Here, we provide additional data in an attempt both to clarify the previously published data as well as to provide new data informing on this controversy. Our results support our earlier contention (*280*) that monomeric GSMs either do not bind monomeric or dimeric forms of C99 or Aβ42 at all (in solution, in micelles, and in membranes), or bind in a weak and non-specific manner that is likely to be unrelated to their GSM activity. Moreover, these studies revealed that sulindac sulfide forms colloid-like assemblies at concentrations above 50μM, a phenomenon that may have been a source of experimental artifacts in some previous studies of GSMs.

Materials and Methods

Reagents, Peptides, and Proteins

Aβ40 and Aβ42 peptides in both isotopically unlabeled and uniformly-^{15}N labeled forms were obtained from rPeptide, LLC (Bogart, GA). For all experiments, peptides were first "monomerized" as previously described (*285, 286*) by dissolving lyophilized material in 98% formic acid and then immediately evaporating the solvent. This "monomerized" material was stored at -20°C and thawed immediately before use. The

compounds used in this study, sulindac sulfide, sulindac sulfone, and flurbiprofen, were obtained from Toronto Research Chemicals (North York, ON, CA), MP Biomedicals (Solon, OH), and Sigma-Aldrich (St. Louis, MO).

C99 was recombinantly expressed as described by Beel *et al* (*280*). The mammalian C99 vector was cloned into a pET-21a vector and then transformed into the BL21(DE3) *E. coli* strain. Protein overexpression was induced via the addition of isopropyl thiogalactoside to 1mM when cells reached an optical density of approximately 0.800. Cells were harvested and lysed, resulting in C99 localization to inclusion bodies. The inclusion bodies were solubilized using a 0.2% SDS/8M urea buffer. C99 was purified via IMAC, during which SDS and urea were removed and replaced with 0.05% LMPG, a lyso-phospholipid detergent. C99 was eluted from the IMAC column using a buffer containing 250mM imidazole and 0.05% LMPG at pH 7.8. For all experiments performed on C99 in LMPG micelles, the final buffer concentration was 100mM imidazole, 10% LMPG, and 2mM EDTA at pH 6.5.

Sample Preparation

All Aβ40 and Aβ42 samples were prepared by dissolving the "monomerized" polypeptide in 20mM NaOH at a concentration of 1mg/ml. The resulting solution was the diluted with sample buffer (50mM sodium phosphate, pH 7.0, 10% D_2O) to the desired concentrations, typically 100μM.

C99 reconstitution into lipid vesicles began with protein purification as described above, with the only difference being that the final elution buffer consisted of 0.2% SDS in lieu of 0.05% LMPG. Purified C99 in SDS was concentrated using centrifugal ultrafiltration to a final concentration of 1mM. The concentrated C99 solution was then mixed with a SDS/lipid mixture of 400mM SDS/75mM POPC/25mM POPG (400mM SDS:100mM lipid), resulting in a clear solution. The C99/SDS/lipid mixture was then

subjected to extensive dialysis to remove all SDS present and during which process C99/POPC/POPG vesicles spontaneously formed. The 4L dialysis buffer (50mM imidazole and 2.25mM EDTA at pH 6.5) was changed three times daily. The conclusion of dialysis was determined when the C99/lipid solution became cloudy and the surface tension of the dialysate indicated complete removal of detergent. The C99/lipid vesicles solution was then extruded using a 50nM filter to generate unilamellar vesicles, concentrated to a 1mM:100mM C99:lipid ratio, and flash frozen for later experiments. For the NMR studies (GSM titrations), the solution was diluted with buffer to achieve 100µM C99 plus 10mM lipid. For vesicle-only control samples, the same dialysis procedure was carried out in parallel, minus C99.

CD Spectroscopy

Far-UV CD spectra were obtained on an AppliedPhotophysics Chirascan spectropolarimeter at ambient temperature. The peptides were analyzed at a concentration of 0.5-1mg/ml, using a quartz cuvette with a pathlength of 0.02 cm (far UV CD, 180-250 nm); the spectra were corrected for contributions from the buffer. Each spectrum represents an average of 3 scans.

Dynamic Light Scattering

DLS experiments were conducted on a DynaPro Plate Reader WPR-06 (Wyatt Technology Corporation, Santa Barbara, CA) using a laser wavelength of 832.4nm. Briefly, 100uL volumes of solutions of Triton X-100, sulindac sulfide, sulindac sulfone, and flurbiprofen were prepared (from DMSO stocks) at concentrations of 5, 10, 25, 50, 100, 200, 300, 400, 600, 800, and 1000µM. All solutions were prepared so that the final DMSO concentration was constant at 2% in all samples. Triton X-100 was used as a positive control, and the intensity of the scattered light was measured as a function of

drug concentration (Fig 3.4). All experiments were performed in triplicate at 15°C. Ten acquisitions were performed (10s acquisition time) for each concentration point. Data were processed using the Dynamics 6.10.0.10 software (Wyatt Technology Corporation, Santa Barbara, CA). The average laser light scattering from three experiments were plotted versus concentration to obtain the critical micelle concentration (CMC) or "critical aggregate concentration", (CAC). The CMC of Triton X-100 was determined to be approximately 200-300μM, a value consistent with that in the literature (*287*).

NMR Spectroscopy

NMR experiments were performed on a Bruker Avance II 500MHz NMR spectrometer and a Bruker Avance III 800 MHz NMR spectrometer, both using TCI cryoprobes. ^{19}F NMR measurements were performed on the Avance II 500 MHz system using an SEF cryoprobe. All experiments using the amyloid peptides were performed at 5°C. Relaxation and diffusion measurements were used to verify the oligomeric state of the Aβ peptides used in this study. It is well know that Aβ40 has a lower propensity to form large oligomeric fibril species (*288*). Thus, this peptide was used to compare the behavior of the Aβ42 species in solution. For ^{15}N relaxation measurements, NMR experiments were performed at 500 MHz. T_1 and T_2 values were measured as described in Kay *et al* (*289*). T_1 and T_2 values for Aβ40 and Aβ42 were determined from measurements performed on the 500 MHz system using 100 μM solutions of Aβ40 and Aβ42. Peak intensities were measured by integration of the region between 7.5 – 8.8 ppm. T_1 measurements were made using delays of 2, 20, 50, 100, 200, 300, 400, 600, 800, 1000, and 1200 ms. T_2 measurements were made using delays of 0, 16, 32, 48, 64, 80, 96, 128, 160, 192, and 240 ms. The intensities were fit to a single exponential function ($I(t) = I_0 e^{-t/T}$) using the program GraphPad Prism (GraphPad Software, La Jolla, CA). T_1 and T_2 values for both Aβ40 and Aβ42 were estimated to be approximately

620ms and 150ms, respectively. The resulting correlation time (τ_c) for both molecules was then calculated using the following equation (*290*):

$$(5) \qquad t_c = \frac{\sqrt{\frac{6T_1}{T_2}-7}}{4\pi v_n}$$

where T_1 and T_2 are the respective relaxation times and v_n is the spectrometer frequency in Hertz. The resulting calculations yielded correlation times of 3.9 ns for both Aβ40 and Aβ42, which, at 5°C and taking into account the water viscosity at this temperature (approximately 1.5x that at ambient), corresponds to a protein of approximately 4.9 kDa – a value consistent with the rotational correlation time for a 4.2 kDa protein (as calculated from the Stokes-Einstein equation) (*291*).

To further classify the oligomeric state of the peptides in solution, pulsed field gradient diffusion measurements were performed at 500 MHz using a stimulated echo experiment (*292*). Using dioxane in the solution as a reference (as in (*293*)), solutions of Aβ40 and Aβ42 (both 100 μM) were measured with diffusion gradient strengths varying between 1% and 90% of maximum value. The lengths of the diffusion gradient and stimulated echo were optimized to give a total decay in the protein signal of ~80%. The spectra were acquired with 32K complex points and a spectral window of approximately 6500 Hz. Data was processed using Topspin 2.1 (Bruker Biospin, Billerica, MA). To obtain diffusion decay rates, the dioxane peak and the methyl region of the spectra (0.3-0.7ppm) were integrated at each data point and fit to equation (9) to determine the decay rate:

$$(6) \qquad s(g) = Ae^{-dg^2}$$

where the intensities of the protein signals *s* are plotted as a function of gradient strength, *g,* to enable determination of the decay rate, *d.* Decay rates were determined

to be 1.6 x 10^{-4} s^{-1} for both peptides. The hydrodynamic radii for Aβ40 and Aβ42 were then calculated as in Wilkins *et al* (*293*) to both be approximately 16Å, which as in Wilkins *et al*. correspond to a polypeptide chain of approximately 42 residues (*293*). Using this hydrodynamic radius and the viscosity of water at 5 degrees Celsius, the diffusion coefficient, D, was calculated using the Stokes-Einstein relationship:

(7) $D = \frac{K_B T}{6\pi\eta r}$

Where K_B is the Boltzmann constant, T is temperature (K), η is solvent viscosity in kg/m·s at 5°C, and r is the hydrodynamic radius in meters.

Titrations of ^{15}N-labeled Aβ40 and Aβ42 were performed on an 800 MHz NMR spectrometer at 5°C with 100 μM protein solutions. Titrations were performed with sulindac sulfide, sulindac sulfone, flurbiprofen, and DMSO (as a control) and were carried out in two modes. First, 50mM ligand stocks were prepared in DMSO-d$_6$. Sulindac sulfide and sulindac sulfone were added to 100μM protein solutions at concentrations of 5, 10, 50, 100, 300, and 500μM. Flurbiprofen was added at concentrations of 500μM and 1mM. Control DMSO-only titrations were performed for each series using the final titration point, which contained 2% DMSO by volume. In addition, titrations with sulindac sulfide, sulindac sulfone, and DMSO were performed as in Richter *et al* (*281*), where one titration data point was acquired using 100μM Aβ42 and either 300μM sulindac sulfide, 300μM sulindac sulfone, or DMSO-only control. In each case a fresh peptide sample was prepared, the appropriate amount of compound was added (from 50mM DMSO-d6 stock), and spectra were acquired immediately at 5°C. Time course spectra were acquired at t=0, 1hr, and 24hr. When it became evident that the sulindac sulfide was causing aggregation of Aβ42, a separate time course experiment was carried out using identical solutions at t=0, 15min, and 1hr. All two-dimensional ^{15}N-HSQC spectra were acquired using spectral widths of 12,820 Hz and

2432 Hz in the direct and indirect dimensions, respectively. Data were acquired using 1024 X 64 complex data points and 8 scans per increment. Two-dimensional experiments were also accompanied by 1D proton NMR spectra so that the concentrations of the compounds could be monitored throughout the titration.

NMR solubility measurements of sulindac sulfide, sulindac sulfone, and flurbiprofen were performed using a 500 MHz NMR spectrometer in experimental buffer (50mM sodium phosphate, pH 7.0, 10% D2O) with 2% DMSO-d_6. Briefly, 50mM stock solutions of each compound were prepared in DMSO-d_6. For each compound, a 1mM solution was prepared in buffer. Quickly, serial dilutions were made to a final concentration of 5 μM, while keeping the DMSO concentration constant at 2%. 1D proton spectra were measured for each concentration using identical parameters.

To test whether colloidal aggregates of sulindac sulfide can act as promiscuous enzyme inhibitors, β-secretase activity assays were performed in the presence and absence of sulindac sulfide and sulindac sulfone. An NMR-based enzymatic assay was designed using a ^{19}F-labeled BACE-1 substrate peptide—EVNLDAEF(CF_3)—where the trifluoromethyl group is at the meta position on the benzyl ring of Phe. BACE-1 cleaves this peptide between the L and D residues, which results in distinct ^{19}F NMR signals for the substrate and product. The assay was conducted in a 96 well plate format, where each well contained 220nM of CHO-expressed BACE-1 prepared in 20mM sodium acetate buffer, pH 5.0, to which were added sulindac sulfide and sulindac sulfone at various concentrations (3.15, 6.25, 12.5, 25, 50, 100, and 200μM) followed by a blank DMSO control and a positive control using an inhibitor with a known K_i value. The reaction was started by addition of 100μM substrate peptide prepared from a 100mM DMSO stock in buffer (20mM sodium acetate, pH 5.0). The experiment was allowed to react for a period of 20 minutes, at which time the reaction was quenched by the addition of 300uL of 8M urea. Samples were then transferred from the 96 well plate to NMR

tubes for analysis. ^{19}F NMR spectra showed the presence of both substrate and product, the peak integrals of which were used to calculate the concentration of each species and to assess the degree of inhibition (*294*). All experiments were conducted on a Bruker Avance III 500 MHz NMR spectrometer with an SEF cryoprobe for ^{19}F direct detection.

Surface Plasmon Resonance

SPR experiments were performed using a Biacore S51 instrument and a CM5 sensor chip (GE Healthcare). Monomerized A 42 peptide (1mg/ml diluted 1:10 with 10mM sodium acetate, pH 3.4) was immobilized to the sensor chip by standard amine coupling (with ~3000 response units (RU)). Compounds were diluted from DMSO stock solutions in three different running buffers (50mM sodium phosphate, 100mM NaCl, pH 7.0, 2% DMSO (0.2% Tween-20, 0.005% Tween-20, and no detergent). Injections were performed for 1min at a flow rate of 30uL/min. Data were analyzed using the Scrubber software (BioLogic Software, Campbell ACT, Australia) and were plotted using GraphPad Prism (GraphPad Software, La Jolla, CA).

Transmission Electron Microscopy

Samples were prepared for transmission electron microscopy (TEM) in an identical manner to the NMR samples. Briefly, "monomerized" peptide was dissolved in 20mM NaOH at a concentration of 1mg/ml. Solutions for TEM were prepared at 100μM. Subsequently, sulindac sulfide and sulindac sulfone were added to final concentrations of 300μM with a DMSO concentration of 2%. Lastly, a drug-free control sample was prepared containing 2% DMSO only. Formvar-coated copper grids were inverted over 50ul sample droplets for 15 minutes. The grids were then briefly rinsed with one drop of ultrapure water, and the excess water was removed by wicking to the side with blotter

paper. Samples were then inverted over drops of 2% aqueous uranyl acetate for 15 minutes and the grids were subsequently washed over three drops of ultrapure water. Following air drying, the grids were examined on a Philips CM120 transmission electron microscope (FEI, Inc., Hillsboro, OR) operated at 80kev. Representative images were captured using a Gatan Model 830 SC200 CCD camera (Gatan, Inc., Pleasanton, CA).

Results

Selection of NSAIDs for Study

The finding that certain NSAIDs decreased the production of Aβ42 produced by γ-secretase cleavage led to the observation these compounds had various effects on the cleavage of APP. For example, compounds such as ibuprofen, fenofibrate, sulindac sulfide, R-flurbiprofen, and indomethacin were shown to decrease the amount of Aβ42 produced. Thus, they were considered Aβ42-lowering NSAIDs (see reviews in (*283, 295*)). Other compounds, such as celecoxib functioned to increase the amount of Aβ42 and were thus termed Aβ42-increasing NSAIDs. Lastly, several NSAIDs, such as naproxen and sulindac sulfone, were found to have no effect on the production of Aβ42. The sulindacs were chosen because these were the primary focus of the recently published studies (*281, 282*) that closely concern this paper. Sulindac sulfide acts as a GSM while sulindac sulfone has previously been shown to have no GSM-like effect on the production of Aβ42 and serves as a negative control. The well-characterized GSM R-flurbiprofen was also chosen for a limited number of experiments. It has a much higher aqueous solubility (up to ca. 1 mM) than sulindac sulfide and therefore can be tested as a representative GSM for experiments that were hindered by the relatively low solubility of sulindac sulfide.

Verification of the Oligomeric State of Amyloid Peptides

Because the supposed binding of GSMs to Aβ42 has been invoked to support the idea that binding of GSMs to C99 is central to how these compound modulate amyloid production , we sought to reproduce results that were previously interpreted (*281*) to indicate that GSMs bind specifically and avidly to monomeric Aβ42. Amyloid peptides, especially Aβ42, are known for their propensity to aggregate and form large molecular weight fibrils. For this reason, we first set out to verify the presence of stable, monomeric polypeptide in our samples. The Aβ40 and Aβ42 peptides were first "monomerized" as previously described (*285, 286*) before studies. CD spectra of Aβ42 were obtained to verify that limited or no β-sheet structure existed in resulting solutions (the presence of which would indicate the formation of fibril-like species). Both peptides exhibited predominantly random coil conformations (figure 3.1).
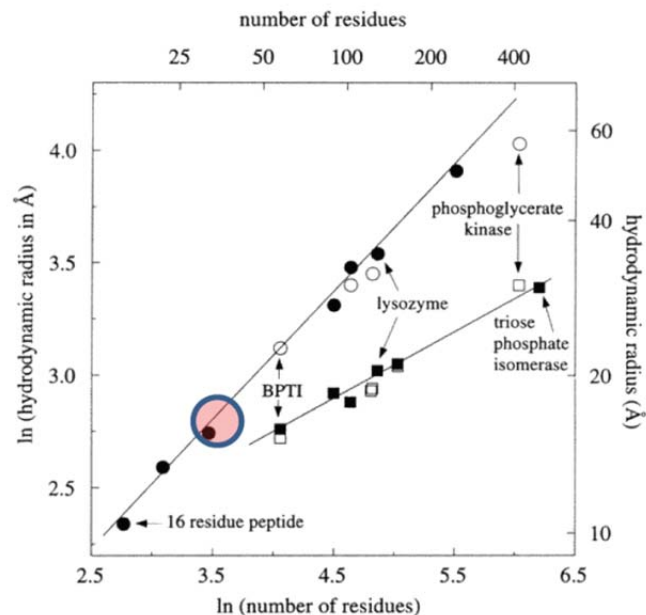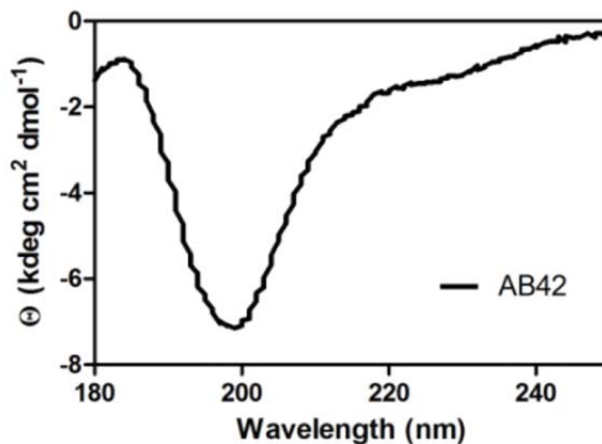
Figure 3.1. Top panel is a figure from Wilkins *et al*, "Hydrodynamic radii of native and denatured proteins measured by pulse field gradient NMR techniques", Biochemistry 38, 16424-16431, which were used in this work to conclude that the hydrodynamic radius of Aβ40 and Aβ42 is ~16Å. The bottom panel is the CD spectrum of 100µM Aβ42 in 50mM sodium phosphate, pH 7.0, 25°C, which indicates that the peptide has a predominantly random coil conformation and a very small degree of β-sheet structure.

The oligomeric states of both the Aβ40 and Aβ42 peptides were then assessed

via NMR diffusion measurements. As indicated in figure 3.2, the diffusion decay rates of

both Aβ40 and Aβ42 were seen to be identical, and correspond to a hydrodynamic

radius of approximately 16Å, matching that expected for a ~40 residue peptide (figure 3.1) (*293*). This allowed calculation of the absolute diffusion coefficient, *D*, of both peptides (figure 3.2B), which correspond to that of a small protein in an aqueous solution. In addition, we carried out ^{15}N NMR relaxation measurements for both Aβ40 and Aβ42. From these values, a rotational correlation time of 3.9 ns was determined at 5°C (*291*). This value corresponds to a protein with molecular weight of ~4.9kDa, and demonstrates that the peptides populated only the monomeric form as prepared (figure 3.3).
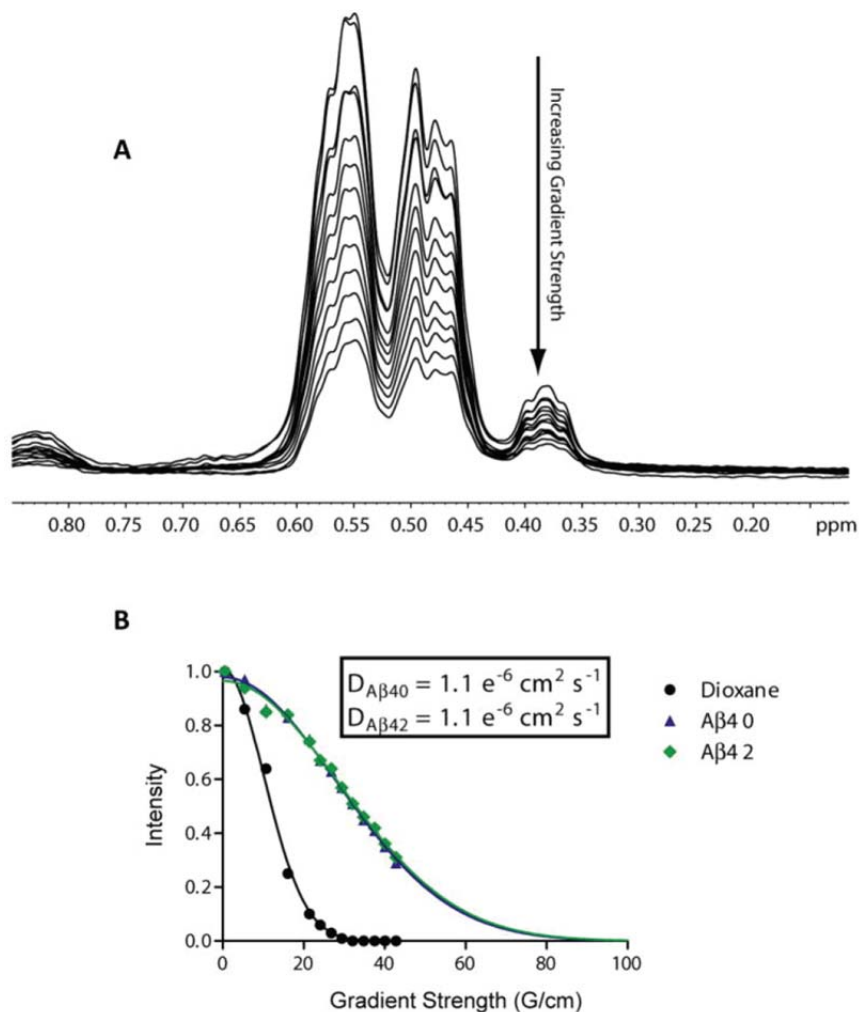
Figure 3.2. (A) ^{1}H NMR-based translation diffusion data for Aβ42 at Z-gradient strengths varying from 0.5 to 42.3 G/cm. The methyl region of the spectrum between 0.7 and 0.3 PPM was integrated for each point to yield relative intensitites that were plotted against gradient strength in (B). The intensities in (A) were measured using dioxane as an internal reference and were fit to a single exponential to determine the hydrodynamic radius and diffusion coefficient, *D*, as presented in the inset. Data for the dioxane standard are represented by black circles, Aβ40 by blue triangles, and Aβ42 by green diamonds. Curve fits are represented by solid lines of corresponding colors.
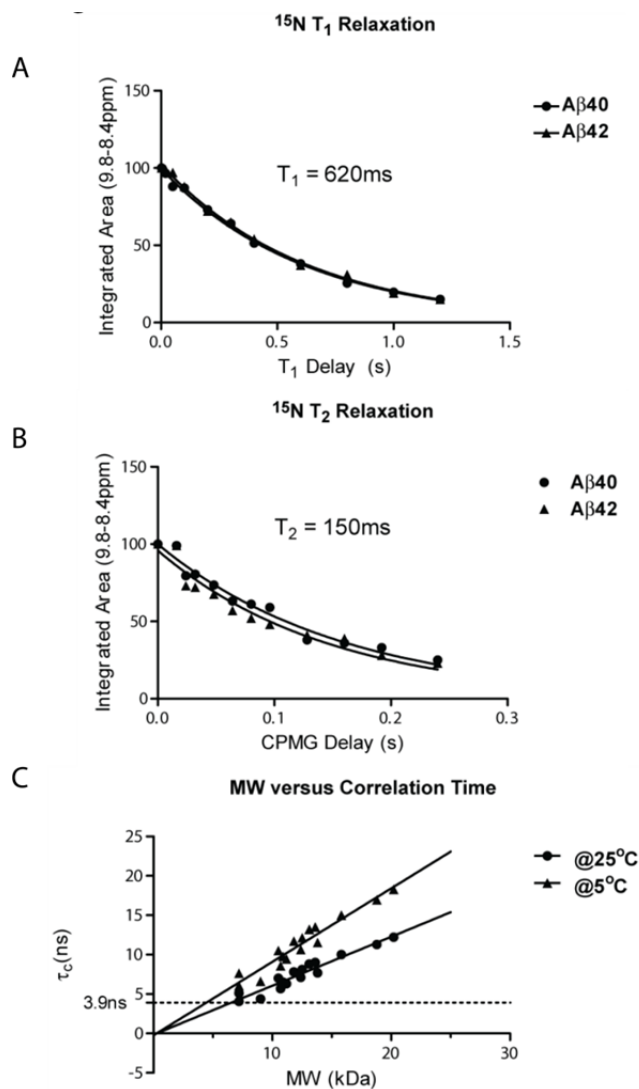
Figure 3.3. Aβ42 exists as a monomer under the experimental conditions of this work. ^{15}N T$_1$ (A) and T$_2$ (B) relaxation time determinators for Aβ40 and Aβ42. Values were extracted by plotting the decay of integrated ^{1}H^N intensity between 8.4-9.8 ppm and fitting a single exponential equation to the data using GraphPad Prism. These values were used to determine a rotational correlation time for both peptides of 3.9ns, which corresponds to a peptide of molecular weight of ~4.9 kDa. **(C)** Plot of MW versus correlation time, demonstrating that the Aβ40 and Aβ42 species correspond to monomers with molecular weights of ca. 4.9 kDa at 5°C (plot adapted from Rossi *et al.*, "A microscale protein NMR sample screening pipeline" *J. Biomol. NMR* 2010, 46, 11-22, and adapted to account for the difference in viscosity of water at 5°C)

Characterization of GSMs

Sulindac sulfide, sulindac sulfone, and flurbiprofen were characterized by

dynamic light scattering (DLS) and NMR to determine their solubility and to assess their

oligomeric states at the concentrations tested in this and previous work. Using DLS, sulindac sulfide was found to be monomeric below ca. 50 µM. However, between 50 and 100 µM, colloidal aggregates of sulindac sulfide clearly form, indicative of a "critical aggregate concentration" for this compound in the 50-100 µM range (*296*). At much higher concentrations (starting at 400 micromolar) sulindac sulfide begins to precipitate, which is the cause of the linear increase in laser light scattering above this concentration (Figure 3.4). Sulindac sulfone and flurbiprofen were found to be monomeric up to concentrations of 1mM, as the scattering intensity over the entire range of concentrations of these compounds was found to be the same as buffer alone.
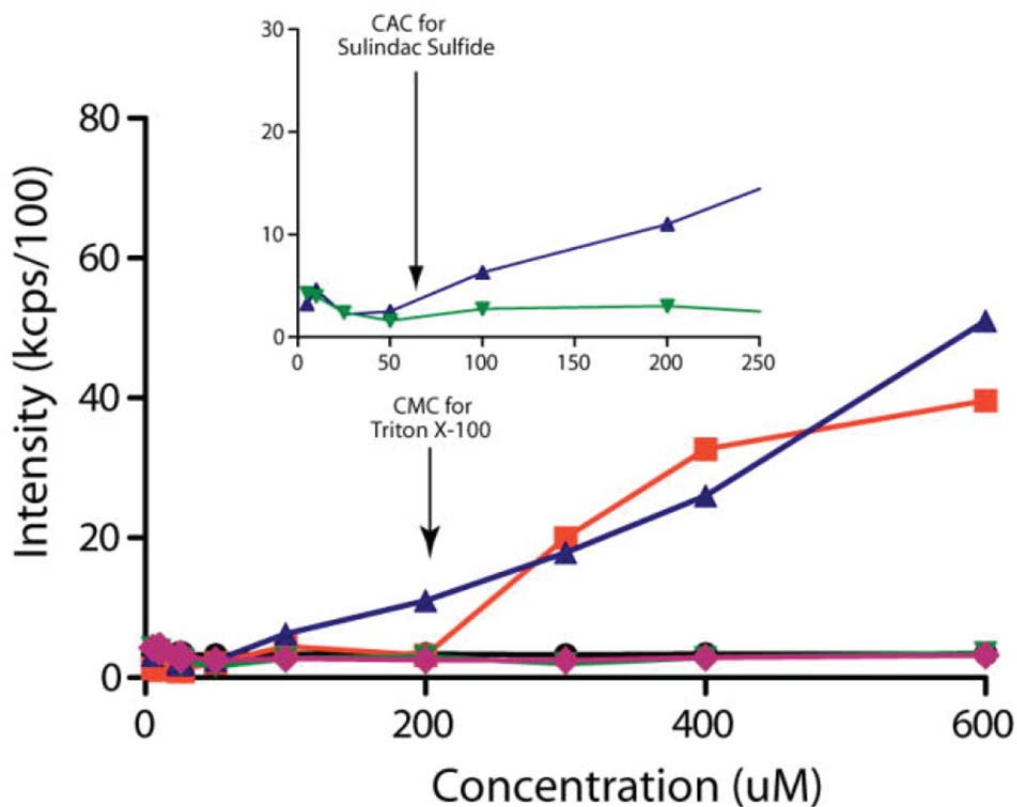
Figure 3.4. Measurement of the critical aggregation concentration (CAC) by dynamic light scattering (DLS). Scattering intensities were plotted versus concentration, and the CAC was determined as the point when the scattering intensities began to increase. The legend is as follows: buffer only (black circles), Triton X-100 (orange squares), sulindac sulfide (purple triangles), sulindac sulfone (green triangles), and flurbiprofen (green diamonds). Notice that no increase in scattering intensity was observed for buffer, sulindac sulfone, or flurbiprofen. However, a significant increase in scattering intensity was observed for a positive control (Triton X-100) upon micelle formation at 200-300µM and for sulindac sulfide starting above 50µM, indicating that the latter begins to form aggregates at concentrations above 50µM, which is consistent with NMR data (Figures 3.5, 3.8, and 3.9).

As an orthogonal method for measuring compound solubility, ^{19}F NMR experiments were performed at concentrations ranging from 5µM to 1mM in aqueous buffer and with a fixed concentration of 2% DMSO. From the NMR spectra in figure 3.5 it is clear that sulindac sulfide begins to form colloidal aggregates at some point between 30 and 62µM as evidenced by the significant broadening and decreasing intensity of the

NMR signals at and above 62 µM, demarking the "CAC" of this compound.
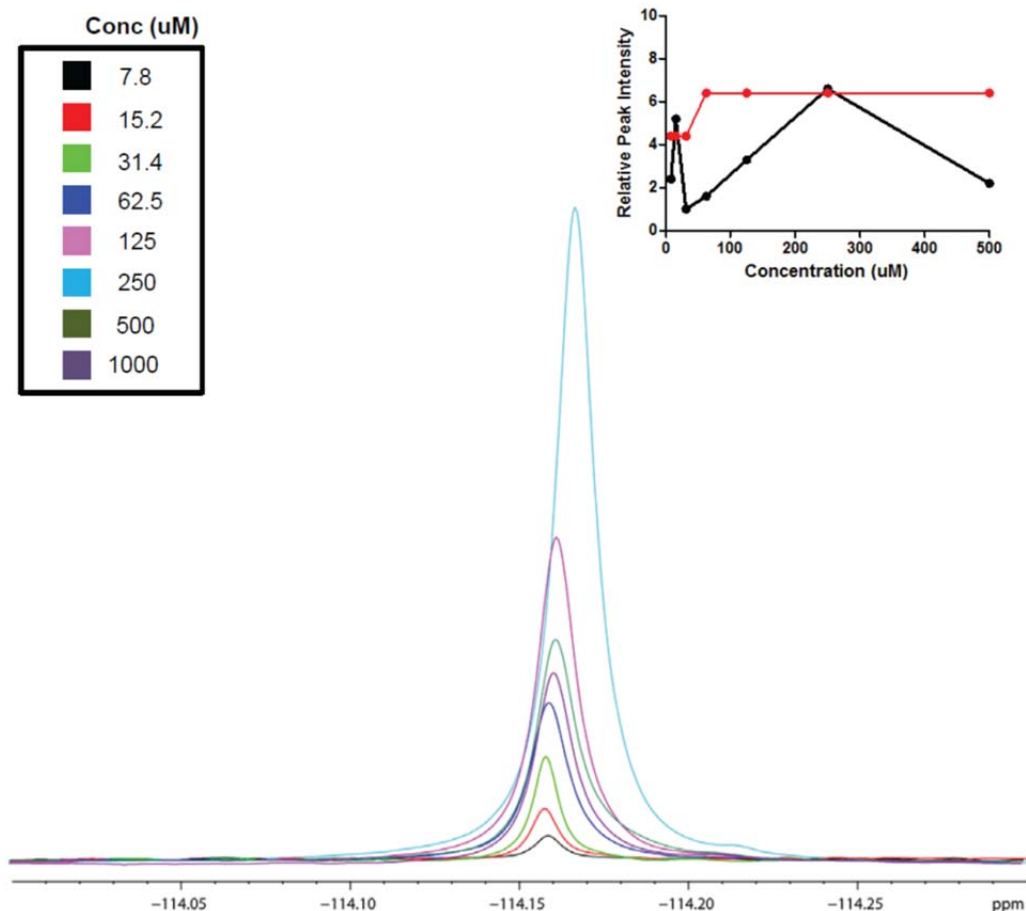
Figure 3.5. **^{19}F NMR spectra of sulindac sulfide at concentrations of 7.8, 15.2, 31.3, 62.5, 125, 250, 500, and 1000µM. Linewidths (in red) at half height ($\Delta v_{1/2}$, in Hz) and intensities (in black) of peaks in inset were plotted versus concentrations as shown in the upper right inset. At the 62.5µM point, the peak intensities and linewidths change significantly, indicating aggregation of the compound. The large decrease in relative intensity above 250µM is due to precipitation of the compound.**

On the other hand, both sulindac sulfone and flurbiprofen exhibit no significant changes in their NMR spectra (figure 3.6) and appear to remain monodisperse up to concentrations of 1mM. These NMR data confirm and complement the results of DLS and show that sulindac sulfide forms colloidal (water soluble) aggregates with a critical aggregation concentration in the range of 50-60 µM, whereas sulindac sulfone and flurbiprofen remain monomeric up through 500 µM.
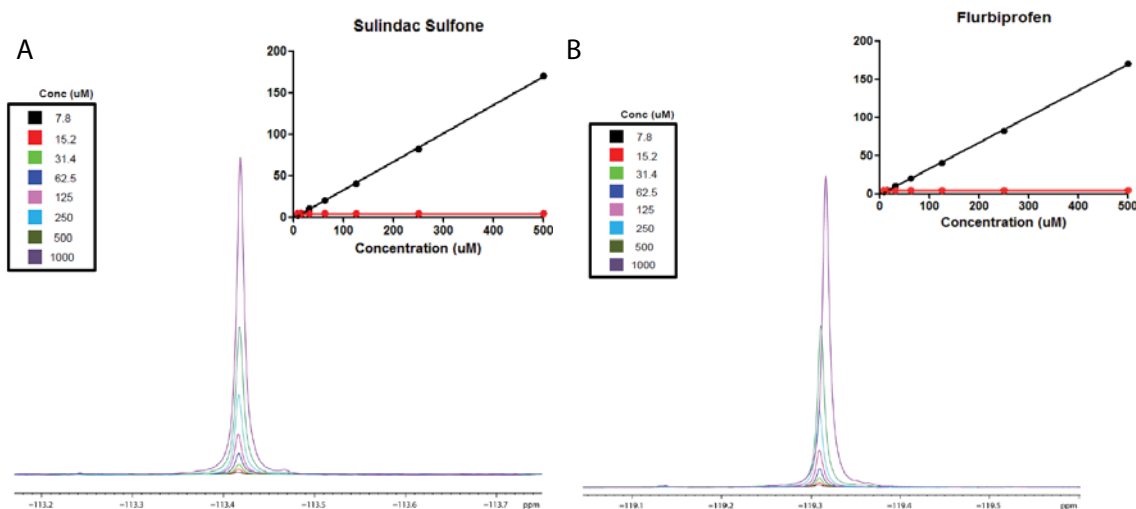
Figure 3.6. ^{19}F NMR spectra of sulindac sulfone (A) or flurbiprofen (B) at concentrations of 7.8, 15.2, 31.3, 62.5, 125, 250, 500, and 1000μM. Linewidths (in red) at half height ($\Delta v_{1/2}$, in Hz) and intensities (in black) of peaks were plotted versus concentration (upper right inserts). The peak intensities scaled linearly with concentration and the linewidths are identical through the full range (1mM not shown), demonstrating that the compounds remained soluble and do not aggregate and/or form colloids in solution. ^{19}F NMR is extremely sensitive to DMSO concentration, and the small changes in chemical shift are due to small variances in the DMSO concentration due to pipetting errors.

NMR Titrations of Aβ42 with GSMs

To determine if NMR spectroscopy demonstrates binding of sulindac sulfide to monomeric Aβ42, as claimed in previous work (*281*) NMR titration experiments were performed with each compound (using 50mM stock solutions of the drugs in DMSO-d$_6$). Control titrations were also performed using DMSO only, which was used to dissolve the GSMs in stock solutions. Figures 3.7-3.9 show ^{15}N-HSQC spectra of Aβ42 titrated with sulindac sulfide and flurbiprofen (both are NSAIDS and GSMs), sulindac sulfone (a NSAID but not a GSM), and DMSO control. It is clear that the titrations for all three NSAIDs led to only very small spectral changes in the HSQC spectrum of Aβ42 (Figures 28A-30A) and that these changes are virtually identical to those observed during the DMSO control titration (Figure 3.10A). This data provides no evidence for binding of any of the three compounds to monomeric Aβ42. However, in the case of sulindac sulfide,

1-D proton NMR spectra showing both the GSM peaks and the aromatic resonances from the peptides (Fig. 3.7B) reveal that the peaks from monomeric Aβ42 begin to lose intensity at sulindac sulfide concentrations above 50 micromolar—concentrations at which we have shown this GSM to form colloidal aggregates.   This is confirmed by examining the 1-D ^{1}H NMR projections of the 2-D TROSY data (Figure 3.7C).   Such changes were not observed for the flurbiprofen, sulindac sulfone, or for the DMSO control (Figures 3.8B-C, 3.9B-C, and 3.10B-C).   These data strongly suggest that colloid formation by sulindac sulfide triggers aggregation of Aβ42.
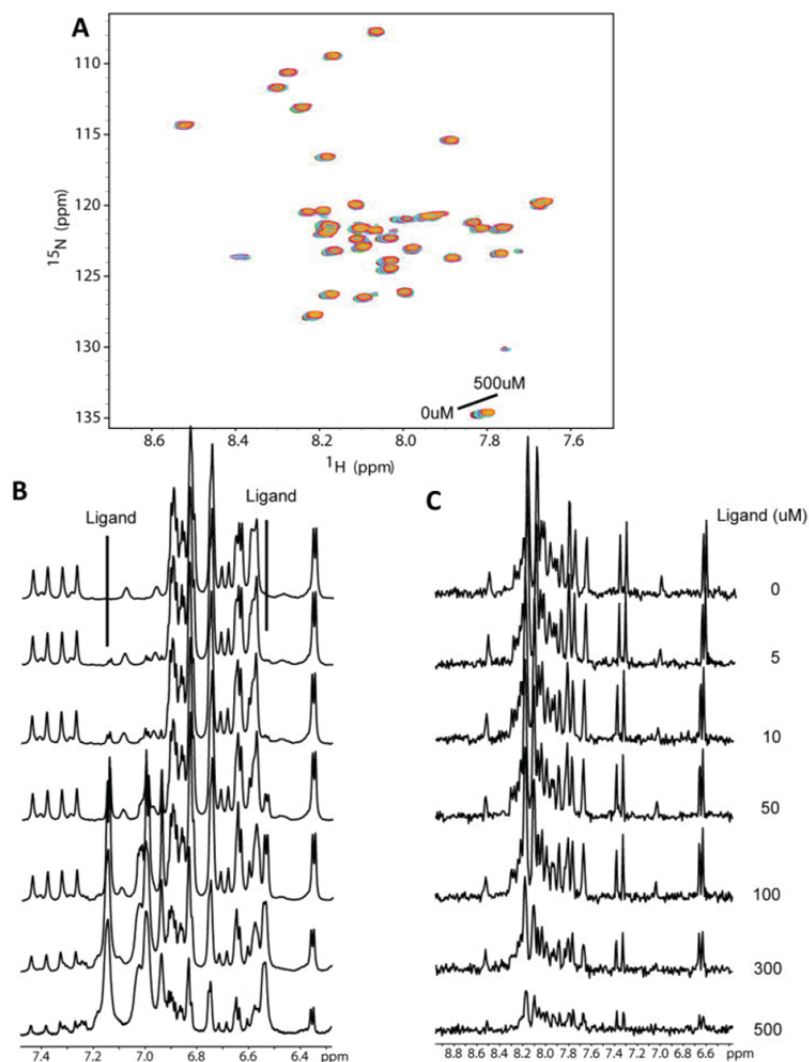
Figure 3.7. Titration of U-^{15}N-Aβ42 with sulindac sulfide. (A) ^{15}N-HSQC spectra of Aβ42 upon titration with sulindac sulfide (from a 50mM stock solution in DMSO) at concentration ranging from 0 to 0.5mM. There are no shifts in peaks of these spectra beyond what is observed for the DMSO-only control titration (see figure 3.10). However, peak intensities decrease at higher sulindac sulfide concentrations. (B) ^{1}H NMR spectra taken at each titration point to allow observation of the ligand peaks throughout the titration. Notice that ligand peaks are observable even at the lowest concentration (5μM) and with a nearly 20-fold excess of protein but begin to broaden or disappear above 50-100μM, indicating aggregation of the compound. (C) 1-D ^{1}H NMR projections of the HSQC spectra shown in (A) illustrate the decrease in amide ^{1}H signal intensity from the peptide, which demonstrates that Aβ42 begins to aggregate upon addition of sulindac sulfide at concentrations above 50μM.
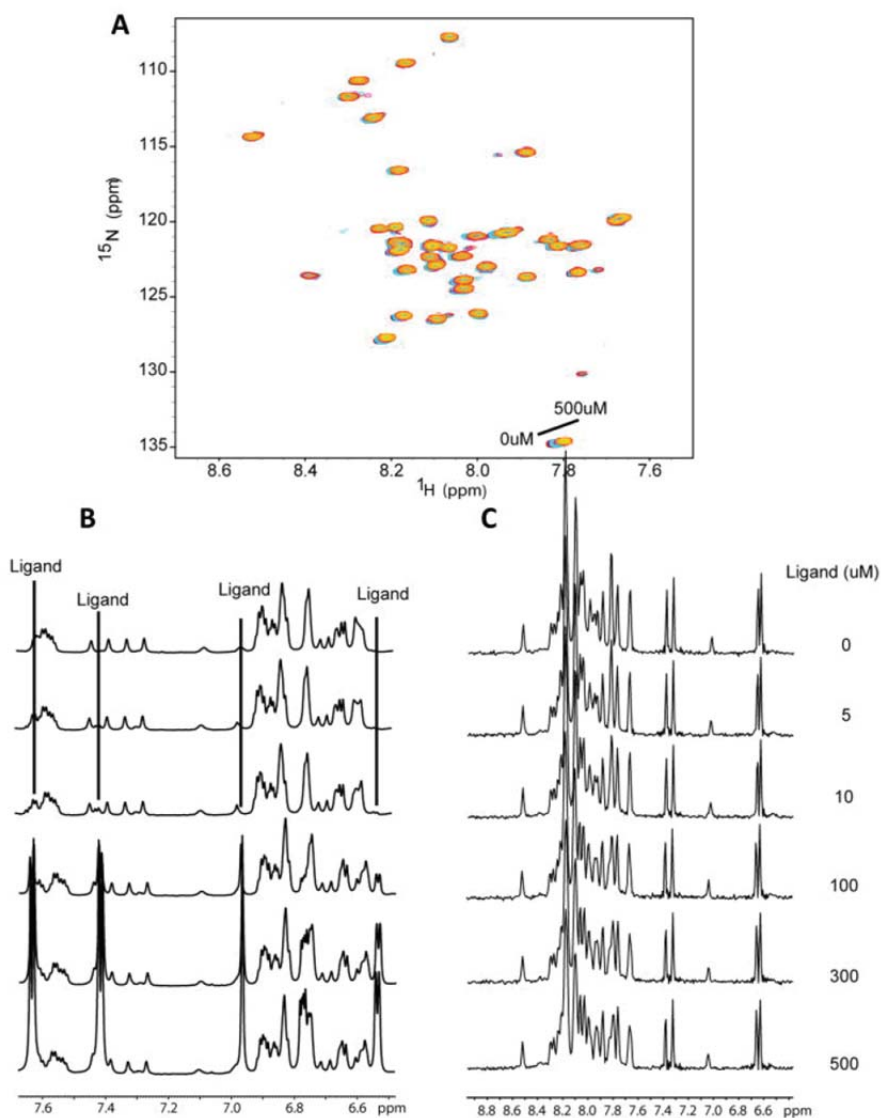
Figure 3.8. Titration of U-^{15}N-Aβ42 with sulindac sulfone. (A) ^{15}N-HSQC spectra of Aβ42 upon titration of sulindac sulfone at concentrations ranging from 0 to 0.5mM. there are no shifts in the peaks of these spectra beyond what is observed for the DMSO-only control titration (figure 3.10) and peak intensities do not vary. **(B)** ^{1}H NMR spectra taken at each titration point to allow observation of ligand peaks throughout the titration. It can be seen that the sulindac sulfone peaks remain sharp throughout, reflecting the fact that this compound does not aggregate at concentrations below 0.5mM. **(C)** 1-D ^{1}H NMR projections of the HSQC shown in (A) demonstrate that the solubility of Aβ42 remains unchanged at all points.
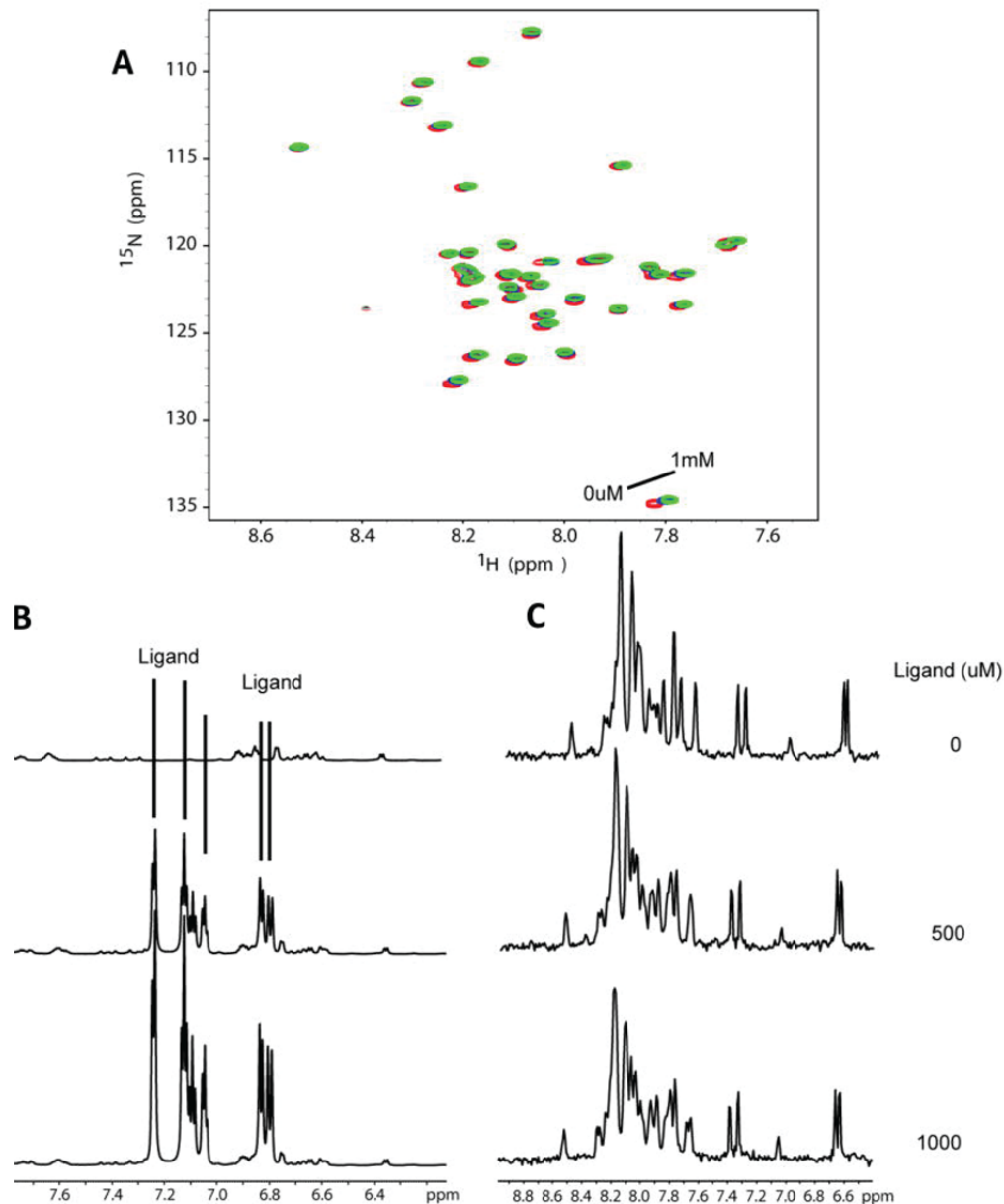
Figure 2.9. Titration of U-^{15}N-Aβ42 with flurbiprofen. (A) ^{15}N-HSQC spectra of Aβ42 upon titration of flurbiprofen at concentrations ranging from 0 to 0.5mM. there are no shifts in the peaks of these spectra beyond what is observed for the DMSO-only control titration (figure 3.10) and peak intensities do not vary. (B) ^{1}H NMR spectra taken at each titration point to allow observation of ligand peaks throughout the titration. It can be seen that the flurbiprofen peaks remain sharp throughout, reflecting the fact that this compound does not aggregate at concentrations below 1mM. (C) 1-D ^{1}H NMR projections of the HSQC shown in (A) demonstrate that the solubility of Aβ42 remains unchanged at all points.
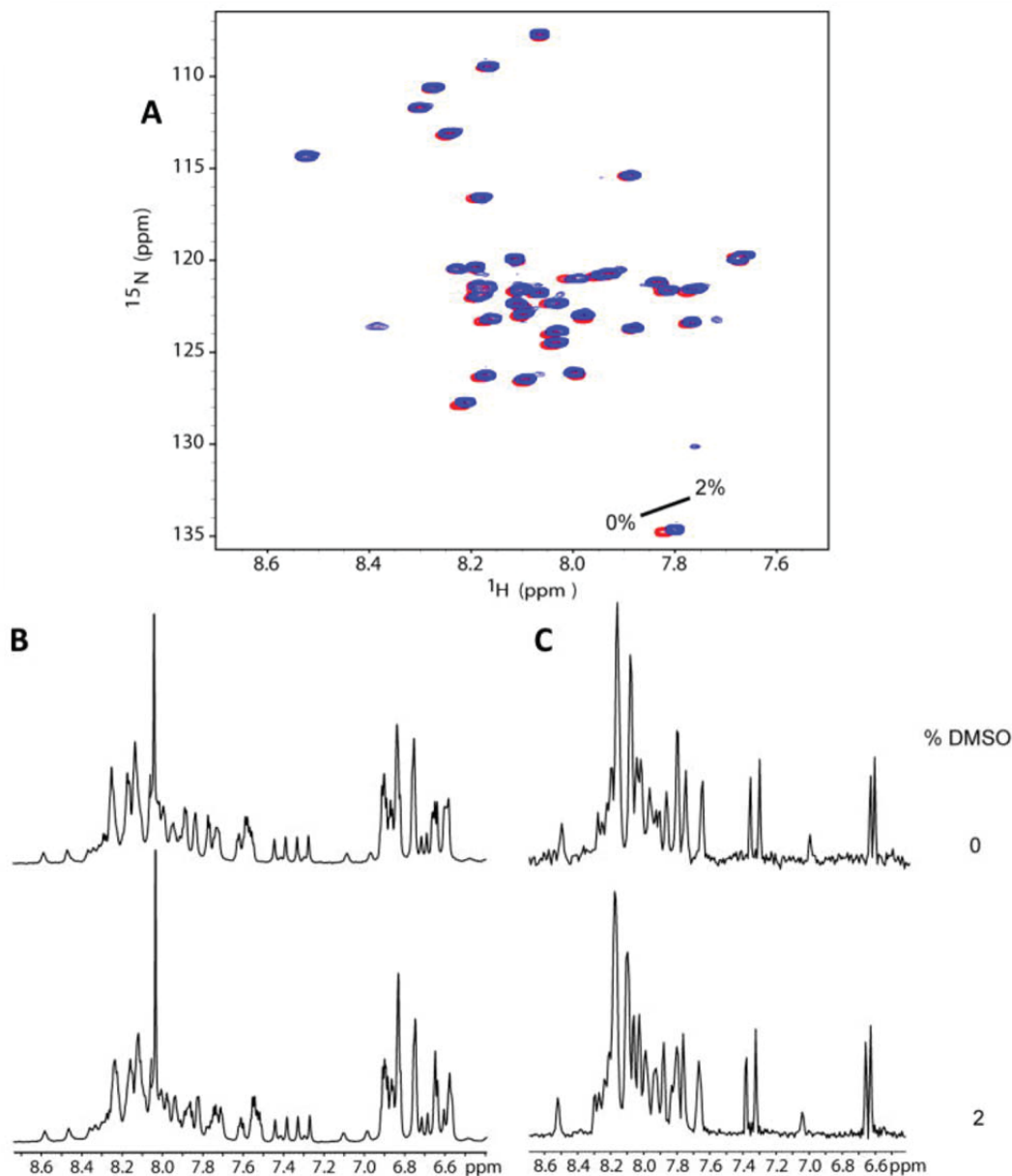
Figure 3.10. DMSO control titration spectra of Aβ42. (A) ^{15}**N HSQC spectra of U-**^{15}**N-Aβ42 upon addition of DMSO-d_6 at 0% and 2% (initial and final concentrations in titrations of figures 3.7-3.9). (B)** ^{1}**H NMR spectra taken at each titration point to allow observation of ligand peaks throughout the titration. It can be seen that the DMSO peaks remain sharp throughout. (C) 1-D** ^{1}**H NMR projections of the HSQC experiments taken in (A) demonstrate that Aβ42 remains soluble and monomeric upon addition of DMSO to 2%.**

In addition to performing an entire titration series with the NSAIDs, experiments were

performed as in Richter *et al*. (*281*) where a single point was examined at 1:3

protein:ligand concentration (100µM Aβ42 plus 300µM of either sulindac sulfide, sulindac sulfone, or 2% DMSO control). Upon addition of 300 µM sulindac sulfide, and by the time the sample could be transferred to the instrument and the HSQC experiment recorded, some peaks from Aβ42 had begun to disappear (figure 3.11). This phenomenon was monitored over the next hour. After 15 minutes, nearly all of the Aβ42 had aggregated and become NMR-invisible. By 1 hour, none of the ^{15}N-HSQC signals were visible in NMR spectra. This effect was not observed with sulindac sulfone, flurbiprofen, or DMSO (data not shown). To investigate the whereabouts of the Aβ42 peptides, the NMR samples were submitted for transmission electron microscopy (TEM), the results of which are also shown in Fig. 3.11 D, E, and F. Clearly, the addition of sulindac sulfide at concentrations where it forms colloidal aggregates induced the formation of Aβ42 fibrils, whereas the addition of an identical concentration of DMSO (Fig 3.11F) or monomeric sulindac sulfone (data not shown) had no effect on the oligomeric state of Aβ42.
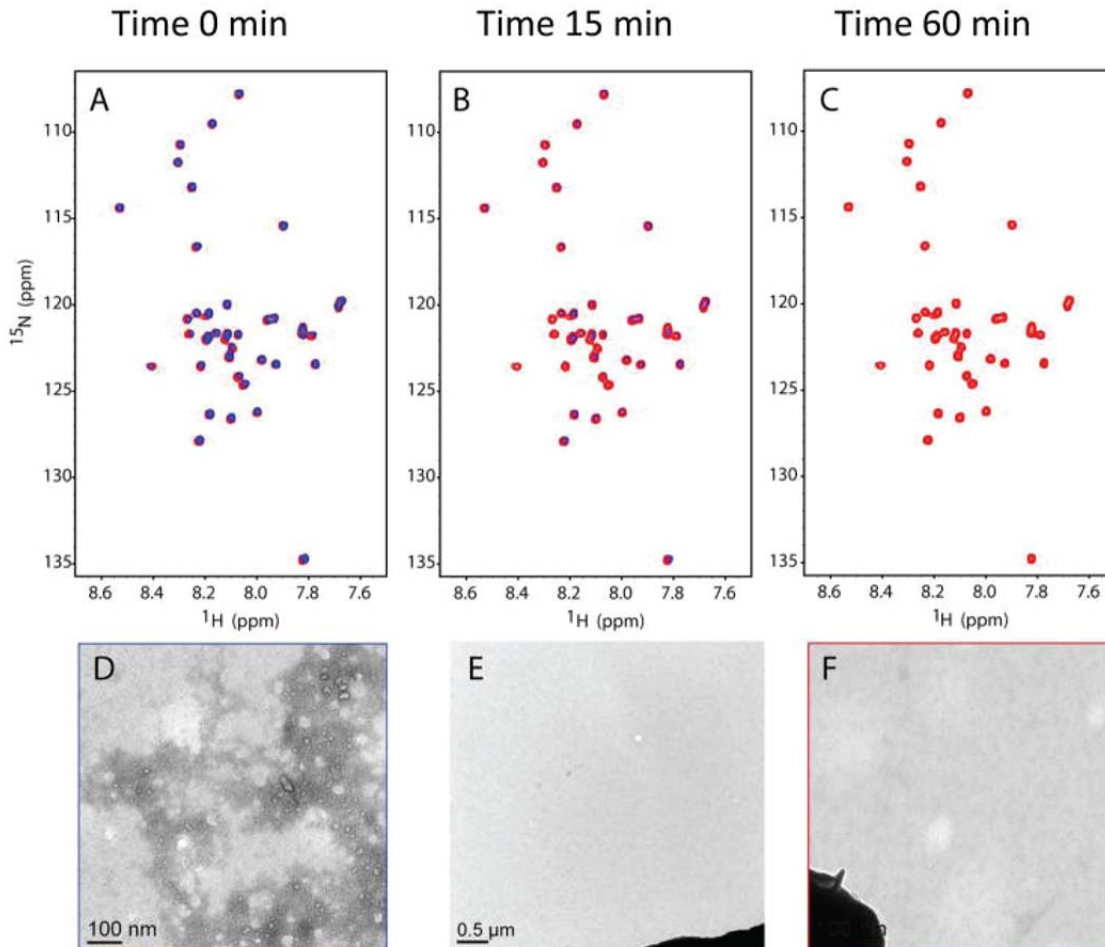
Figure 3.11. Time course ^{15}N-HSQC spectra of 100µM U-^{15}N-Aβ42 following addition of sulindac sulfide to 0.3mM. Panels A, B, and C show spectra taken of 0.1mM Aβ42 alone (red) and upon addition of sulindac sulfide (blue) at times = 0, 15 min, and 1 hr, respectively. Notice the decrease in intensity of all the blue peaks as Aβ42 begins to form aggregates. Panels D, E, and F show transmission electron micrographs (66000x) of 0.1mM Aβ42 NMR samples fixed to a TEM grid ~ 2 hr after addition of (D) 0.3mM sulindac sulfide, (E) 0.3mM sulindac sulfide alone (no protein, 11600x) and (F) DMSO only to a final concentration of 2%, matching that in (D) and (E) (dark blob in (E) and (F) is grid bar included for camera gain). In (D), fibrils of Aβ42 are clearly visible.

We also looked for direct interaction of three NSAIDs with Aβ42 using surface plasmon resonance (SPR). Previously published results from Richter *et al* (*281*) suggested that sulindac sulfide binds specifically to Aβ42. However, upon closer inspection of the SPR data presented in the previous work, it can be observed that

binding of sulindac sulfide to immobilized Aβ42 was non-saturable over the concentration range tested, suggestive of very weak and/or non-specific binding. To test this hypothesis, we performed SPR experiments in a similar manner as presented in Richter *et al*. using immobilized Aβ42 peptide. For our studies, we also incorporated varying amounts of Tween-20 in the running buffer—zero detergent (as in the Richter *et al*.), 0.005% (40 μM, below its CMC of 60μM) and 0.2% (1.6 mM, above CMC) to illuminate whether drug and/or protein aggregation was a factor in the observed SPR response. The results for sulindac sulfone illustrate the patterns expected in the absence of binding (Figure 3.12, left). It can be seen that the SPR traces for flurbiprofen (Figure 3.12B, right), even up to 1 mM, are very similar to those of sulindac sulfone, indicative of no binding.
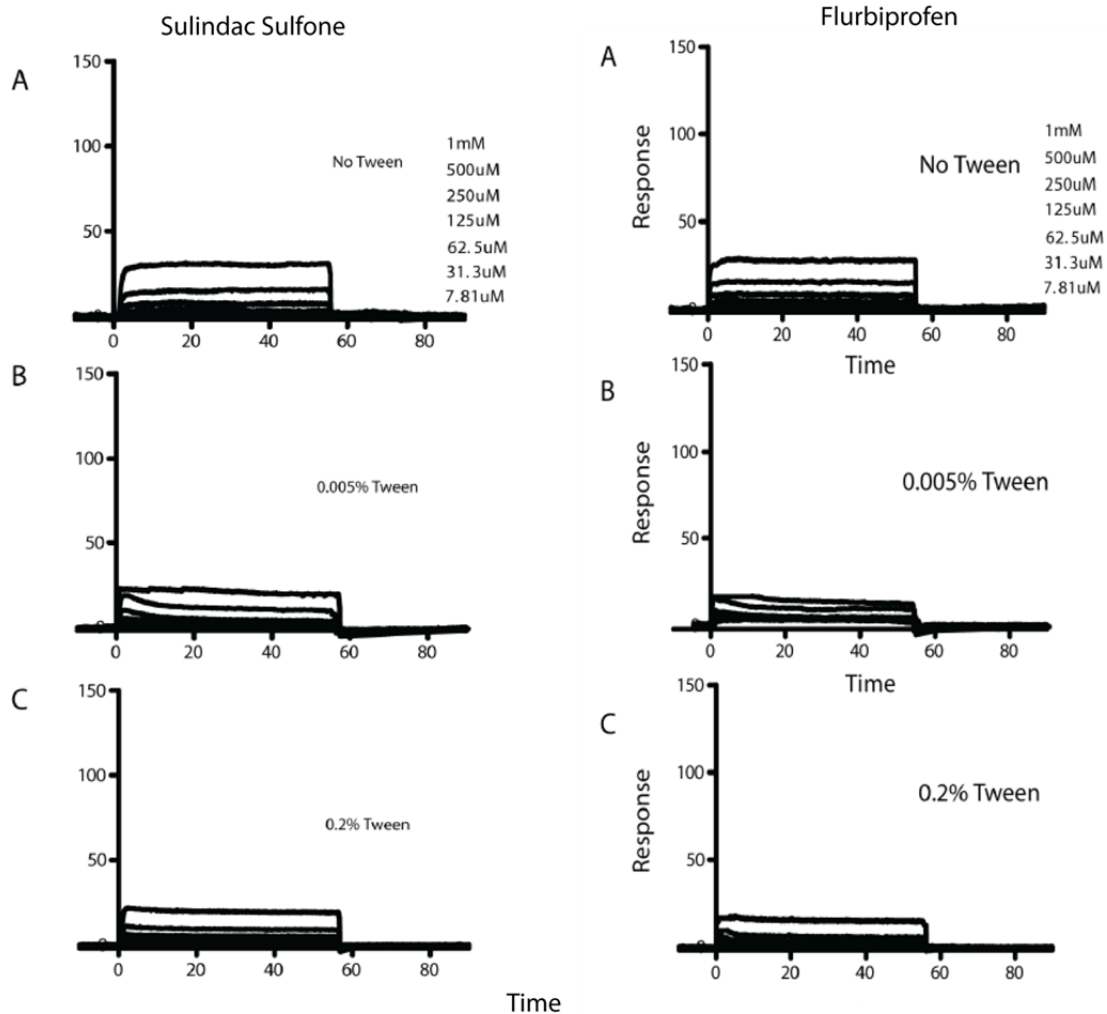
Figure 3.12. SPR analysis of sulindac sulfone (left) and flurbiprofen (right) with immobilized Aβ42. Overlays of SPR sensograms obtained from injections of compounds into solutions containing 50mM sodium phosphate, 50mM NaCl, pH 7 with (A) No detergent, (B) 0.005% Tween-20 and (C) 0.2% Tween-20. Aβ42 was immobilized with ~3000 response units (RUs). Sulindac sulfone or flurbiprofen at the indicated concentrations were injected for 60s at a flow rate of 30μL/min. None of the binding curves saturate, indicating that the observed response is due to non-specific binding.

In the case of sulindac sulfide (Figure 3.13), the data is more complex. In the absence of detergent, sulindac sulfide induces a biphasic response suggestive of a rapid binding event followed by a slower second binding event. This second phase is eliminated when the titration is carried out in the presence of a sub-critical micelle concentration (CMC) of detergent, indicating that the slow binding seen in Figure 3.13A

likely represents non-specific association of sulindac sulfide with Aβ42 on the sensor chip—association that can be reduced in the presence of another hydrophobic small molecule (i.e. Tween-20 monomers). When the detergent concentration (Tween-20) is raised still higher to >CMC, it is seen that the SPR response (Figure 3.13C) is comparable to the negative control SPR response observed at similar concentrations of sulindac sulfone. This indicates that the rapid binding event observed in Figs. 3.13A and 3.13B is of colloidal aggregates of sulindac sulfide to Aβ42.   Sub-micellar concentrations of detergents (as in 3.13B) do not break up those soluble aggregates, but the presence of detergent micelles (as in 3.13C) effectively dissolves the aggregates, which is seen to eliminate binding.
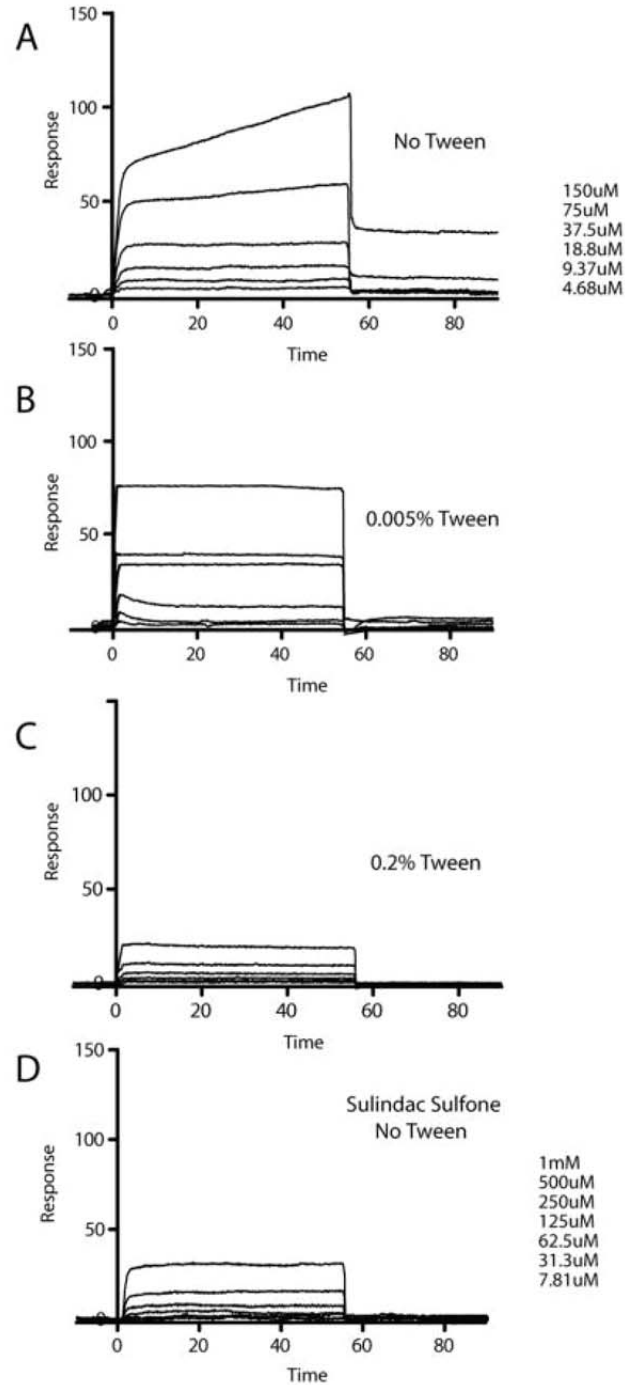
Figure 3.13. SPR analysis of sulindac sulfide with immobilized Aβ42. Overlays of SPR sensorgrams obtained from injections of sulindac sulfide in 50mM sodium phosphate, 50mM NaCl, pH 7, with (A) no detergent, (B) 0.005% Tween-20, and (C) 0.2% Tween-20. Panel D shows corresponding sensograms of sulindac sulfone used as a negative control. Aβ42 was immobilized with ~3000 response units (RUs). Compounds at indicated concentration were injected for 55s at a flow rate of 30μL/min at 25ºC.

Inhibition of β-Secretase by Sulindac Sulfide

The formation of water soluble colloidal drug aggregates is a commonly encountered phenomenon (*283, 284, 297, 298*). Moreover, such aggregates are known to often have very general and non-specific activities as enzyme inhibitors; sometimes being referred to as "promiscuous inhibitors"(*297, 299*). To provide additional verification of the nature of the aggregates formed by sulindac sulfide at concentrations about 50 μM we tested to see whether these aggregates have enzyme inhibitory activity. β-secretase (BACE-1) was used as the test enzyme for this experiment. Indeed, we found that sulindac sulfide began to significantly inhibit BACE-1 at concentrations around 50μM, with near complete inhibition being approached at 200μM (Fig 3.14). No inhibition was observed with sulindac sulfone, which we showed above does not form aggregates, at least not below 1 mM. We also found that the level of inhibition with sulindac sulfide was significantly reduced by doubling the BACE-1 concentration from 220nM to 440nM. Such acute sensitivity to enzyme concentration is a common trait of aggregation-based inhibitors (*283, 284, 297, 298, 300*), which inhibit enzyme action through a non-specific binding type mechanism (*300*). These colloidal aggregates can bind to proteins with high affinity and can envelop the protein, preventing substrate access and thus inhibiting protein function (*297, 299*). Maintaining a constant compound concentration and doubling the enzyme concentration can allow this effect to be at least partially overcome, resulting in decreased inhibition of the enzyme (*297*). These combined results indicate that not only do aggregates formed by sulindac sulfide trigger fibrillization of Aβ42, but also that these aggregates share properties in common with other "promiscuous inhibitors".
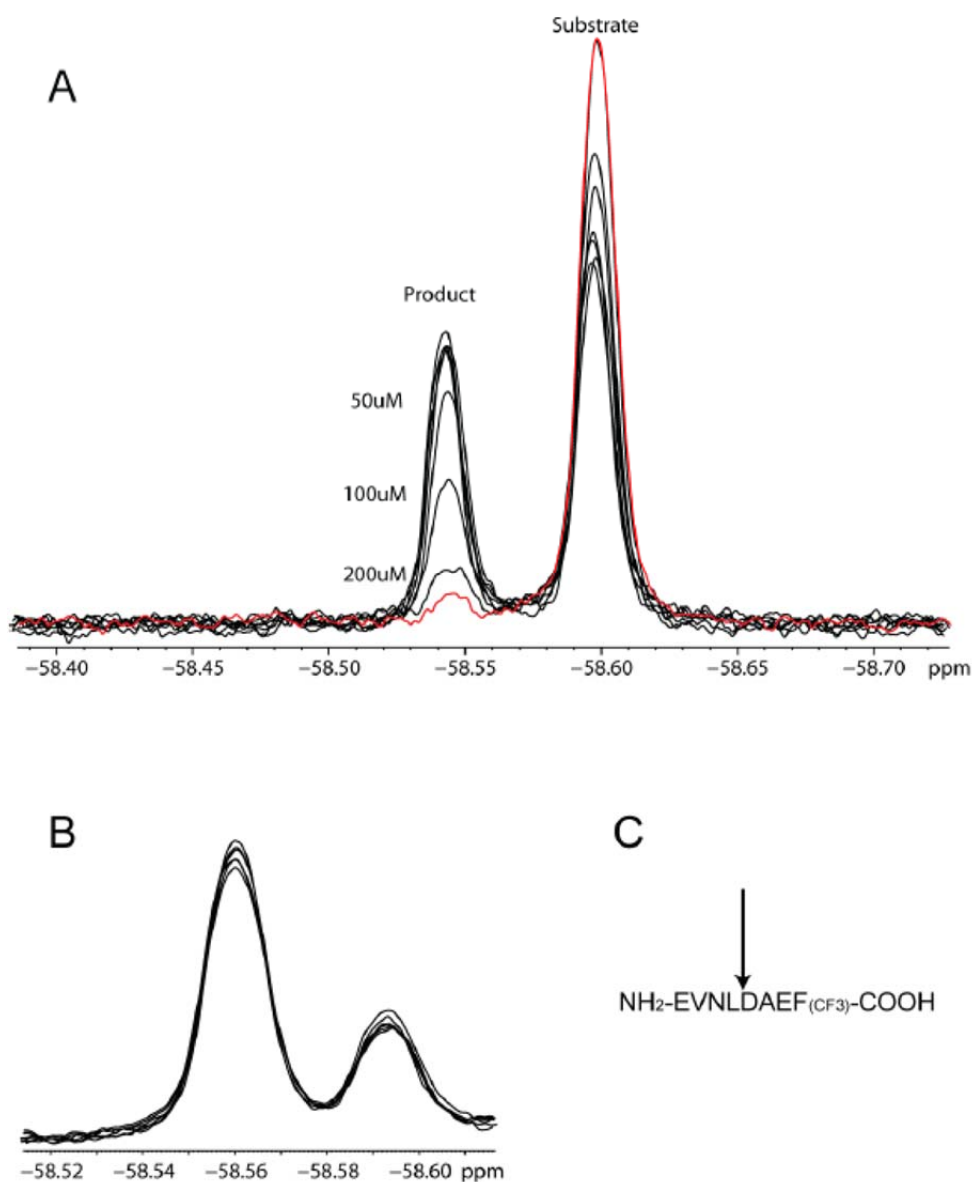
Figure 3.14. Inhibition of β-Secretase by sulindac sulfide. (A) ^{19}F-NMR enzymatic assay showing the substrate and product of the cleavage reaction in the presence of varying concentrations of sulindac sulfide. Notice that significant inhibition of the enzyme is observed at 50µM sulindac sulfide (near its CAC), with near complete inhibition being observed at 200µM. The red trace is a control inhibitor of known K_i (400nM). **(B)** Enzymatic assay run identically but in the presence of varying concentrations of sulindac sulfone. No inhibition of BACE activity is observed. **(C)** Schematic of BACE cleavage reaction using a CF_3-labeled phenylalanine (cleaved site depicted by arrow). In both cases 220nM enzyme and 100µM substrate were used. Reactions were initiated by addition of substrate and were quenched by addition of 8M urea after 20 mins.

NMR Titrations of Membrane-Associated C99 with GSMs

In a previous study, we showed that certain GSMs did not bind to C99 monomers and dimers in micellar model membranes (*280*). Here, we extend this observation to C99 reconstituted into bilayered lipid membranes. Sulindac sulfide, sulindac sulfone, and flurbiprofen each include fluorine atoms, potentiating the use of ^{19}F NMR to monitor binding. ^{19}F NMR chemical shifts are exquisitely sensitive to even very minor changes in local environment. C99 was reconstituted into lipid vesicles with a protein to lipid ratio of 1:100 (100µM C99:10mM POPC/POPG). Vesicles were then titrated with sulindac sulfide, sulindac sulfone, and R-flurbiprofen. ^{19}F NMR spectra were acquired for each compound in the presence of protein-free vesicles and in the presence of an identical concentration of vesicles containing reconstituted C99 (100 µM).

Unfortunately, no ^{19}F signal could be detected for sulindac sulfide in both the absence and presence of C99, indicating that this compound binds avidly to the vesicles whether the protein is present or not. Vesicles represent a solids-like environment from an NMR standpoint such that a combination of chemical shift anisotropy and ^{1}H-^{19}F dipolar coupling lead to extensive linebroadening and disappearance of signals when sulindac sulfide binds to the vesicles. However, the results were more clearly interpretable for an alternative GSM, fluribiprofen, and for the negative control, sulindac sulfone. These compounds yield sharp ^{19}F NMR peaks in the presence of protein-free vesicles (Figure 3.15), which indicates that these compounds either do not bind to lipid bilayers at all or bind only weakly such that exchange between solution and the membrane is rapid on the NMR time scale and such that the free population predominates. When C99 is also present in the vesicles at a C99-to-drug mole-to-mole ratio of 5:1, it can be seen in Figure 3.14 that there are no changes in the spectra relative to protein-free conditions: chemical shifts, linewidths, and peak intensities are unchanged by the presence of the protein. This indicates that sulindac sulfone and

flurbiprofen do not bind to C99 even when the protein is present at a five-fold molar excess over the 20 µM drug concentration.
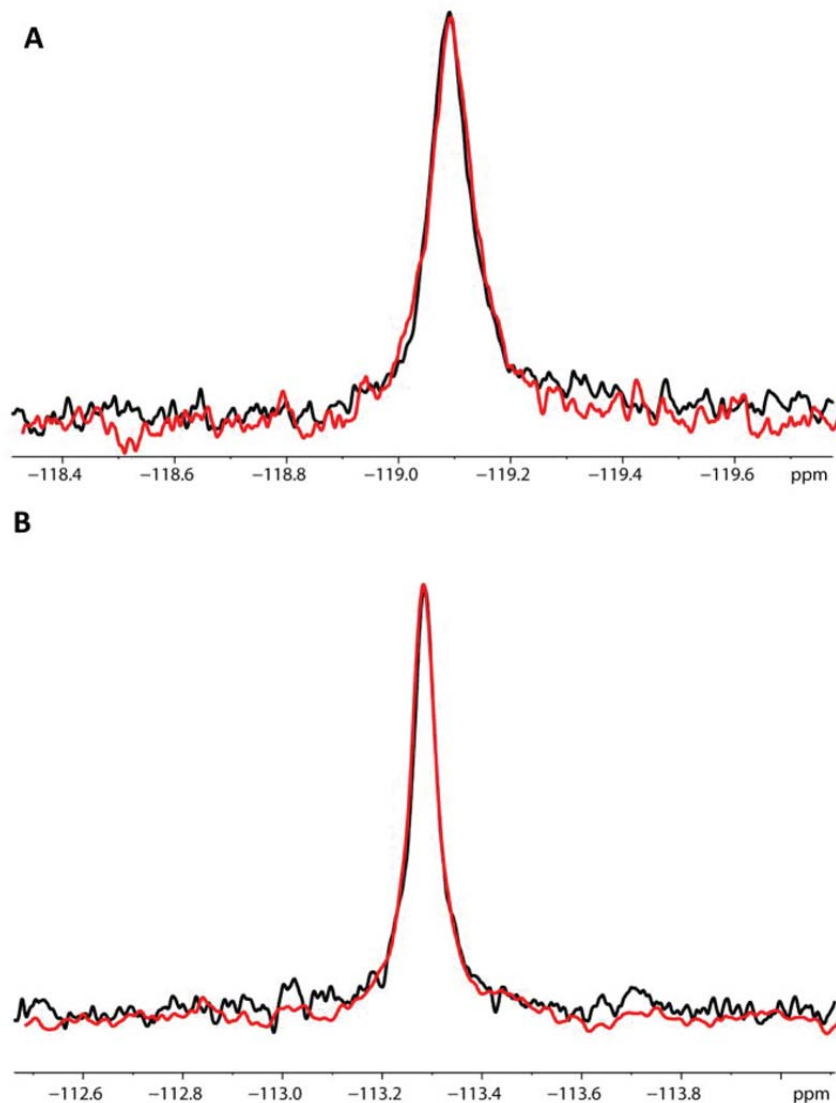
Figure 3.15. Comparison of ^{19}F spectra of flurbiprofen (A) and sulindac sulfone (B) in the presence of bilayered lipid vesicles in the absence (black) and presence (red) of C99. (A) The samples contained 20µM flurbiprofen both in the absence (black) and presence (red) of 100µM C99 incorporated into 10mM POPC/POPG vesicles (1:100 C99:lipid). (B) The samples contained 20µM sulindac sulfone in both the absence (black) and presence (red) of 100µM C99 in vesicles. All control samples (black) contained only 10mM phospholipid. The lack of change in both sets of spectra indicates that no interaction exists between compounds and C99.

Discussion

The subject of substrate-targeting GSMs has been a topic of extensive research and discussion over the past several years. Based largely on photoaffinity-crosslinking experiments, the initial paper by Kukar *et al*. (*279*) proposed that NSAID-type GSMs targeted the APP substrate (C99) of γ-secretase. However, a variety of evidence has been presented that disfavors this interpretation (see review in(*295*)). As described in the introduction, this evidence includes previous results from our lab indicating that non-aggregated C99 in model membranes does not bind GSMs (*280*). In our previous work we also presented data suggesting that C99 was very likely to have been in an aggregated form in critical experiments of the original Kukar *et al*. studies (*279*). While GSMs do appear to bind to *aggregated* C99 (*280*), this is unlikely to be relevant to processing of C99 by γ-secretase *in vivo*. Moreover, the binding was seen to be non-specific in nature.

Our previous work was disputed in a pair of papers by the Multhaup lab (*281, 282*) which presented data that was interpreted as demonstrating that GSMs, sulindac sulfide in particular, specifically recognize and bind to both membrane-associated C99 and the water soluble monomer form of Aβ42, the latter of which includes the putative GSM binding site proposed in the original Kukar *et al*. work (*279*). In the introduction, we hypothesized that key results and conclusions in the Multhaup papers may have reflected experimental artifacts due to the poor behavior of sulindac sulfide in aqueous solutions. The results of this work support this hypothesis based on the two primary sets of results, both of which are closely related to our observation that the GSM sulindac sulfide forms colloidal aggregates with a CAC of roughly 50-60 μM. In a first set of results, titrations of monomeric Aβ42 by GSMs sulindac sulfide and R-flurbiprofen were followed by NMR spectroscopy, which yielded no evidence for binding of the monomeric

drugs to monomeric Aβ42. However, it was found that the colloidal aggregates formed by sulindac sulfide at concentrations above 50-60 μM induce aggregation of Aβ42. Based on this result we believe that the one point titration presented by the Multhaup lab (*281*) showing dramatic changes in the NMR spectrum of Aβ42 upon addition of 300 μM sulindac sulfide represents the observation of aggregated Aβ42 formed in response to the presence of colloidal aggregates of sulindac sulfide.

The second set of results involves our repetition of SPR experiments (see Fig 2 in (*281*)) in which binding of sulindac sulfide to immobilized Aβ42 was tested over a range of drug concentration from 5 to 100 μM. We reproduced the observation that sulindac sulfide, but not the negative control sulindac sulfone, induces a strong and dose dependent SPR response. However, we also observed that there was no SPR response beyond what was observed for negative control conditions when the sulindac sulfide titration was repeated in the presence of Tween-20 micelles. This strongly suggests the binding of sulindac sulfide to Aβ42 observed in the earlier work represents *non-specific* association these two compounds. Such association is highest when sulindac sulfide is in its colloidal form (at concentrations >50μM) and may also be promoted by the structural properties of sensor chip surface-associated Aβ42, which may itself have aggregate-like properties as a result of being locally concentrated at on the sensor chip surface. Association between the GSM and surface associated Aβ42 is eliminated by the presence of detergent micelles that can disperse the colloidal drug and can also coat exposed hydrophobic sites on sensor surface-associated Aβ42, making such sites less-susceptible to non-specific hydrophobic interactions with hydrophobic compounds such as sulindac sulfide.

Multhaup *et al*. also carried out SPR experiments in which titration of immobilized C99 with sulindac sulfide also led to a linear dose/response curve, which was interpreted as being in support of specific binding (*282*). Similar SPR experiments carried out on

immobilized C99 also led to a linear dose/response curve. In addition to the fact that the linearity of the data precludes the conclusion that a specific complex is forming, we believe that there was also a serious artifact in their experiment. In that work, the sensor chips were coated with C99 and then subjected to experiments under, in both cases, essentially membrane- and micelle-free conditions. (Tween-20 was present during all these steps, but only at 40 µM, which is below its critical micelle concentration of 60 µM). However, C99 is an integral membrane protein which is expected to be insoluble under aqueous conditions in the absence of detergent micelles or some other membrane-mimetic medium. Therefore, the immobilized C99 present in the SPR experiments of (*282*) was almost certainly in an aggregated form. We have previously shown that aggregated C99 can bind GSMs in a non-specific fashion (*280*) and so it is no surprise that this is what was seen in the more recent work (*282*). In the present work, we observed that the GSM R-flurbiprofen exhibits no binding to C99 reconstituted lipid in vesicles. This result extends the conclusions from our earlier observations of the lack of GSM binding to non-aggregated C99 in *micellar* model membranes to non-aggregated C99 in actual lipid bilayers.

One additional set of experiments from Multhaup and co-workers that yielded support for sulindac sulfide binding to C99 in membranes was a series of ToxR experiments carried out in *E. coli* (*281*). In those experiments homodimerization of C99 was assessed following expression into *E. coli* based on coupling homodimerization of C99 to transcriptional activation of a gene that expresses a colorimetric reporter enzyme. Using this assay, it was seen that sulindac sulfide reduces apparent dimerization of C99 in *E. coli* in a dose-dependent fashion, consistent with inhibition of dimerization of C99 by GSM binding. These studies were carefully carried out and can indeed be interpreted as being supportive of GSM/C99 binding. However, when conducting *in vitro* experiments involving GSM drugs, living cells, and an indirect phenotype-based assay

the possibility cannot be ruled out that the GSM induces a positive assay response as a result of off-target drug effects that lead to the artifact-based activation of the assay response (i.e., induction of reporter enzyme expression). In light of the biophysical results of this paper, we suggest that this alternative explanation of the ToxR data is very likely applicable.

The experiments and results summarized above lead to the conclusion that the GSM sulindac sulfide does not bind to Aβ42 when both compounds are in monomeric form. On the other hand, non-specific binding between aggregates of Aβ42 or with colloidal aggregates of sulindac sulfide appears to occur. Promiscuous binding of small molecule aggregates to proteins, often accompanied by inhibition of protein function, is a very common occurrence (*283, 284, 297, 298*). Indeed, in this study aggregated sulindac sulfide was found not only to bind to Aβ42, but also to inhibit β-secretase (here used as a representative enzyme). It has previously been shown that Congo red can form colloidal micelle-like aggregates that bind to Aβ and induce its aggregation (*284*). It has also been observed that a number of drug-like molecules form colloidal aggregates that interact with amyloid-forming yeast prion proteins in a way that inhibits fibril formation(*298*).

Evidence is accumulating that NSAID-based GSMs target a component other than the APP substrate in the amyloid cascade (review in (*295*)). Previous publications have suggested that GSMs act by causing conformational changes within Presenilin 1 (PS1)(*301-303*), or by altering membrane architecture and thereby changing the manner in which γ-secretase cleaves its APP substrate (*304*). More recent studies have indicated that the action of GSMs may be allosteric in nature. Uemura *et al* demonstrated that GSM-induced conformational changes in PS1 only occur in the presence of substrate, suggesting that substrate binding to γ-secretase uncovers an allosteric site for GSM binding that is only present in the substrate-enzyme complex

125

(*305*). Another recent study focused on a mutational analysis of APP and demonstrated that mutations in the GxxxG motif (the proposed GSM binding site) still caused an effect on Aβ42 production upon treatment with GSMs (*306*). The compounds were then shown to display differential or no effects on Aβ42 and Aβ38 levels when PS1 mutants were used. These conclusions contradict a substrate-targeted model of GSM action and instead suggest that these molecules target the γ-secretase enzyme itself or the enzyme-substrate complex (*306*). Taken as a whole, the evidence is becoming overwhelming that GSMs do not target the γ-secretase substrate, at least not in the absence of complexed γ-secretase.

Acknowledgements

CHAPTER IV

BINDING OF CHOLESTEROL PROMOTED C99 PARTITIONING TO CHOLESTEROL

RICH MEMBRANE DOMAINS[6]

Introduction

The long term production and accumulation of Aβ in the human brain is closely

related to the etiology of Alzheimer's disease (*307, 308*). The amyloidogenic pathway

involves the β-secretase-mediated proteolysis of APP to liberate its transmembrane C99

domain which is in turn cleaved by γ-secretase to release Aβ. Elevated cholesterol

levels appear to promote this pathway (*309-314*). Previous studies suggested that C99

could potentially bind cholesterol utilizing a modified cholesterol recognition amino acid

consensus sequence (CRAC) motif (*223*). CRAC motifs are known residues that

facilitate the binding of cholesterol (*315, 316*). This CRAC-like motif is located in the N-

helix/N-loop/TMD structural element of C99. Due to the low solubility of native

cholesterol, previous work utilized the soluble cholesterol analogue β-cholbimalt to

determine the binding region. Saturable binding was shown for the residues in the N-

loop, specifically residues V695-G700 by NMR chemical shift perturbation titration

analysis. The K_d of this binding was a modest 28 ± 14 mol% (*28*). Although possessing

a low solubility, a similar initial titration was performed with cholesterol (up to 5 mol%).

Chemical shift perturbation analysis showed that similar residues interacted with β-

Cholbimalt and cholesterol, though a full titration with cholesterol was not performed.

Results below will show that C99 forms a 1:1 complex with cholesterol with an affinity (K_d = 5.1 ± 1.2 mol%)(*26*) that is well within the known range of cholesterol concentrations in mammalian membranes (*317-320*). The binding of cholesterol by C99 is an interesting topic since both β- and γ-Secretase are thought to reside in cholesterol rich membrane domains. By showing that C99 can specifically bind cholesterol, it suggests that full length APP can as well. Better understanding of the C99 (and APP)/cholesterol complex could offer a unique therapeutic approach to block the movement of APP to these cholesterol rich domains and ultimately Aβ production.

Based on this fact and many reports that the amyloidogenic pathway is associated with cholesterol rich domains (*309-314*), the formation of C99-cholesterol complexes has been hypothesized to enhance partitioning of C99 into cholesterol-rich raft (L_o) domains from the surrounding bulk membrane (L_d) domain, thereby promoting its cleavage by γ-secretase to release Aβ (*26, 28, 310*). Here we test whether C99 has an intrinsic preference to partition into raft-like L_o phase membrane domains and examine whether various sterol binding partners can regulate partitioning of the protein between L_o and L_d phase domains.

Materials and Methods

Reconstitution of Wild Type C99 in Bicelles and Titration With Cholesterol as Monitored by $^1H, ^{15}N$ TROSY NMR

The ^{15}N labeled-C99 from 1 g of cell pellet was bound to and purified on 2 mL Ni-resin as described above. The pure protein on the resin was then equilibrated with 1% isotropic q=0.3 dimyristoylphosphatidylcholine/dihexanoylphosphatidylcholine (DMPC/DHPC) bicelles plus 10 mM imidizole, pH 7.8 (where q is the DMPC to DHPC

mole ratio). The protein was then eluted from the column with 7 mL of elution buffer

containing 2% isotropic DMPC/DHPC bicelles and 250 mM imidazole, pH of 7.8. 5 mL

of protein solution was collected and concentrated to 0.5 mL by centrifugal ultrafiltration

using a 10 kDa MWCO cutoff filter. D2O was then added to 10% (v/v) for the NMR lock

and EDTA was added to a concentration of 1 mM. The pH of the sample was lowered to

4.5 with acetic acid. The NMR sample therefore contains 20% DMPC-DHPC bicelles

(q=0.3), 30 mM acetic acid, 1 mM EDTA, 10% (v/v) D2O and approximately 0.25 mM

C99. Another four samples were prepared in parallel that contained cholesterol. These

samples were prepared by eluting C99 from the resin using bicelle solutions that

contained 2.5, 5, 10, or 20 mol% cholesterol (relative to DMPC). Cholesterol-containing

bicelle solutions were prepared by co-dissolving DMPC and cholesterol in chloroform,

removing all solvent under high vacuum, and then mixing with DHPC and buffer,

followed by freeze-thaw cycles until the solutions became transparent. ^{1}H, ^{15}N-TROSY

spectra were acquired for each sample at 318K using a Bruker 600 MHz Bruker NMR

spectrometer (Figure 4.1). The chemical shifts for three peaks that exhibited relatively

large cholesterol-induced shifts were plotted as a function of the amount of cholesterol

(Figure 4.1). The data were fit using Origin 8.0 (OriginLab Corp. Northampton, MA) by a

single binding site model with the equation of y=X*Bmax/(Kd+X), where y is change in

chemical shift (relative to 0 cholesterol conditions), X is the cholesterol concentration,

Bmax is the maximum change in chemical shift observed for a given resonance upon the

saturation of binding by cholesterol, and Kd is the dissociation constant. While the data

presented in Figure 4.3 were collected at pH 4.5, a titration was also carried out at pH

7.0 (where NMR spectral quality for C99 in bicelle solutions is of lower quality), which

verified that cholesterol binds with the same avidity at both pH values.

Scanning Alanine Mutagenesis to Map the Cholesterol Binding Site

The TROSY NMR peaks of C99 that exhibited the largest changes in chemical shifts in response to cholesterol binding are located in the N-loop, N-helix, and extracellular end of the transmembrane domain (Figure 4.3C). To pinpoint which residues are specifically involved in binding cholesterol we carried out alanine-scanning mutagenesis for residues 690 to 710. Each alanine mutant was prepared for ^{1}H, ^{15}N-TROSY NMR as described in the previous section, with a full cholesterol titration being carried out in some cases (F691A, E693A, G696A, G700A, G704A, G708A, G709, and V710A). For other mutants, samples were examined at only 0 and 10 mol% cholesterol concentrations, (WT C99 was seen to be nearly saturated by cholesterol at 10 mol%, Fig. 4.3B). Spectra for each mutant in the absence of cholesterol were overlayed with the spectrum of WT C99 (figure 4.1), which shows that in no case was a global change in the conformation of C99 induced by the mutation of a wild type residue to Ala.
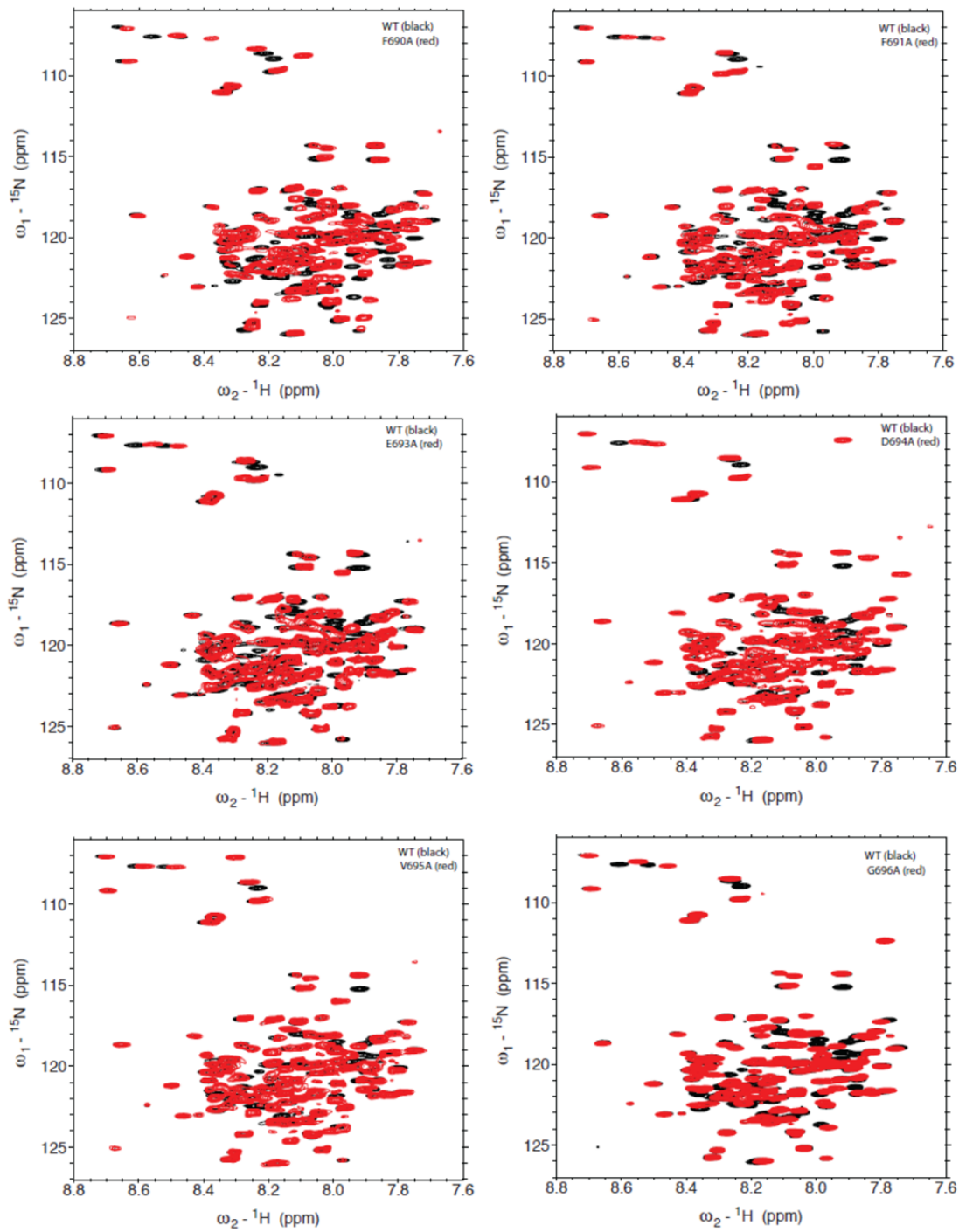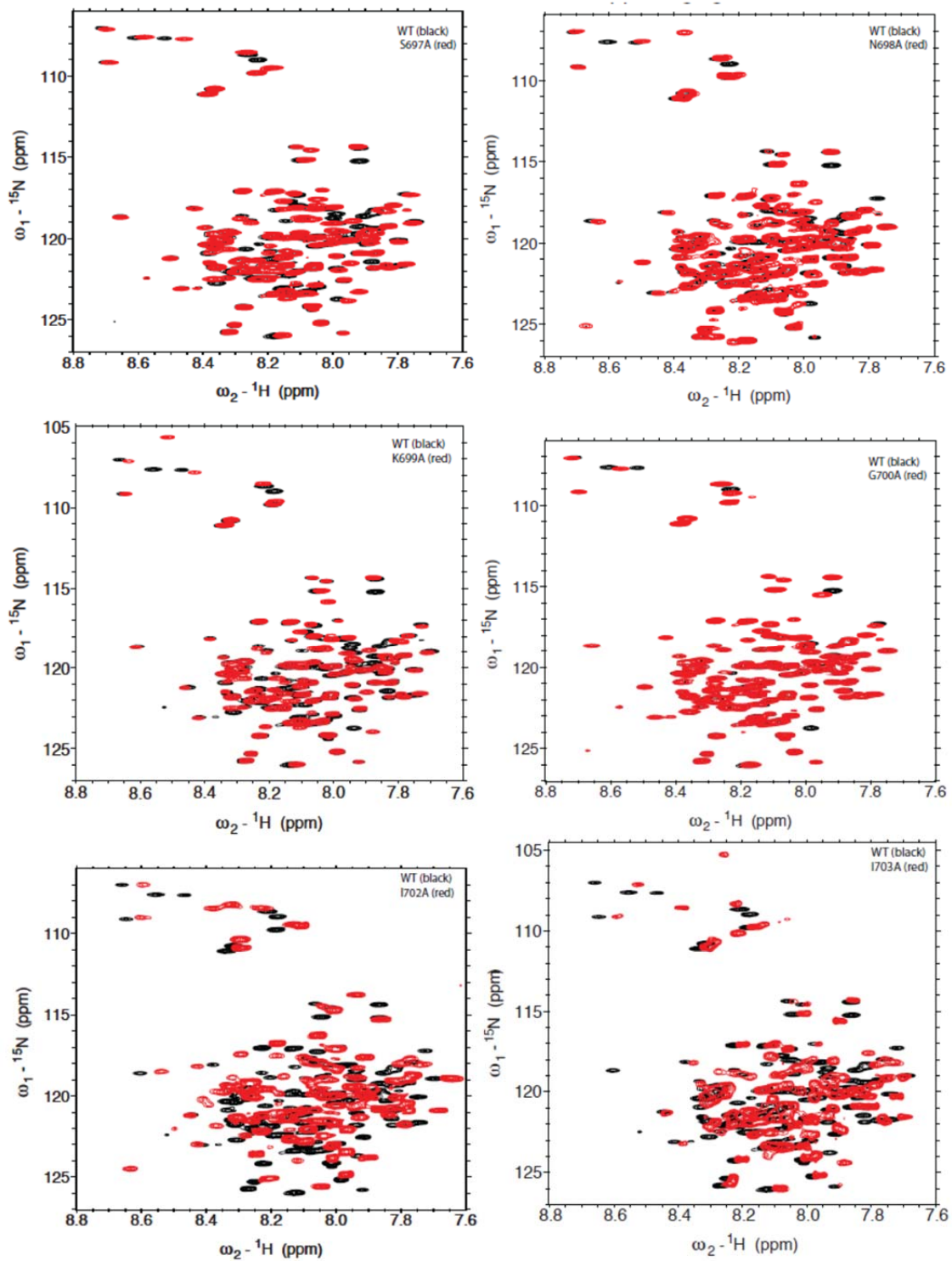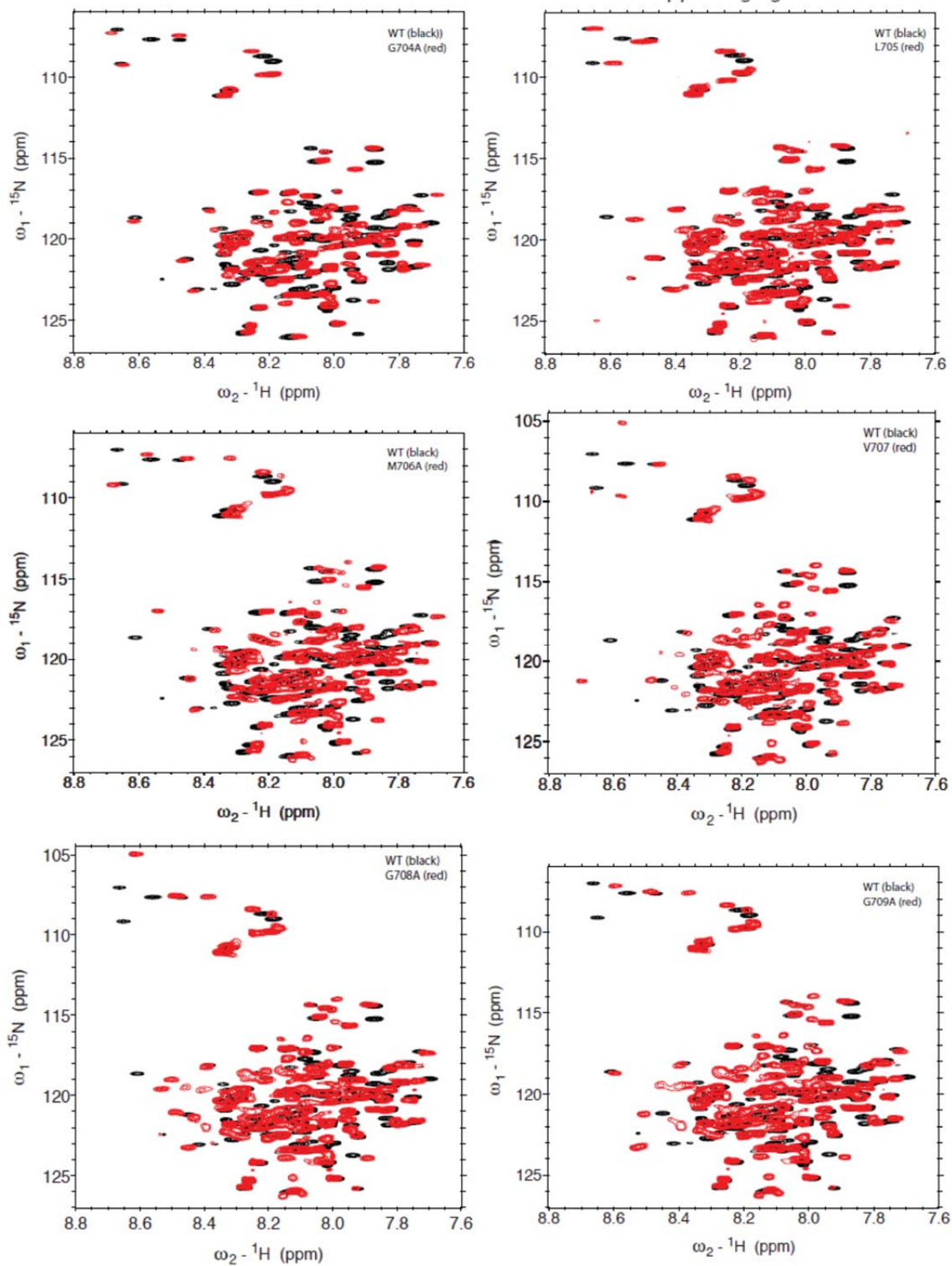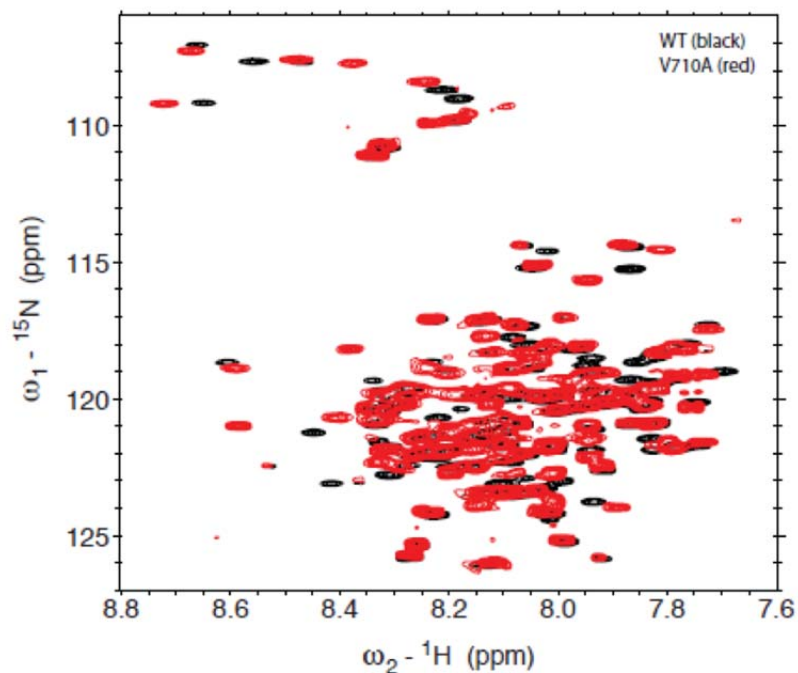
Figure 4.1. Comparisons of the ^{1}H-^{15}N TROSY spectra from each alanine mutant form of C99 with the spectrum for wild type C99. The 600 MHz ^{1}H-^{15}N TROSY spectrum (red) of each alanine mutant form of C99 (for scanning Ala-mutagenesis in the range of residues 690-710) is superimposed on the spectrum of C99 (black). The samples contain 20% DMPC-DHPC bicelles, 30mM acetic acid, 10% (v//v) D$_2$O, 1mM EDTA, and approximately 250μM C99 at pH 4.5.

To assess impact of each mutation on cholesterol binding, the spectrum from each cholesterol-free sample was overlayed with the spectrum (or spectra) from a cholesterol-containing sample (figure 4.2). The magnitude for the changes in resonance positions for the amide peaks of E693, Gly700, and Gly704 were in each case measured and compared to the corresponding changes for wild type C99. If the magnitude of the cholesterol-induced changes in resonance frequency for a given mutant was 80-100% that observed for wild type, the mutation site was judged to have wild type-like binding affinity (green sites in Figure 4.3E). If the observed peak changes were 20-80% relative to those observed for WT, the mutant was judged to be moderately-impaired in terms of

cholesterol binding (yellow sites in Figure 4.3E). If 10 mol% cholesterol induced negligible changes in peak positions (<20% of the changes seen for WT) the mutant was judged to have little affinity for cholesterol, reflecting a key role for the mutated residue in cholesterol binding (red sites in Figure 4.3E).
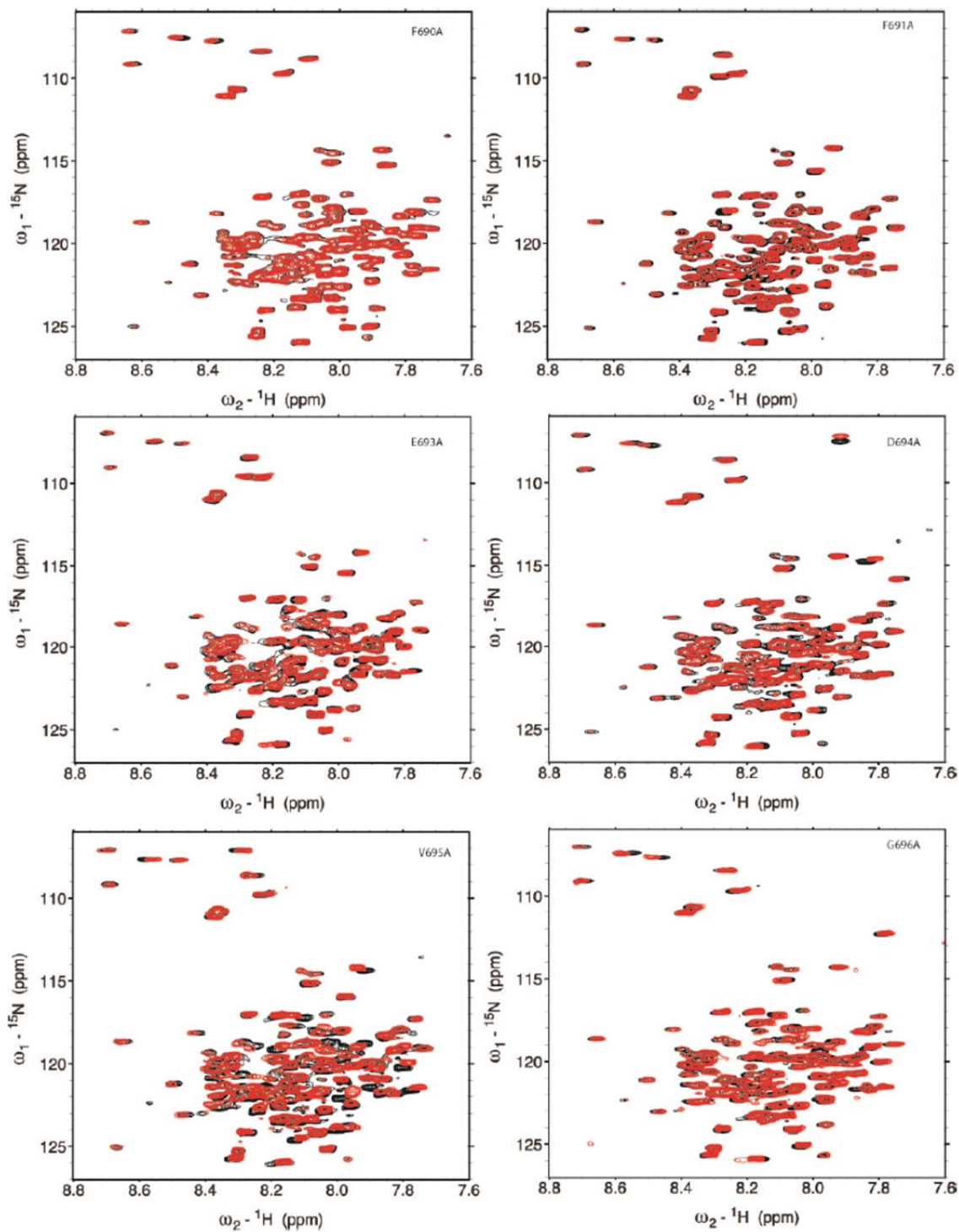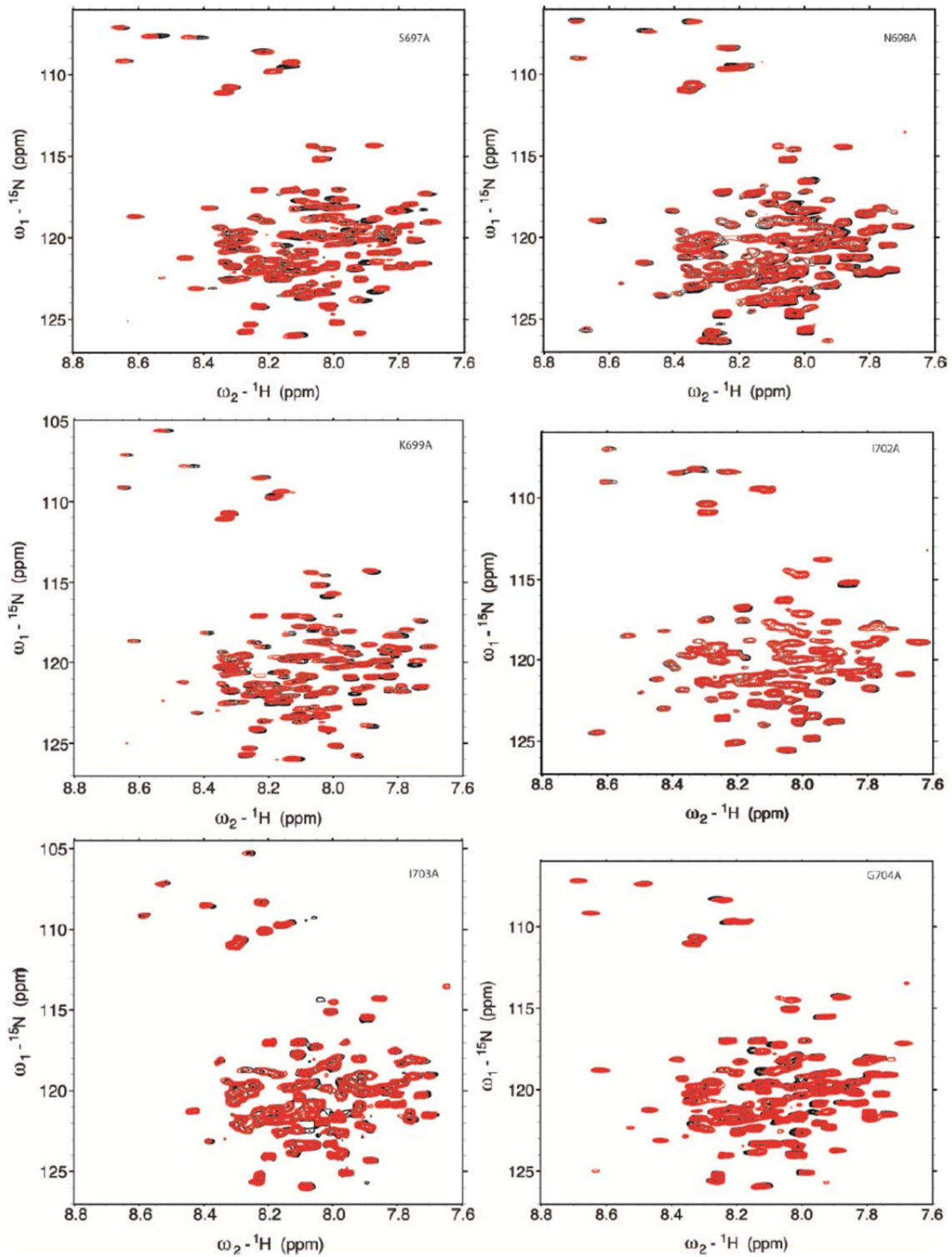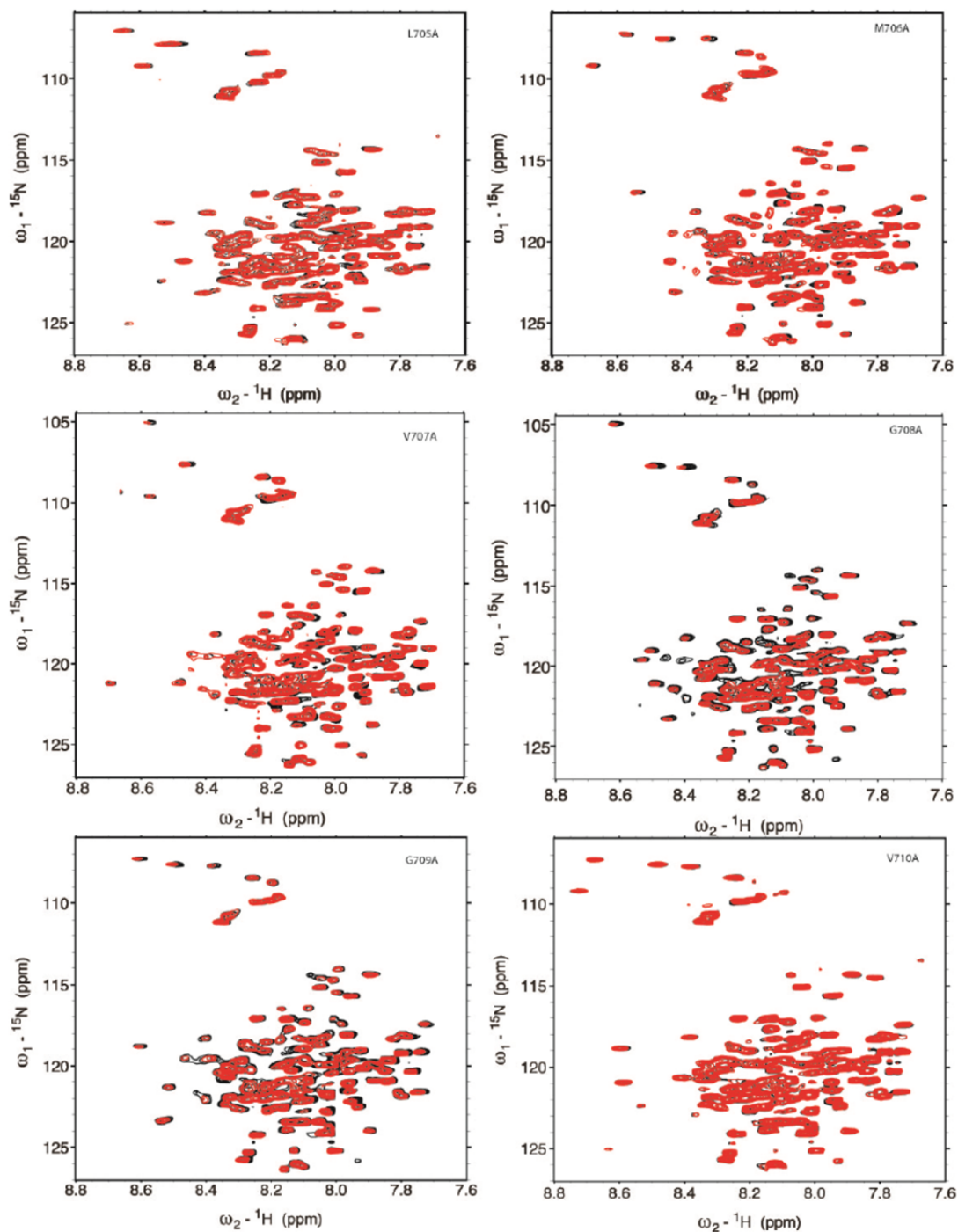
Figure 4.2. Cholesterol-induced changes in the NMR spectrum for each alanine mutant. Cholesterol-induced changes in the NMR spectrum for each alanine mutant form of C99 in bicelles. The 1H-15N TROSY spectra of each alanine mutant examined in the Ala-scanning mutagenesis study is shown in the presence (red) and absence (black) of 10 mol% cholesterol.

Materials for Lipid Vesicles

Dihexanoylphosphatidylcholine (DHPC), dimyristoylphosphatidylcholine (DMPC), 1-palmitoyl-2-oleoyl-phosphatidylcholine (POPC), dioleoylphosphatidylcholine (DOPC), distearoylphosphatidylcholine (DSPC), palmitoyl-sphingomyelin (SM), and cholesterol (Chol) were purchased from Avanti Polar Lipids, Inc (Alabaster, AL). Coprostanol was purchased from Steraloids Inc (Newport, RI). The lipophilic tracers 3,3'-dioctadecyloxacarbocyanine percholorate ('DiO', $DiOC_{18}$) and fluorescent dyes Alexa Fluor 488 C_5 maleimide and Alexa Fluor 546 C_5 maleimide were purchased from Invitrogen (Grand Island, NY). The fluorescent lipid 1,2-dioleoyl-*sn*-glycero-3-phosphoethanolamine-N-(lissamine rhodamine B sulfonyl) (ammonium salt) (Rho-PE) was purchased from Avanti Polar Lipids, Inc. Lipid and fluorescent lipophilic tracer stocks were prepared to concentrations of 10-25 mg/ml by solubilizing the powder in chloroform in amber glass vials and stored at -20°C.

Preparation of Alexa-Modified C99

Wild type C99 has no cysteine residues. Selected residues (F675 or H732) were mutated to cysteine using a C99-encoding plasmid (*28*) and the QuikChange protocol (Stratagene, La Jolla, CA, USA) utilizing whole plasmid PCR. The F675C and H732C mutation sites were selected on the basis that both sites are located in dynamic regions of the protein: F675 is located at the extreme (and extracellular) N-terminus and H732 is located in the cytosolic dynamic loop that connects the transmembrane helix to the C-terminus. Fluorescent labeling efficiency was high for both sites. Cholesterol binding knockout mutations were selected based on previous binding studies (*26, 28*). The single-Cys mutant form of C99 (WT or cholesterol knockout mutant background) was overexpressed and purified as described for wild type in 0.2 % SDS (*26, 28*). Following purification, the pH was lowered to 6.5 and single-cysteine mutants were concentrated to

ca. 0.5mM in 0.5mL. The protein was then reduced with 2.5 mM DTT, with gentle agitation at room temperature for 24 hours to ensure complete reduction of any disulfide bonds. An aliquot of the protein was then diluted 100 fold (to a ca. 5 µM final concentration) in reconstitution buffer (40mM HEPES, 150 mM NaCl, 5% SDS, pH 7.5) to a final volume of 0.5 mL. A 10 mM stock of Alexa Fluor 488 C5 maleimide or of Alexa Fluor 546 C5 maleimide was prepared by solubilizing the powder in DMSO as instructed by Invitrogen. Alexa fluorophores were individually added to the 5 µM C99 sample by adding 10 µL of the stock solution, resulting in a final fluorophore concentration of 1mM. The sample was then covered with argon, sealed with parafilm, wrapped in aluminum foil, and gently tumbled overnight. Labeled samples were then reconstituted into proteoliposomes.

Reconstitution of Alexa-Modified C99 into Unilamellar Vesicles

The protocol for reconstitution of C99 into unilamellar vesicles (for use in preparing GUVs, see next section) was adopted from P. Bassereau's method (*321*). Dehydrated lipid films, which included fluorescent lipid probes (less than 1 mol%) and coprostanol (when appropriate), were formed in glass culture tubes 24 hours prior to reconstitution. Lipids in chloroform were then added to the glass culture tubes at the desired molar ratios and vortexed under a stream of nitrogen until all chloroform was removed (approximately 2-3 minutes), which resulted in the formation of a lipid film. The glass culture tube was them further dehydrated overnight in the dark in a glass desiccator under a constant vacuum (~60 torr) to ensure the evaporation of any residual chloroform. The lipid film was then rehydrated by adding reconstitution buffer (RB) to a final volume the same as the amount of chloroform initially used. After addition of the RB, the sample was vortexed for 10 minutes to ensure formation of a mixed micellar solution. After vortexing, Alexa-modified C99 (in 1x RB with 5% SDS) was added to the

mixed micelle solution to a final lipid to protein ratio of 400:1. The Alexa-modified C99/mixed micelle solution was then covered with argon, sealed with parafilm, wrapped in aluminum foil, and allowed to gently tumble at room temperature for at least 30 minutes in a 15 mL Falcon tube. 160 mg of wet, pre-washed SM-2 adsorbent BioBeads from BioRad were then added per 500 µL of sample. (BioBeads were pre-washed with at least 20 mL of 40 mM HEPES, 150 mM NaCl, pH 7.5 buffer.) The sample was then covered with argon gas, sealed with Parafilm, wrapped in aluminum foil, and allowed to gently tumble overnight. The following morning, the solution was transferred into dialysis tubing (Spectra/Por 2, 6.4 mm flat width, molecular weight cut-off of 12-14 kDa) and then dialyzed versus 4L of dialysis buffer (10 mM HEPES, pH 7.5) in the dark. The samples were then allowed to dialyze for 3 days, with daily changes of the dialysis bath. Once dialysis was complete, samples were stored in an Eppendorf tube, covered with argon, sealed with Parafilm, and wrapped in aluminum foil.

Formation of Giant Unilamellar Vesicles (GUVs)

Lipid and fluorescent lipophilic tracer chloroform stocks were removed from storage at -20ºC and warmed to room temperature. Fluorescent lipophilic tracers were protected from exposure to light. While the stocks were warming, indium tin oxide (ITO) covered glass cover slips were cleaned using water and 70% ethanol and then dried with Kimwipes. Slides were placed on a 55ºC hot plate to finalize drying. For each sample, the required volumes of lipid chloroform stocks were mixed with 160µL of chloroform to form a final lipid weight of 0.35 mg. Three ternary lipid mixtures were used for these studies: 8:1:1 POPC/SM/Chol (disordered L_d phase only, no phase separation), 2:1:1 POPC/SM/Chol, (small punctate liquid ordered L_o domains and large continuous disordered L_d domains), and 1:2:2 POPC/SM/Chol (large continuous L_o domains and small punctate L_d domains). These ratios were based on recently published phase

diagrams the for ternary mixture of POPC/PSM/Chol(*322-324*). Lipophilic tracers were added to a total molar concentration of less than 1 mol%. For coprostanol containing samples, quaternary mixtures of lipids were made in the same fashion by adding appropriate volumes of coprostanol stock. Lipids in chloroform were mixed using a Hamilton syringe. To create the lipid film on the indium tin oxide (ITO) slide, 80 µl of the lipid mixture was added to the ITO slide and, using a glass Pasteur pipette, was gently drawn back and forth, allowing for chloroform evaporation and the formation of a dry lipid film. Samples were placed in the desiccator with a vacuum pressure of ~60-70 mm torr overnight in the dark. After all residual chloroform was removed, the ITO slides were prepared for GUV formation via electroswelling (*325, 326*). If C99 was being incorporated into the GUV, C99-containing unilamellar vesicles (prepared as described in the preceding section) were placed on the ITO slide in 2µL droplets (approximately 6-8 drops per slide). After all droplets had been deposited, the slides were returned to the vacuum-connected desiccator for 15 minutes to allow the water from the vesicle solutions to evaporate. Once all liquids were evaporated from the ITO slides, a rubber O-ring with a diameter of approximately 4 cm was placed directly over the dry lipid film. For support, 4 small O-rings (approximately 1 cm in diameter) were placed in the four corners around the center O-ring. 500 µL of an electroformation solution of 100 mM sucrose was added to the large O-ring, followed by the sandwiching of another ITO slide (lipid film down) on top, creating an electroformation chamber. Care was taken to ensure that no air bubbles were present in the chamber. The chamber was sealed by placing two small binder clips on either side of the large O-ring. The ITO slide was then attached to two aluminum bus bars, with the lipid film side facing the aluminum bar using a binder clip. The electroformation assembly was then attached to a form generator and placed in a 50 °C incubator. The form generator emanates a sinusoidal shaped wave with a frequency of 10 Hz and 1 volt. This leads to formation of GUVs in the 500 µL

sucrose solution. The electroformation procedure was performed for 1-2 hours. In addition to the electroformation assembly, a 50ml Falcon tube containing 10-40 mL of 100 mM glucose was placed in the incubator during electroformation. It was important to keep the 100 mM glucose solution at the same temperature as the forming GUVs, as temperature differences could disrupt GUV formation later in the procedure. Following electroformation, 3 ml of the 100mM glucose was added to a glass culture tube. The 500 µL100 mM sucrose GUV solution was added to the 3 ml 100 mM glucose buffer and allowed to cool and settle for 20 minutes. The difference in the density of the sucrose solution within the GUV and the glucose solution outside the GUV results in a density gradient, which effectively concentrates the vesicles. A 15 µL aliquot was then taken and placed in the middle of a square glass cover slip. A second cover slip was placed on top and the chamber was sealed with vacuum grease in order to create an imaging chamber for confocal microscopy.

Confocal Imaging

All fluorescence microscopy images were taken on a Zeiss 510 Laser Scanning Confocal Microscope (Carl Zeiss MicroImaging, Inc., Thornwood, NY) using a 40x 1.4 NA Zeiss Plan-Neofluar objective with the confocal pinhole open. Fluorophores were excited using the 488 nm line of a 40mW Argon laser and a 543 HeNe lasers. Fluorescence emission was detected using filter sets provided by the manufacturer. All GUV images were obtained at room temperature. Images were processed using the ImageJ software package (*327*).If needed, contrast and brightness were enhanced using a linear histogram stretch. All images were then filtered using a Gaussian blur with a sigma value of 2 µM (scaled units). GUVs containing both fluorophores (either Rho-PE and DiOC18, Rho-PE and C99-Alexa488, or DiOC18 and C99-Alexa546) were selected for imaging. Imaging was carried out by first collecting a whole field, low zoom image

showing multiple GUVs. Then, individual GUVs were imaged with higher zoom for analysis. Multiple independent proteoliposome preparations were used for experiments with both WT and most mutant forms of C99 to ensure reproducibility.

For quantification of the partitioning of C99 between L_d and L_o phases, both in the absence and presence of coprostanol, we compared the total pixel intensity from C99 fluorescence in a fixed area of the L_d phase to the total pixel intensity from an identical area from the raft phase L_o. Pixel intensities both inside and out of raft domains were determined using imageJ software with a square region of interest (ROI) of 2.5 μM^2. Both intensities were corrected for background C99 fluorescence that was observed within the GUVs. Background intensity values were determined for each individual GUV used during quantification. The fluorescent intensity from the inside of each GUV (using the same ROI as above) was determined by examining an image showing the equatorial cross section of that GUV. This intensity value accounts for any fluorescence derived from C99 that was trapped inside the GUV during electroformation as SUVs. The background intensity value was then subtracted from both the L_o and L_d phases to generate background normalized intensity values. The corrected intensity values are proportional to the concentration of C99 present in each phase. We believe this interior population of C99 is in the form of smaller vesicles trapped inside the GUVs (rather than being fused with the GUVs) during the electroformation process (above section). The ratio of the intensity measured in the L_o phase to the intensity measured in the L_d phase gives the concentration ratio for C99 between these two phases (the partition coefficient). Values reported were obtained by averaging multiple GUVs over multiple proteoliposome preparations, accounting for the variability seen between different experimental preparations. Statistical analysis was performed using Prism software by using a one way ANOVA with Newman Keuls post-analysis during the comparison between WT C99 partitioning in the absence and presence of coprostanol.

144

Summaries of the various GUV experiments conducted in this study are given in Tables 2 and 3.

Table 2

Quantification of C99 Partitioning in GUVs with Varying Lipid Compositions

Form of C99	Lipid Composition	% GUVs Showing Phase Separation	% GUVs Containing C99	% GUVs Showing Phase Separation and Containing C99	% GUVs Containing C99, Showing Phase Separation, and That Show Preferred Partitioning of C99 to L_o Phase
	8:1:1 POPC/SM/Chol				
WT C99		0% (As Expected)	83%	0% (As Expected)	0% (NV=10) (As Expected)
G704A Cholesterol KO		0% (As Expected)	100%	0% (As Expected)	0% (NV=4) (As Expected)
E693A Cholesterol KO		0% (As Expected)	80%	0% (As Expected)	0% (NV=4) (As Expected)
G696A WT-Like		0% (As Expected)	83%	0% (As Expected)	0% (NV=5) (As Expected)
	2:1:1 POPC/SM/Chol				
WT C99		97 ± 3% (NP=6)	51 ± 17% (NP=6)	51 ± 17% (NP=6)	70 ± 4% (NP=6, NV=128)
G704A Cholesterol KO		88 ± 15% (NP=2)	67 ± 15% (NP=2)	67 ± 15% (NP=2)	0% (NP=2, NV=12)
E693A Cholesterol KO		100%	43%	43%	0% (NV=6)
G696A WT-Like		91%	91%	91%	80% (NV=10)
	1:2:2 POPC/SM/Chol				
WT C99		95 ± 6% (NP=2)	89 ± 15% (NP=2)	89 ± 15% (NP=2)	81 ± 27% (NP=2, NV=26)
G704A Cholesterol KO		95 ± 7% (NP=3)	86 ± 20% (NP=3)	86 ± 20% (NP=3)	0% (NP=3, NV=45)
E693A Cholesterol KO		75	75%	75%	0% (NV=13)
G696A WT-Like		100%	90%	90%	78% (NV=9)
	2:1:1 DOPC/DSPC/Chol				
WT C99		96 ± 5% (NP=2)	71 ± 15% (NP=2)	71 ± 15% (NP=2)	67 ± 7% (NP=2, NV=40)

KO= Knock Out
WT= Wild Type
NP= Number of Proteoliposome Preparations
NV= Number of Vesicles Analyzed

Table 3

Quantification of C99 Partitioning in GUVs with Varying Amounts of Coprostanol

Form of C99	Lipid Composition	% GUVs Showing Phase Separation	% GUVs Containing C99	% GUVs Showing Phase Separation and Containing C99	% GUVs Containing C99, Showing Phase Separation, and That Show Preferred Partitioning of C99 to L_o Phase	Partition Coefficient $[C99]L_o/[C99]L_d$
WT C99	2:1:1 POPC/SM/Chol 0% Coprostanol	97 ± 3% (NP=6)	51 ± 17% (NP=6)	51 ± 17% (NP=6)	70 ± 4% (NP=6, NV=128)	15 ± 5.5 (NV=14)
WT C99	50/25/22.5/2.5% POPC/SM/Chol/Coprostanol	87 ± 3% (NP=3)	23 ± 7% (NP=3)	21 ± 7% (NP=3)	46 ±12% (NP=3, NV=58)	7 ± 2 (NV=19)
WT C99	50/25/20/5 % POPC/SM/Chol/Coprostanol	80 ± 0.7% (NP=2)	43 ± 12% (NP=2)	36 ± 11% (NP=2)	23 ± 5% (NP=2, NV=72)	2.5 ± 0.37 (NV=16)
WT C99	55/25/20% POPC/SM/Chol 0% Coprostanol	85 ± 5% (NP=2)	72 ± 32% (NP=2)	66 ± 24% (NP=2)	42 ±17% (NP=2, NV=64)	17 ± 6 (NV=17)

NP= Number of Proteoliposome Preparations
NV= Number of Vesicles Analyzed

Determination of Kd for Binding of Coprostanol to C99 in Bicelles

900 MHz solution NMR spectroscopy was used to monitor binding of coprostanol to uniformly ^{15}N-labeled C99 (0.2 mM) in DHPC-DMPC bicelles (20% w/v DHPC+DMPC, DMPC:DHPC = 1:3). Coprostanol-containing samples (titration points) were prepared using the exact same methods as used to prepare samples for cholesterol titration of C99 in previous work (*26*). As in previous work, titrations were monitored by collecting a 2-D ^{1}H,[15]N-TROSY spectrum for each titration point. Coprostanol-dependent chemical shifts were then plotted as a function of the concentration of coprostanol and fit by the model for 1:1 ligand-protein complex formation using ORIGIN 8.0 (OriginLab Corp., Northampton, MA) software in order to determine the K_d for 1:1 complex formation between C99 and coprostanol (see Fig. 4.5).

Results

C99 can Specifically Bind Cholesterol in Bicelles

During structure determination of C99, it was found that the N-helix/N-loop/TMD formed a putative ligand binding pocket (*26*). Previous studies suggested that this region of C99 could specifically bind the soluble cholesterol analogue β-Cholbimalt and potentially native cholesterol (*28*). Titrations of C99 with cholesterol were carried out using bicelles as the model membranes because this medium is able to solubilize cholesterol up to ~20 mol%. Cholesterol titration of C99 results in substantial changes in NMR resonance positions for a subset of C99 peaks (Fig 4.3A). The shifts in these peaks saturate at high cholesterol concentrations and can be fit by a 1:1 binding model, indicating a K_d of 5.1 ± 1.2 mol% (Fig 4.3B). This falls within the range of cholesterol concentrations in mammalian plasma and organelle membranes (*328*), supporting the physiological relevance of this complex. Full-length APP is likely to bind cholesterol with an avidity similar to C99 because its ectodomain is expected to have no influence on the architecture of the cholesterol binding site.

The resonances in C99 exhibiting the most profound chemical shifts in response to cholesterol are all localized to the N-helix, N-loop, and extracellular end of the TMD and include G700, G704, and G708 (Fig 4.3C). To identify residues critical to cholesterol binding, we employed alanine scanning mutagenesis to replace each residue in the 690-710 range, followed by cholesterol titrations (Fig 4.3, D and E, and figs 4.1 and 4.2). Mutations at some sites eliminated detectable cholesterol binding, even at 20 mol% cholesterol (Fig 4.3E). The cholesterol binding site of C99 involves residues from the N-helix, N-loop, and TMD and is different from previously characterized cholesterol binding sites in proteins (*329*). Based on Fig 4.3C, it is likely that N698 donates a hydrogen bond to the hydroxyl head group of cholesterol, whereas E693 accepts a

hydrogen bond. Also essential to cholesterol binding are G700 and G704, located in tandem GxxxG motifs of the TMD and, to a less degree, G708. GxxxG motifs and the related GxxxGxxxG glycine zipper sequence have long been recognized as common structural elements that can drive homo- and hetero-oligomerization of membrane proteins (*330-332*). Though there has been much interest in the possibility that these motifs drive homodimerization of C99 (*14-16, 332, 333*), our observation that the GxxxG motifs are critical for cholesterol binding indicates an additional, and novel, role for these motifs in C99.
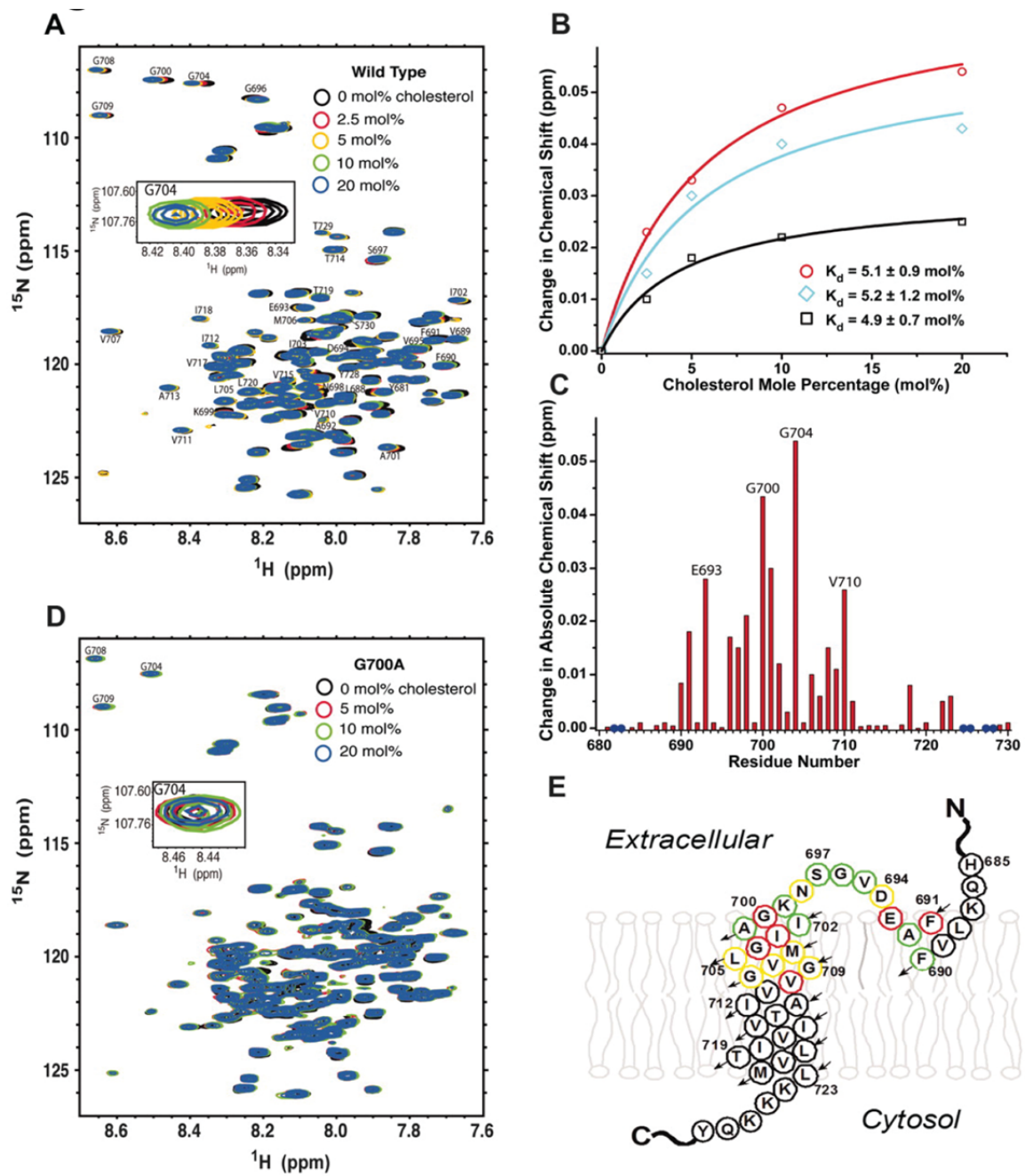
Figure 4.3. Cholesterol binding to C99 in bicelles. (A) Cholesterol titration of U-^{15}N-C99 in DHPC-DMPC bicelles, as monitored by ^{1}H, ^{15}N-TROSY NMR. Cholesterol was varied from 0 to 20 mol% (relative to total moles of lipid). **(B)** Changes in amide ^{1}H NMR chemical shifts for E693 (black), G700 (light blue), and G704 (red) in response to cholesterol titration of wild-type C99. Also shown are the fits of a 1:1 binding model to each data set, with resulting K_d values for complex formation indicated as well. Units of mole percent are appropriate to describe the binding of two molecules that are both associated with model membranes {mole percent = [moles cholesterol/(moles DMPC + moles cholesterol)] X 100}. **(C)** Changes in ^{1}H NMR chemical shifts for wild-type C99 in response to the addition of cholesterol to 20 mol% concentration. Results are shown for residues at or near the cholesterol binding site. **(D)** Titration of the G700A mutant form of C99 with cholesterol. (Data for other C99 mutants shown in figure 4.2). **(E)** Results of Ala-scanning mutagenesis. Residue color indicates the impact on cholesterol binding of substituting each position in the 690 to 710 range, as assessed by NMR. Red indicates that mutation to Ala for that site eliminates binding, yellow indicates significantly attenuated binding, and green indicates that mutation results in little change in cholesterol binding affinity.

C99 can Specifically Bind Coprostanol in Bicelles

The discovery that C99 can specifically bind cholesterol suggests that it may also bind various cholesterol analogues or sterols with different phase partitioning properties. Drawing on a body of previous work on the phase partitioning of cholesterol metabolites and analogs (*334-336*) we sought a compound that would compete with cholesterol for binding to C99 without promoting L$_o$ phase partitioning. This led us to investigate coprostanol, a compound that is chemically identical to cholesterol except that the C5-C6 double bond has been stereospecifically reduced (fig 4.4).
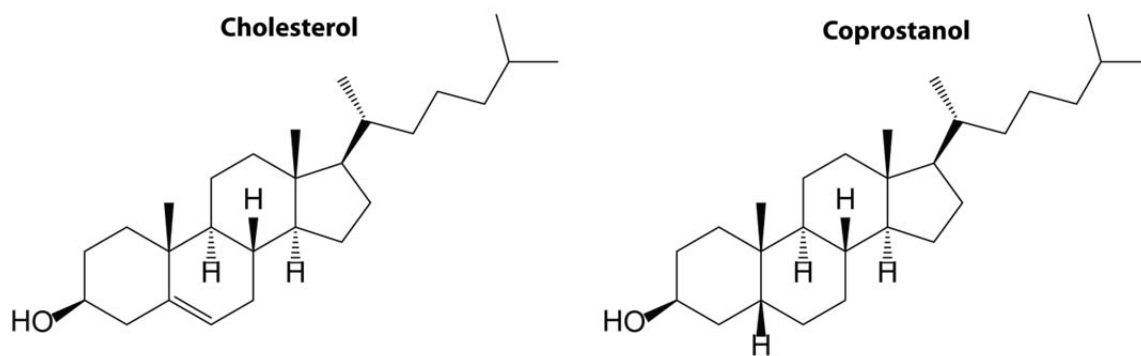
Figure 4.4. Chemical structures of cholesterol and coprostanol.

This sterol has a distinct preference for the fluid phase relative to L$_o$ (*334-336*). We first tested binding of coprostanol to C99 in bicelles using NMR spectroscopy (Fig. 4.5) and found that it binds to C99 with the same affinity (4.5 ± 0.6 mol%) as cholesterol (5.1 ± 1.2 mol%) under identical conditions (*26*).
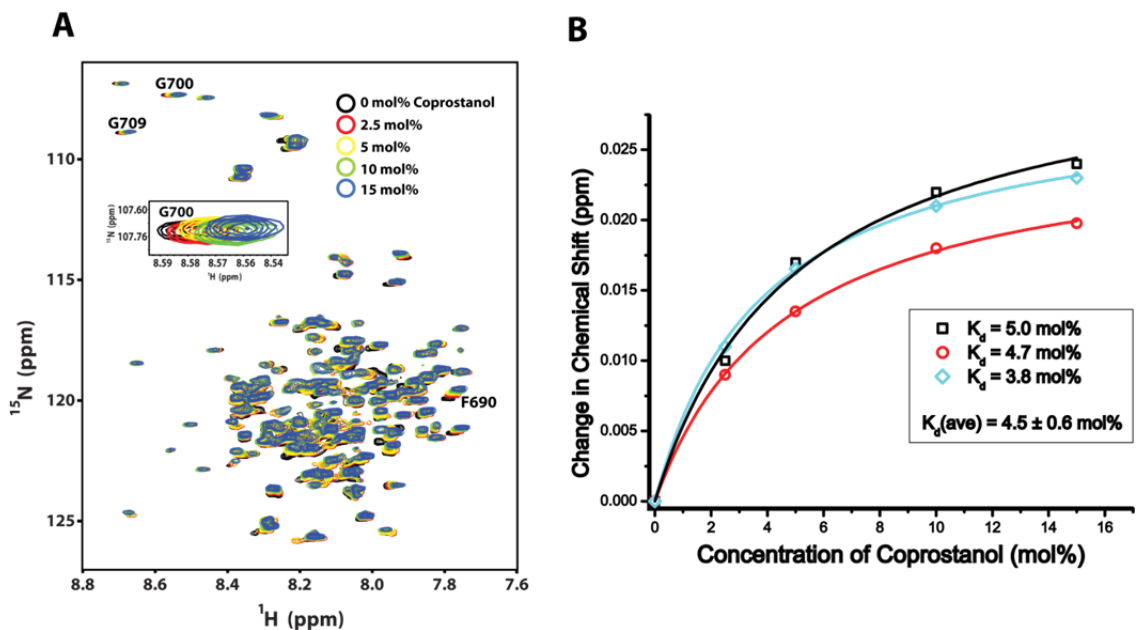
Figure 4.5. Binding of coprostanol to C99 in bicelles. (A) An overlay of five ^{1}H,^{15}N-TROSY NMR spectra from titration samples with increasing coprostanol (from 0 mol% to 15 mol%). The inset highlights the resonance from G700, which showed significant changes in chemical shift in response to coprostanol. (B) Changes in backbone amide ^{1}H NMR chemical shifts for G700 (black), G709 (cyan), and F690 (red) in response to coprostanol titration of WT C99. Also shown are fits of the 1:1 binding model to each data set along with the determined K_d values for complex formation. Note that units of mole percent are appropriate to describe the binding of two molecules that are both associated with model membranes, where mole percent= [mol cholesterol/(mol DMPC + mol cholesterol)] x 100.

The C99 backbone amide ^{1}H-^{15}N peaks that were most responsive to coprostanol binding largely overlap with peaks previously seen to shift the most in response to cholesterol, indicating that both sterols bind to essentially the same site on C99 (fig. 4.6). However, the directions and magnitudes of the induced shifts in peak positions seen for coprostanol are in some case significantly different than those observed for cholesterol (fig. 4.6). Of particular note is the difference in the induced chemical shift changes in the resonance from Gly709, a site located in the flexible hinge contained within the C99 TMD. This result suggests that these sterols induce distinct changes in the structure of C99 that may alter the end to end distance and dynamics of its TMD.

152
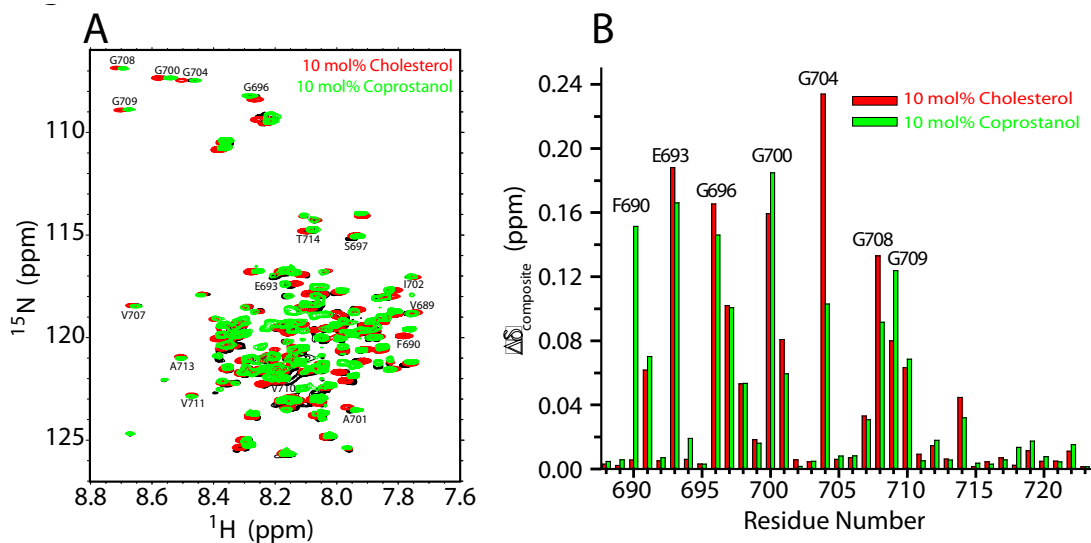
Figure 4.6. Changes in the NMR spectrum of C99 in response to cholesterol and coprostanol. (A) Comparison of the ^{1}H,^{15}N-TROSY NMR spectra of C99 in DHPC-DMPC bicelles in the presence of 10 mol% coprostanol (green) and 10 mol% cholesterol (red). The black reference spectrum for C99 in the absence of either cholesterol or coprostanol. The red and black spectra were collected at 900 and 600 MHz, respectively, and have been reported in previous work (*26*), while the green (coprostanol) spectrum was collected for this study at 900 MHz. Note that 10 mol% coprostanol and 10 mol% cholesterol are both 2X higher concentrations than their respective measured K_d for binding to C99 under the conditions of these experiment. (B) Changes in the composite chemical shift (relative to ligand-free conditions) induced by 10 mol% cholesterol vs. changes induced by coprostanol. The composite chemical shift assesses the magnitude of ligand-induced peak shift in both dimensions (corrected for the 10-fold difference in resonance frequencies for ^{1}H vs. ^{15}N) as described:

$$\Delta\delta_{composite} = [\text{(induced change in } ^1\text{H shift)}^2 + (0.1 * \text{induced change in } ^{15}\text{N shift})^2]^{1/2}$$

C99 Partitions to Cholesterol Rich Domains in GUVs

The phase partitioning of C99 in giant unilamellar vesicles (GUVs) containing coexisting liquid-ordered (L_o) and fluid (L_d) phase membrane domains was visualized using fluorescent microscopy(*337*). GUVs were prepared (*338*) using a 2:1:1 ternary mixture of 1-palmitoyl-2-oleoyl-phosphatidylcholine (POPC), palmitoyl-sphingomyelin (SM), and cholesterol that forms membranes with separated L_d and L_o phase domains

(*339-341*). The total cholesterol concentration in these vesicles was 25 mol%, well within the range of cholesterol levels of mammalian plasma membranes (*342-345*). Phase separation was verified by imaging GUVs doped with L_d-specific and L_o-specific fluorescent marker lipids. L_o domains appear as mobile, round, and smooth-edged domains within the surrounding L_d membrane (Fig. 4.7A and fig. 4.8A). Alexa488-tagged C99 was reconstituted into these mixed phase GUVs at a 1:400 protein:lipid molar ratio, a concentration at which C99 is known to be monomeric (*346*). While the presence of some degree of heterogeneity in the composition of the GUVs is typical for phase-separated ternary lipid mixtures (*347*), C99 was seen to strongly partition into the L_o domains in most of the vesicles (Fig. 4.7B and table 2). Within these vesicles the measured ratio of concentrations of C99 in the L_o phase relative to the L_d phase was 15 ± 5.5. Efficient partitioning of C99 to the L_o phase was also observed in GUVs composed of 1:2:2 POPC:SM:cholesterol, in which phase separation of a reciprocal nature occurs in which the L_d phase forms punctate domains that are surrounded by a continuous L_o phase (fig. 4.8B).
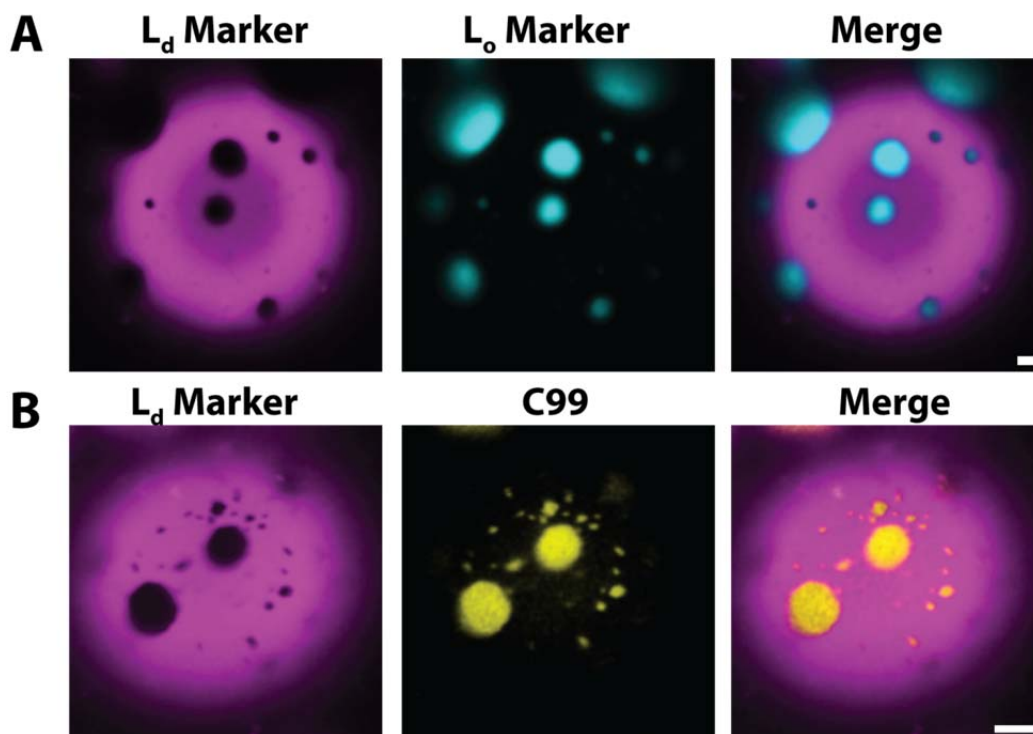
Figure 4.7. C99 is strongly enriched in raft-like L$_o$ domains of GUVs containing co-existing L$_d$ and L$_o$ domains. (A) GUVs composed of a 2:1:1 molar ratio of POPC/SM/cholesterol were doped with tracer amounts of the L$_d$ phase marker rhodamine-phosphoethanolamine (Rho-PE, magenta) and the L$_o$ phase marker DiOC18 (cyan). (B) C99 labeled with Alexa488 (yellow) at site F675C was incorporated into GUVs composed of a 2:1:1 molar ratio of POPC/SM/cholesterol. L$_d$ domains were labeled with Rho-PE (magenta). Scale bars, 5 microns.

In control experiments partitioning of C99 to the L$_o$ domains was seen to be independent both of the fluorescent lipid probes used to mark the L$_d$ and L$_o$ domains (fig. 4.9A) and also of the site of fluorophore attachment to the protein (fig. 4.9B). Moreover, in other control experiments C99 was seen to be uniformly distributed in GUVs containing only a uniform L$_d$ phase (fig. 4.8B), indicating that C99 does not itself trigger phase separation.

A

	L_d Marker	L_o Marker	Merge
8:1:1 POPC/SM/Chol			
1:2:2 POPC/SM/Chol			

B

	L_d Marker	C99	Merge
8:1:1 POPC/SM/Chol			
1:2:2 POPC/SM/Chol			

156
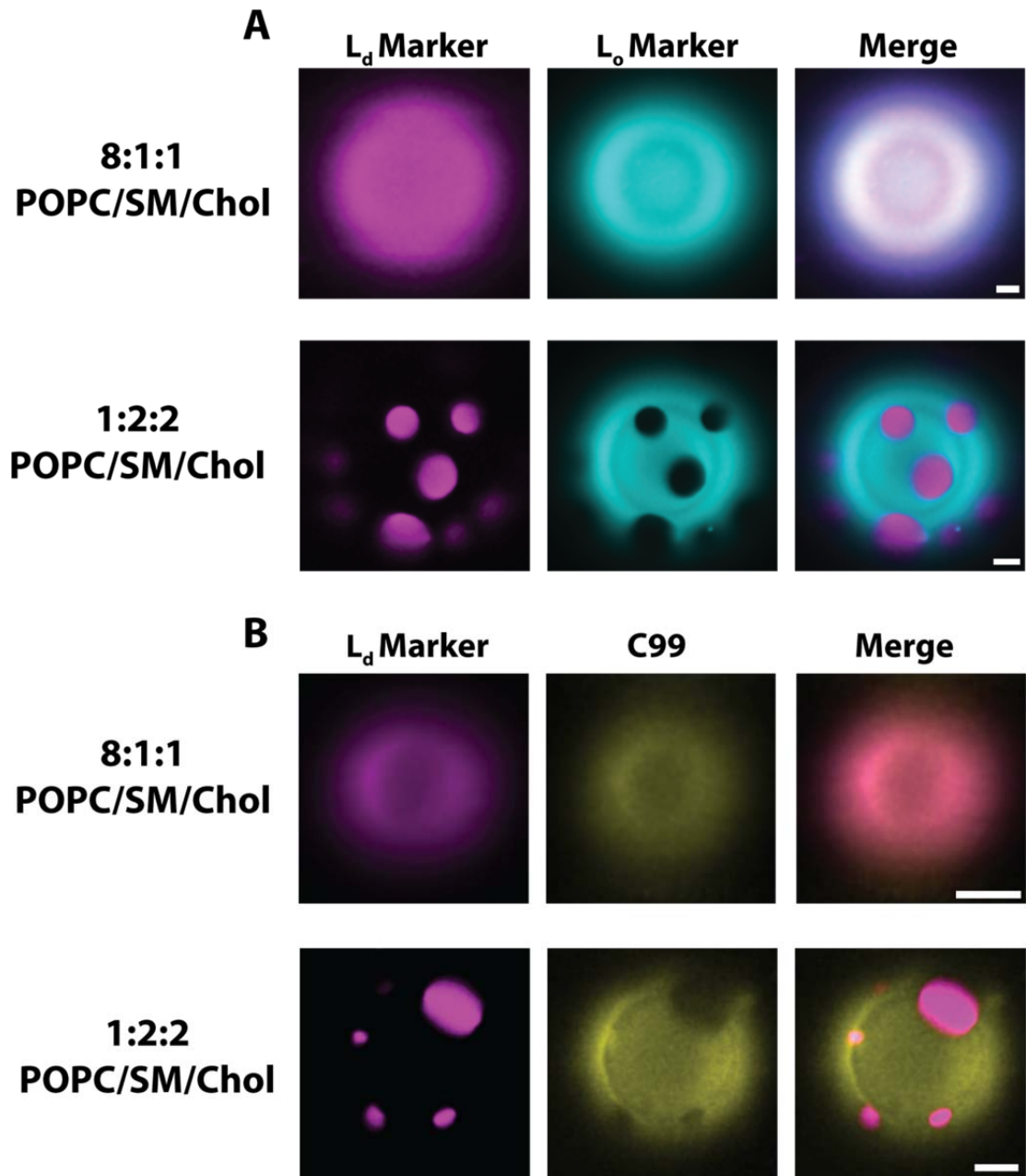
Figure 4.8. Partitioning of lipids and C99 in GUVs of varying lipid and C99 compositions. (A) Protein-free GUVs comprised of 8:1:1 POPC/SM/Chol show no visible phase separation of the disordered phase marker Rho-PE (magenta) and L_o phase marker DiOC18 (cyan), indicating that this mixture generates a uniform disordered L_d phase, as expected (*322-324*). (B) Protein-Free GUVs consisting of 1:2:2 POPC/SM/Chol contain co-existing L_d (marked with Rho-PE, magenta) and L_o (marked with DiOC18, cyan) phases. *Note that this mixture was dominated by a continuous L_o phase, with punctuate disordered L_d domains. (Inverse of the case for the 2:1:1 mixture of Fig. 4.7).* The merged images show both fluorophores. (C, D) Observation of Alexa 488-labeled C99 (yellow) in GUVs comprised of 8:1:1 (C) or 1:2:2 POPC/SM/Cholesterol (D). In both cases disordered domains are labeled with Rho-PE (magenta). In all cases C99 was fluorescently labeled with Alexa 488 (yellow) at F675C. *Note that the mixture in panel D was dominated by a continuous L_o phase, with punctuate disordered L_d domains.* Scale bars, 5 microns.

Preferred partitioning into L_o domains was also observed for C99 using vesicles composed of 2:1:1 DOPC/DSPC/cholesterol (fig. 4.9C and table 2), indicating that the domain preference of the protein does not require the presence of sphingomyelin. Collectively, these results indicate that C99 has an intrinsic and pronounced preference for raft-like L_o phases in model membranes and that this phenomenon does not require other protein co-factors or posttranslational modifications such as palmitoylation (*348*).

A

| L_o Marker | C99 | Merge |

2:1:1
POPC/SM/Chol

B

| L_d Marker | C99 | Merge |

2:1:1
POPC/SM/Chol
F675C-Alexa488

2:1:1
POPC/SM/Chol
H732C-Alexa488

C

| L_d Marker | C99 | Merge |

2:1:1
DOPC/DSPC/Chol
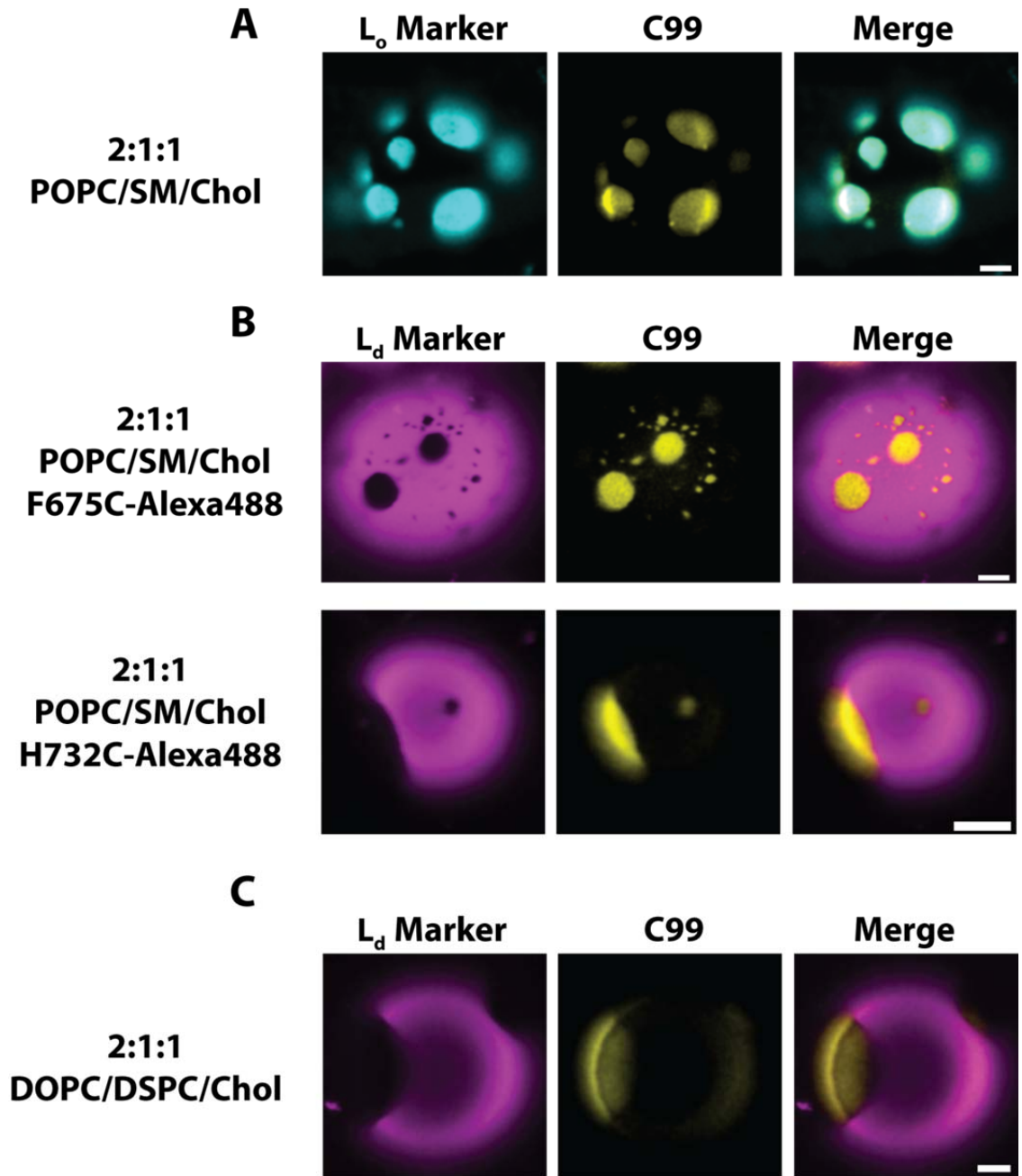
Figure 4.9. **Control experiments demonstrate that the localization of C99 to L_o domains is independent of the fluorophores used to label the protein, the position of the dye on the protein, the lipophilic dye used to highlight the L_o/L_d domains, or of the presence of SM and POPC. Experiments were performed to show that only cholesterol binding, and not the presence of other lipids or the fluorophores used, drive C99 partitioning to L_o domains. (A) Alexa546-labeled C99 (yellow) was incorporated into GUVs comprised of 2:1:1 POPC/SM/cholesterol. DiOC18 was used to label L_o domains (cyan). C99 was labeled at position F675C. C99 co-localizes with DiOC18 in L_o (raft-like) domains.** *These studies show that C99 partitioning into Lo domains is independent of both the fluorescent dye used to label C99 and the lipophilic marker of lipid domains.* **(B) Alexa 488-labeled C99 (yellow) was incorporated into GUVs comprised of 2:1:1 POPC/SM/cholesterol. In the top panel, C99 was labeled at mutation site F675C and in the bottom panel C99 was labeled at mutation site H732C. L_d domains were marked with Rho-PE (magenta). C99 partitions to L_o (raft-like) domains in both cases.** *These studies show that our choice of sites for mutation to cysteine and subsequent fluorescent labeling did not impact C99 partitioning.* **(C) Alexa 488-C99 (yellow) was incorporated into GUVs comprised of 2:1:1 DOPC/DSPC/cholesterol. As with the 2:1:1 POPC/SM/Cholesterol mixture, the 2:1:1 DOPC/DSPC/cholesterol lipid mixtures also exhibit the presence of coexisting L_d and L_o domains (*349*). L_d domains were marked with Rho-PE. C99 was labeled at position F675C. As for the case of GUVs prepared from POPC/SM/cholesterol, C99 partitions to Lo domains.** *These studies indicate that POPC and SM are not required to support C99 partitioning to L_o domains.* **Scale bars, 5 microns.**

Effects of Mutations on C99 Partitioning

Since C99 has the capacity to directly bind cholesterol, we hypothesized that this interaction may regulate its domain preference. This was tested by experiments using two mutant forms of C99 that do not bind cholesterol (*26*). Alanine substitution of ectoplasmic (E693A) or TMD (G704A) residues critical for cholesterol binding produced a striking shift in the domain preference of C99 towards the L_d phase in phase-separated GUVs (Fig. 4.10 and fig. 4.11). As a control, we also examined the G696A C99 mutant, which involves a site proximal to E693 and G704 but that exhibits wild type-like cholesterol binding (*26*). Consistent with its unaltered cholesterol binding activity, the G696A mutant preferentially partitioned to L_o domains in the same manner as the wild type protein (Fig. 4.9 and fig. 4.11). These results show that the preferential partitioning of C99 into L_o domains is absolutely dependent on retention of an unperturbed cholesterol binding site.
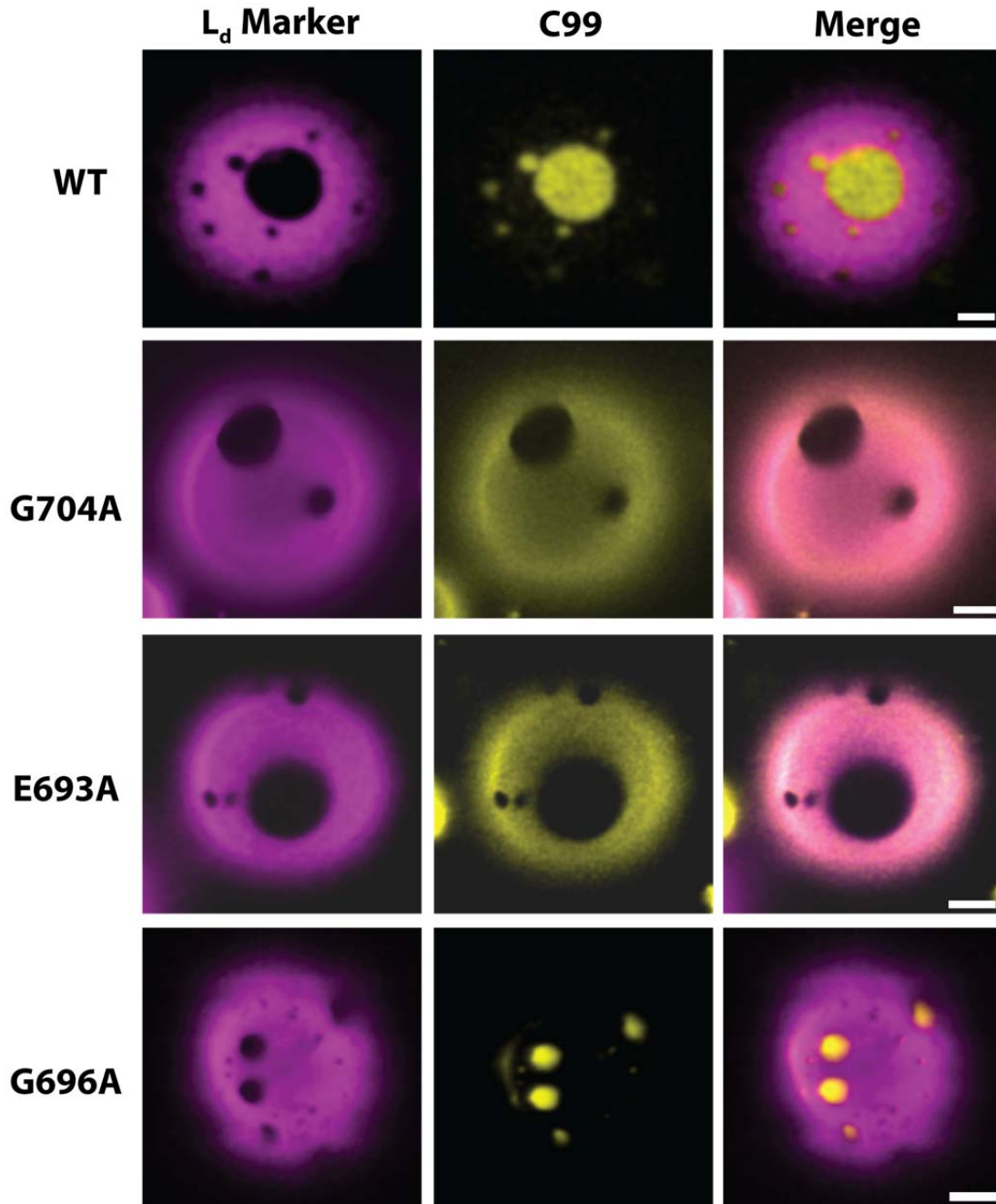
Figure 4.10. Mutations that abolish cholesterol binding to C99 (G704A and E693A) shift partitioning of C99 from L$_o$ domains into L$_d$ domains, whereas a control mutation (G696A) that preserves cholesterol binding has little effect on the partitioning of C99. Wild type or mutant forms of Alexa 488-labeled C99 (yellow) were incorporated into GUVs composed of 2:1:1 POPC/SM/cholesterol containing tracer levels of the L$_d$ domain marker Rho-PE (magenta). Scale bars, 5 microns.
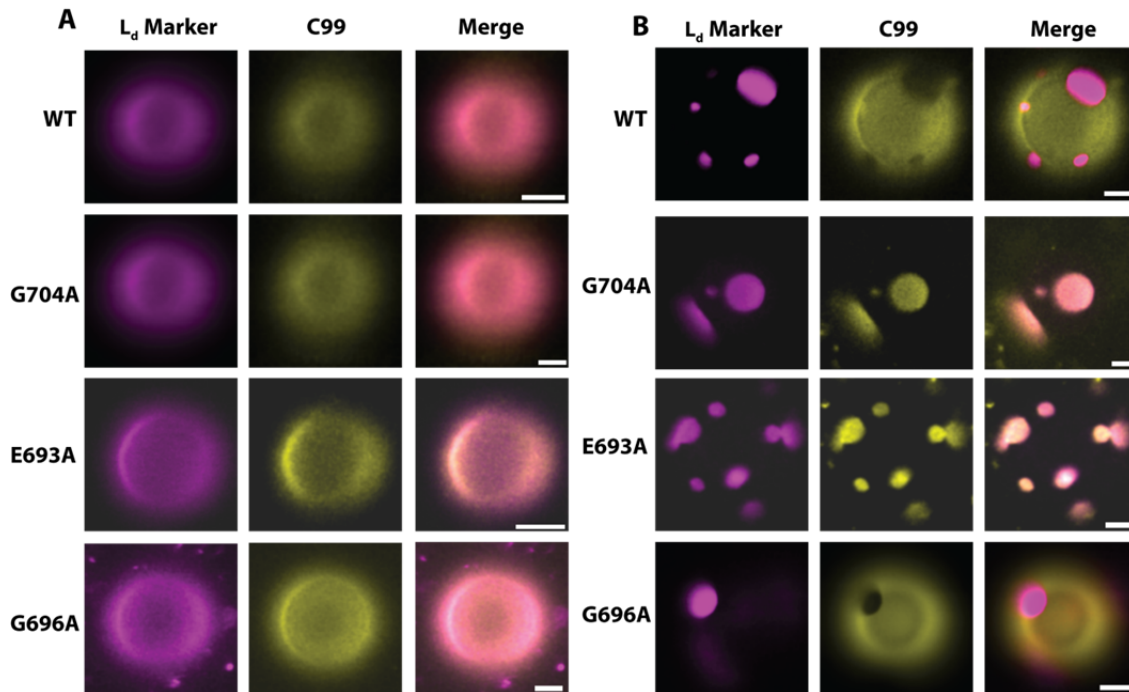
Figure 4.11. Partitioning of fluorescently labeled C99 containing mutations at its cholesterol binding site in GUVs composed of lipid mixtures having varying phase compositions. The 8:1:1 POPC/SM/Cholesterol GUVs do not exhibit visible phase separation (disordered phase only). The 1:2:2 POPC/SM/cholesterol GUV's exhibit phase separation between L_d and L_o domains. At this composition, L_o represents the dominant (continuous) phase and the disordered L_d phase domains now appear as punctae. (A) Distribution of wild type and mutant forms of C99 (yellow) in GUVs comprised of an 8:1:1 POPC/SM/cholesterol mixture. L_d domains were marked with Rho-PE (magenta). C99 and its mutants were labeled with Alexa 488 (yellow) at site F675C. As in Fig. 4.9, phase separation was not observed in these GUVs. The cholesterol binding site mutants G704A or E693A were uniformly distributed on the GUV surface. Similar results were obtained for wild type C99 and the G696A mutant, which binds cholesterol normally. *These results indicate that when no lipid phase separation is present, C99 (with or without an intact cholesterol binding site) is uniformly distributed within the GUVs.* (B) Distribution of wild type and mutant forms of C99 (yellow) in GUVs comprised of a 1:2:2 POPC/SM/cholesterol mixture. L_d domains were marked with Rho-PE (magenta). C99 and its mutants were labeled with Alexa 488 (yellow) at site F675C. At this lipid composition, the GUV surface is dominated by a continuous L_o domain with punctate L_d domains. WT and G696A (which binds cholesterol normally) both localize to the L_o domain*. E693A and G704A (cholesterol binding mutants) do not partition to the L_o domains, indicating that cholesterol binding is essential for C99 partitioning to L_o domains.* Scale bars, 5 microns.

Coprostanol Reduces Partitioning of C99 to Cholesterol Rich Domains

To determine whether coprostanol can compete with cholesterol binding and thereby alter the phase preference of C99, we conducted GUV experiments in which the total sterol concentration (cholesterol+coprostanol) was fixed at 25 mol%. The ratio of cholesterol and coprostanol was then varied by including coprostanol up to 5 mol%, the concentration beyond which phase separation in GUVs is strongly reduced. Upon reconstitution of fluorescently labeled C99 into these GUVs, a coprostanol-dependent reduction in the partitioning of C99 to the L_o domains was observed (Fig. 4.12, fig. 4.13, and table 3). Given that cholesterol and coprostanol bind to the same site on C99 and with similar affinity, the 5-fold reduction in the partitioning coefficient seen at 5 mol% coprostanol and 20 mol% cholesterol relative to coprostanol-free conditions is consistent with the effects of competitive binding between the sterols for C99. Binding of coprostanol to C99 thus reverses the phase preference of this protein compared to the cholesterol-complexed form.
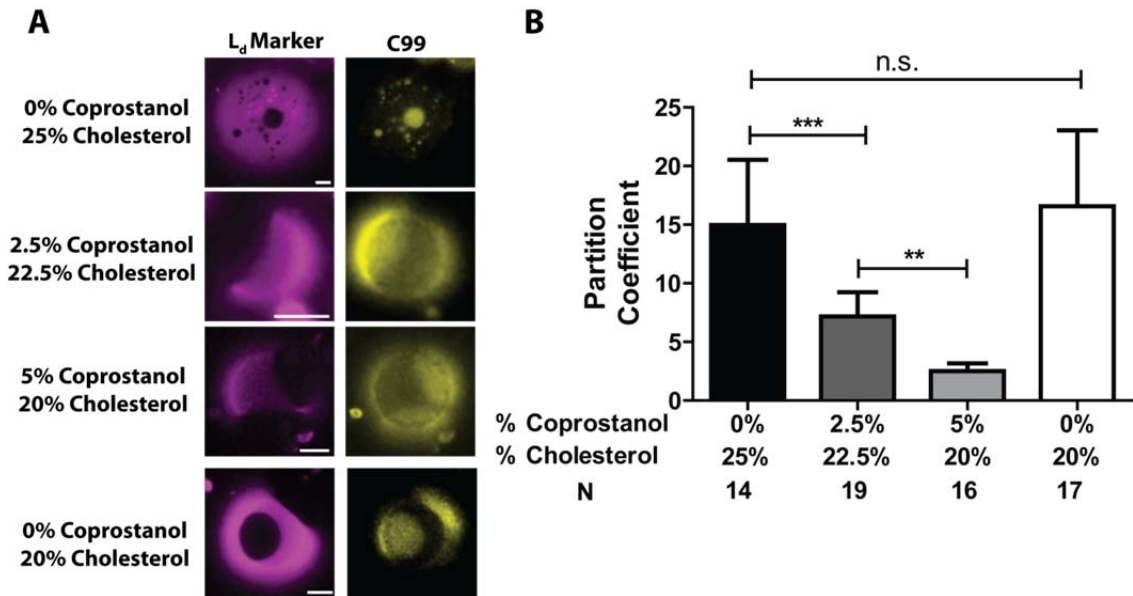
Figure 4.12. Incorporation of coprostanol into cholesterol-containing GUVs induces a shift in localization of C99 away from raft-like L_o phase and into L_d phase domains in a dose-dependent manner. (A) In the top 3 panels, C99 was incorporated into GUVs containing 50 mol% POPC, 25 mol% SM, and the indicated mol% concentrations of cholesterol and coprostanol. The bottom panel represents a control sample in which the cholesterol concentration was 20 mol%, but coprostanol was absent: 55:25:20 mol% POPC/SM/cholesterol. Disordered domains are marked by Rho-PE (magenta). C99 was fluorescently labeled with Alexa488 (yellow) at F675C. Scale bars, 5 microns. (B) Quantification of changes in C99 partitioning to raft-like L_o domains with increasing levels of coprostanol. The partition coefficient is defined as (mol% C99 in the L_o domain)/(mol% C99 in the L_d domain), as determined from multiple GUVs for each of the lipid compositions shown in panel A. The error bars indicated standard deviation, N is the number of GUVs used for quantification, n.s. indicates lack of a statistical variation, and ** and *** indicates that statistical *P* values are less than 0.001 and 0.01, respectively.
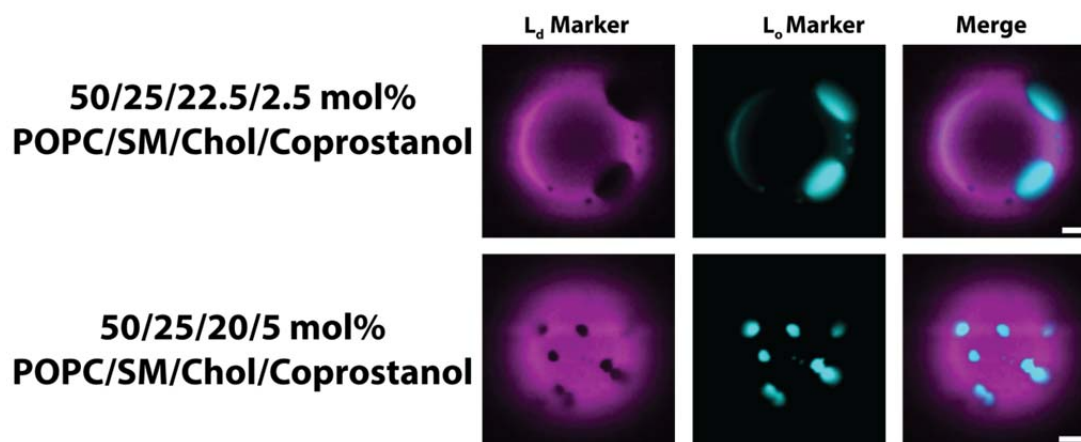
Figure 4.13. **L$_o$ phase separation in POPC/SM/cholesterol lipid mixtures. Disordered L$_d$ domains are marked by the non-raft marker Rho-PE (magenta). L$_o$ domains are highlighted by DiOC18 (cyan). The addition of varying amounts of coprostanol, from 2.5 mol% to 5 mol%, does not impact phase separation or L$_o$ (raft-like) domain formation. Scale bars, 5 microns.**

Discussion

The finding that GxxxG motifs within the TMD of C99 play a crucial role for cholesterol binding elucidates a totally novel mechanism for these motifs, implicating them in more than potentially just protein homo- and hetero-oligomerization. It should be added that the G$_{700}$AIIG$_{704}$ segment of C99 has also been shown to be important in establishing the production ratio between long and short forms of the Aβ polypeptide by γ-Secretase (*14, 15*) and in making that ratio susceptible to alterations by druglike small molecules known as GSMs (*279, 350*).

A space-filling surface representation shows that G700 and G704 are located on the outer face of the curved TM helix and result in that face of the helix having a locally flat surface (Fig 2.7C), which is probably optimal for van der Waals interactions with cholesterol, which itself is relatively flat. Pairing the surface afforded by the GxxxG motifs with a rigid cholesterol molecule is expected to be entropically advantageous compared with association with more flexible lipids.

Binding of cholesterol to C99 appears to rely on the flexibility of the N-loop to allow induced fit conformational changes required to optimize interactions of cholesterol with key residues in this loop and in the N-helix (Fig 4.14). This is supported by observation of a number of N-loop residues for which substantial changes in NMR resonance chemical shifts are observed in response to cholesterol binding (e.g. S697, see fig 4.5D) but do not appear to make direct connects with the lipid (Fig 4.5E).
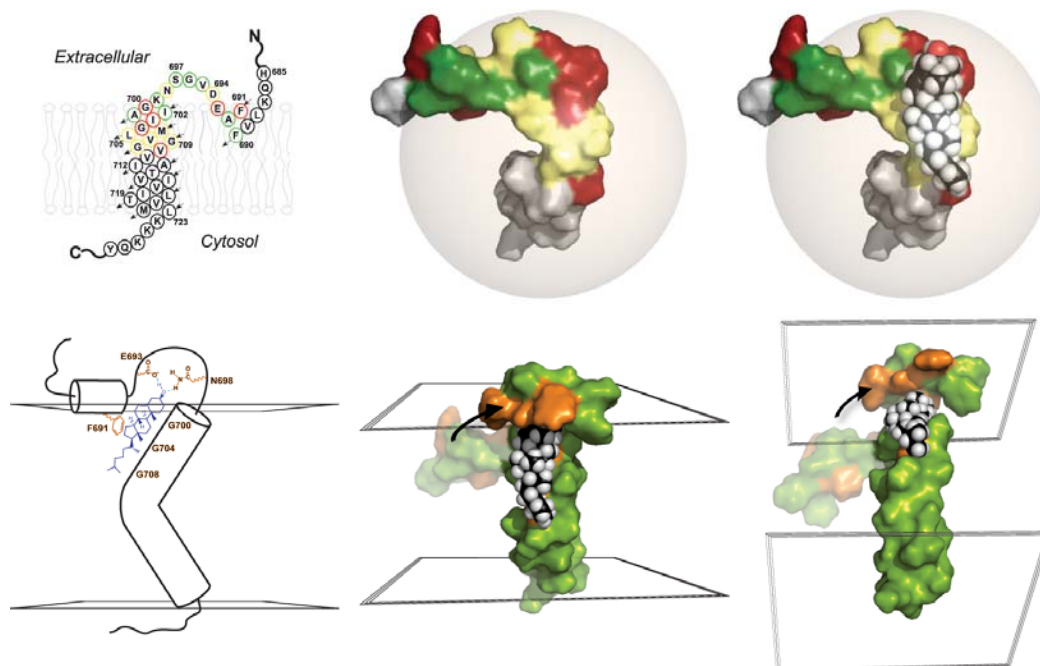
Figure 4.14. In the top panel residues are colored according to the importance of each site in cholesterol binding, as judged by mutation of each site to alanine (from figure 4.3, green: mutation to alanine leads to no change in cholesterol binding affinity; yellow: intermediate change; red: mutation to alanine eliminates detectable cholesterol binding). The conformer of C99 illustrated in the top panel was selected from among the 30 lowest energy conformers from structural determination. In the top right panel, cholesterol has been manually docked against the flat surface of C99's TMD provided by the GxxxGxxxG motif. We speculate that cholesterol initially binds C99 in this mode, followed by a conformational change involving the N-helix and N-loop that lead to the completion of complex formation. The lower left panel is a cartoon illustrating the expected topology of the final complete complex, highlighting important residues involved in binding. The two panels on the lower right illustrate the sort of reorientation the N-helix is expected to undergo during cholesterol binding, indicated by black arrows. This reorientation would be enabled by conformation changes in the N-loop, which is not depicted. The orange sites in the two panels on the lower right highlight F691, E693, D694, N698, G700, G704, and G708; all residues important in cholesterol binding (top left panel).

The literature suggests plausible mechanisms by which complex formation between C99 or APP and cholesterol contributes to amyloidogenesis and AD. First, there are numerous reports that β- and γ-Secretase associate with cholesterol rich membrane domains often referred to as lipid rafts (*119, 310, 351*). Association of C99/APP with cholesterol may favor partitioning of the protein into membrane domain

enriched in the proteases of the amyloidogenic pathway. Secondly, cholesterol binding to C99 may play a cofactor role to promote substrate recognition or catalysis. The addition of cholesterol to purified γ-Secretase in model membranes enhances the cleavage rate of purified C99 in lipid vesicles (*352*). Third, given that the α-Secretase cleavage site (K687) is immediately adjacent to the cholesterol binding site, direct binding of cholesterol to APP could reduce non-amyloidogenic cleavage by α-Secretase (*41, 42*). Finally, the cholesterol binding site in C99 is contained within its amyloid-β domain (C99 residues 672-711 correspond to Aβ40), such that complex formation between cholesterol and Aβ may contribute to known profibrillogenic effects of membrane cholesterol (*131*).

To test the hypothesis that cholesterol binding by C99 favors partitioning of the protein into cholesterol rich domains, we utilized the giant unilamellar vesicle (GUV) system. When incorporated into GUVs containing a 2:1:1 ratio or a 1:2:2 ratio of POPC/SM/Cholesterol, C99 strongly partitioned to the L_o domain, as indicated by the 15 $\pm$ 5.5 fold enrichment of C99 in the L_o phase compared to the L_d phase. We found that this partitioning was contingent solely upon the binding of cholesterol by C99, as mutations that abolished this binding event were the only variable to prevent C99 partitioning to L_o domains.

The finding that C99 preferentially partitions to a high degree into L_o domains is remarkable given that helical transmembrane proteins or peptides studied to date exhibit low partitioning into the cholesterol-enriched, ordered environment characteristic of this phase (*337, 353-357*). This suggests that the transmembrane domain (TMD) of C99 has unique properties that facilitate its efficient targeting into rafts. The simplest explanation for our findings is that direct interaction of C99 with cholesterol drives entry into the cholesterol-enriched L_o phase. However, cholesterol is only moderately enriched in L_o domains relative to co-existing L_d domains (< 3-fold) (*340, 341, 347*). Assuming equally

avid binding of cholesterol to C99 in both phases and a 3-fold enrichment of cholesterol in the L_o domain, the binding energetics can account for a maximum enrichment of C99 in the L_o phase of only 3:1, well below the observed 15-fold concentration difference. Therefore, while cholesterol binding is essential for the L_o phase preference of C99 there must be at least one colluding factor. The most likely possibility is that cholesterol binding to C99 induces a structural change in the protein that results in reduced free energy for the protein-cholesterol complex in the L_o phase relative to the fluid phase. The $^1H,^{15}N$-TROSY NMR spectrum of C99 has been shown to undergo significant changes in response to cholesterol binding (26), consistent with this possibility.

This work confirms the hypothesis that binding of cholesterol to C99 activates partitioning of the protein into raft-like L_o membrane domains. Based on these findings, we hypothesize that cholesterol functions as an important regulator of the partitioning of C99 in intact cells. The plasma and endosomal membranes have sufficient cholesterol contents to constitutively activate raft partitioning of C99 (>15 mol%, which is more than three times the K_d for cholesterol binding to C99 (342-345) (26, 346)). On the other hand, the membranes of the Golgi and endoplasmic reticulum contain levels of cholesterol that vary in the range of the K_d for cholesterol binding (342-345), suggesting that modest changes in cholesterol concentration may dynamically regulate partitioning of C99 between fluid and L_o domains. Given that full length APP contains the same cholesterol binding domain as C99, these observations may also apply to APP, although palmitoylation of APP outside its C99 domain also appears to be important in determining its membrane sorting (358). Our observations shed considerable light on an array of previous data suggesting that amyloidogenic processing of C99 and APP is promoted by elevated cholesterol and is preferentially localized to raft-like L_o membrane domains (359-364), whereas non-amyloidogenic processing is reduced by elevated

cholesterol and is preferentially localized to bulk (fluid phase-like) membranes (*365, 366*).

The observation that competitive binding of coprostanol to the cholesterol binding site of C99 triggers reversal of the protein's phase preference demonstrates the possibility of manipulating the phase partitioning of integral membrane proteins with pharmacological agents. While the affinity of coprostanol for C99 is insufficient for use of this compound under physiological conditions, it may serve as a lead for compounds that target the cholesterol binding site. Importantly, such compounds could potentially serve as Aβ-lowering agents to help prevent or treat Alzheimer's disease. Moreover, our findings suggest it should be feasible to develop additional compounds that alter the membrane phase/domain preferences of other membrane proteins for therapeutic, cell biological, or biotechnological purposes.

CHAPTER V

DISCUSSION AND FUTURE DIRECTIONS

Summary of This Work

The results of the work provided in the above studies divulge new avenues for therapeutic intervention or prevention for Alzheimer's disease. We found that the transmembrane domain of APP is both curved and flexible, properties not often found during membrane protein structure determination. By obtaining a 3D structure of the direct precursor to the Aβ peptide (C99), better therapeutic agents can now be developed that will specifically interact with APP, potentially limiting the toxic side effects of inhibiting the cleavage of off-target γ-Secretase substrates, such as Notch. In addition to allowing for more potent drug design, the results of the structural studies provide valuable insight into the mechanisms behind γ-Secretase processing of APP, yielding a fundamental understanding of how intramembraneous proteolysis occurs.

While the structural studies give insight into the physical properties of C99 that promote Aβ generation, the cholesterol studies provide functional information of a mechanism that may promote the overproduction of Aβ in AD. We were able to show that the transmembrane domain of APP can specifically bind cholesterol, lending credence to the hypothesis that APP may serve as a putative cholesterol sensor in the cell membrane. By obtaining definitive evidence that C99 partitions to cholesterol rich membrane domains, where it is known that key enzymes that generate Aβ reside, there is the potential for developing novel therapeutics to disrupt this partitioning. In fact, the coprostanol studies already provide a foundation that this phenomenon of membrane partitioning is a potential druggable target worthy of further studies.

This chapter will consider in more detail all of these findings, examining what the deeper meaning of the findings are, and in some cases, suggesting new ways to interpret the results. In all, the results of these experiments provide evidence of how the structure and function of C99 may contribute to the pathogenesis of AD, and how targeting specific aspects of the structure or function may lead, potentially, to regulating Aβ production.

Implication of Results

Structural Regulation of Aβ Production

Our results reveal that the 3D structure of the TMD of APP has many unique and unforeseen structural features. Significantly, the transmembrane helix was found to be highly curved, with the apex of curvature occurring at two consecutive glycine residues (G708 and G709), which are located in the middle of the TMD. While the average distance from the beginning to end of the TMD is roughly 35Å, DEER EPR studies revealed that the TMD is highly flexible, and can adopt structures that accommodate distances from end-to-end of the TMD that reach extremes of 20-40Å. This large window of end-to-end distance for the TMD may account, at least partially, for the wide variety of functions in which APP has been shown to be involved. We hypothesize that this curvature is vital for proper processing of APP by γ-Secretase, which has been shown to most likely accommodate a curved substrate best (*256*). Based on our docking studies of the experimentally determined 3D structure of C99 into the cryo-EM structure of γ-Secretase (See figure 2.11), it appears that G708 and G709 are positioned at a curved site within presenilin, positioning the initial ε-cleavage site in the proximity of the active site. The flexibility found within the curved TMD of APP may facilitate the

processive cleavage event of γ-Secretase processing, by permitting the new γ-Secretase cut sites to be preferentially exposed within the active site of the enzyme.

In addition to permitting proper γ-Secretase cleavage of APP, a flexibly curved TMD may play a role in organelle sorting of APP as it moves from the ER to the plasma membrane. It is known that as proteins move from the ER to the plasma membrane, the properties of the membranes change. The membranes initially appear thin with less cholesterol in the ER. They exhibit moderate thickness and cholesterol in the TGN. Finally, membranes at the plasma membrane contain the thickest membranes with the highest cholesterol levels (*110*). Possessing a flexible TMD would allow APP to accommodate more readily to changes in membrane thickness. Work from Hartmann *et al* showed that Aβ40 was preferentially formed in the TGN and endosomal compartments, while the more toxic Aβ42 species was generated in the ER (*110*). These findings suggest that organelle sorting may play a role in Aβ generation, and specifically, the generation of Aβ polypeptide species. Based on our findings that C99 can bind cholesterol, this raises the possibility that even slight alterations in cholesterol levels within the ER and TGN may have an impact on regulating APP trafficking and Aβ generation. Membrane thickness is also different between L_d and L_o phases of the membrane, with L_o domains having an increased thickness (~35Å) when compared to L_d domains (~28Å) (*124, 367, 368*). This suggests that on average, it is energetically favorable for the TMD of APP to exist in L_o domains, due to the matching hydrophobic thickness, however, due to the flexibility of the TMD it can accommodate the thickness of L_d domains.

It is the flexible nature of the TMD that may also account for the variance of phase preference when bound to cholesterol (L_o phase) or coprostanol (L_d phase). The results from the GUV studies showed that C99 had a ~15 fold increased preference for cholesterol rich domains over the bulk membrane. Based on the relative distribution of

cholesterol between the two phases (L$_o$ domains have only a modest 2 fold enrichment in the L$_o$ phase (*229*)), an additional property beyond simple cholesterol binding must account for the increased abundance of C99 in this phase. In fact, previous studies of membrane protein partitioning in GUVs showed low or only modest enrichment in the L$_o$ phase (*369, 370*), making our findings very different. In conjunction, a mechanism of decreasing the preference for L$_o$ domains in the presence of coprostanol must be accounted for. An explanation for both phenomenon may be found within the structural data and the NMR titration studies for both compounds. When comparing the two NMR titration studies for cholesterol and coprostanol, it is evident that while both compounds bind in the same general vicinity, there are select residues that interact differently with each compound (figure 4.6). Paramount in these minute discrepancies between compounds are the interactions with residues G708 and G709, the two glycine residues crucial for maintaining a flexible, curved TMD. DEER EPR results showed that when G708 was mutated to a leucine, the TMD saw a marked decrease in flexibility, however, when G709 was mutated to leucine, no change in flexibility was seen (figure 2.10C). When examining the NMR titrations, the results show that cholesterol preferentially interacts with G708 and G709, while coprostanol interacts almost exclusively with G709. Based on these slightly different interactions, we hypothesize that cholesterol locks the TMD of APP in a more rigid conformation by interacting with G708 and G709, while coprostanol permits a more flexible TMD with preferential interactions with G709. The increased rigidity induced by the cholesterol/G708/G709 interaction leads to better packing within the more rigid environment of cholesterol rich domains. This leads to an entropically favorable scenario of APP partitioning to cholesterol rich domains (figure 5.1) and may account for the extreme preference for these domains we witnessed in the GUV studies.
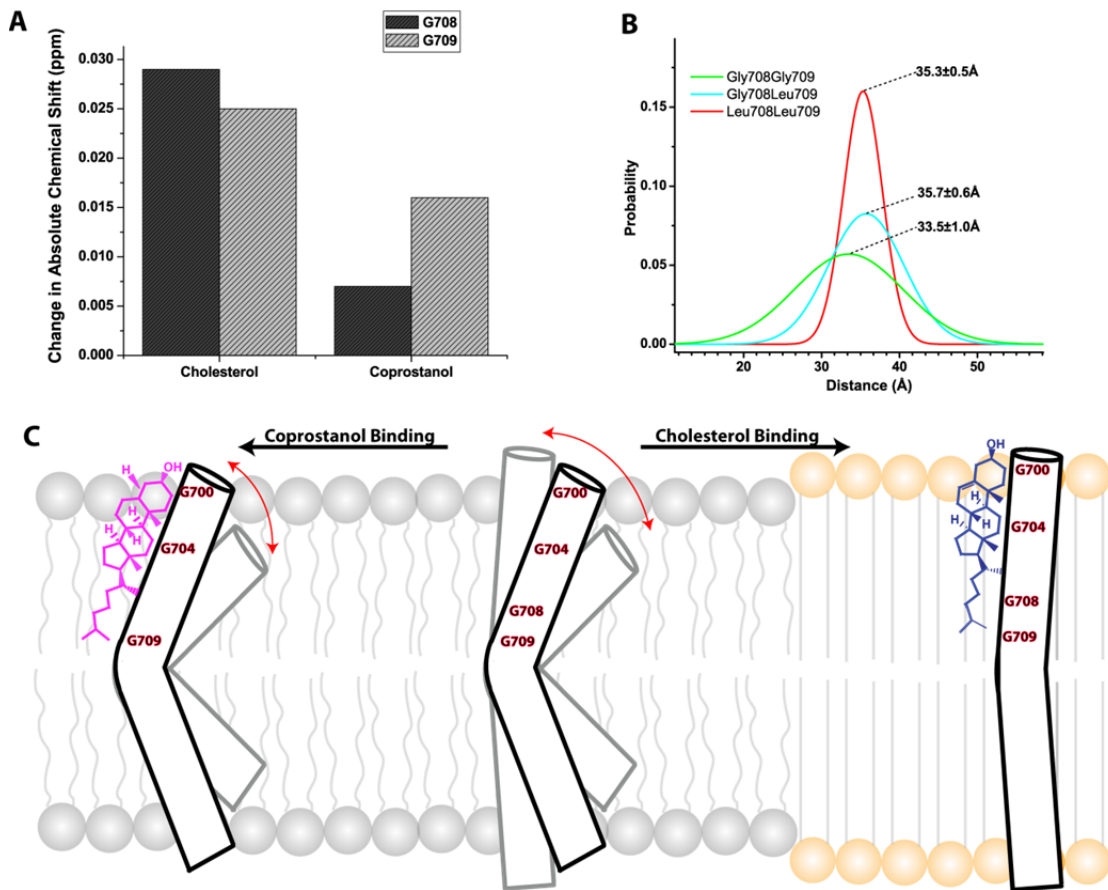
Figure 5.1. **The effect of cholesterol and coprostanol on APP TMD partitioning.** **(A)** Quantification of NMR chemical shift perturbation in the presence of cholesterol or coprostanol for residues G708 (black) or G709 (striped). When binding cholesterol, both G708 and G709 show significant chemical shift. In the presence of coprostanol, only G709 demonstrates chemical shift perturbation. **(B)** DEER EPR data taken from (*26*) showing that when mutated to leucine, only the G708L mutation induced a change in TMD flexibility compared to the wild type protein. **(C)** The model for how cholesterol binding induces rigidity in the TMD of APP and promotes partitioning to cholesterol rich domains (orange head groups) while coprostanol permits a flexible TMD that promotes partitioning to L_d membrane domains (grey head groups).

While the curvature and flexibility of the TMD as a whole may play important roles in regulating γ-Secretase cleavage and Aβ generation, our HDX data gives a more detailed picture as to how local dynamics within the TMD may regulate these processes as well. In collaboration with the Langosch laboratory, we found that in addition to being curved and flexible as a whole, the TMD contained three distinct regions of local

dynamics. The three regions were the N-terminus of the TMD (above the hinge region at G708/G709), a middle C-terminus region (residues 710-718), and the extreme C-terminal section (residues 718-723). The N-terminal region (which contains the GxxxGxxxG motif) is highly dynamic in nature. We speculate the local dynamics of the backbone atoms in this region may facilitate the binding of ligands, such as cholesterol, or may promote protein/protein interactions using the GxxxGxxxG motif. In addition, high backbone dynamics in this region may not only facilitate the movement of APP through the active site of γ-Secretase, but could also play a role in permitting release of the Aβ peptide, once a desired peptide length has been reached.

The fraying of the lower C-terminal region of the TMD may be very important for allowing processive cleavage of APP by γ-Secretase. Given that substrate helix unraveling is considered to promote proteolysis, the increased dynamics of this region may facilitate local hydration of bonds being prepared for cleavage. The HDX data suggests that dynamics increase downstream of the ε-cleavage site. This local unraveling at the helix C-terminus results from absent H-bonds and side-chain/side-chain interactions between the respective i and i + 3,4 residues as well as from increased solvation. It is plausible, that this fraying of the substrate helix promotes the initial endoproteolytic cuts at the ε-site. The newly formed C-termini of the resulting C48 and C49 fragments would then be frayed themselves which would facilitate ζ-cleavages; this, in turn, would produce frayed C45 and C46 fragments, etc. It is unclear if these local dynamics regulate the difference between Aβ40/42 production, but the possibility is strong (*237*), and requires further investigation.

APP, Cholesterol, and Redefining the Amyloid Hypothesis

Findings from our lab give concrete evidence linking the binding of cholesterol by the TMD of APP to AD, by connecting this binding event to partitioning of C99 to

175

cholesterol rich (L_o) membrane domains.   These events led to a model of how cholesterol binding by APP may promote the amyloidogenic pathway (figure 5.2).
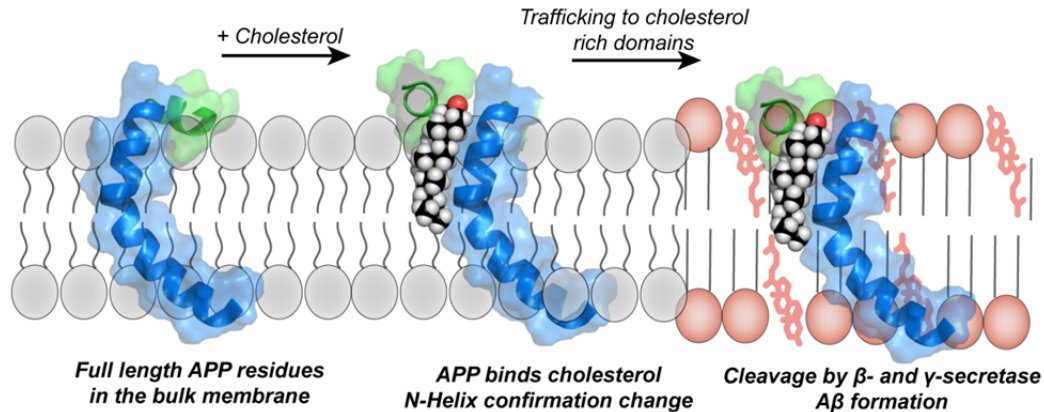
Figure 5.2.   A model of how cholesterol binding promotes the amyloidogenic cleavage pathway.   When not in complex with cholesterol, APP is preferentially cleaved by α-Secretase at the plasma membrane surface.   Binding of cholesterol promotes a conformational change in the N-helix of APP, occluding the α-Secretase cleavage site.   Following this binding event, APP is partitioned to cholesterol rich membrane domains, which is followed by cleavage by β- and γ-Secretase and leads to Aβ generation.   In AD, changes in cholesterol metabolism enhance the APP/cholesterol binding event and increase Aβ production.

It is known that cleavage of APP by α-Secretase occurs at the plasma membrane surface in L_d membrane domains (*1*).   It is suggested that this dynamic membrane environment exposes the α-Secretase cleavage site (K687) (*42*).   When examining the 30 lowest energy structures calculated during structure determination of C99, the results show that the N-helix (which includes the α-Secretase cleavage site) is highly dynamic when placed in a bicelle environment that mimics L_d membrane domains (see figure 17B), supporting the notion that increased dynamics of the N-helix promote the non-amyloidogenic pathway.   Findings from the Kramer lab corroborate this in the reverse manner, showing that when placed in model membranes mimicking L_o domains, accessibility to the α-Secretase cleavage site is decreased.   Using solid state NMR, they showed that when placed in L_o membrane domains (albeit, domains without cholesterol),

the α-Secretase cleavage site showed a marked decrease in dynamics. In addition, experiments utilizing the enzyme trypsin showed that the α-Secretase cleavage location was not only less dynamic, but also occluded. This result was obtained as the amino acid sequence of C99 contains a trypsin cut site proximal to residue K687 (*40*). These results suggest that cholesterol binding, and more specifically partitioning to cholesterol rich membrane domains, by APP may preferentially promote Aβ production by not only promoting the enhanced proximity between APP and β-Secretase in cholesterol rich domains, but also by actively preventing α-Secretase cleavage by occluding the cleavage site (Figure 5.3).
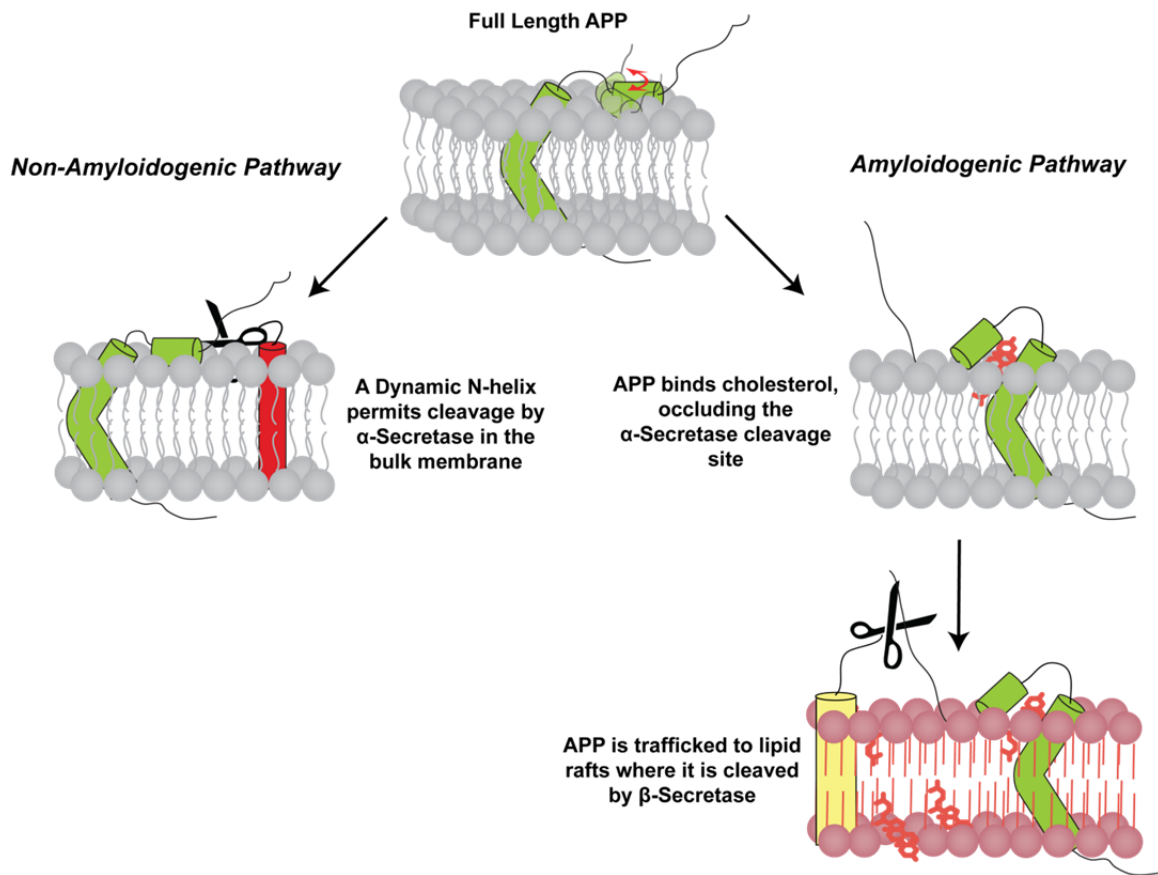
Figure 5.3. Cholesterol binding mediates selection between the non-amyloidogenic and amyloidogenic cleavage pathways by altering the α-Secretase cleavage site. Full length APP (green) contains a flexible N-helix that sits on the membrane surface. The dynamic nature of this helix preferentially exposes the α-Secretase cleavage site, allowing for enhanced α-Secretase (red) cleavage in the dynamic, bulk membrane (gray). Cholesterol binding to APP promotes the amyloidogenic cleavage pathway by two mechanisms; the first is to occlude the α-Secretase cleavage site and the second is to partition APP to cholesterol rich domains (pink) by β-Secretase (yellow).

Our results shed new light as to how cholesterol binding and membrane partitioning by APP may play crucial roles in promoting Aβ generation via the amyloidogenic pathway, but further investigation must be done in order to connect the events that lead to over stimulation of the amyloidogenic pathway in AD. Carefully studying the vast literature on cholesterol and AD, makes it appear that at first glance there are two distinct schools of thought. The first contends there are increased levels of cholesterol in AD. The second hypothesizes that decreased levels of cholesterol

stimulate the overproduction of Aβ. However, when the mechanisms that drive both the increase and decrease of cholesterol in AD are coupled with the mechanisms found in our current work on cholesterol binding and membrane partitioning, it may be possible to link both increased and decreased cholesterol levels into one, unifying, mechanism that promotes Aβ generation in AD.

Under physiological conditions APP is preferentially cleaved by the non-amyloidogenic pathway, resulting in low, biologically relevant, levels of Aβ within the brain. This means that APP is preferentially cleaved by α-Secretase, an event that occurs at the plasma membrane surface, indicating the majority of APP leaves the TGN, is transported to the plasma membrane and is cleaved. Cleavage at the plasma membrane by α-Secretase needs to be a relatively fast event, as the turnover of APP at the plasma membrane surface is quite rapid, as very little APP can be detected at the cell surface at a given time (*1*). This process leaves very little APP to be cleaved by β-Secretase, an event that is known to occur predominantly in endosomal compartments. APP and β-Secretase co-localize in endosomal compartments either following endocytosis from the cell membrane in a clathrin dependent manner, or from direct transport from the TGN to endosomal compartments (*121*).

It is known that many pro-AD risk factors have altered expression levels in AD. The protein CYP46 has increased expression (*95, 96*), while the protein Seladin-1 is down regulated (*87*). CYP46 is the enzyme that converts cholesterol to 24-hydroxycholesterol, which is the form of cholesterol able to cross the blood brain barrier and exit the brain. Overexpression of this enzyme in AD would lead to an overabundance of 24-hydroxycholesterol, ultimately depleting the levels of cholesterol within the brain. Seladin-1 is the enzyme responsible for converting demosterol to cholesterol, the last step in the cholesterol synthesis pathway. Down regulation of this protein would lead to the over accumulation of demosterol, and, as with the

overexpression of CYP46, the ultimate decrease in total brain cholesterol levels. While a decrease of ~20% cholesterol is expected during normal aging, a loss of 30% cholesterol is connected to neurodegeneration (*95*), highlighting the delicate balance of cholesterol metabolism in AD.

Work from the Chochina lab demonstrated that there is an asymmetry in the distribution of cholesterol between the two faces of the plasma membrane; in young neurons approximately 85% of the total cholesterol is found in the cytofacial leaflet, where cholesterol rich domains do not form. As neurons age, there is a marked increase in the levels of cholesterol in the exofacial leaflet (up to 35%), leading to increased cholesterol rich domain formation at the plasma membrane surface (*111*).

When combined with the evidence of altered cholesterol metabolism by either CYP46 or Seladin-1, the hypothesis is generated that decreased levels of cholesterol will create a "cholesterol sink" at the plasma membrane surface, resulting in overcompensation and increased movement of cholesterol to the exofacial leaflet. This increase of cholesterol in the exofacial leaflet will create a higher probability of cholesterol binding by APP and partitioning to cholesterol rich domains, with an overall increase in Aβ production. This increase in Aβ due to the imbalance of cholesterol in the plasma membrane leaflets leads to local neuronal cell death. As neurons begin to die, this forces the surrounding neurons to uptake the cholesterol being synthesized and shuttled by the neighboring astrocytes.

Additionally, the cholesterol content is increased within these cells as the imbalance between exo- and cytofacial leaflets generates more cholesterol uptake and synthesis, resulting in increased cholesterol levels not only at the plasma membrane, but also in the ER and potentially the TGN. Feeding into this increase in neuronal cholesterol levels is the evidence that the ApoE4 protein (pro-AD risk factor) is overexpressed in some forms of AD (*222*). While the exact role ApoE4 plays in AD is

still being investigated, a known function for this protein is transporting cholesterol from neighboring astrocytes to neurons. An increase in ApoE4 expression (due to the extra allele found in some forms of AD (*93*)) could ultimately lead to an increase in this cholesterol transport, thus increasing the levels of cholesterol in neighboring neurons. The net increase of cholesterol stimulates an increase in the production of APP, as seen by the study from the Octave lab (*29*). The combination of increased APP expression and increased cholesterol levels, both at the plasma membrane and TGN, initiates a vicious cycle of overproduction of Aβ, neuronal death, and increased cholesterol update by surrounding cells. In both cases of decreased and increased cholesterol, there is a higher prevalence of cholesterol rich domains present in the membrane. Thus here is a new mechanism uniting how decreased, and eventually increased, levels of cholesterol promote the overproduction of the Aβ peptide in AD (figure 5.4).
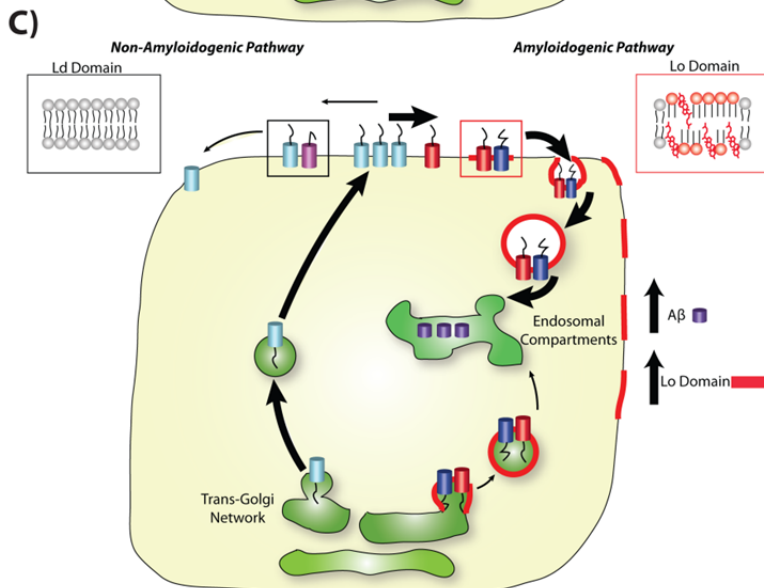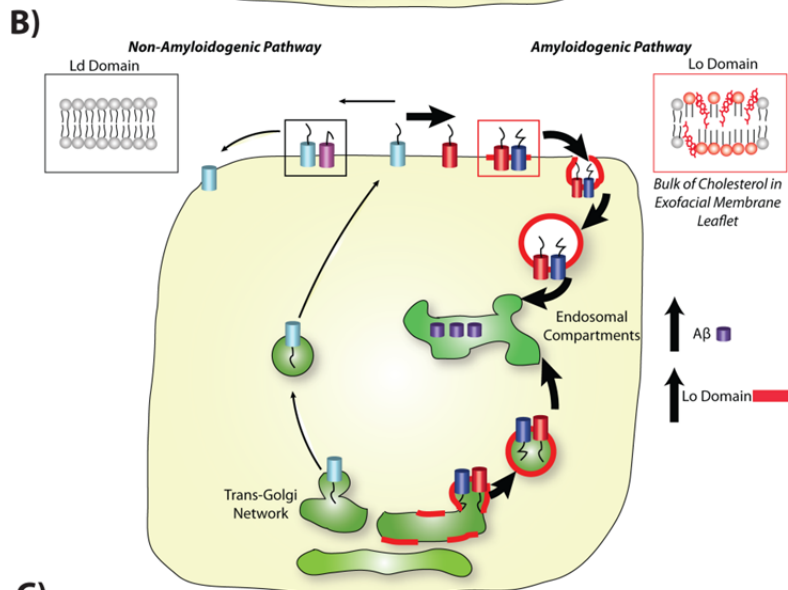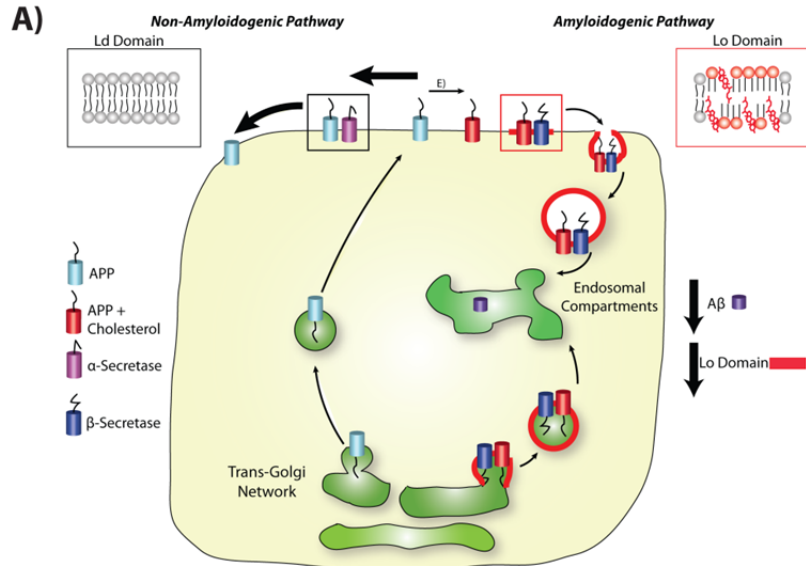
Figure 5.4. A new model for how both decreased and increased levels of cholesterol contribute to Aβ generation in AD. **(A)** The top panel represents APP processing under normal conditions. APP is preferentially trafficked to the plasma membrane where it is rapidly processed by α-Secretase. A small portion of APP is processed by the amyloidogenic pathway, by binding cholesterol and partitioning to cholesterol rich domains either at the plasma membrane or in the TGN. Partitioning to cholesterol rich (L$_o$) domains results in Aβ generation in endosomal compartments. **(B)** The middle panel represents Aβ generation under conditions of decreased cholesterol. Cholesterol levels are decreased by over expression of CYP46 or decreased expression of Seladin-1. This causes the enhanced movement of cholesterol from the cytofacial to the exofacial leaflet, creating more cholesterol rich domains at the plasma membrane, which increases APP partitioning to L$_o$ domains and increases Aβ production. In addition, this change in cholesterol content induces the cell to uptake more cholesterol, creating a larger pool of cholesterol rich domains in the ER and TGN, which increases Aβ production. This increase in Aβ causes abnormal cell death, and as neurons begin to die, the neighboring neurons uptake cholesterol being shuttled by the surrounding astrocytes. **(C)** This increases the cholesterol content of neighboring neurons (bottom panel). An increase in cholesterol stimulates the over expression of APP. Due to the increase in APP and cholesterol at the plasma membrane, this enhances APP partitioning to cholesterol rich domains, and ultimately, Aβ production. This furthers neuronal death, and is propagated throughout the brain in AD. APP unbound to cholesterol is represented by a cyan cylinder, APP bound to cholesterol is red, α-Secretase is colored magenta, and β-Secretase is colored blue. Aβ is colored purple. Cholesterol rich L$_o$ domains are colored red. Stimulated pathways are highlighted with enlarged arrows. It should be noted that endocytosis of APP and β-Secretase can be a separate event, it is for simplicity that they are shown being endocytosed in the same vesicle in the cartoon.

Future Directions

Investigation of How the Structure of C99 Regulates γ-Secretase Cleavage

The results from the 3D structure determination of C99 indicate that the curved structure of the TMD may be an ideal shape for proper cleavage by γ-Secretase. In order to validate this theory, the structure of the TMD should be altered via mutagenesis to create a straight TMD, to test whether a curved substrate is not only ideal, but necessary, for γ-Secretase cleavage. Changes in TMD structure should be monitored by DEER EPR to assess the magnitude of distance change from residues G700 and L723 following mutagenesis. Information gained during these studies would highlight

key structural features needed for intramembrane proteolysis, and may yield insight regarding means of selection for enzymes that cleave numerous substrates.

In addition with the effect of different TMD structures on γ-Secretase cleavage, the effect of altered TMD dynamics on γ-Secretase cleavage should also be investigated. Both our DEER EPR and HDX results suggest that the TMD of APP is not only curved, but dynamic in nature. In addition to the curvature being important for γ-Secretase cleavage, the flexibility of the TMD may also play a pivotal role in not only regulating the overall cleavage event, but also in determining which length Aβ peptide is generated. Mutations should be made at residues G708 and G709 to modify TMD flexibility. Changes in flexibility should be monitored by DEER EPR to determine the magnitude of the change.

As well as investigating how changes in TMD structure via designed manipulation impact γ-Secretase cleavage, these same concepts could be used to study how known mutations in familial AD (FAD) or changes in membrane dynamics influence cleavage. Multiple FAD mutations occur within the TMD of APP, with most occurring near the γ-Secretase cleavage region. The effect of these mutations is still not known, and the impact could range from a change as simple as altering the accessibility of γ-Secretase during cleavage to something as complex as altering the curvature or flexibility of the TMD. We have shown that binding of cholesterol leads to increased partitioning of C99 to cholesterol rich membrane domains, domains that have unique biophysical properties when compared to the bulk membrane. Research has shown that cholesterol may serve as a co-factor to increase γ-Secretase activity (*352*). While cholesterol could be having an impact on γ-Secretase itself, the compound could also be inducing changes in the flexibility of the TMD of C99 or having an impact on the accessibility of the γ-Secretase cleavage locations. Investigating how these changes in

the TMD of C99 impact γ-Secretase cleavage, might provide a window into decreasing the production of Aβ during AD.

In order to determine changes in both structure and flexibility an *in vitro* γ-Secretase assay should be developed, similar to those used by the Wolfe lab (*371*). These assays work by purifying intact γ-Secretase complexes from cell membranes (they utilize Chinese hamster ovary (CHO) cells, but other cell lines can be investigated) utilizing a relatively mild detergent such as CHAPSO. Using a mild detergent is key as to not disrupt the integrity and function of the γ-Secretase complex. C99 should be expressed and purified from *E. Coli* as described (*28*) into a CHAPSO containing solution. Cleavage of C99 by γ-Secretase should be conducted by mixing the two solutions together and monitoring the production of the AICD via western blot analysis. In addition, differences in Aβ40 versus Aβ42 levels could be detected utilizing both western blot analysis or sandwich ELISA assays.

By determining the impact that changes in curvature and flexibility have on proper γ-Secretase cleavage of the TMD of APP, we can gain a better understanding of how to specifically manipulate this event to ultimately prevent Aβ production. If changes in curvature or flexibility (via mutagenesis or different membrane environments) reduce or inhibit γ-Secretase cleavage, compounds could be investigated or designed that mimic these changes. This type of information would be paramount in investigating means that prevent cleavage of APP by γ-Secretase, but still permit cleavage of Notch and other substrates to reduce toxicity.

Impact of Cholesterol Binding and Membrane Fluidity on APP Cleavage

Our results demonstrate that C99 can specifically bind cholesterol in the DHPC/DMPC bicelle model membrane system. Additionally, we have shown that this binding event partitions C99 to cholesterol rich membrane domains, where it is

hypothesized that full length APP is cleaved by the amyloidogenic pathway to generate the Aβ peptide. While our findings are for the APP cleavage product C99, we hypothesize that the results would be consistent for full length APP, as both proteins contain the same TMD regions that could potentially interact with cholesterol. These results indicate that the binding event between APP and cholesterol may be a key step in promoting the etiology of AD.

In order to gain a more in depth understanding of how cholesterol binding actually promotes amyloidogenesis, we must determine the 3D structure of C99 in complex with cholesterol. Determining the 3D structure of this complex by NMR, will further the research from the Kramer lab (40), which indicates that following partitioning to L_o like membrane domains, the α-Secretase cleavage site becomes occluded. 3D structure determination of the C99/cholesterol complex with NMR will not only show if the N-helix (which contains the α-Secretase cleavage site) has an altered structure following cholesterol binding, but we will also help achieve a better understanding of the dynamics of this region following the interaction with cholesterol. Our initial structural studies show that the N-helix is highly dynamic when in a cholesterol free/L_d like membrane domain. Moving forward, the observation of any changes upon cholesterol binding will illuminate possible structural means of regulating the non-amyloidogenic and amyloidogenic cleavage pathways.

In addition to providing critical insight regarding mechanisms of promoting Aβ generation, the determination of the 3D structure of the C99/cholesterol complex will introduce a strong foundation for developing potent therapeutics to potentially abrogate Aβ production *in vivo*. Initial results from our lab indicate that the partitioning of C99 to cholesterol rich membrane domains is a pharmacological target, as the addition of the L_d favoring compound coprostanol was able to actively remove C99 from L_o membrane domains. By determining the 3D structure of the C99/cholesterol complex, key

interactions between the protein and the lipid will be identified, allowing for the development of compounds that mimic these interactions more tightly. This information can be coupled with features of sterols that prefer the L_d phase (like coprostanol), to potentially develop a therapeutic agent that will bind APP more tightly than cholesterol and also prevent its partitioning to L_o domains. This novel approach to preventing Aβ generation has the potential to be very effective, as it would be a means to specifically block the amyloidogenic processing of only APP, while simultaneously not interrupting cholesterol rich domain formation in cells, which could potentially harm the function of other vital proteins.

While our results on membrane partitioning are very encouraging to show that C99 partitions to cholesterol rich domains *in vivo*, it is recognized that this is a difficult phenomenon to recapitulate in cells, as L_o domains have yet to be imaged in real time. While not the ideal solution of monitoring the partitioning of APP *in vivo*, a new method has been developed that is more physiological than the GUV studies utilized in our work. These experiments are in the form of plasma membrane derived vesicles (GPMVs) (*232, 372*). The end results of GPMV studies appear very similar to GUV experiments, however, the vesicles being imaged are derived from cellular membranes as opposed to being synthetically generated by electroformation. The fact that these vesicles are derived from cells (such as Chinese hamster ovary (CHO), human embryonic kidney (HEK), or COS-7) allows for a better membrane mimetic to study membrane protein partitioning as these membranes contain a larger milieu of native lipids as well as potentially containing a variety of membrane proteins. This means they more efficiently replicate the crowded cell membrane environment. In addition, GPMV experiments will allow us to monitor the membrane partitioning of full length APP (with an N-terminal CFP tag), hopefully validating the hypothesis that full length APP partitions to L_o domains in native cell membranes. In order to monitor full length APP partitioning, exogenous

overexpression of APP is required, giving the opportunity to add in the specific cholesterol binding mutations (E693A and G704A as cholesterol deficient binding and G696A as no effect on cholesterol binding) to monitor whether the interaction between APP and cholesterol is the ultimate driving force behind APP partitioning, or if other factors, such as L_o associated adaptor proteins like AP-4 and flotillin, are needed for APP partitioning.

One final area of research that should be pursued in the vein of cholesterol and amyloidogenesis is the observed co-localization between APP/C99 and β-Secretase in GUV and GPMV membrane mimetics. Previous studies have been down showing that APP and β-Secretase can co-localize in cells by using such methods as detergent resistant membrane preparation (*33*), FRET (*121*), and antibody cross-linking (*122*). Examining the interaction between C99 and β-Secretase in GUVs and GPMVs would reveal that this interaction does in fact occur within cholesterol rich membrane domains, findings that are only speculative to date. In addition, by utilizing the C99 mutants that cannot bind cholesterol, it can be determined if this reduces the co-localization between C99 and β-Secretase. Finally, by using a raftophobic compound such as coprostanol, it would be possible to investigate if one could pharmacologically reduce the co-localization between C99 and β-Secretase in cholesterol rich membrane domains.

Projection of Future Work on C99 and AD

The studies presented in this dissertation have highlighted key structural and functional aspects of C99 and how they regulate and promote amyloidogenesis. These findings have established a strong predicate for furthering our understanding of how the structure of the TMD of APP regulates AD as well as how cholesterol is a key component in regulating β-Secretase cleavage. To expand on these findings, potential future experiments in the realm of cellular biology could be of great significance.

Published work and potential future experiments will show that the curved nature of the TMD of APP is vital for not only proper cleavage by γ-Secretase, but we hypothesize may also be a key feature in determining γ-Secretase substrate specificity. Once results establish how changes in flexibility and curvature, either by mutations or changes in membrane properties, influence the ability of γ-Secretase to cleave C99, ensuing experiments should investigate how these changes influence the ratio between Aβ40 and Aβ42 production. Initial studies should be performed using *in vitro* γ-Secretase assays as described above, and should they prove successful transfection of full length APP and any mutant forms into cells containing γ-Secretase should be the undertaken in the next stage of experiments. Results from cellular studies would verify that key changes in the structure of the TMD would result in phenotypic changes in Aβ production seen in AD. One could envision that key FAD mutations may influence the structure or flexibility of the TMD and preferentially produce Aβ42. A better understanding of the mechanism of γ-Secretase cleavage, specifically by observing how changes in APP TMD structure influence cleavage and Aβ production, might lead to the development of novel therapeutics to more tightly regulate any changes in TMD structure or flexibility.

In conjunction with determining how structural features of the TMD of APP regulate γ-Secretase cleavage in a more cellular setting, it is important to pursue how the cholesterol binding properties of APP translate to changes in Aβ production in cells. While our findings have shown that C99 can partition to cholesterol rich membrane domains (results hopefully validated using GMPVs and full length APP), future work showing that altering this partitioning, either via mutagenesis or partitioning altering compounds, reduces Aβ production is paramount. Elucidating how the disruption of this membrane partitioning decreases Aβ production, will not only definitively show that membrane partitioning is vital to Aβ production in AD, but will also show that this event is

a previously unexplored, viable therapeutic target for treating, and potentially preventing, AD onset.

Concluding Remarks

The initial structural and function studies on C99 and their impact on the understanding of how AD progresses have been established in our reports. These findings highlight how 3D structure determination can play a vital role in gaining a better picture of how a protein functions. Additionally, our results have shown definitive evidence that C99 can specifically bind cholesterol, and that this binding event is directly responsible for partitioning C99 into cholesterol rich membrane domains. Both findings highlight the important need for further studies exploring the relationship between cholesterol and AD, as intricacies of this relationship may hold critical keys into unlocking potential therapeutics to treat and prevent AD onset. By furthering the initial studies that explore how the structure of the TMD of APP plays a role in γ-Secretase cleavage and how the interaction with cholesterol and the membrane partitioning to cholesterol rich domains influence Aβ production, we may begin to gain a better understanding of how these mechanisms influence the etiology of AD.

BIBLIOLGRAPHY

1. O'Brien, R. J., and Wong, P. C. (2011) Amyloid Precursor Protein Processing and Alzheimer's Disease, *Annual Review of Neuroscience 34*, 185-204.

2. Stelzmann, R. A., Norman Schnitzlein, H., and Reed Murtagh, F. (1995) An english translation of alzheimer's 1907 paper, "über eine eigenartige erkankung der hirnrinde", *Clinical Anatomy 8*, 429-431.

3. Tanzi, R. E., and Bertram, L. (2005) Twenty years of the Alzheimer's disease amyloid hypothesis: a genetic perspective, *Cell 120*, 545-555.

4. Glenner, G. G., and Wong, C. W. (1984) Alzheimer's disease: Initial report of the purification and characterization of a novel cerebrovascular amyloid protein, *Biochemical and Biophysical Research Communications 120*, 885-890.

5. Kang, J., Lemaire, H.-G., Unterbeck, A., Salbaum, J. M., Masters, C. L., Grzeschik, K.-H., Multhaup, G., Beyreuther, K., and Muller-Hill, B. (1987) The precursor of Alzheimer's disease amyloid A4 protein resembles a cell-surface receptor, *Nature 325*, 733-736.

6. Hardy, J., and Selkoe, D. J. (2002) The Amyloid Hypothesis of Alzheimer's Disease: Progress and Problems on the Road to Therapeutics, *Science 297*, 353-356.

7. Hardy, J., and Allsop, D. (1991) Amyloid deposition as the central event in the aetiology of Alzheimer's disease, *Trends in Pharmacological Sciences 12*, 383-388.

8. Nistor, M., Don, M., Parekh, M., Sarsoza, F., Goodus, M., Lopez, G. E., Kawas, C., Leverenz, J., Doran, E., Lott, I. T., Hill, M., and Head, E. (2007) Alpha- and beta-secretase activity as a function of age and beta-amyloid in Down syndrome and normal brain, *Neurobiology of Aging 28*, 1493-1506.

9. Ferreira, A., Caceres, A., and Kosik, K. (1993) Intraneuronal compartments of the amyloid precursor protein, *The Journal of Neuroscience 13*, 3112-3123.

10. Wolfe, M. S., and Guenette, S. Y. (2007) APP at a glance, *J Cell Sci 120*, 3157-3161.

11. Heidinger, J. Potential Parallels in Presenilin Dependant γ-Secretase Cleavage: A Research Investigation of Notch, APP, and the EGFR.

12. Annaert, W., and De Strooper, B. (1999) Presenilins: molecular switches between proteolysis and signal transduction, *Trends in Neurosciences 22*, 439-443.

13. Beher, D., Hesse, L., Masters, C. L., and Multhaup, G. (1996) Regulation of amyloid protein precursor (APP) binding to collagen and mapping of the binding sites on APP and collagen type I, *Journal of Biological Chemistry 271*, 1613-1620.

14. Munter, L.-M., Voigt, P., Harmeier, A., Kaden, D., Gottschalk, K. E., Weise, C., Pipkorn, R., Schaefer, M., Langosch, D., and Multhaup, G. (2007) GxxxG motifs within the amyloid precursor protein transmembrane sequence are critical for the etiology of A[beta]42, *EMBO J 26*, 1702-1712.

15. Kienlen-Campard, P., Tasiaux, B., Van Hees, J., Li, M., Huysseune, S., Sato, T., Fei, J. Z., Aimoto, S., Courtoy, P. J., Smith, S. O., Constantinescu, S. N., and Octave, J.-N. (2008) Amyloidogenic Processing but Not Amyloid Precursor Protein (APP) Intracellular C-terminal Domain Production Requires a Precisely Oriented APP Dimer Assembled by Transmembrane GXXXG Motifs, *Journal of Biological Chemistry 283*, 7733-7744.

16. Sato, T., Tang, T.-c., Reubins, G., Fei, J. Z., Fujimoto, T., Kienlen-Campard, P., Constantinescu, S. N., Octave, J.-N., Aimoto, S., and Smith, S. O. (2009) A helix-to-coil transition at the ε-cut site in the transmembrane dimer of the amyloid precursor protein is required for proteolysis, *Proceedings of the National Academy of Sciences 106*, 1421-1426.

17. Melnyk, R. A., Kim, S., Curran, A. R., Engelman, D. M., Bowie, J. U., and Deber, C. M. (2004) The affinity of GXXXG motifs in transmembrane helix-helix interactions is modulated by long-range communication, *Journal of Biological Chemistry 279*, 16591-16597.

18. Russ, W. P., and Engelman, D. M. (2000) The GxxxG motif: a framework for transmembrane helix-helix association, *Journal of Molecular Biology 296*, 911-919.

19. Kleiger, G., Grothe, R., Mallick, P., and Eisenberg, D. (2002) GXXXG and AXXXA: common α-helical interaction motifs in proteins, particularly in extremophiles, *Biochemistry 41*, 5990-5997.

20. Yarden, Y. (2001) The EGFR family and its ligands in human cancer: signalling mechanisms and therapeutic opportunities, *European journal of cancer 37*, 3-8.

21. Sako, Y., Minoghchi, S., and Yanagida, T. (2000) Single-molecule imaging of EGFR signalling on the surface of living cells, *Nature cell biology 2*, 168-172.

22. Escher, C., Cymer, F., and Schneider, D. (2009) Two GxxxG-like motifs facilitate promiscuous interactions of the human ErbB transmembrane domains, *Journal of Molecular Biology 389*, 10-16.

23. Li, R., Gorelik, R., Nanda, V., Law, P. B., Lear, J. D., DeGrado, W. F., and Bennett, J. S. (2004) Dimerization of the transmembrane domain of integrin αIIb subunit in cell membranes, *Journal of Biological Chemistry 279*, 26666-26673.

24. Schneider, D., and Engelman, D. M. (2004) Involvement of transmembrane domain interactions in signal transduction by α/β integrins, *Journal of Biological Chemistry 279*, 9840-9846.

25. Li, W., Metcalf, D. G., Gorelik, R., Li, R., Mitra, N., Nanda, V., Law, P. B., Lear, J. D., DeGrado, W. F., and Bennett, J. S. (2005) A push-pull mechanism for regulating integrin

function, *Proceedings of the National Academy of Sciences of the United States of America 102*, 1424-1429.

26. Barrett, P. J., Song, Y., Van Horn, W. D., Hustedt, E. J., Schafer, J. M., Hadziselimovic, A., Beel, A. J., and Sanders, C. R. (2012) The amyloid precursor protein has a flexible transmembrane domain and binds cholesterol, *Science 336*, 1168-1171.

27. Song, Y., Hustedt, E. J., Brandon, S., and Sanders, C. R. (2013) Competition Between Homodimerization and Cholesterol Binding to the C99 Domain of the Amyloid Precursor Protein, *Biochemistry*.

28. Beel, A. J., Mobley, C. K., Kim, H. J., Tian, F., Hadziselimovic, A., Jap, B., Prestegard, J. H., and Sanders, C. R. (2008) Structural studies of the transmembrane C-terminal domain of the amyloid precursor protein (APP): does APP function as a cholesterol sensor?, *Biochemistry 47*, 9428-9446.

29. Pierrot, N., Tyteca, D., D'Auria, L., Dewachter, I., Gailly, P., Hendrickx, A., Tasiaux, B., Haylani, L. E., Muls, N., N'Kuli, F., Laquerrière, A., Demoulin, J.-B., Campion, D., Brion, J.-P., Courtoy, P. J., Kienlen-Campard, P., and Octave, J.-N. (2013) Amyloid precursor protein controls cholesterol turnover needed for neuronal activity, *EMBO Molecular Medicine 5*, 608-625.

30. Beel, A. J., Sakakura, M., Barrett, P. J., and Sanders, C. R. (2010) Direct binding of cholesterol to the amyloid precursor protein: An important interaction in lipid–Alzheimer's disease relationships?, *Biochimica et Biophysica Acta (BBA) - Molecular and Cell Biology of Lipids 1801*, 975-982.

31. Beel, A., and Sanders, C. (2008) Substrate specificity of γ-secretase and other intramembrane proteases, *Cellular and Molecular Life Sciences 65*, 1311-1334.

32. Xia, W., Zhang, J., Perez, R., Koo, E. H., and Selkoe, D. J. (1997) Interaction between amyloid precursor protein and presenilins in mammalian cells: Implications for the pathogenesis of Alzheimer disease, *Proceedings of the National Academy of Sciences 94*, 8208-8213.

33. Ehehalt, R., Keller, P., Haass, C., Thiele, C., and Simons, K. (2003) Amyloidogenic processing of the Alzheimer β-amyloid precursor protein depends on lipid rafts, *The Journal of Cell Biology 160*, 113-123.

34. Cordy, J. M., Hussain, I., Dingwall, C., Hooper, N. M., and Turner, A. J. (2003) Exclusively targeting β-secretase to lipid rafts by GPI-anchor addition up-regulates β-site processing of the amyloid precursor protein, *Proceedings of the National Academy of Sciences of the United States of America 100*, 11735-11740.

35. Nunan, J., and Small, D. H. (2000) Regulation of APP cleavage by α-, β-and γ-secretases, *FEBS letters 483*, 6-10.

36. Colciaghi, F., Borroni, B., Pastorino, L., Marcello, E., Zimmermann, M., Cattabeni, F., Padovani, A., and Di Luca, M. (2002) [alpha]-Secretase ADAM10 as well as [alpha] APPs is reduced in platelets and CSF of Alzheimer disease patients, *Molecular medicine 8*, 67.

37. Tolia, A., and De Strooper, B. (2009) Structure and function of [gamma]-secretase, *Seminars in Cell & Developmental Biology 20*, 211-218.

38. Wolfe, M., Xia, W., Ostaszewski, B., Diehl, T., Kimberly, W., and Selkoe, D. (1999) Two transmembrane aspartates in presenilin-1 required for presenilin endoproteolysis and gamma-secretase activity, *Nature 398*, 513 - 517.

39. Shah, S., Lee, S.-F., Tabuchi, K., Hao, Y.-H., Yu, C., LaPlant, Q., Ball, H., Dann Iii, C. E., Südhof, T., and Yu, G. (2005) Nicastrin Functions as a [gamma]-Secretase-Substrate Receptor, *Cell 122*, 435-447.

40. Marenchino, M., Williamson, P. T. F., Murri, S., Zandomeneghi, G., Wunderli-Allenspach, H., Meier, B. H., and Krämer, S. D. (2008) Dynamics and Cleavability at the [alpha]-Cleavage Site of APP(684-726) in Different Lipid Environments, *Biophysical Journal 95*, 1460-1473.

41. Bodovitz, S., and Klein, W. L. (1996) Cholesterol Modulates -Secretase Cleavage of Amyloid Precursor Protein, *Journal of Biological Chemistry 271*, 4436-4440.

42. Kojro, E., Gimpl, G., Lammich, S., März, W., and Fahrenholz, F. (2001) Low cholesterol stimulates the nonamyloidogenic pathway by its effect on the α-secretase ADAM 10, *Proceedings of the National Academy of Sciences 98*, 5815-5820.

43. von Arnim, C. A. F., Einem, B. v., Weber, P., Wagner, M., Schwanzar, D., Spoelgen, R., Strauss, W. L. S., and Schneckenburger, H. (2008) Impact of cholesterol level upon APP and BACE proximity and APP cleavage, *Biochemical and Biophysical Research Communications 370*, 207-212.

44. Roch, J.-M., Masliah, E., Roch-Levecq, A.-C., Sundsmo, M. P., Otero, D., Veinbergs, I., and Saitoh, T. (1994) Increase of synaptic density and memory retention by a peptide representing the trophic domain of the amyloid beta/A4 protein precursor, *Proceedings of the National Academy of Sciences 91*, 7450-7454.

45. Meziane, H., Dodart, J.-C., Mathis, C., Little, S., Clemens, J., Paul, S., and Ungerer, A. (1998) Memory-enhancing effects of secreted forms of the β-amyloid precursor protein in normal and amnestic mice, *Proceedings of the National Academy of Sciences 95*, 12683-12688.

46. Oh, E. S., Savonenko, A. V., King, J. F., Fangmark Tucker, S. M., Rudow, G. L., Xu, G., Borchelt, D. R., and Troncoso, J. C. (2009) Amyloid precursor protein increases cortical neuron size in transgenic mice, *Neurobiology of Aging 30*, 1238-1244.

47. Young-Pearse, T. L., Bai, J., Chang, R., Zheng, J. B., LoTurco, J. J., and Selkoe, D. J. (2007) A critical function for β-amyloid precursor protein in neuronal migration revealed by in utero RNA interference, *The Journal of Neuroscience 27*, 14459-14469.

48. Vassar, R., Bennett, B. D., Babu-Khan, S., Kahn, S., Mendiaz, E. A., Denis, P., Teplow, D. B., Ross, S., Amarante, P., and Loeloff, R. (1999) β-Secretase cleavage of Alzheimer's amyloid precursor protein by the transmembrane aspartic protease BACE, *Science 286*, 735-741.

49. Schneider, A., Rajendran, L., Honsho, M., Gralle, M., Donnert, G., Wouters, F., Hell, S. W., and Simons, M. (2008) Flotillin-Dependent Clustering of the Amyloid Precursor Protein Regulates Its Endocytosis and Amyloidogenic Processing in Neurons, *The Journal of Neuroscience 28*, 2874-2882.

50. Wolfe, M. S., and Selkoe, D. J. (2010) Giving Alzheimer's the Old One-Two, *Cell 142*, 194-196.

51. Nikolaev, A., McLaughlin, T., O'Leary, D. D., and Tessier-Lavigne, M. (2009) APP binds DR6 to trigger axon pruning and neuron death via distinct caspases, *Nature 457*, 981-989.

52. Butterfield, D. A., Drake, J., Pocernich, C., and Castegna, A. (2001) Evidence of oxidative damage in Alzheimer's disease brain: central role for amyloid β-peptide, *Trends in Molecular Medicine 7*, 548-554.

53. Butterfield, D. A., Galvan, V., Lange, M. B., Tang, H., Sowell, R. A., Spilman, P., Fombonne, J., Gorostiza, O., Zhang, J., Sultana, R., and Bredesen, D. E. (2010) In vivo oxidative stress in brain of Alzheimer disease transgenic mice: Requirement for methionine 35 in amyloid β-peptide of APP, *Free Radical Biology and Medicine 48*, 136-144.

54. Dumont, M., Wille, E., Stack, C., Calingasan, N. Y., Beal, M. F., and Lin, M. T. (2009) Reduction of oxidative stress, amyloid deposition, and memory deficit by manganese superoxide dismutase overexpression in a transgenic mouse model of Alzheimer's disease, *The FASEB Journal 23*, 2459-2466.

55. Jo, D.-G., Arumugam, T. V., Woo, H.-N., Park, J.-S., Tang, S.-C., Mughal, M., Hyun, D.-H., Park, J.-H., Choi, Y.-H., Gwon, A. R., Camandola, S., Cheng, A., Cai, H., Song, W., Markesbery, W. R., and Mattson, M. P. (2010) Evidence that γ-secretase mediates oxidative stress-induced β-secretase expression in Alzheimer's disease, *Neurobiology of Aging 31*, 917-925.

56. Beel, A. J., Barrett, P., Schnier, P. D., Hitchcock, S. A., Bagal, D., Sanders, C. R., and Jordan, J. B. (2009) Nonspecificity of Binding of γ-Secretase Modulators to the Amyloid Precursor Protein, *Biochemistry 48*, 11837-11839.

57. Esler, W. P., and Wolfe, M. S. (2001) A portrait of Alzheimer secretases--new features and familiar faces, *Science 293*, 1449-1454.

58. Borchelt, D. R., Thinakaran, G., Eckman, C. B., Lee, M. K., Davenport, F., Ratovitsky, T., Prada, C.-M., Kim, G., Seekins, S., and Yager, D. (1996) Familial Alzheimer's Disease–Linked Presenilin 1 Variants Elevate Aβ1–42/1–40 Ratio In Vitro and In Vivo, *Neuron 17*, 1005-1013.

59.   Vetrivel, K. S., and Thinakaran, G. (2010) Membrane rafts in Alzheimer's disease beta-amyloid production, *Biochimica et Biophysica Acta (BBA) - Molecular and Cell Biology of Lipids 1801*, 860-867.

60.   Reid, P. C., Urano, Y., Kodama, T., and Hamakubo, T. (2007) Alzheimer's Disease: cholesterol, membrane rafts, isoprenoids and statins, *Journal of Cellular and Molecular Medicine 11*, 383-392.

61.   Zawia, N. H., Lahiri, D. K., and Cardozo-Pelaez, F. (2009) Epigenetics, oxidative stress, and Alzheimer disease, *Free Radical Biology and Medicine 46*, 1241-1249.

62.   Praticò, D. (2008) Evidence of Oxidative Stress in Alzheimer's Disease Brain and Antioxidant Therapy, *Annals of the New York Academy of Sciences 1147*, 70-78.

63.   Wong, G. T., Manfra, D., Poulet, F. M., Zhang, Q., Josien, H., Bara, T., Engstrom, L., Pinzon-Ortiz, M., Fine, J. S., and Lee, H.-J. J. (2004) Chronic treatment with the γ-secretase inhibitor LY-411,575 inhibits β-amyloid peptide production and alters lymphopoiesis and intestinal cell differentiation, *Journal of Biological Chemistry 279*, 12876-12882.

64.   Weggen, S., Eriksen, J. L., Sagi, S. A., Pietrzik, C. U., Ozols, V., Fauq, A., Golde, T. E., and Koo, E. H. (2003) Evidence That Nonsteroidal Anti-inflammatory Drugs Decrease Amyloid β42 Production by Direct Modulation of γ-Secretase Activity, *Journal of Biological Chemistry 278*, 31831-31837.

65.   Lleo, A., Berezovska, O., Herl, L., Raju, S., Deng, A., Bacskai, B. J., Frosch, M. P., Irizarry, M., and Hyman, B. T. (2004) Nonsteroidal anti-inflammatory drugs lower A[beta]42 and change presenilin 1 conformation, *Nat Med 10*, 1065-1066.

66.   Czirr, E., Leuchtenberger, S., Dorner-Ciossek, C., Schneider, A., Jucker, M., Koo, E. H., Pietrzik, C. U., Baumann, K., and Weggen, S. (2007) Insensitivity to Aβ42-lowering Nonsteroidal Anti-inflammatory Drugs and γ-Secretase Inhibitors Is Common among Aggressive Presenilin-1 Mutations, *Journal of Biological Chemistry 282*, 24504-24513.

67.   Takahashi, Y., Hayashi, I., Tominari, Y., Rikimaru, K., Morohashi, Y., Kan, T., Natsugari, H., Fukuyama, T., Tomita, T., and Iwatsubo, T. (2003) Sulindac Sulfide Is a Noncompetitive γ-Secretase Inhibitor That Preferentially Reduces Aβ42 Generation, *Journal of Biological Chemistry 278*, 18664-18670.

68.   Ebke, A., Luebbers, T., Fukumori, A., Shirotani, K., Haass, C., Baumann, K., and Steiner, H. (2011) Novel γ-Secretase Enzyme Modulators Directly Target Presenilin Protein, *Journal of Biological Chemistry 286*, 37181-37186.

69.   Ohki, Y., Higo, T., Uemura, K., Shimada, N., Osawa, S., Berezovska, O., Yokoshima, S., Fukuyama, T., Tomita, T., and Iwatsubo, T. (2011) Phenylpiperidine-type [gamma]-secretase modulators target the transmembrane domain 1 of presenilin 1, *EMBO J 30*, 4815-4824.

70.   Sato, T., Nyborg, A. C., Iwata, N., Diehl, T. S., Saido, T. C., Golde, T. E., and Wolfe, M. S. (2006) Signal peptide peptidase: biochemical properties and modulation by nonsteroidal antiinflammatory drugs, *Biochemistry 45*, 8649-8656.

71.   Okochi, M., Fukumori, A., Jiang, J., Itoh, N., Kimura, R., Steiner, H., Haass, C., Tagami, S., and Takeda, M. (2006) Secretion of the Notch-1 Aβ-like peptide during Notch signaling, *Journal of Biological Chemistry 281*, 7890-7898.

72.   Kukar, T. L., Ladd, T. B., Bann, M. A., Fraering, P. C., Narlawar, R., Maharvi, G. M., Healy, B., Chapman, R., Welzel, A. T., Price, R. W., Moore, B., Rangachari, V., Cusack, B., Eriksen, J., Jansen-West, K., Verbeeck, C., Yager, D., Eckman, C., Ye, W., Sagi, S., Cottrell, B. A., Torpey, J., Rosenberry, T. L., Fauq, A., Wolfe, M. S., Schmidt, B., Walsh, D. M., Koo, E. H., and Golde, T. E. (2008) Substrate-targeting [ggr]-secretase modulators, *Nature 453*, 925-929.

73.   Botev, A., Münter, L.-M., Wenzel, R., Richter, L., Althoff, V., Ismer, J., Gerling, U., Weise, C., Koksch, B., Hildebrand, P. W., Bittl, R., and Multhaup, G. (2010) The APP C-terminal fragment C100 occurs in monomeric and dimeric stable conformations and binds gamma-secretase modulators, *Biochemistry*, null-null.

74.   Richter, L., Munter, L.-M., Ness, J., Hildebrand, P. W., Dasari, M., Unterreitmeier, S., Bulic, B., Beyermann, M., Gust, R., and Reif, B. (2010) Amyloid beta 42 peptide (Aβ42)-lowering compounds directly bind to Aβ and interfere with amyloid precursor protein (APP) transmembrane dimerization, *Proceedings of the National Academy of Sciences 107*, 14597-14602.

75.   Wolozin, B. (2001) A fluid connection: Cholesterol and Aβ, *Proceedings of the National Academy of Sciences 98*, 5371-5373.

76.   Simons, M., Keller, P., Dichgans, J., and Schulz, J. B. (2001) Cholesterol and Alzheimer's disease: Is there a link?, *Neurology 57*, 1089-1093.

77.   Runz, H., Rietdorf, J., Tomic, I., de Bernard, M., Beyreuther, K., Pepperkok, R., and Hartmann, T. (2002) Inhibition of Intracellular Cholesterol Transport Alters Presenilin Localization and Amyloid Precursor Protein Processing in Neuronal Cells, *The Journal of Neuroscience 22*, 1679-1689.

78.   Nicholson, A. M., and Ferreira, A. (2009) Increased Membrane Cholesterol Might Render Mature Hippocampal Neurons More Susceptible to β-Amyloid-Induced Calpain Activation and Tau Toxicity, *The Journal of Neuroscience 29*, 4640-4651.

79.   Di Paolo, G., and Kim, T.-W. (2011) Linking lipids to Alzheimer's disease: cholesterol and beyond, *Nat Rev Neurosci 12*, 284-296.

80.   Abramov, A. Y., Ionov, M., Pavlov, E., and Duchen, M. R. (2011) Membrane cholesterol content plays a key role in the neurotoxicity of β-amyloid: implications for Alzheimer's disease, *Aging Cell 10*, 595-603.

81. Marquer, C., Devauges, V., Cossec, J.-C., Liot, G., Lécart, S., Saudou, F., Duyckaerts, C., Lévêque-Fort, S., and Potier, M.-C. (2011) Local cholesterol increase triggers amyloid precursor protein-Bace1 clustering in lipid rafts and rapid endocytosis, *The FASEB Journal 25*, 1295-1305.

82. Xiong, H., Callaghan, D., Jones, A., Walker, D. G., Lue, L.-F., Beach, T. G., Sue, L. I., Woulfe, J., Xu, H., Stanimirovic, D. B., and Zhang, W. (2008) Cholesterol retention in Alzheimer's brain is responsible for high β- and γ-secretase activities and Aβ production, *Neurobiology of Disease 29*, 422-437.

83. Refolo, L. M., Pappolla, M. A., Malester, B., LaFrancois, J., Bryant-Thomas, T., Wang, R., Tint, G. S., Sambamurti, K., and Duff, K. (2000) Hypercholesterolemia accelerates the Alzheimer's amyloid pathology in a transgenic mouse model, *Neurobiology of Disease 7*, 321-331.

84. Sparks, D. L., Scheff, S. W., Hunsaker III, J. C., Liu, H., Landers, T., and Gross, D. R. (1994) Induction of Alzheimer-like β-amyloid immunoreactivity in the brains of rabbits with dietary cholesterol, *Experimental Neurology 126*, 88-94.

85. Ghribi, O., Larsen, B., Schrag, M., and Herman, M. M. (2006) High cholesterol content in neurons increases BACE, β-amyloid, and phosphorylated tau levels in rabbit hippocampus, *Experimental Neurology 200*, 460-467.

86. Pappolla, M., Bryant-Thomas, T., Herbert, D., Pacheco, J., Garcia, M. F., Manjon, M., Girones, X., Henry, T., Matsubara, E., and Zambon, D. (2003) Mild hypercholesterolemia is an early risk factor for the development of Alzheimer amyloid pathology, *Neurology 61*, 199-205.

87. Stefani, M., and Liguri, G. (2009) Cholesterol in Alzheimers Disease: Unresolved Questions, *Curr Alzheimer Res 6*, 15-29.

88. Björkhem, I., and Meaney, S. (2004) Brain Cholesterol: Long Secret Life Behind a Barrier, *Arteriosclerosis, Thrombosis, and Vascular Biology 24*, 806-815.

89. Bloch, K., Berg, B. N., and Rittenberg, D. (1943) The biological conversion of cholesterol to cholic acid, *Journal of Biological Chemistry 149*, 511-517.

90. Waelsch, H., Sperry, W. M., and Stoyanoff, V. (1940) A study of the synthesis and deposition of lipids in brain and other tissues with deuterium as an indicator, *Journal of Biological Chemistry 135*, 291-296.

91. Björkhem, I., Lütjohann, D., Diczfalusy, U., Ståhle, L., Ahlborg, G., and Wahren, J. (1998) Cholesterol homeostasis in human brain: turnover of 24S-hydroxycholesterol and evidence for a cerebral origin of most of this oxysterol in the circulation, *Journal of lipid research 39*, 1594-1600.

92. Snipes, G., and Suter, U. (1997) Cholesterol and myelin, *Sub-cellular biochemistry 28*, 173.

93.   Poirier, J. (2008) Apolipoprotein E represents a potent gene-based therapeutic target for the treatment of sporadic Alzheimer's disease, *Alzheimer's & Dementia 4*, S91-S97.

94.   Cucchiara, B., and Kasner, S. E. (2001) Use of statins in CNS disorders, *Journal of the Neurological Sciences 187*, 81-89.

95.   Martin, M., Dotti, C. G., and Ledesma, M. D. (2010) Brain cholesterol in normal and pathological aging, *Biochimica et Biophysica Acta (BBA) - Molecular and Cell Biology of Lipids 1801*, 934-944.

96.   Leduc, V., Jasmin-Bélanger, S., and Poirier, J. (2010) APOE and cholesterol homeostasis in Alzheimer's disease, *Trends in Molecular Medicine 16*, 469-477.

97.   van Es, M. A., and van den Berg, L. H. (2009) Alzheimer/'s disease beyond APOE, *Nat Genet 41*, 1047-1048.

98.   Bu, G. (2009) Apolipoprotein E and its receptors in Alzheimer's disease: pathways, pathogenesis and therapy, *Nat Rev Neurosci 10*, 333-344.

99.   Lund, E. G., Guileyardo, J. M., and Russell, D. W. (1999) cDNA cloning of cholesterol 24-hydroxylase, a mediator of cholesterol homeostasis in the brain, *Proceedings of the National Academy of Sciences 96*, 7238-7243.

100.   Greeve, I., Hermans-Borgmeyer, I., Brellinger, C., Kasper, D., Gomez-Isla, T., Behl, C., Levkau, B., and Nitsch, R. M. (2000) The human DIMINUTO/DWARF1 homolog seladin-1 confers resistance to Alzheimer's disease-associated neurodegeneration and oxidative stress, *The Journal of Neuroscience 20*, 7345-7352.

101.   Waterham, H. R., Koster, J., Romeijn, G. J., Hennekam, R., Vreken, P., Andersson, H. C., FitzPatrick, D. R., Kelley, R. I., and Wanders, R. J. (2001) Mutations in the 3β-Hydroxysterol Δ^{24}-Reductase Gene Cause Desmosterolosis, an Autosomal Recessive Disorder of Cholesterol Biosynthesis, *The American Journal of Human Genetics 69*, 685-694.

102.   Iivonen, S., Hiltunen, M., Alafuzoff, I., Mannermaa, A., Kerokoski, P., Puoliväli, J., Salminen, A., Helisalmi, S., and Soininen, H. (2002) Seladin-1 transcription is linked to neuronal degeneration in Alzheimer's disease, *Neuroscience 113*, 301-310.

103.   Crameri, A., Biondi, E., Kuehnle, K., Lütjohann, D., Thelen, K. M., Perga, S., Dotti, C. G., Nitsch, R. M., Ledesma, M. D., and Mohajeri, M. H. (2006) The role of seladin-1/DHCR24 in cholesterol biosynthesis, APP processing and Aβ generation in vivo, *The EMBO journal 25*, 432-443.

104.   Brown, D. A., and London, E. (2000) Structure and Function of Sphingolipid- and Cholesterol-rich Membrane Rafts, *Journal of Biological Chemistry 275*, 17221-17224.

105.   Silvius, J. R. (2003) Role of cholesterol in lipid raft formation: lessons from lipid model systems, *Biochimica et Biophysica Acta (BBA) - Biomembranes 1610*, 174-183.

106. Sankaram, M. B., and Thompson, T. E. (1990) Interaction of cholesterol with various glycerophospholipids and sphingomyelin, *Biochemistry 29*, 10670-10675.

107. Veatch, S. L., and Keller, S. L. (2005) Miscibility Phase Diagrams of Giant Vesicles Containing Sphingomyelin, *Physical Review Letters 94*, 148101.

108. Saher, G., Brugger, B., Lappe-Siefke, C., Mobius, W., Tozawa, R.-i., Wehr, M. C., Wieland, F., Ishibashi, S., and Nave, K.-A. (2005) High cholesterol level is essential for myelin membrane growth, *Nat Neurosci 8*, 468-475.

109. Heino, S., Lusa, S., Somerharju, P., Ehnholm, C., Olkkonen, V. M., and Ikonen, E. (2000) Dissecting the role of the Golgi complex and lipid rafts in biosynthetic transport of cholesterol to the cell surface, *Proceedings of the National Academy of Sciences 97*, 8375-8380.

110. Hartmann, T., Bieger, S. C., Brühl, B., Tienari, P. J., Ida, N., Allsop, D., Roberts, G. W., Masters, C. L., Dotti, C. G., and Unsicker, K. (1997) Distinct sites of intracellular production for Alzheimer's disease Aβ40/42 amyloid peptides, *Nature medicine 3*, 1016-1020.

111. Wood, W. G., Schroeder, F., Igbavboa, U., Avdulov, N. A., and Chochina, S. V. (2002) Brain membrane cholesterol domains, aging and amyloid beta-peptides, *Neurobiology of Aging 23*, 685-694.

112. Schroeder, F. (1985) Role of membrane lipid asymmetry in aging, *Neurobiology of Aging 5*, 323-333.

113. Muralikrishna Rao, A., Igbavboa, U., Semotuk, M., Schroeder, F., and Gibson Wood, W. (1993) Kinetics and size of cholesterol lateral domains in synaptosomal membranes: modification by sphingomyelinase and effects on membrane enzyme activity, *Neurochemistry international 23*, 45-52.

114. Igbavboa, U., Avdulov, N. A., Schroeder, F., and Wood, W. G. (1996) Increasing age alters transbilayer fluidity and cholesterol asymmetry in synaptic plasma membranes of mice, *Journal of Neurochemistry 66*, 1717-1725.

115. Simons, K., and Ikonen, E. (2000) How cells handle cholesterol, *Science 290*, 1721-1726.

116. Cordy, J. M., Hooper, N. M., and Turner, A. J. (2006) The involvement of lipid rafts in Alzheimer's disease (Review), *Molecular Membrane Biology 23*, 111-122.

117. Rushworth, J. V., and Hooper, N. M. (2011) Lipid Rafts: Linking Alzheimer's Amyloid-Beta; Production, Aggregation, and Toxicity at Neuronal Membranes, *International Journal of Alzheimer's Disease 2011*.

118. Hicks, D. A., Nalivaeva, N. N., and Turner, A. J. (2012) Lipid rafts and Alzheimer's disease: protein-lipid interactions and perturbation of signalling, *Frontiers in Physiology 3*.

119. Simons, M., Keller, P., De Strooper, B., Beyreuther, K., Dotti, C. G., and Simons, K. (1998) Cholesterol depletion inhibits the generation of β-amyloid in hippocampal neurons, *Proceedings of the National Academy of Sciences 95*, 6460-6464.

120. Kosicek, M., Malnar, M., Goate, A., and Hecimovic, S. (2010) Cholesterol accumulation in Niemann Pick type C (NPC) model cells causes a shift in APP localization to lipid rafts, *Biochemical and Biophysical Research Communications 393*, 404-409.

121. Kinoshita, A., Fukumoto, H., Shah, T., Whelan, C. M., Irizarry, M. C., and Hyman, B. T. (2003) Demonstration by FRET of BACE interaction with the amyloid precursor protein at the cell surface and in early endosomes, *J Cell Sci 116*, 3339-3346.

122. Rajendran, L., Schneider, A., Schlechtingen, G., Weidlich, S., Ries, J., Braxmeier, T., Schwille, P., Schulz, J. B., Schroeder, C., Simons, M., Jennings, G., Knölker, H.-J., and Simons, K. (2008) Efficient Inhibition of the Alzheimer's Disease β-Secretase by Membrane Targeting, *Science 320*, 520-523.

123. Kalvodova, L., Kahya, N., Schwille, P., Ehehalt, R., Verkade, P., Drechsel, D., and Simons, K. (2005) Lipids as Modulators of Proteolytic Activity of BACE, *Journal of Biological Chemistry 280*, 36815-36823.

124. Pralle, A., Keller, P., Florin, E.-L., Simons, K., and Hörber, J. (2000) Sphingolipid–cholesterol rafts diffuse as small entities in the plasma membrane of mammalian cells, *The Journal of Cell Biology 148*, 997-1008.

125. Walsh, D. M., Klyubin, I., Fadeeva, J. V., Cullen, W. K., Anwyl, R., Wolfe, M. S., Rowan, M. J., and Selkoe, D. J. (2002) Naturally secreted oligomers of amyloid β protein potently inhibit hippocampal long-term potentiation in vivo, *Nature 416*, 535-539.

126. Simakova, O., and Arispe, N. J. (2007) The cell-selective neurotoxicity of the Alzheimer's Aβ peptide is determined by surface phosphatidylserine and cytosolic ATP levels. Membrane binding is required for Aβ toxicity, *The Journal of Neuroscience 27*, 13719-13729.

127. Kawarabayashi, T., Shoji, M., Younkin, L. H., Wen-Lang, L., Dickson, D. W., Murakami, T., Matsubara, E., Abe, K., Ashe, K. H., and Younkin, S. G. (2004) Dimeric amyloid β protein rapidly accumulates in lipid rafts followed by apolipoprotein E and phosphorylated tau accumulation in the Tg2576 mouse model of Alzheimer's disease, *The Journal of Neuroscience 24*, 3801-3809.

128. Gylys, K. H., Fein, J. A., Yang, F., Miller, C. A., and Cole, G. M. (2007) Increased cholesterol in Aβ-positive nerve terminals from Alzheimer's disease cortex, *Neurobiology of Aging 28*, 8-17.

129. Fujinaga, Y., Wolf, A. A., Rodighiero, C., Wheeler, H., Tsai, B., Allen, L., Jobling, M. G., Rapoport, T., Holmes, R. K., and Lencer, W. I. (2003) Gangliosides that associate with lipid rafts mediate transport of cholera and related toxins from the plasma membrane to endoplasmic reticulm, *Molecular biology of the cell 14*, 4783-4793.

130. Molander-Melin, M., Blennow, K., Bogdanovic, N., Dellheden, B., Månsson, J. E., and Fredman, P. (2005) Structural membrane alterations in Alzheimer brains found to be associated with regional disease development; increased density of gangliosides GM1 and GM2 and loss of cholesterol in detergent-resistant membrane domains, *Journal of Neurochemistry 92*, 171-182.

131. Yanagisawa, K., Odaka, A., Suzuki, N., and Ihara, Y. (1995) GM1 ganglioside–bound amyloid β–protein (Aβ): A possible form of preamyloid in Alzheimer's disease, *Nature medicine 1*, 1062-1066.

132. Matsuzaki, K., Kato, K., and Yanagisawa, K. (2010) Aβ polymerization through interaction with membrane gangliosides, *Biochimica et Biophysica Acta (BBA)-Molecular and Cell Biology of Lipids 1801*, 868-877.

133. Hynd, M. R., Scott, H. L., and Dodd, P. R. (2004) Glutamate-mediated excitotoxicity and neurodegeneration in Alzheimer's disease, *Neurochemistry international 45*, 583-595.

134. Ascher, P., and Nowak, L. (1988) The role of divalent cations in the N-methyl-D-aspartate responses of mouse central neurones in culture, *The Journal of Physiology 399*, 247-266.

135. Swanwick, C., Chang, K., and Wenthold, R. (2006) Interaction of N-methyl-D-aspartate (NMDA) receptors with flotillin-1, a lipid raft-associated protein, *Soc Neurosci Abs 31*, 4.

136. Hering, H., Lin, C.-C., and Sheng, M. (2003) Lipid Rafts in the Maintenance of Synapses, Dendritic Spines, and Surface AMPA Receptor Stability, *The Journal of Neuroscience 23*, 3262-3271.

137. Besshoh, S., Chen, S., Brown, I. R., and Gurd, J. W. (2007) Developmental changes in the association of NMDA receptors with lipid rafts, *Journal of neuroscience research 85*, 1876-1883.

138. Deshpande, A., Kawai, H., Metherate, R., Glabe, C. G., and Busciglio, J. (2009) A role for synaptic zinc in activity-dependent Aβ oligomer formation and accumulation at excitatory synapses, *The Journal of Neuroscience 29*, 4004-4015.

139. Renner, M., Lacor, P. N., Velasco, P. T., Xu, J., Contractor, A., Klein, W. L., and Triller, A. (2010) Deleterious Effects of Amyloid β Oligomers Acting as an Extracellular Scaffold for mGluR5, *Neuron 66*, 739-754.

140. Shankar, G. M., Bloodgood, B. L., Townsend, M., Walsh, D. M., Selkoe, D. J., and Sabatini, B. L. (2007) Natural oligomers of the Alzheimer amyloid-β protein induce reversible synapse loss by modulating an NMDA-type glutamate receptor-dependent signaling pathway, *The Journal of Neuroscience 27*, 2866-2875.

141. Tackenberg, C., and Brandt, R. (2009) Divergent pathways mediate spine alterations and cell death induced by amyloid-β, wild-type tau, and R406W tau, *The Journal of Neuroscience 29*, 14439-14450.

142.   De Felice, F. G., Velasco, P. T., Lambert, M. P., Viola, K., Fernandez, S. J., Ferreira, S. T., and Klein, W. L. (2007) Aβ oligomers induce neuronal oxidative stress through an N-methyl-D-aspartate receptor-dependent mechanism that is blocked by the Alzheimer drug memantine, *Journal of Biological Chemistry 282*, 11590-11601.

143.   Lau, A., and Tymianski, M. (2010) Glutamate receptors, neurotoxicity and neurodegeneration, *Pflügers Archiv-European Journal of Physiology 460*, 525-542.

144.   Wu, J., Harney, S., Rowan, M. J., and Anwyl, R. (2008) Involvement of group I mGluRs in LTP induced by strong high frequency stimulation in the dentate gyrus in vitro, *Neuroscience letters 436*, 235-238.

145.   Bonsi, P., Cuomo, D., De Persis, C., Centonze, D., Bernardi, G., Calabresi, P., and Pisani, A. (2005) Modulatory action of metabotropic glutamate receptor (mGluR) 5 on mGluR1 function in striatal cholinergic interneurons, *Neuropharmacology 49*, 104-113.

146.   Barrett, P. J., Chen, J., Cho, M.-K., Kim, J.-H., Lu, Z., Mathew, S., Peng, D., Song, Y., Van Horn, W. D., and Zhuang, T. (2013) The quiet renaissance of protein nuclear magnetic resonance, *Biochemistry 52*, 1303-1320.

147.   Meyer, B., and Peters, T. (2003) NMR Spectroscopy Techniques for Screening and Identifying Ligand Binding to Protein Receptors, *Angewandte Chemie International Edition 42*, 864-890.

148.   Hong, M., Zhang, Y., and Hu, F. (2012) Membrane protein structure and dynamics from NMR spectroscopy, *Annual Review of Physical Chemistry 63*, 1-24.

149.   Filler, A. G. (2011) The History, Development and Impact of Computed Imaging in Neurological Diagnosis and Neurosurgery: CT, MRI, and DTI, *Nature Procedings Web site.*

150.   Rabi, I. I., Zacharias, J. R., Millman, S., and Kusch, P. (1938) A New Method of Measuring Nuclear Magnetic Moment, *Physical Review 53*, 318-318.

151.   Keeler, J. (2011) *Understanding NMR spectroscopy*, Wiley. com.

152.   Danielson, M. A., and Falke, J. J. (1996) Use of 19F NMR to Probe Protein Structure and Conformational Changes, *Annual Review of Biophysics and Biomolecular Structure 25*, 163-195.

153.   Gerig, J. (1994) Fluorine NMR of proteins, *Progress in Nuclear Magnetic Resonance Spectroscopy 26*, 293-370.

154.   Kitevski-LeBlanc, J. L., and Prosser, R. S. (2012) Current applications of 19F NMR to studies of protein structure and dynamics, *Progress in Nuclear Magnetic Resonance Spectroscopy 62*, 1-33.

155.   Jackson, J. C., Hammill, J. T., and Mehl, R. A. (2007) Site-Specific Incorporation of a 19F-Amino Acid into Proteins as an NMR Probe for Characterizing Protein Structure and Reactivity, *Journal of the American Chemical Society 129*, 1160-1166.

156. Shi, P., Wang, H., Xi, Z., Shi, C., Xiong, Y., and Tian, C. (2011) Site-specific 19F NMR chemical shift and side chain relaxation analysis of a membrane protein labeled with an unnatural amino acid, *Protein Science 20*, 224-228.

157. Bodenhausen, G., and Ruben, D. J. (1980) Natural abundance nitrogen-15 NMR by enhanced heteronuclear spectroscopy, *Chemical Physics Letters 69*, 185-189.

158. Pervushin, K., Riek, R., Wider, G., and Wüthrich, K. (1997) Attenuated T2 relaxation by mutual cancellation of dipole–dipole coupling and chemical shift anisotropy indicates an avenue to NMR structures of very large biological macromolecules in solution, *Proceedings of the National Academy of Sciences 94*, 12366-12371.

159. Endo, Y., and Sawasaki, T. (2006) Cell-free expression systems for eukaryotic protein production, *Current Opinion in Biotechnology 17*, 373-380.

160. Selenko, P., Serber, Z., Gadea, B., Ruderman, J., and Wagner, G. (2006) Quantitative NMR analysis of the protein G B1 domain in Xenopus laevis egg extracts and intact oocytes, *Proceedings of the National Academy of Sciences 103*, 11904-11909.

161. Serber, Z., Selenko, P., Hansel, R., Reckel, S., Lohr, F., Ferrell, J. E., Wagner, G., and Dotsch, V. (2007) Investigating macromolecules inside cultured and injected cells by in-cell NMR spectroscopy, *Nat. Protocols 1*, 2701-2709.

162. Gardner, K. H., and Kay, L. E. (1998) THE USE OF 2H, 13C, 15N MULTIDIMENSIONAL NMR GTO STUDY THE STRUCTURE AND DYNAMICS OF PROTEINS, *Annual Review of Biophysics and Biomolecular Structure 27*, 357-406.

163. Venters, R. A., Huang, C.-C., Farmer II, B. T., Trolard, R., Spicer, L. D., and Fierke, C. A. (1995) High-level 2H/13C/15N labeling of proteins for NMR studies, *Journal of Biomolecular NMR 5*, 339-344.

164. Kemmink, J., Darby, N. J., Dijkstra, K., Nilges, M., and Creighton, T. E. (1996) Structure determination of the N-terminal thioredoxin-like domain of protein disulfide isomerase using multidimensional heteronuclear 13C/15N NMR spectroscopy, *Biochemistry 35*, 7684-7691.

165. Agnew, W. S., and Raftery, M. A. (1979) Solubilized tetrodotoxin binding component from the electroplax of Electrophorus electricus. Stability as a function of mixed lipid-detergent micelle composition, *Biochemistry 18*, 1912-1919.

166. Fernández, C., and Wüthrich, K. (2003) NMR solution structure determination of membrane proteins reconstituted in detergent micelles, *FEBS letters 555*, 144-150.

167. Sanders, C. R., and Landis, G. C. (1995) Reconstitution of membrane proteins into lipid-rich bilayered mixed micelles for NMR studies, *Biochemistry 34*, 4030-4040.

168. Losonczi, J. A., and Prestegard, J. H. (1998) Improved dilute bicelle solutions for high-resolution NMR of biological macromolecules, *Journal of Biomolecular NMR 12*, 447-451.

169. Marcotte, I., and Auger, M. (2005) Bicelles as model membranes for solid-and solution-state NMR studies of membrane peptides and proteins, *Concepts in Magnetic Resonance Part A 24*, 17-37.

170. Klammt, C., Maslennikov, I., Bayrhuber, M., Eichmann, C., Vajpai, N., Chiu, E. J. C., Blain, K. Y., Esquivies, L., Kwon, J. H. J., Balana, B., Pieper, U., Sali, A., Slesinger, P. A., Kwiatkowski, W., Riek, R., and Choe, S. (2012) Facile backbone structure determination of human membrane proteins by NMR spectroscopy, *Nat Meth advance online publication*.

171. Van Horn, W. D., Kim, H.-J., Ellis, C. D., Hadziselimovic, A., Sulistijo, E. S., Karra, M. D., Tian, C., Sönnichsen, F. D., and Sanders, C. R. (2009) Solution Nuclear Magnetic Resonance Structure of Membrane-Integral Diacylglycerol Kinase, *Science 324*, 1726-1729.

172. Schwieters, C. D., Kuszewski, J. J., Tjandra, N., and Marius Clore, G. (2003) The Xplor-NIH NMR molecular structure determination package, *Journal of Magnetic Resonance 160*, 65-73.

173. Trbovic, N., Klammt, C., Koglin, A., Löhr, F., Bernhard, F., and Dötsch, V. (2005) Efficient Strategy for the Rapid Backbone Assignment of Membrane Proteins, *Journal of the American Chemical Society 127*, 13504-13505.

174. Salzmann, M., Wider, G., Pervushin, K., Senn, H., and Wüthrich, K. (1999) TROSY-type triple-resonance experiments for sequential NMR assignments of large proteins, *Journal of the American Chemical Society 121*, 844-848.

175. Ikura, M., Kay, L. E., and Bax, A. (1990) A novel approach for sequential assignment of proton, carbon-13, and nitrogen-15 spectra of larger proteins: heteronuclear triple-resonance three-dimensional NMR spectroscopy. Application to calmodulin, *Biochemistry 29*, 4659-4667.

176. Bax, A., and Ikura, M. (1991) An efficient 3D NMR technique for correlating the proton and15N backbone amide resonances with the α-carbon of the preceding residue in uniformly15N/13C enriched proteins, *Journal of Biomolecular NMR 1*, 99-104.

177. Wishart, D., Sykes, B., and Richards, F. (1992) The chemical shift index: a fast and simple method for the assignment of protein secondary structure through NMR spectroscopy, *Biochemistry 31*, 1647-1651.

178. Wishart, D. S., and Sykes, B. D. (1994) The 13C chemical-shift index: a simple method for the identification of protein secondary structure using 13C chemical-shift data, *Journal of Biomolecular NMR 4*, 171-180.

179. Shen, Y., Delaglio, F., Cornilescu, G., and Bax, A. (2009) TALOS+: a hybrid method for predicting protein backbone torsion angles from NMR chemical shifts, *Journal of Biomolecular NMR 44*, 213-223.

180. Kaiser, R. (1963) Use of the Nuclear Overhauser Effect in the Analysis of High-Resolution Nuclear Magnetic Resonance Spectra, *The Journal of Chemical Physics 39*, 2435.

181. Anet, F., and Bourn, A. (1965) Nuclear Magnetic Resonance Spectral Assignments from Nuclear Overhauser Effects1, *Journal of the American Chemical Society 87*, 5250-5251.

182. Kumar, A., Ernst, R., and Wüthrich, K. (1980) A two-dimensional nuclear Overhauser enhancement (2D NOE) experiment for the elucidation of complete proton-proton cross-relaxation networks in biological macromolecules, *Biochemical and Biophysical Research Communications 95*, 1-6.

183. Keepers, J. W., and James, T. L. (1984) A theoretical study of distance determinations from NMR. Two-dimensional nuclear Overhauser effect spectra, *Journal of Magnetic Resonance (1969) 57*, 404-426.

184. Religa, T. L., Ruschak, A. M., Rosenzweig, R., and Kay, L. E. (2011) Site-Directed Methyl Group Labeling as an NMR Probe of Structure and Dynamics in Supramolecular Protein Systems: Applications to the Proteasome and to the ClpP Protease, *Journal of the American Chemical Society 133*, 9063-9068.

185. Gill, M., and Palmer, A. (2011) Multiplet-filtered and gradient-selected zero-quantum TROSY experiments for ^{13}C, ^{1}H$_3$ methyl groups in proteins, *Journal of Biomolecular NMR 51*, 245-251.

186. Isaacson, R. L., Simpson, P. J., Liu, M., Cota, E., Zhang, X., Freemont, P., and Matthews, S. (2007) A New Labeling Method for Methyl Transverse Relaxation-Optimized Spectroscopy NMR Spectra of Alanine Residues, *Journal of the American Chemical Society 129*, 15428-15429.

187. Fischer, M., Kloiber, K., Häusler, J., Ledolter, K., Konrat, R., and Schmid, W. (2007) Synthesis of a 13C-Methyl-Group-Labeled Methionine Precursor as a Useful Tool for Simplifying Protein Structural Analysis by NMR Spectroscopy, *ChemBioChem 8*, 610-612.

188. Battiste, J. L., and Wagner, G. (2000) Utilization of Site-Directed Spin Labeling and High-Resolution Heteronuclear Nuclear Magnetic Resonance for Global Fold Determination of Large Proteins with Limited Nuclear Overhauser Effect Data†, *Biochemistry 39*, 5355-5365.

189. Solomon, I. (1955) Relaxation Processes in a System of Two Spins, *Physical Review 99*, 559-565.

190. Kosen, P. A. (1989) [5] Spin labeling of proteins, In *Methods in Enzymology* (Norman, J. O., and Thomas, L. J., Eds.), pp 86-121, Academic Press.

191. Donaldson, L. W., Skrynnikov, N. R., Choy, W.-Y., Muhandiram, D. R., Sarkar, B., Forman-Kay, J. D., and Kay, L. E. (2001) Structural Characterization of Proteins with an Attached ATCUN Motif by Paramagnetic Relaxation Enhancement NMR Spectroscopy, *Journal of the American Chemical Society 123*, 9843-9847.

192. Berardi, M. J., Shih, W. M., Harrison, S. C., and Chou, J. J. (2011) Mitochondrial uncoupling protein 2 structure determined by NMR molecular fragment searching, *Nature advance online publication*.

193. Tang, C., Schwieters, C. D., and Clore, G. M. (2007) Open-to-closed transition in apo maltose-binding protein observed by paramagnetic NMR, *Nature 449*, 1078-1082.

194. Otting, G. (2010) Protein NMR Using Paramagnetic Ions, *Annual Review of Biophysics 39*, 387-405.

195. Rodriguez-Castañeda, F., Haberz, P., Leonov, A., and Griesinger, C. (2006) Paramagnetic tagging of diamagnetic proteins for solution NMR, *Magnetic Resonance in Chemistry 44*, S10-S16.

196. Iwahara, J., Tang, C., and Marius Clore, G. (2007) Practical aspects of 1H transverse paramagnetic relaxation enhancement measurements on macromolecules, *Journal of Magnetic Resonance 184*, 185-195.

197. Liang, B., Bushweller, J. H., and Tamm, L. K. (2006) Site-Directed Parallel Spin-Labeling and Paramagnetic Relaxation Enhancement in Structure Determination of Membrane Proteins by Solution NMR Spectroscopy, *Journal of the American Chemical Society 128*, 4389-4397.

198. Zhou, Y., Cierpicki, T., Jimenez, R. H. F., Lukasik, S. M., Ellena, J. F., Cafiso, D. S., Kadokura, H., Beckwith, J., and Bushweller, J. H. (2008) NMR solution structure of the integral membrane enzyme DsbB: functional insights into DsbB-catalyzed disulfide bond formation, *Molecular Cell 31*, 896-908.

199. Chen, H., Ji, F., Olman, V., Mobley, C. K., Liu, Y., Zhou, Y., Bushweller, J. H., Prestegard, J. H., and Xu, Y. (2011) Optimal mutation sites for PRE data collection and membrane protein structure prediction, *Structure 19*, 484-495.

200. Zhuang, T., Vishnivetskiy, S. A., Gurevich, V. V., and Sanders, C. R. (2010) Elucidation of Inositol Hexaphosphate and Heparin Interaction Sites and Conformational Changes in Arrestin-1 by Solution Nuclear Magnetic Resonance, *Biochemistry 49*, 10473-10485.

201. Venditti, V., Fawzi, N., and Clore, G. (2011) Automated sequence- and stereo-specific assignment of methyl-labeled proteins by paramagnetic relaxation and methyl–methyl nuclear overhauser enhancement spectroscopy, *Journal of Biomolecular NMR 51*, 319-328.

202. Theillet, F.-X., Binolfi, A., Liokatis, S., Verzini, S., and Selenko, P. (2011) Paramagnetic relaxation enhancement to improve sensitivity of fast NMR methods: application to intrinsically disordered proteins, *Journal of Biomolecular NMR 51*, 487-495.

203. Sivakolundu, S. G., Nourse, A., Moshiach, S., Bothner, B., Ashley, C., Satumba, J., Lahti, J., and Kriwacki, R. W. (2008) Intrinsically Unstructured Domains of Arf and Hdm2 Form Bimolecular Oligomeric Structures In Vitro and In Vivo, *Journal of Molecular Biology 384*, 240-254.

204. Madl, T., Güttler, T., Görlich, D., and Sattler, M. (2011) Structural Analysis of Large Protein Complexes Using Solvent Paramagnetic Relaxation Enhancements, *Angewandte Chemie International Edition 50*, 3993-3997.

205. Tang, C., Louis, J. M., Aniana, A., Suh, J.-Y., and Clore, G. M. (2008) Visualizing transient events in amino-terminal autoprocessing of HIV-1 protease, *Nature 455*, 693-696.

206. Clore, G. M. (2011) Exploring sparsely populated states of macromolecules by diamagnetic and paramagnetic NMR relaxation, *Protein Science 20*, 229-246.

207. Prestegard, J., Al-Hashimi, H., and Tolman, J. (2000) NMR structures of biomolecules using field oriented media and residual dipolar couplings, *Quarterly reviews of biophysics 33*, 371-424.

208. Prestegard, J. H., Bougault, C. M., and Kishore, A. I. (2004) Residual Dipolar Couplings in Structure Determination of Biomolecules, *Chemical Reviews 104*, 3519-3540.

209. Lipsitz, R. S., and Tjandra, N. (2004) RESIDUAL DIPOLAR COUPLINGS IN NMR STRUCTURE ANALYSIS*1, *Annual Review of Biophysics and Biomolecular Structure 33*, 387-413.

210. Chen, K., and Tjandra, N. (2007) Top-down approach in protein RDC data analysis: de novo estimation of the alignment tensor, *Journal of Biomolecular NMR 38*, 303-313.

211. Schweiger, A., and Jeschke, G. (2001) *Principles of pulse electron paramagnetic resonance spectroscopy*, Oxford University Press.

212. Borbat, P., Costa-Filho, A., Earle, K., Moscicki, J., and Freed, J. (2001) Electron spin resonance in studies of membranes and proteins, *Science 291*, 266-269.

213. Altenbach, C., Froncisz, W., Hyde, J. S., and Hubbell, W. L. (1989) Conformation of spin-labeled melittin at membrane surfaces investigated by pulse saturation recovery and continuous wave power saturation electron paramagnetic resonance, *Biophysical Journal 56*, 1183-1191.

214. Altenbach, C., Greenhalgh, D. A., Khorana, H. G., and Hubbell, W. L. (1994) A collision gradient method to determine the immersion depth of nitroxides in lipid bilayers: application to spin-labeled mutants of bacteriorhodopsin, *Proceedings of the National Academy of Sciences 91*, 1667-1671.

215. Altenbach, C., Froncisz, W., Hemker, R., Mchaourab, H., and Hubbell, W. L. (2005) Accessibility of nitroxide side chains: absolute Heisenberg exchange rates from power saturation EPR, *Biophysical Journal 89*, 2103-2112.

216. Kevan, L., and Kispert, L. D. (1976) *Electron spin double resonance spectroscopy*, Wiley New York.

217. Larsen, R. G., and Singel, D. J. (1993) Double electron–electron resonance spin–echo modulation: spectroscopic measurement of electron spin pair separations in orientationally disordered solids, *The Journal of Chemical Physics 98*, 5134.

218. Martin, R. E., Pannier, M., Diederich, F., Gramlich, V., Hubrich, M., and Spiess, H. W. (1998) Determination of End-to-End Distances in a Series of TEMPO Diradicals of up to 2.8 nm Length with a New Four-Pulse Double Electron Electron Resonance Experiment, *Angewandte Chemie International Edition 37*, 2833-2837.

219. Jeschke, G. (2002) Distance Measurements in the Nanometer Range by Pulse EPR, *ChemPhysChem 3*, 927-932.

220. Wishart, D. S., and Sykes, B. D. (1994) [12] Chemical shifts as a tool for structure determination, In *Methods in Enzymology* (Thomas L. James, N. J. O., Ed.), pp 363-392, Academic Press.

221. Lau, T.-L., Kim, C., Ginsberg, M. H., and Ulmer, T. S. (2009) The structure of the integrin [alpha]IIb[beta]3 transmembrane complex explains integrin transmembrane signalling, *EMBO J 28*, 1351-1361.

222. Soler-López, M., Zanzoni, A., Lluís, R., Stelzl, U., and Aloy, P. (2011) Interactome mapping suggests new mechanistic details underlying Alzheimer's disease, *Genome Research 21*, 364-376.

223. Tamayev, R., Zhou, D., and D'Adamio, L. (2009) The interactome of the amyloid beta precursor protein family members is shaped by phosphorylation of their intracellular domains, *Molecular Neurodegeneration 4*, 28.

224. Lee, M.-S., Kao, S.-C., Lemere, C. A., Xia, W., Tseng, H.-C., Zhou, Y., Neve, R., Ahlijanian, M. K., and Tsai, L.-H. (2003) APP processing is regulated by cytoplasmic phosphorylation, *The Journal of Cell Biology 163*, 83-95.

225. Angelova, M., Soléau, S., Méléard, P., Faucon, F., and Bothorel, P. (1992) Preparation of giant vesicles by external AC electric fields. Kinetics and applications, In *Trends in Colloid and Interface Science VI* (Helm, C., Lösche, M., and Möhwald, H., Eds.), pp 127-131, Springer Berlin / Heidelberg.

226. Moscho, A., Orwar, O., Chiu, D. T., Modi, B. P., and Zare, R. N. (1996) Rapid preparation of giant unilamellar vesicles, *Proceedings of the National Academy of Sciences 93*, 11443-11447.

227. Korlach, J., Schwille, P., Webb, W. W., and Feigenson, G. W. (1999) Characterization of lipid bilayer phases by confocal microscopy and fluorescence correlation spectroscopy, *Proceedings of the National Academy of Sciences 96*, 8461-8466.

228. Veatch, S. L., and Keller, S. L. (2003) Separation of Liquid Phases in Giant Vesicles of Ternary Mixtures of Phospholipids and Cholesterol, *Biophysical Journal 85*, 3074-3083.

229. Veatch, S. L., Polozov, I. V., Gawrisch, K., and Keller, S. L. (2004) Liquid Domains in Vesicles Investigated by NMR and Fluorescence Microscopy, *Biophysical Journal 86*, 2910-2922.

230. de Almeida, R. F. M., Fedorov, A., and Prieto, M. (2003) Sphingomyelin/Phosphatidylcholine/Cholesterol Phase Diagram: Boundaries and Composition of Lipid Rafts, *Biophysical Journal 85*, 2406-2416.

231. Zhao, J., Wu, J., Heberle, F. A., Mills, T. T., Klawitter, P., Huang, G., Costanza, G., and Feigenson, G. W. (2007) Phase studies of model biomembranes: Complex behavior of DSPC/DOPC/Cholesterol, *Biochimica et Biophysica Acta (BBA) - Biomembranes 1768*, 2764-2776.

232. Sengupta, P., Hammond, A., Holowka, D., and Baird, B. (2008) Structural determinants for partitioning of lipids and proteins between coexisting fluid phases in giant plasma membrane vesicles, *Biochimica et Biophysica Acta (BBA) - Biomembranes 1778*, 20-32.

233. Ionova, Irina V., Livshits, Vsevolod A., and Marsh, D. (2012) Phase Diagram of Ternary Cholesterol/Palmitoylsphingomyelin/Palmitoyloleoyl-Phosphatidylcholine Mixtures: Spin-Label EPR Study of Lipid-Raft Formation, *Biophysical Journal 102*, 1856-1865.

234. Angelova, M., and Dimitrov, D. (1988) A mechanism of liposome electroformation, In *Trends in Colloid and Interface Science II* (Degiorgio, V., Ed.), pp 59-67, Springer Berlin / Heidelberg.

235. Veatch, S. L., and Keller, S. L. (2002) Organization in Lipid Membranes Containing Cholesterol, *Physical Review Letters 89*, 268101.

236. Zhou, Y., Berry, C. K., Storer, P. A., and Raphael, R. M. (2007) Peroxidation of polyunsaturated phosphatidyl-choline lipids during electroformation, *Biomaterials 28*, 1298-1306.

237. Pester, O., Barrett, P. J., Hornburg, D., Hornburg, P., Pröbstle, R., Widmaier, S., Kutzner, C., Dürrbaum, M., Kapurniotu, A., and Sanders, C. R. (2013) The Backbone Dynamics of the Amyloid Precursor Protein Transmembrane Helix Provides a Rationale for the Sequential Cleavage Mechanism of γ-Secretase, *Journal of the American Chemical Society 135*, 1317-1329.

238. Haass, C., and Selkoe, D. J. (2007) Soluble protein oligomers in neurodegeneration: lessons from the Alzheimer's amyloid β-peptide, *Nature reviews Molecular cell biology 8*, 101-112.

239. Kukar, T. L., Ladd, T. B., Robertson, P., Pintchovski, S. A., Moore, B., Bann, M. A., Ren, Z., Jansen-West, K., Malphrus, K., Eggert, S., Maruyama, H., Cottrell, B. A., Das, P., Basi, G. S., Koo, E. H., and Golde, T. E. (2011) Lysine 624 of the amyloid precursor protein (APP) is a critical determinant of amyloid β peptide length: support for a sequential model of γ-secretase intramembrane proteolysis and regulation by the APP juxtamembrane region, *Journal of Biological Chemistry*.

240. Takami, M., Nagashima, Y., Sano, Y., Ishihara, S., Morishima-Kawashima, M., Funamoto, S., and Ihara, Y. (2009) γ-Secretase: successive tripeptide and tetrapeptide release from the transmembrane domain of β-carboxyl terminal fragment, *The Journal of Neuroscience 29*, 13042-13052.

241. Lu, J.-X., Yau, W.-M., and Tycko, R. (2011) Evidence from Solid-State NMR for Nonhelical Conformations in the Transmembrane Domain of the Amyloid Precursor Protein, *Biophysical Journal 100*, 711-719.

242. Botev, A., Munter, L.-M., Wenzel, R., Richter, L., Althoff, V., Ismer, J., Gerling, U., Weise, C., Koksch, B., Hildebrand, P. W., Bittl, R., and Multhaup, G. (2010) The Amyloid Precursor Protein C-Terminal Fragment C100 Occurs in Monomeric and Dimeric Stable Conformations and Binds γ-Secretase Modulators, *Biochemistry 50*, 828-835.

243. Nadezhdin, K., Bocharova, O., Bocharov, E., and Arseniev, A. (2011) Structural and Dynamic Study of the Transmembrane Domain of the Amyloid Precursor Protein, *Acta naturae 3*, 69.

244. Johnson, B. A., and Blevins, R. A. (1994) NMR View: A computer program for the visualization and analysis of NMR data, *Journal of Biomolecular NMR 4*, 603-614.

245. Kneller, T. D. G. a. D. G., and (2007) Sparky, In *University of California*, San Francisco.

246. Delaglio, F., Grzesiek, S., Vuister, G. W., Zhu, G., Pfeifer, J., and Bax, A. (1995) NMRPipe: A multidimensional spectral processing system based on UNIX pipes, *Journal of Biomolecular NMR 6*, 277-293.

247. Beel, A. J., Mobley, C. K., Kim, H. J., Tian, F., Hadziselimovic, A., Jap, B., Prestegard, J. H., and Sanders, C. R. (2008) Structural Studies of the Transmembrane C-Terminal Domain of the Amyloid Precursor Protein (APP): Does APP Function as a Cholesterol Sensor?, *Biochemistry 47*, 9428-9446.

248. Cornish, V. W., Kaplan, M. I., Veenstra, D. L., Kollman, P. A., and Schultz, P. G. (1994) Stabilizing and Destabilizing Effects of Placing .beta.-Branched Amino Acids in Protein .alpha.-Helixes, *Biochemistry 33*, 12022-12031.

249. Poschner, B. C., Quint, S., Hofmann, M. W., and Langosch, D. (2009) Sequence-specific conformational dynamics of model transmembrane domains determines their membrane fusogenic function, *Journal of Molecular Biology 386*, 733-741.

250. Stelzer, W., Poschner, B. C., Stalz, H., Heck, A. J., and Langosch, D. (2008) Sequence-specific conformational flexibility of SNARE transmembrane helices probed by hydrogen/deuterium exchange, *Biophysical Journal 95*, 1326-1335.

251. Bahar, I., Wallqvist, A., Covell, D., and Jernigan, R. (1998) Correlation between native-state hydrogen exchange and cooperative residue fluctuations from a simple model, *Biochemistry 37*, 1067-1075.

252. Demmers, J. A., Haverkamp, J., Heck, A. J., Koeppe, R. E., and Killian, J. A. (2000) Electrospray ionization mass spectrometry as a tool to analyze hydrogen/deuterium exchange kinetics of transmembrane peptides in lipid bilayers, *Proceedings of the National Academy of Sciences 97*, 3189-3194.

253. Zhuang, T., Jap, B. K., and Sanders, C. R. (2011) Solution NMR Approaches for Establishing Specificity of Weak Heterodimerization of Membrane Proteins, *Journal of the American Chemical Society 133*, 20571-20580.

254. Kroenke, C. D., Ziemnicka-Kotula, D., Xu, J., Kotula, L., and Palmer, A. G. (1997) Solution Conformations of a Peptide Containing the Cytoplasmic Domain Sequence of the β Amyloid Precursor Protein†, *Biochemistry 36*, 8145-8152.

255. Ramelot, T. A., Gentile, L. N., and Nicholson, L. K. (2000) Transient Structure of the Amyloid Precursor Protein Cytoplasmic Tail Indicates Preordering of Structure for Binding to Cytosolic Factors†, *Biochemistry 39*, 2714-2725.

256. Osenkowski, P., Li, H., Ye, W., Li, D., Aeschbach, L., Fraering, P. C., Wolfe, M. S., Selkoe, D. J., and Li, H. (2009) Cryoelectron Microscopy Structure of Purified γ-Secretase at 12 Å Resolution, *Journal of Molecular Biology 385*, 642-652.

257. Renzi, F., Zhang, X., Rice, W. J., Torres-Arancivia, C., Gomez-Llorente, Y., Diaz, R., Ahn, K., Yu, C., Li, Y.-M., Sisodia, S. S., and Ubarretxena-Belandia, I. (2011) Structure of γ-Secretase and Its Trimeric Pre-activation Intermediate by Single-particle Electron Microscopy, *Journal of Biological Chemistry 286*, 21440-21449.

258. Urban, S. (2010) Taking the plunge: integrating structural, enzymatic and computational insights into a unified model for membrane-immersed rhomboid proteolysis, *Biochem J 425*, 501 - 512.

259. Wolfe, M. S. (2009) Intramembrane proteolysis, *Chemical Reviews 109*, 1599-1612.

260. Coomaraswamy, J., Kilger, E., Wölfing, H., Schäfer, C., Kaeser, S. A., Wegenast-Braun, B. M., Hefendehl, J. K., Wolburg, H., Mazzella, M., Ghiso, J., Goedert, M., Akiyama, H., Garcia-Sierra, F., Wolfer, D. P., Mathews, P. M., and Jucker, M. (2010) Modeling familial Danish dementia in mice supports the concept of the amyloid hypothesis of Alzheimer's disease, *Proceedings of the National Academy of Sciences 107*, 7969-7974.

261. Barrett, P. J., Sanders, C. R., Kaufman, S. A., Michelsen, K., and Jordan, J. B. (2011) NSAID-Based γ-Secretase Modulators Do Not Bind to the Amyloid-β Polypeptide, *Biochemistry 50*, 10328-10342.

262. Brookmeyer, R., Johnson, E., Ziegler-Graham, K., and Arrighi, H. M. (2007) Forecasting the global burden of Alzheimer's disease, *Alzheimers Dement 3*, 186-191.

263. Oehlrich, D., Berthelot, D. J., and Gijsen, H. J. (2010) Gamma-Secretase Modulators as Potential Disease Modifying Anti-Alzheimer's Drugs, *J Med Chem*.

264. Tiraboschi, P., Hansen, L. A., Thal, L. J., and Corey-Bloom, J. (2004) The importance of neuritic plaques and tangles to the development and evolution of AD, *Neurology 62*, 1984-1989.

265. Glenner, G. G., and Wong, C. W. (1984) Alzheimer's disease: initial report of the purification and characterization of a novel cerebrovascular amyloid protein, *Biochem Biophys Res Commun 120*, 885-890.

266. Glenner, G. G., Wong, C. W., Quaranta, V., and Eanes, E. D. (1984) The amyloid deposits in Alzheimer's disease: their nature and pathogenesis, *Appl Pathol 2*, 357-369.

267. Masters, C. L., Multhaup, G., Simms, G., Pottgiesser, J., Martins, R. N., and Beyreuther, K. (1985) Neuronal origin of a cerebral amyloid: neurofibrillary tangles of Alzheimer's disease contain the same protein as the amyloid of plaque cores and blood vessels, *EMBO J 4*, 2757-2763.

268. Masters, C. L., Simms, G., Weinman, N. A., Multhaup, G., McDonald, B. L., and Beyreuther, K. (1985) Amyloid plaque core protein in Alzheimer disease and Down syndrome, *Proc Natl Acad Sci U S A 82*, 4245-4249.

269. Hardy, J. A., and Higgins, G. A. (1992) Alzheimer's disease: the amyloid cascade hypothesis, *Science 256*, 184-185.

270. Hardy, J., and Selkoe, D. J. (2002) The amyloid hypothesis of Alzheimer's disease: progress and problems on the road to therapeutics, *Science 297*, 353-356.

271. Grill, J. D., and Cummings, J. L. Current therapeutic targets for the treatment of Alzheimer's disease, *Expert Rev Neurother 10*, 711-728.

272. Galimberti, D., and Scarpini, E. Alzheimer's disease: from pathogenesis to disease-modifying approaches, *CNS Neurol Disord Drug Targets 10*, 163-174.

273. Aguzzi, A., and O'Connor, T. Protein aggregation diseases: pathogenicity and therapeutic perspectives, *Nat Rev Drug Discov 9*, 237-248.

274. Weggen, S., Rogers, M., and Eriksen, J. (2007) NSAIDs: small molecules for prevention of Alzheimer's disease or precursors for future drug development?, *Trends Pharmacol Sci 28*, 536-543.

275. Imbimbo, B. P. (2009) An update on the efficacy of non-steroidal anti-inflammatory drugs in Alzheimer's disease, *Expert Opin Investig Drugs 18*, 1147-1168.

276. Imbimbo, B. P. (2009) Why did tarenflurbil fail in Alzheimer's disease?, *J Alzheimers Dis 17*, 757-760.

277. Weggen, S., Eriksen, J. L., Das, P., Sagi, S. A., Wang, R., Pietrzik, C. U., Findlay, K. A., Smith, T. E., Murphy, M. P., Bulter, T., Kang, D. E., Marquez-Sterling, N., Golde, T. E., and Koo, E. H. (2001) A subset of NSAIDs lower amyloidogenic Abeta42 independently of cyclooxygenase activity, *Nature 414*, 212-216.

278. Eriksen, J. L., Sagi, S. A., Smith, T. E., Weggen, S., Das, P., McLendon, D. C., Ozols, V. V., Jessing, K. W., Zavitz, K. H., Koo, E. H., and Golde, T. E. (2003) NSAIDs and enantiomers

of flurbiprofen target gamma-secretase and lower Abeta 42 in vivo, *J Clin Invest 112*, 440-449.

279. Kukar, T. L., Ladd, T. B., Bann, M. A., Fraering, P. C., Narlawar, R., Maharvi, G. M., Healy, B., Chapman, R., Welzel, A. T., Price, R. W., Moore, B., Rangachari, V., Cusack, B., Eriksen, J., Jansen-West, K., Verbeeck, C., Yager, D., Eckman, C., Ye, W., Sagi, S., Cottrell, B. A., Torpey, J., Rosenberry, T. L., Fauq, A., Wolfe, M. S., Schmidt, B., Walsh, D. M., Koo, E. H., and Golde, T. E. (2008) Substrate-targeting gamma-secretase modulators, *Nature 453*, 925-929.

280. Beel, A. J., Barrett, P., Schnier, P. D., Hitchcock, S. A., Bagal, D., Sanders, C. R., and Jordan, J. B. (2009) Nonspecificity of binding of gamma-secretase modulators to the amyloid precursor protein, *Biochemistry 48*, 11837-11839.

281. Richter, L., Munter, L. M., Ness, J., Hildebrand, P. W., Dasari, M., Unterreitmeier, S., Bulic, B., Beyermann, M., Gust, R., Reif, B., Weggen, S., Langosch, D., and Multhaup, G. Amyloid beta 42 peptide (Abeta42)-lowering compounds directly bind to Abeta and interfere with amyloid precursor protein (APP) transmembrane dimerization, *Proc Natl Acad Sci U S A 107*, 14597-14602.

282. Botev, A., Munter, L. M., Wenzel, R., Richter, L., Althoff, V., Ismer, J., Gerling, U., Weise, C., Koksch, B., Hildebrand, P. W., Bittl, R., and Multhaup, G. The amyloid precursor protein C-terminal fragment C100 occurs in monomeric and dimeric stable conformations and binds gamma-secretase modulators, *Biochemistry 50*, 828-835.

283. Coan, K. E., and Shoichet, B. K. (2008) Stoichiometry and physical chemistry of promiscuous aggregate-based inhibitors, *J Am Chem Soc 130*, 9606-9612.

284. Lendel, C., Bolognesi, B., Wahlstrom, A., Dobson, C. M., and Graslund, A. Detergent-like interaction of Congo red with the amyloid beta peptide, *Biochemistry 49*, 1358-1360.

285. Harmeier, A., Wozny, C., Rost, B. R., Munter, L. M., Hua, H., Georgiev, O., Beyermann, M., Hildebrand, P. W., Weise, C., Schaffner, W., Schmitz, D., and Multhaup, G. (2009) Role of amyloid-beta glycine 33 in oligomerization, toxicity, and neuronal plasticity, *J Neurosci 29*, 7582-7590.

286. Schmechel, A., Zentgraf, H., Scheuermann, S., Fritz, G., Pipkorn, R., Reed, J., Beyreuther, K., Bayer, T. A., and Multhaup, G. (2003) Alzheimer beta-amyloid homodimers facilitate A beta fibrillization and the generation of conformational antibodies, *J Biol Chem 278*, 35317-35324.

287. Ash, M., and Ash, I. (2010) *The Handbook of Industrial Surfactants*, Synapse Information Resources, Inc., Endicott, NY.

288. Roher, A. E., Chaney, M. O., Kuo, Y. M., Webster, S. D., Stine, W. B., Haverkamp, L. J., Woods, A. S., Cotter, R. J., Tuohy, J. M., Krafft, G. A., Bonnell, B. S., and Emmerling, M. R. (1996) Morphology and toxicity of Abeta-(1-42) dimer derived from neuritic and vascular amyloid deposits of Alzheimer's disease, *J Biol Chem 271*, 20631-20635.

289. Farrow, N. A., Muhandiram, R., Singer, A. U., Pascal, S. M., Kay, C. M., Gish, G., Shoelson, S. E., Pawson, T., Forman-Kay, J. D., and Kay, L. E. (1994) Backbone dynamics of a free and phosphopeptide-complexed Src homology 2 domain studied by 15N NMR relaxation, *Biochemistry 33*, 5984-6003.

290. Kay, L. E., Torchia, D. A., and Bax, A. (1989) Backbone dynamics of proteins as studied by 15N inverse detected heteronuclear NMR spectroscopy: application to staphylococcal nuclease, *Biochemistry 28*, 8972-8979.

291. Cavanagh, J., Fairbrother, W. J., Palmer, A. G., and Skelton, N. J. (1996) *Protein NMR Spectroscopy: Principles and Practice*, Academic Press, San Diego, CA.

292. Zheng, G., Stait-Gardner, T., Anil Kumar, P. G., Torres, A. M., and Price, W. S. (2008) PGSTE-WATERGATE: an STE-based PGSE NMR sequence with excellent solvent suppression, *J Magn Reson 191*, 159-163.

293. Wilkins, D. K., Grimshaw, S. B., Receveur, V., Dobson, C. M., Jones, J. A., and Smith, L. J. (1999) Hydrodynamic radii of native and denatured proteins measured by pulse field gradient NMR techniques, *Biochemistry 38*, 16424-16431.

294. Cheng, Y., Judd, T., Bartberger, M., Chen, K., Fremeau, R., Hickman, D., Hitchcock, S., Jordan, J., Li, V., Lopez, P., Louie, S., Luo, Y., Michelsen, K., Nixey, T., Powers, T., Rattan, C., Sickmier, E., St. Jean, D., Wahl, R., Wen, P., and Wood, S. (2011) From Fragment Screening to In Vivo Efficacy: Optimization of a Series of 2-Aminoquinolines as Potent Inhibitors of BACE1 *J Med Chem*.

295. Zettl, H., Weggen, S., Schneider, P., and Schneider, G. Exploring the chemical space of gamma-secretase modulators, *Trends Pharmacol Sci 31*, 402-410.

296. Feng, B. Y., and Shoichet, B. K. (2006) Synergy and antagonism of promiscuous inhibition in multiple-compound mixtures, *J Med Chem 49*, 2151-2154.

297. McGovern, S. L., Caselli, E., Grigorieff, N., and Shoichet, B. K. (2002) A common mechanism underlying promiscuous inhibitors from virtual and high-throughput screening, *J Med Chem 45*, 1712-1722.

298. Feng, B. Y., Toyama, B. H., Wille, H., Colby, D. W., Collins, S. R., May, B. C., Prusiner, S. B., Weissman, J., and Shoichet, B. K. (2008) Small-molecule aggregates inhibit amyloid polymerization, *Nat Chem Biol 4*, 197-199.

299. McGovern, S. L., Helfand, B. T., Feng, B., and Shoichet, B. K. (2003) A specific mechanism of nonspecific inhibition, *J Med Chem 46*, 4265-4272.

300. Giannetti, A. M., Koch, B. D., and Browner, M. F. (2008) Surface plasmon resonance based assay for the detection and characterization of promiscuous inhibitors, *J Med Chem 51*, 574-580.

301. Lleo, A., Berezovska, O., Herl, L., Raju, S., Deng, A., Bacskai, B. J., Frosch, M. P., Irizarry, M., and Hyman, B. T. (2004) Nonsteroidal anti-inflammatory drugs lower Abeta42 and change presenilin 1 conformation, *Nat Med 10*, 1065-1066.

302. Berezovska, O., Lleo, A., Herl, L. D., Frosch, M. P., Stern, E. A., Bacskai, B. J., and Hyman, B. T. (2005) Familial Alzheimer's disease presenilin 1 mutations cause alterations in the conformation of presenilin and interactions with amyloid precursor protein, *J Neurosci 25*, 3009-3017.

303. Uemura, K., Lill, C. M., Li, X., Peters, J. A., Ivanov, A., Fan, Z., DeStrooper, B., Bacskai, B. J., Hyman, B. T., and Berezovska, O. (2009) Allosteric modulation of PS1/gamma-secretase conformation correlates with amyloid beta(42/40) ratio, *PLoS One 4*, e7893.

304. Gamerdinger, M., Clement, A. B., and Behl, C. (2008) Effects of sulindac sulfide on the membrane architecture and the activity of gamma-secretase, *Neuropharmacology 54*, 998-1005.

305. Uemura, K., Farner, K. C., Hashimoto, T., Nasser-Ghodsi, N., Wolfe, M. S., Koo, E. H., Hyman, B. T., and Berezovska, O. Substrate docking to gamma-secretase allows access of gamma-secretase modulators to an allosteric site, *Nat Commun 1*, 130.

306. Page, R. M., Gutsmiedl, A., Fukumori, A., Winkler, E., Haass, C., and Steiner, H. Beta-amyloid precursor protein mutants respond to gamma-secretase modulators, *J Biol Chem 285*, 17798-17810.

307. O'Brien, R. J., and Wong, P. C. (2011) Amyloid precursor protein processing and Alzheimer's disease, *Annu. Rev. Neurosci. 34*, 185-204.

308. Selkoe, D. J. (2011) Alzheimer's disease, *Cold Spring Harb.Perspect.Biol. 3*, a004457.

309. Vetrivel, K. S., and Thinakaran, G. (2010) Membrane rafts in Alzheimer's disease beta-amyloid production, *Biochim. Biophys. Acta 1801*, 860-867.

310. Ehehalt, R., Keller, P., Haass, C., Thiele, C., and Simons, K. (2003) Amyloidogenic processing of the Alzheimer beta-amyloid precursor protein depends on lipid rafts, *J. Cell Biol. 160*, 113-123.

311. Beel, A. J., Sakakura, M., Barrett, P. J., and Sanders, C. R. (2010) Direct binding of cholesterol to the amyloid precursor protein: An important interaction in lipid-Alzheimer's disease relationships?, *Biochim. Biophys. Acta 1801*, 975-982.

312. Rushworth, J. V., and Hooper, N. M. (2010) Lipid Rafts: Linking Alzheimer's Amyloid-beta Production, Aggregation, and Toxicity at Neuronal Membranes, *Int. J. Alzheimers Dis. 2011*, 603052.

313. Wahrle, S., Das, P., Nyborg, A. C., McLendon, C., Shoji, M., Kawarabayashi, T., Younkin, L. H., Younkin, S. G., and Golde, T. E. (2002) Cholesterol-dependent gamma-secretase activity in buoyant cholesterol-rich membrane microdomains, *Neurobiol. Dis. 9*, 11-23.

314. Hicks, D. A., Nalivaeva, N. N., and Turner, A. J. (2012) Lipid rafts and Alzheimer's disease: protein-lipid interactions and perturbation of signaling, *Front. Physiol. 3*, 189.

315. Jafurulla, M., Tiwari, S., and Chattopadhyay, A. (2011) Identification of cholesterol recognition amino acid consensus (CRAC) motif in G-protein coupled receptors, *Biochemical and Biophysical Research Communications 404*, 569-573.

316. Epand, R. M., Sayer, B. G., and Epand, R. F. (2005) Caveolin scaffolding region and cholesterol-rich domains in membranes, *Journal of Molecular Biology 345*, 339-350.

317. Calderon, R. O., Attema, B., and DeVries, G. H. (1995) Lipid composition of neuronal cell bodies and neurites from cultured dorsal root ganglia, *J. Neurochem. 64*, 424-429.

318. van Meer, G., Voelker, D. R., and Feigenson, G. W. (2008) Membrane lipids: where they are and how they behave, *Nat. Rev. Mol. Cell. Biol. 9*, 112-124.

319. Wood, W. G., Cornwell, M., and Williamson, L. S. (1989) High performance thin-layer chromatography and densitometry of synaptic plasma membrane lipids, *J. Lipid Res. 30*, 775-779.

320. Mesmin, B., and Maxfield, F. R. (2009) Intracellular sterol dynamics, *Biochim. Biophys. Acta 1791*, 636-645.

321. Girard, P., Pecreaux, J., Lenoir, G., Falson, P., Rigaud, J. L., and Bassereau, P. (2004) A new method for the reconstitution of membrane proteins into giant unilamellar vesicles, *Biophys. J. 87*, 419-429.

322. de Almeida, R. F., Fedorov, A., and Prieto, M. (2003) Sphingomyelin/phosphatidylcholine/cholesterol phase diagram: boundaries and composition of lipid rafts, *Biophys. J. 85*, 2406-2416.

323. Ionova, I. V., Livshits, V. A., and Marsh, D. (2012) Phase diagram of ternary cholesterol/palmitoylsphingomyelin/palmitoyloleoyl-phosphatidylcholine mixtures: spin-label EPR study of lipid-raft formation, *Biophys. J. 102*, 1856-1865.

324. Veatch, S. L., and Keller, S. L. (2005) Miscibility phase diagrams of giant vesicles containing sphingomyelin, *Phys. Rev. Lett. 94*, 148101.

325. Zhao, J., Wu, J., Shao, H., Kong, F., Jain, N., Hunt, G., and Feigenson, G. (2007) Phase studies of model biomembranes: macroscopic coexistence of Lalpha+Lbeta, with light-induced coexistence of Lalpha+Lo Phases, *Biochim. Biophys. Acta 1768*, 2777-2786.

326. Veatch, S. L. (2007) Electro-formation and fluorescence microscopy of giant vesicles with coexisting liquid phases, *Methods Mol. Biol. 398*, 59-72.

327. Eliceiri, K. W., Berthold, M. R., Goldberg, I. G., Ibanez, L., Manjunath, B. S., Martone, M. E., Murphy, R. F., Peng, H., Plant, A. L., Roysam, B., Stuurman, N., Swedlow, J. R., Tomancak, P., and Carpenter, A. E. (2012) Biological imaging software tools, *Nat. Methods 9*, 697-710.

328. van Meer, G., Voelker, D. R., and Feigenson, G. W. (2008) Membrane lipids: where they are and how they behave, *Nat Rev Mol Cell Biol 9*, 112-124.

329. Epand, R. M. (2008) Proteins and cholesterol-rich domains, *Biochimica et Biophysica Acta (BBA)-Biomembranes 1778*, 1576-1582.

330. Lemmon, M. A., Treutlein, H. R., Adams, P. D., Brünger, A. T., and Engelman, D. M. (1994) A dimerization motif for transmembrane α–helices, *Nature Structural & Molecular Biology 1*, 157-163.

331. MacKenzie, K. R., Prestegard, J. H., and Engelman, D. M. (1997) A transmembrane helix dimer: structure and implications, *Science 276*, 131-133.

332. Kim, S., Jeon, T.-J., Oberai, A., Yang, D., Schmidt, J. J., and Bowie, J. U. (2005) Transmembrane glycine zippers: physiological and pathological roles in membrane proteins, *Proceedings of the National Academy of Sciences of the United States of America 102*, 14278-14283.

333. Miyashita, N., Straub, J. E., Thirumalai, D., and Sugita, Y. (2009) Transmembrane Structures of Amyloid Precursor Protein Dimer Predicted by Replica-Exchange Molecular Dynamics Simulations, *Journal of the American Chemical Society 131*, 3438-3439.

334. Beattie, M. E., Veatch, S. L., Stottrup, B. L., and Keller, S. L. (2005) Sterol structure determines miscibility versus melting transitions in lipid vesicles, *Biophysical journal 89*, 1760-1768.

335. Wenz, J. J. (2012) Predicting the effect of steroids on membrane biophysical properties based on the molecular structure, *Biochim.Biophys.Acta 1818*, 896-906.

336. Xu, X., and London, E. (2000) The effect of sterol structure on membrane lipid domains reveals how cholesterol can induce lipid domain formation, *Biochemistry 39*, 843-849.

337. Kahya, N. (2010) Protein-protein and protein-lipid interactions in domain-assembly: lessons from giant unilamellar vesicles, *Biochimica et biophysica acta 1798*, 1392-1398.

338. Girard, P., Pecreaux, J., Lenoir, G., Falson, P., Rigaud, J. L., and Bassereau, P. (2004) A new method for the reconstitution of membrane proteins into giant unilamellar vesicles, *Biophysical journal 87*, 419-429.

339. de Almeida, R. F., Fedorov, A., and Prieto, M. (2003) Sphingomyelin/phosphatidylcholine/cholesterol phase diagram: boundaries and composition of lipid rafts, *Biophys.J 85*, 2406-2416.

340. Ionova, I. V., Livshits, V. A., and Marsh, D. (2012) Phase diagram of ternary cholesterol/palmitoylsphingomyelin/palmitoyloleoyl-phosphatidylcholine mixtures: spin-label EPR study of lipid-raft formation, *Biophysical journal 102*, 1856-1865.

341. Veatch, S. L., and Keller, S. L. (2005) Miscibility phase diagrams of giant vesicles containing sphingomyelin, *Physical review letters 94*, 148101.

342. Calderon, R. O., Attema, B., and DeVries, G. H. (1995) Lipid composition of neuronal cell bodies and neurites from cultured dorsal root ganglia, *Journal of neurochemistry 64*, 424-429.

343. van Meer, G., Voelker, D. R., and Feigenson, G. W. (2008) Membrane lipids: where they are and how they behave, *Nature reviews. Molecular cell biology 9*, 112-124.

344. Wood, W. G., Cornwell, M., and Williamson, L. S. (1989) High performance thin-layer chromatography and densitometry of synaptic plasma membrane lipids, *Journal of lipid research 30*, 775-779.

345. Mesmin, B., and Maxfield, F. R. (2009) Intracellular sterol dynamics, *Biochim.Biophys.Acta 1791*, 636-645.

346. Song, Y. H., E.J; Brandon, S.; Sanders, C.R. (2013) Competition Between Homodimerization and Cholesterol Binding to the C99 Domain of the Amyloid Precursor Protein, *Biochemistry 52*, XXX-XXX.

347. Veatch, S. L., and Keller, S. L. (2005) Seeing spots: complex phase behavior in simple membranes, *Biochim.Biophys.Acta 1746*, 172-185.

348. Levental, I., Grzybek, M., and Simons, K. (2010) Greasing their way: lipid modifications determine protein association with membrane rafts, *Biochemistry 49*, 6305-6316.

349. Zhao, J., Wu, J., Heberle, F. A., Mills, T. T., Klawitter, P., Huang, G., Costanza, G., and Feigenson, G. W. (2007) Phase studies of model biomembranes: complex behavior of DSPC/DOPC/cholesterol, *Biochim. Biophys. Acta 1768*, 2764-2776.

350. Sagi, S. A., Lessard, C. B., Winden, K. D., Maruyama, H., Koo, J. C., Weggen, S., Kukar, T. L., Golde, T. E., and Koo, E. H. (2011) Substrate sequence influences γ-secretase modulator activity, role of the transmembrane domain of the amyloid precursor protein, *Journal of Biological Chemistry 286*, 39794-39803.

351. Wahrle, S., Das, P., Nyborg, A. C., McLendon, C., Shoji, M., Kawarabayashi, T., Younkin, L. H., Younkin, S. G., and Golde, T. E. (2002) Cholesterol-Dependent γ-Secretase Activity in Buoyant Cholesterol-Rich Membrane Microdomains, *Neurobiology of Disease 9*, 11-23.

352. Osenkowski, P., Ye, W., Wang, R., Wolfe, M. S., and Selkoe, D. J. (2008) Direct and potent regulation of γ-secretase by its lipid microenvironment, *Journal of Biological Chemistry 283*, 22529-22540.

353. Schafer, L. V., de Jong, D. H., Holt, A., Rzepiela, A. J., de Vries, A. H., Poolman, B., Killian, J. A., and Marrink, S. J. (2011) Lipid packing drives the segregation of transmembrane helices into disordered lipid domains in model membranes, *Proceedings of the National Academy of Sciences of the United States of America 108*, 1343-1348.

354. Silvius, J. R. (2005) Partitioning of membrane molecules between raft and non-raft domains: insights from model-membrane studies, *Biochimica et biophysica acta 1746*, 193-202.

355. Vidal, A., and McIntosh, T. J. (2005) Transbilayer peptide sorting between raft and nonraft bilayers: comparisons of detergent extraction and confocal microscopy, *Biophysical journal 89*, 1102-1108.

356. Lin, Q., and London, E. (2013) Altering hydrophobic sequence lengths shows that hydrophobic mismatch controls affinity for ordered lipid domains (rafts) in the multitransmembrane strand protein perfringolysin O, *The Journal of biological chemistry 288*, 1340-1352.

357. Kaiser, H. J., Orlowski, A., Rog, T., Nyholm, T. K., Chai, W., Feizi, T., Lingwood, D., Vattulainen, I., and Simons, K. (2011) Lateral sorting in model membranes by cholesterol-mediated hydrophobic matching, *Proceedings of the National Academy of Sciences of the United States of America 108*, 16628-16633.

358. Bhattacharyya, R., Barren, C., and Kovacs, D. M. (2013) Palmitoylation of amyloid precursor protein regulates amyloidogenic processing in lipid rafts, *The Journal of neuroscience : the official journal of the Society for Neuroscience 33*, 11169-11183.

359. Vetrivel, K. S., and Thinakaran, G. (2010) Membrane rafts in Alzheimer's disease beta-amyloid production, *Biochim.Biophys.Acta 1801*, 860-867.

360. Beel, A. J., Sakakura, M., Barrett, P. J., and Sanders, C. R. (2010) Direct binding of cholesterol to the amyloid precursor protein: An important interaction in lipid-Alzheimer's disease relationships?, *Biochim.Biophys.Acta 1801*, 975-982.

361. Rushworth, J. V., and Hooper, N. M. (2010) Lipid Rafts: Linking Alzheimer's Amyloid-beta Production, Aggregation, and Toxicity at Neuronal Membranes, *Int.J Alzheimers.Dis. 2011*, 603052.

362. Ehehalt, R., Keller, P., Haass, C., Thiele, C., and Simons, K. (2003) Amyloidogenic processing of the Alzheimer beta-amyloid precursor protein depends on lipid rafts, *J.Cell Biol. 160*, 113-123.

363. Wahrle, S., Das, P., Nyborg, A. C., McLendon, C., Shoji, M., Kawarabayashi, T., Younkin, L. H., Younkin, S. G., and Golde, T. E. (2002) Cholesterol-dependent gamma-secretase activity in buoyant cholesterol-rich membrane microdomains, *Neurobiol.Dis. 9*, 11-23.

364. Hicks, D. A., Nalivaeva, N. N., and Turner, A. J. (2012) Lipid rafts and Alzheimer's disease: protein-lipid interactions and perturbation of signaling, *Front Physiol 3*, 189.

365. Bodovitz, S., and Klein, W. L. (1996) Cholesterol modulates alpha-secretase cleavage of amyloid precursor protein, *J.Biol.Chem. 271*, 4436-4440.

366. Kojro, E., Gimpl, G., Lammich, S., Marz, W., and Fahrenholz, F. (2001) Low cholesterol stimulates the nonamyloidogenic pathway by its effect on the alpha -secretase ADAM 10, *Proc.Natl.Acad.Sci.U.S.A 98*, 5815-5820.

367. Simons, K., and Ikonen, E. (1997) Functional rafts in cell membranes, *Nature 387*, 569-572.

368. Binder, W. H., Barragan, V., and Menger, F. M. (2003) Domains and rafts in lipid membranes, *Angewandte Chemie International Edition 42*, 5802-5827.

369. Tong, J., Briggs, M. M., Mlaver, D., Vidal, A., and McIntosh, T. J. (2009) Sorting of Lens Aquaporins and Connexins into Raft and Nonraft Bilayers: Role of Protein Homo-Oligomerization, *Biophysical Journal 97*, 2493-2502.

370. Nikolaus, J., Scolari, S., Bayraktarov, E., Jungnick, N., Engel, S., Plazzo, A. P., Stöckl, M., Volkmer, R., Veit, M., and Herrmann, A. (2010) Hemagglutinin of Influenza Virus Partitions into the Nonraft Domain of Model Membranes, *Biophysical Journal 99*, 489-498.

371. Holmes, O., Paturi, S., Ye, W., Wolfe, M. S., and Selkoe, D. J. (2012) Effects of Membrane Lipids on the Activity and Processivity of Purified γ-Secretase, *Biochemistry 51*, 3565-3575.

372. Baumgart, T., Hammond, A. T., Sengupta, P., Hess, S. T., Holowka, D. A., Baird, B. A., and Webb, W. W. (2007) Large-scale fluid/fluid phase separation of proteins and lipids in giant plasma membrane vesicles, *Proceedings of the National Academy of Sciences 104*, 3165-3170.